Stochastic Modeling of Reversible Biochemical Reaction-Diffusion Systems and High-Resolution Shock-Capturing Methods for Fluid Interfaces

Mauricio J Del Razo Sarmina

A dissertation submitted in partial fulfillment of the
requirements for the degree of

Doctor of Philosophy

University of Washington

2016

Reading Committee:

Randall J. LeVeque, Chair

Hong Qian, Chair

Ulrich L. Hetmaniuk

Thomas J. Matula

Program Authorized to Offer Degree:
Department of Applied Mathematics

University of Washington

Abstract

Stochastic Modeling of Reversible Biochemical Reaction-Diffusion Systems and High-Resolution Shock-Capturing Methods for Fluid Interfaces

Mauricio J Del Razo Sarmina

Co-Chairs of the Supervisory Committee:
Professor Randall J. LeVeque
Department of Applied Mathematics

Professor Hong Qian
Department of Applied Mathematics

My thesis contains two parts, both of which are motivated by biological problems. One is on stochastic reaction-diffusion for biochemical systems and the other on shock-capturing methods for fluid interfaces. In both parts, conservation laws are key to determine the dynamics and effective numerical methods.

The first part is motivated by the need for quantitative mathematical models for cell-scale biological systems. Such a mathematical description must be inherently stochastic where the chancy reaction process is mediated by diffusion encounter. Diffusion-influenced reaction theory describes this coupling between diffusion and reaction. We apply this theory to theoretical and numerical kinetic Monte Carlo studies of the robustness of fluorescence correlation spectroscopy (FCS) theory, a widely used experimental method to determine chemical rate constants and diffusion coefficients of stochastic reaction-diffusion systems. We found that current FCS theory can produce significant errors at cell-scales. In addition, we developed a framework to understand diffusion-influenced reaction theory from a stochastic perspective. For irreversible bimolecular reactions, the theory is derived by introducing absorbing boundary conditions to overdamped Brownian motion theory. This provides a clear stochastic interpretation that describes the probability distribution dynamics and the stochastic sample trajectories. However, the stochastic interpretation is not clear for reversible reactions modeled with a back-reaction boundary condition. In order to address this, we developed a discrete stochastic model that conserves probability and recovers the classical equations in the continuous limit. In the case of reversible reactions, it recovers the back-reaction boundary condition and provides an accurate stochastic interpretation. We also explore extensions of this model and its relation to nonequilibrium stochastic processes as well as extensions into volume reactivity using coupled-diffusion processes.

The second part was inspired by a collaboration with experimentalists at Seattle's Veterans Administration (VA) Hospital, who are studying the underlying biological mechanisms behind blast-induced traumatic brain injury (TBI). To better understand the effect of shock waves on the brain, we have investigated an in vitro model in which blood-brain barrier endothelial cells are grown in fluid-filled transwell vessels, placed inside a shock tube and exposed to shocks. As it is difficult to experimentally measure the forces inside the transwell, we developed a computational model of the experimental setup to measure them. First, we implemented a one-dimensional model using Euler equations coupled with a Tammann equation of state (EOS) to model the different materials and interfaces within the experimental setup. From this model, we learned that we can neglect very thin interfaces in our computations. Using this result, we implemented a three-dimensional wave propagation framework modeled with two-dimensional axisymmetric Euler equations and a Tammann EOS. In order to solve these equations, we used high-resolution conservative methods and implemented new Riemann solvers into the Clawpack software in a mixed Eulerian/Lagrangian frame of reference. We found that pressures can fall below vapor pressure due to the interaction of reflecting and diffracting shock waves, suggesting that cavitation bubbles could be a damage mechanism. We also show extensions of this model that allow the implementation of mapped grids and adaptive mesh refinement.

A las raíces de mi familia:

Magrande, Bishara (جد) y Abi,

a sus más recientes miembros,

Elías Nayi y Bruno Leandro,

y a mi madre que nos

mantiene unidos.

ACKNOWLEDGMENTS

I wish to express my gratitude to several individuals that not only made this dissertation possible but also made this endeavor worth pursuing. First and foremost, I am deeply grateful to my two advisors, Hong Qian and Randy LeVeque, for their continuous support, encouragement and guidance. Through their unique work styles, distinctive enthusiasm and sincere advice, they have revealed two different approaches to research and life that have helped me shape my own path and refine my values. Hong and Randy, I will be forever thankful for this. I also wish to thank the rest of my reading committee, Tom Matula and Ulrich Hetmaniuk, for their helpful comments and revisions of this work during its different stages. Special thanks to Vladimir Minin for his interest and youthful advice, and to David Cook and the group at the VA Hospital for their valuable collaborations.

I would also like to thank other current and former members of the applied mathematics department. I thank Bernard Deconinck for his guidance during my first years in graduate school and Nathan Kutz for his interest in my future career. I am also very thankful to the members of my two research groups with whom I have learned and shared so much. Moreover, the day to day writing of this thesis would not have been possible without the camaraderie of my friends in the applied mathematics department. I am particularly grateful to Pedro for his friendship, blunt honesty and all the lunches and "philosophical walks" that kept the everyday routine interesting, or at least tasty.

I am also extremely grateful to my family. Thanks to my mother for her unconditional love and support that can cross any ocean or continent. Thanks to my brothers, Carlos and Jose Victor, for being my friends and role models; I still hope one day I will be able to grow a beard like you both. Thanks to my father for his advice, love and optimism. Also thanks to the rest of my family: Magrande, Doc, Zahia, Ricardo, Ximena, Mateo, Nicolas, Elías, Karla, Friedi and Bruno, without you none of this work makes any sense (although for you, all this mathematics might not make sense anyway). I am also very lucky to say I have friends that I can call brothers (from another mother): Alan, Borro, Carlos, Joanks, Marky and Ricky, thanks for always being there. Also thanks to my college friends who are now spread throughout the world, especially for the chat group messages that undoubtedly wake me up in the middle of the night.

I also want to thank my friends that have made these years in Seattle very special to me. Thanks to the Latona house founding members, McCoy, Miguel, Rod and Shapero, for all the good times and random experiences we have had together. I am also very thankful for all the other old and recent friendships that I have made in Seattle, especially the ones of Ben, Carlos and Lucas. I also want to thank "the Mexicans" and "the Chileans" for their cheerful spirit, rain or shine. Special thanks to Juana for providing a diet full of vitamin T.

I am also very grateful to Kristy and Craig for being my Seattle family and for preparing dinners and cakes for all my birthdays. Last but not least, I want to thank Adrienne for her love, patience and affection, as well as her wholehearted companionship throughout both joyful times and difficult moments.

I also wish to acknowledge the support from CONACYT and the Department of Applied Mathematics at the University of Washington, as well as partial support from NSF grant DMS-1216732 and Moore/Sloan Data Science Environment grant.

TABLE OF CONTENTS

PREFACE

The work presented in this thesis concerns two broad research areas within applied mathematics: stochastic processes and numerical analysis. My work in these two areas have followed distinct lines of studies and applications. Nonetheless, they have recently started to converge into my current research interest: *stochastic reaction-diffusion theory and numerical methods applied to cellular dynamics*. However, this convergence is not evident from the work performed during my doctoral dissertation, and it might still take a couple of years of research to bring it to light. Therefore, in order to keep the projects consistent and not to confuse the reader, the core of this dissertation is divided into two parts: *stochastic biochemical reaction-diffusion systems* and *high resolution shock-capturing methods for fluid interface problems*.

Although the applications of both research areas are unrelated, their mathematical core seems to have promising applicability in developing mathematical models and numerical methods for cellular dynamics. For instance, as the conservation of specific quantities can be fundamental to establish accurate dynamics in both areas, the ideas behind classic conservative numerical schemes can be highly relevant in the development of accurate numerical methods for stochastic processes. For these reasons, having acquired expertise in both research areas is fundamental for future research development, and both need to be included in this dissertation.

The outline of the thesis is as follows. In Chapter 1, we will provide a general motivation for both projects. Then, we will give a brief introduction to the two main parts of this thesis, stochastic reversible biochemical reaction-diffusion systems and shock-capturing numerical methods for fluid interface problems. We end the chapter with a small overview of the relation between conservative dynamics with hyperbolic conservation laws and with stochastic processes. Approaching problems from the point of view of conservative dynamics has the potential to unify these ares in future research.

The next chapters are divided into two main parts corresponding to the two projects. In the first part, Chapters 2 and 3 provide a comprehensive review of biochemical stochastic reaction processes, where most of the material does not correspond to novel results. Chapters 4, 5 and 6 all corresponds to novel developments published in [56], [57] and [58] respectively. In the second part, we follow a similar structure. Chapters 7 and 8 give an overview of high-resolution shock-capturing methods for interface problems, where most of the results were previously obtained elsewhere. Chapters 9, 10 and 11 all corresponds to novel work published

in [52], [55] and [53] respectively. A more detailed overview of each of these chapters will be provided in the introduction. The last chapter will summarize the main results of this thesis and relate this work with future projects in stochastic reaction-diffusion theory and numerical methods to study cellular dynamics.

LIST OF FIGURES

Chapter 1

INTRODUCTION

1.1 Motivation

In recent years, mathematical modeling of biological phenomena in medicine and life science has become a fundamental part in understanding biological processes [117]. The physical and mathematical models developed are often highly simplified versions of reality. Nonetheless, they have been able to provide great insights into the underlying mechanisms of biological processes. Unfortunately, a comprehensive understanding of biological phenomea is far beyond human reach, and its complexity challenges our current physical models and even their mathematical foundations [11, 116]. This inspires new paths of exploration that might lead to a better understanding not only of biology but also of mathematics and physics. It is in this context of symbiotic relation between mathematics, physics and biology where the motivation for this dissertation originated.

The work presented here was constructed within two of the main research areas in applied mathematics: stochastic processes and numerical analysis. These two areas have proved to be extremely useful in biological modeling. For instance, stochastic models of biochemical systems inside a cell are more comprehensive than their continuous counterpart [92, 205, 206, 207, 258], especially those of signaling networks involving transcription regulation and protein phosphorylation [258], like gene expression, where stochastic models provide unique consequences in cellular function [209, 131]. Moreover, more complex and better fitted numerical simulations are constantly required because of the increasing complexity of biological models and the cutting-edge biomedical research, as in biological fluid dynamics [25, 42, 74, 81, 152, 188, 176, 233] and molecular dynamics [130, 157, 180]. The utility provided by these two areas for biological applications is unquestionable. Approaching biological modeling with knowledge on both will help establish bridges between islands of knowledge and generate new questions that challenge our current paradigms in physics and mathematics.

One of the main subjects of this work will be applying stochastic processes to model biochemical reaction systems. These systems are the basis of cellular biological functions, and they often are open complex thermodynamic systems in aqueous medium with space-dependent dynamics [57, 138, 204, 206, 227, 258], played out by fluctuating populations of different chemical species that interact with each other. Consequently, their mathematical description must be stochastic, and it involves a small but significant number of diffusing species that can change their own state and react and interact with one an-

other. In chemical kinetic terms, these are called unimolecular and nonlinear reactions, respectively. Unfortunately, these processes are not yet fully understood from a stochastic perspective, so it is challenging to provide accurate stochastic models and simulations [4, 13, 28, 56, 57, 63, 77, 132, 133, 224, 237, 256, 257]. This is particularly difficult at reaction boundaries where the conservation of probability has to be enforced, while matching the expected behavior of an ensemble of particles. Consequently, understanding better the physics and mathematics behind stochastic reaction-diffusion processes at mesoscopic scales is fundamental to accurately model and simulate the dynamics of cellular biochemical reaction networks, such as specific pathways in cell signaling, E. Coli chemotaxis or even oncogenesis [205].

On the other hand, numerical methods applied to biological problems often deal with fluids and interfaces, another main subject of this work. An application relevant to this type of problems is traumatic brain injury (TBI); a leading cause of death and disability for people under the age of 45 years [272]. It is also associated with increased risk of developing neurologic diseases that include Alzheimer's disease, Parkinson's disease, and amyotrophic lateral sclerosis [31, 85, 149, 196]. As part of a collaboration within this work, experimental researchers at the Veterans Administration (VA) Hospital are investigating how repeated exposure to shock waves cause mild traumatic brain injury [38, 39, 40, 97, 109, 121, 143, 169, 172, 178, 213, 263]. Their laboratory is equipped with a shock-tube in which they can introduce samples of endothelial cells and measure the effects before and after the shock wave has passed. In order to provide better insight and feedback on the important mechanisms, they are interested in computational simulations of the interaction between the biological sample and the pressure shock waves. This often requires modeling the shock wave crossing an interface between a compressible and almost incompressible material, like air, plastic and water. Conservative numerical methods that couple these type of interfaces with shock wave dynamics are not yet fully developed and often depend on specific applications [148, 155, 248, 275] . As this and many other biomedical applications require simulations with this coupling, it is crucial to develop more general, efficient and accurate numerical methods to tackle them.

The research projects presented in this dissertation focus on developing theory, methods and biological applications of both areas within applied mathematics: stochastic processes and numerical analysis. The research in stochastic reaction-diffusion processes aims to accurately model biochemical reaction-diffusion systems at mesoscopic scales by assuring conservation of probability. This is relevant to understand biological processes ranging from cell biochemistry pathways to the fundamental origin of cancerous cells. The research in numerical methods aims to provide high-resolution shock-capturing conservative numerical methods for interface problems. This will provide insight into the underlying damage mechanisms in traumatic brain injury experiments. Although the projects presented here are motivated by independent and very different applications, the underlying mathematical

core of the research has promising applicability in stochastic reaction-diffusion processes and numerical methods for biochemical cellular dynamics.

1.2 Stochastic reversible biochemical reaction-diffusion systems

The ultimate goal of this research is to give a coherent and complete theory to model and simulate stochastic reaction-diffusion processes at mesoscopic scales. Having a cogent stochastic process formulation that accurately models biochemical reaction-diffusion systems is essential to develop accurate simulation algorithms and predictions for cellular and sub-cellular biochemical systems. The formulation along with the simulations would provide highly valuable insights on the behavior of fundamental biological processes at cellular scales.

In order to approach this problem, a brief review of spatially homogeneous biochemical reaction systems is provided in Chapter 2. The chapter begins exploring the relations between the deterministic approach, the stochastic approach, and some other approximations. It shows that the stochastic model given by the chemical master equation (CME) is more general, and it provides a more general description of chemical kinetics at a mesoscopic scale, as shown in [207, 206, 205]. To further show this claim, the simplest model that exhibits bistable behavior, called the Schlögl model, is studied using deterministic and stochastic dynamics, as done in [258]. The stochastic approach again proves to yield a much more rich description of the dynamics with different relevant time scales and truly bistable behavior independent of the initial conditions. Additionally, a couple of numerical methods are presented. Of particular relevance is the stochastic sampling given by the Gillespie algorithm [94], which allows to exactly simulate a trajectory following the appropriate probability density function without solving the CME. All these results are tied together by observing that the probability density function given by the CME and the trajectories of the Gillespie algorithm are just different representations of the same fundamental stochastic process, the Delbrück-Gillespie process [206].

In Chapter 3, within the context established by spatially homogeneous biochemical stochastic reaction systems, we begin to explore the spatially non-homogeneous system, i.e. biochemical stochastic reaction-diffusion systems. We begin by introducing the classic Smoluchowski problem [230], which yields the probability density function along with the reaction rate of a diffusion controlled bimolecular irreversible reaction undergoing Brownian motion. An extension of this model for a partially diffusion-controlled bimolecular irreversible reaction is given by Collins and Kimball [46, 47]. Furthermore, Kramers introduced the additional effect of an interaction potential [141], and Shoup and Szabo provided the connection to the first passage time problem as the inverse of the reaction rate [227]. However, biochemical reactions often involve reversible reactions that are not completely described by these models and involve the complexity of geminate recombinations when dealing with diffusion [3, 4, 13, 28, 135, 136, 224]. Nonetheless, there has been plenty of research in

kinetic Monte Carlo (KMC) methods and other numerical algorithms to simulate stochastic reaction-diffusion system [13, 41, 71, 77, 106, 107, 257, 278], many without a rigorous stochastic process foundation. Of particular interest is the reaction-diffusion master equation (RDME) used in MesoRD software [106] and pyURDME [64] as well as other algorithms and software as Smolydyn [13], FPKMC [63], eGFRD [237, 257] and others [223, 244, 268].

As an experimental application, in Chapter 4, we applied a part of this work to fluorescence correlation spectroscopy (FCS), an experimental technique to determine chemical reaction rates and diffusion coefficients that is sensitive to stochasticity and reaction-diffusion processes. A particle tracking simulation based on Collins and Kimball dynamics [46, 47] and Andrews algorithm [13] is implemented to simulate stochastic reaction-diffusion processes in bimolecular reactions. The simulation is coupled with a computational experiment of FCS to show that for a small number of molecules, like in cell biochemistry, the commonly used FCS theory fails. The theory's failure is because FCS uses a linear approximation to a non-linear problem. This fact is not commonly known by experimentalists, and it is important to point out under which circumstances it is relevant.

In Chapter 5, we develop a model for bimolecular reactions via diffusion encounter using a discrete stochastic process. The model is based on over-damped Langevin dynamics, and it unifies reversible diffusion-influenced reaction theory with a well defined stochastic interpretation, providing a clear underlying stochastic process and its probabilistic dynamics. It also clarifies the constant binding, unbinding and rebinding process that occurs at an absorption boundary, which is usually referred as geminate recombination process. In Chapter 6, a general model for stochastic reaction-diffusion processes is developed and analyzed. It provides insights and further understanding of the physical and mathematical mechanisms of biochemical stochastic reaction-diffusion systems as the CME did in the spatially homogeneous scenario. It could also help establish a new guideline for future and more appropriate simulation algorithms. Under limiting cases, it already recovers the Smoluchowski type models of [46, 47, 141, 227, 230]. We are doing ongoing research on this model.

1.3 Shock-capturing numerical methods for fluid interface problems

The main goal of this research is to develop high-resolution shock-capturing numerical methods for sharp interface problems. The work was inspired by a collaboration with an experimental group at Seattle's Veterans Administration (VA) Hospital. This group is studying the underlying biological mechanisms behind blast-induced traumatic brain injury (TBI) [194], a leading cause of death among people under 45 years old [272]. Their research is mostly in the context of affected civilians and soldiers in war zones; however, similar injuries have been observed in football players, boxers and car accidents [50].

Repetitive low-intensity non-impact blast wave exposure leads to mild TBI (mTBI), which similar to impact TBI, can initiate slow-developing and potentially permanent brain

disturbances [172, 39, 40, 38, 97, 121, 169, 178, 263]. It has been suggested that the injury mechanisms in mild TBI occur at very small length scales, even that of a single cell [55]. One of the main proposed hypotheses is blood-brain barrier (BBB) disruption [122, 143, 226]. The BBB is a highly selective permeability barrier formed around brain blood vessels that prevents passage of toxins from the blood into the brain. This collaboration with the VA Hospital produced experimental studies of BBB disruption related to blast-induced TBI as well as a computational model of the experiment [55]. The developed computational methods are likely to have applications not only in TBI but also on localized drug delivery [42, 81, 89], biofilm breaking [30, 183] and bone regeneration with shock-wave therapy [261]

The numerical algorithms to perform these simulations are briefly reviewed in Chapter 7. As we are interested in wave propagation and shock waves, we will phrase our problem in terms of hyperbolic systems of conservation laws, i.e. as a system of hyperbolic partial differential equations that express conservation of mass, momentum, energy and/or other physically relevant quantities. In order to solve these equations, we will use finite volume methods based on the first order accurate Godunov-type methods [155, 248]. These methods are further generalized to higher resolution methods with the aid of limiters. Although these methods are general for any hyperbolic system of conservation laws, they all require a specific solution of a fundamental problem called the Riemann problem. Even though the Riemann problem can be stated simply, its exact solution is not always trivial nor possible; however, several different approximate Riemann solvers exist [155, 215, 248]. Numerical methods for hyperbolic conservation laws are very well developed; however, the implementation of interfaces is still a research area. In Chapter 8, we show the essential numerical methods we developed to deal with interface and shock interaction. The interfaces are defined by employing different parameters for different materials in the equations. In the case of fluids, these parameters are usually given in the equation of state (EOS), an empirical relation that states how the pressure of your system depends on the internal energy and density, and it is necessary in order to close the system of equations. It is noteworthy that if the parameters differ by orders of magnitudes, as in water and air, the problem can easily become unstable, and it is not trivial how to deal with the interface coupling [2, 119, 118, 120]. In order to deal with this adversity, multiple methods have emerged including hybrid approximate solvers methods [120], ghost fluid methods [78], the adaptive moving mesh method [260], mass fraction models and volume of fluid models [2, 16, 129, 190]. These are sometimes coupled with level set methods or even immersed interface methods [275]. In our case, we introduce an approximate Riemann hybrid solver for the Euler equations, a system of hyperbolic conservation laws used to describe compressible fluid dynamics. The hybrid solver is designed to deal with a fixed interface aligned with the grid. For our experimental applications, we must also model the three-dimensional wave propagation using axisymmetric Euler equations with fixed interfaces. Solving this problem is equivalent to solving a two-dimensional problem with additional geometrical source terms. These source terms are

included using operator splitting [155] along with a time integrator.

In Chapter 9, we state a simple one-dimensional model for an air-plastic-water interface. Through computational experiments, it is shown that, if the plastic interface is thin in comparison to the characteristic length of the problem, it can be neglected. This result is essential to extend the problem to higher dimensions, as done in Chapter 10, where we describe how the simulation for the TBI experiments has been implemented, as well as computational and experimental results. The verification of the model is done by comparing to an exact solution obtained in the previous chapter. As previously mentioned, a 2D Axisymmetric model of the Euler equations is implemented using a hybrid HLLC-exact Riemann solver [120, 248], and the interface is modeled using different parameters for a stiffened gas equation of state. Chapter 10 shows how these algorithms are extended to more arbitrary interface geometry by using mapped grid. It also addresses how to implement adaptive mesh-refinement (AMR) into the algorithms, as well as all the subtleties that arise at the interface when employing AMR.

1.4 Conservation laws in hyperbolic problems and stochastic processes

Although conservation laws will be approached from very different points of view within this work, they will play a very relevant and unifying role in the two main projects of this work we just described.

Conservation laws have been essential in many areas of Physics and Mathematics. The conservation of physical quantities, like mass, momentum, energy and others, have provided the scaffolding to build most of the main theories in Physics [84]. However, the scope of conservation laws has proven to be beyond Physics; they have become a mathematical abstraction that imposes a constraint to a mathematical system and forces it to have a specific structure. One example of how conservation laws have moved into a more abstract domain is given by Noether's theorem, where each conservation law emerges from a corresponding symmetry of the underlying equations. One example outside Physics where conservation has proved to be very important is in stochastic processes. In this case, the conservation law is not for a physical quantity but for an abstract mathematical quantity, the probability.

In this work, we will explore two different dynamic problems where conservation laws are relevant: stochastic reversible biochemical reaction-diffusion systems in aqueous medium and high-resolution shock-capturing methods for interfaces between compressible and almost incompressible media. In both problems, conservation plays a fundamental role in establishing accurate dynamics. The first problem is built using stochastic theory, so the conservation of probability becomes essential, especially at reaction boundaries. The second project is framed in terms of hyperbolic conservation laws, which in our case correspond to the conservation of mass, momentum and energy. In both cases, stable and accurate numerical methods require taking into account conservation into the numerical discretization.

In general, conservation laws can be stated following some form of the continuity equation

$$\frac{\partial \rho(\bar{x},t)}{\partial t} + \nabla \cdot J(\rho(\bar{x},t)) = 0,$$

where ρ is the density of the conserved quantity (amount per unit volume) and J is the flux (amount crossing unit area per unit time) of the conserved quantity. The nature of conservation is easier to understand from its integral form,

$$\frac{d}{dt}\int_{x_1}^{x_2} q(x,t)dx = f(q(x_1,t)) - f(q(x_2,t)),$$

where the left hand side is the change of the total amount of the conserved quantity in the interval (x_1, x_2), and it changes only due to fluxes at the end points. The quantity $f(q(x_1,t))$ is the flux coming from the left into the (x_1, x_2) region and $f(q(x_2,t))$ is the flux leaving from the same region through the right endpoint.

A simple example of such an equation is the advection equation

$$\frac{\partial q(x,t)}{\partial t} + \frac{\partial}{\partial x}\left(u(x)q(x,t)\right) = 0.$$

This equation describes the passive advection of a tracer carried along by a flow with speed $u(x)$. The equation states the conservation of tracer density q. The flux in this case is proportional to the flow speed and the tracer density, $J = uq$. This equation is of hyperbolic type as we will study in Section 7.2; intuitively, this means it models the propagation of waves. In this case, the flux function was linear; however, there are many hyperbolic conservation laws with nonlinear fluxes, some of which we will study in this work. Other examples of hyperbolic equations are the acoustic equations, shallow water equations, Euler equations and Maxwell equations among others.

In probability and stochastic analysis, there is different type of conservation law. For instance, a diffusion process, usually described in continuous time and space, can be described by a probability conservation equation, which describes the dynamics of the probability density $f(x,t)$ of the diffusion process. A simple example is the diffusion of a Brownian particle in one dimension described by the Fokker-Planck equation

$$\frac{\partial f(x,t)}{\partial t} + \frac{\partial}{\partial x}\left[\mu(x)f(x,t) - \frac{\partial}{\partial x}\left(D(x)f(x,t)\right)\right],$$

where $f(x,t)dx$ is the probability of finding the Brownian particle in position x at time t, $\mu(x)$ is the drift coefficient and $D(x)$ is the diffusion coefficient. In this case, the flux is given

by

$$J = \mu(x)f(x,t) - \frac{\partial}{\partial x}\left(D(x)f(x,t)\right),$$

which is a linear flux, and it is not only a function of $f(x,t)$ but also of its derivative. This flux should be interpreted as a probability flux. We should also mention that conservative dynamics in stochastic processes can also be stated in a different form. In the case of continuous and discrete Markov chains, the conservation is enforced by constraining the structure of their corresponding Kolmogorov Forward equations [1], which are respectively given by

$$\pi^{t+1} = \pi^t \mathbb{P},$$

$$\frac{dP(t)}{dt} = P(t)\mathbb{Q},$$

where π^t and $P(t)$ are the time-dependent vectors of the probabilities. Each entry of these vectors denotes the probability of a discrete state of the system. In these case, the conservation of probability is enforced by imposing that any given row of the stochastic matrix, $\mathbb{P}$, sums to one for discrete time Markov chains, or equivalently, any given row of the transition rate matrix $\mathbb{Q}$ should sum to zero for continuous time Markov processes, as well as the initial condition for the probability sums or integrates to one [267]. Examples of these two cases will be explored in Chapter 5 and 6, respectively.

When we are using mathematics to model a physical, biological or any kind of model, we always need to be certain that the conserved quantities, like momentum or probability, are indeed conserved. On the other hand, complex systems cannot be usually solved analytically, so they require the use of numerical methods or other techniques. In such cases, it is somewhat easy to forget the importance of conservative dynamics. In other words, it is easy to derive a non-conservative numerical method for a conservative model. An example of this issue is given by 1950s and 1960s computational fluid dynamics (CFD). At this time, the CFD numerical methods for compressible flow were plagued with difficulties [155]. Godunov, in his 1959 revolutionary paper [95], provided the first steps to solve many of these issues by providing more of a discrete conservation law instead of a discretization of a conservation law solely [48, 67, 95, 147, 210, 155, 248]. One of our premises throughout this work is that all phenomena we observe as the physical reality at some time and space scales, in applied mathematics, can be formulated and implemented as discrete models, just like in Godunov's original work. The inherent discrete nature of these models is very convenient for numerical endeavors, and it blends in mathematical modeling with numerical analysis.

[1] The Fokker Planck equation is the Kolmogorov Forward equation for diffusion processes.

The two areas explored in this thesis also converge in a broader context on how computations, physics and mathematics problems are understood today. In the 1920s, Courant, Friedrichs and Lewy showed that one can prove the existence of solutions for classical linear partial differential equations arising in mathematical physics by replacing the derivatives by difference quotients on some mesh [48]. They obtain a simple existence proof by using the limiting process as the mesh size goes to zero. This was the groundwork for Godunov's and others future work [95, 147] in numerical conservation laws. On the other hand, in a very recent effort, Martin Hairer [104] constructed solutions (and consequently proved their existence) to nonlinear stochastic differential equations through the limiting process of a sequence of discrete equations. Both of these works used numerical discretizations to prove rigorous mathematical results. The discretizations have a very significant relevance within applied mathematics since they provide accurate models for numerical computations. The works by Courant, Hairer and others show the lines between numerical analysis, mathematical modeling, physics and pure mathematics are not necessarily well defined. Most of the work presented in this thesis is based or follows a similar line of reasoning. Most importantly, using these ideas as a guideline, it also hopes to inspire the development of new numerical methods for conservation laws in hyperbolic problems and stochastic processes. An interesting example is given by stochastic models of physical processes with very high-dimensional phase space. In these cases, it is not enough to deal with the numerical conservation of probability or the relevant physical quantities, we also have to accurately capture the dissipative properties of the system. In these models, the stochasticity is usually introduced to account for coarser degrees of freedom, so the dissipative properties of the stochastic component of the numerical scheme have to follow physically consistent constraints. The ideas we just presented provide a guideline that could help develop numerical schemes that accurately capture dissipative properties.

The dissertation is divided into two main parts, one for each of the two problems. Each part is devoted to the introduction, background and developments of its corresponding problem.

Part I

STOCHASTIC BIOCHEMICAL REACTION-DIFFUSION SYSTEMS

Chapter 2

BIOCHEMICAL REACTIONS SYSTEMS

There are several mathematical models to describe spatially homogeneous biochemical reaction systems. In this chapter, we will introduce the different mathematical models commonly used in chemical kinetics. As it will be shown below, the stochastic approach to model chemical dynamics is a comprehensive approach that allows descriptions in different fronts by using stochastic sampling or by studying the probability distribution dynamics. A particularly useful description for numerical endeavors called the random time-change representation is presented. We also provide an overview of some of the most useful numerical methods for biochemical reaction systems. In the final section, we show an application of biochemical stability.

We will mention some key reference for this chapter here. The most relevant references related to chemical kinetics are [24, 131, 205, 207, 206, 267]. The random time-change representation can be studied in [8, 9, 267]. The main source for the numerical methods presented are given in [8, 9, 36, 35, 90, 91, 92]. The main source for the last section related to an application to bistability is [258].

2.1 The equations of chemical kinetics

We will start reviewing the well-known deterministic model for chemical reactions, the law of mass action. We will then approach its stochastic counterpart given by the chemical master equation and it's approximations usually in the form of Fokker-Planck equations. How these theories are related is explored and illustrated in Figure 2.2.

2.1.1 The law of mass action (LMA)

The default model for chemical kinetics is given by the LMA. This law describes the rate at which chemical concentrations grow or decay by chemical reactions. Suppose two chemical A and B react upon collision to form a C,

$$A + B \xrightarrow{k} C$$

The rate at which c, the concentration of C, changes is the product of the number of collision between A and B and the probability that the collision is sufficiently energetic to overcome the free energy. The number of collisions is proportional to A and B concentration, a and

b, while the probability is given by a proportionality factor k that depends on the geometry, temperature and so on. The LMA yields the differential equation,

$$\frac{dc}{dt} = kab$$

The LMA is also employed for more complex reactions like

$$A + B \underset{k_b}{\overset{k_f}{\rightleftharpoons}} C, \tag{2.1}$$

with A, B and C denoting the number of particles of each chemical, and the quantities $M = A + C$ and $N = B + C$ kept constant.

Using the Law of Mass Action for this chemical reaction, we obtain the following differential equation

$$\frac{dc}{dt} = -k_b c + k_f(m - c)(n - c), \tag{2.2}$$

where a, b, c, m and n denote the concentrations of A, B, C, M and N respectively. The steady state or equilibrium solution, c^*, is obtained from the simple quadratic equation $c^2 - (m + n + \frac{k_b}{k_f})c + mn = 0$. We can also linearize around the equilibrium solution using $c = c^* + z$ to obtain an equation for the fluctuations,

$$\begin{aligned}
& \frac{d(c^* + z)}{dt} = -k_b c^* - k_b z + k_f(m - c^* - z)(n - c^* - z), \\
\Rightarrow \quad & \frac{dz}{dt} = -k_b c^* - k_b z + k_f((m - c^*)(n - c^*) - z * (m - 2c^* + n) + \cancel{z^2})), \\
\Rightarrow \quad & \frac{dz}{dt} = -z(k_b + k_f(m + n - 2c^*),
\end{aligned}$$

where z is small. This last equation's solution is clearly

$$z(t) = z_0 e^{-t/\tau}, \tag{2.3}$$

with $\tau = (k_b + k_f(m + n - 2c^*)^{-1}$ and $z_0 = c_0 - c^*$. This means that small fluctuations from equilibrium decay exponentially with rate $1/\tau$.

It is easy to generalize the LMA approach for very complicated reaction systems. In such cases, the chemical kinetics can have very complicated dynamics. A more detailed explanation of the LMA along with some examples can be found in [24, 131]. Much like Ohm's law and Hooke's law, the law of mass action is more a model than a law. This means it is not always valid. For instance, for very low concentrations, it may not be appropriate to model concentration as a continuous variable.

2.1.2 The chemical master equation (CME)

A quantitative mathematical description of biochemical systems at a cellular scale is complex involving many cell types and/or molecular species. Furthermore, these are thermodynamic systems usually on a scale that is so small that a quantitative mathematical description must be inherently stochastic and often involve a small but significant numbers of diffusing species that interact and react with each other.

In the most simple cases, we can assume our system is well-mixed and that diffusion is not relevant. As these systems often involve a small number of molecules, the traditional method of modeling systems by describing concentration changes with the Law of Mass Action is inappropriate. Therefore, a stochastic approach that accounts for the discrete, probabilistic nature of the chemical reaction systems is more suitable. This is given in the form of a continuous time Markov chain usually referred as the Chemical Master Equation (CME) [207]; however, the CME, even when it's a relatively simple system of ODE's, can be difficult to solve and analyze because of its high dimensionality. Under certain limits a simpler diffusion approximation to the CME can be done by means of the Fokker-Planck equation.

In order to introduce the CME, we can think of the deterministic dynamics of N chemical species in the LMA. These dynamics can be visualized as the trajectory of $(c_1(t),c_2(t),\cdots,c_N(t))$ in a phase space of concentration coordinates, where $c_i(t)$ is the time dependent concentration of the X_i. As mentioned before, in the CME approach, we will no longer be interested in the concentrations. Instead, we will focus on the number of molecules of a given chemical species at time t. However, as the CME is a probabilistic model, the number of molecules of every chemical species involved at a given time are actually random variables. The best way to describe such a model is to provide the dynamics for the probability of the number of molecules being $n_1,n_2,\cdots,n_N$ at time t, where n_i refers to the number of molecules of the ith chemical species X_i. In other words,

$$p(n_1, n_2, \cdots, n_N, t) = Pr\{N_1(t) = n_1, N_2(t) = n_2, \cdots, N_N(t) = n_N\},$$

where $N_k(t)$ is the random variable denoting the number of the ith chemical species at time t. Considering a system with M chemical reactions, where the jth chemical reaction is represented by the stochiometric coefficients ν_i^j and μ_i^j, such that the jth reaction is given by

$$\nu_1^j X_1 + \nu_2^j X_2 + \cdots + \nu_N^j X_N \xrightarrow{k^j} \mu_1^j X_1 + \mu_2^j X_2 + \cdots + \mu_N^j X_N,$$

where k^j is the reaction rate for the jth reaction. Note the stochiometric coefficients have to be integers and can be zero. The probability distribution of such a system will have stochastic dynamics, so a reaction j occurs at a random time T^j, which follows an exponential

distribution, $f_{T_j}(t) = \lambda^j e^{-\lambda^j t}$. The dynamics are given by the general CME,

$$\frac{dp(n,t}{dt} = \sum_{j=1}^{M} \left[\lambda^j(n - \mu^j + \nu^j)p(n - \mu^j + \nu^j, t) - \lambda^j(n)p(n,t)\right],$$

where $n = (n_1, n_2, \cdots, n_N)$, $\mu^j = (\mu_1^j, \mu_2^j, \cdots, \mu_N^j)$ and $\nu^j = (\nu_1^j, \nu_2^j, \cdots, \nu_N^j)$. The reaction rates λ^j are related to their deterministic rates k^j in the LMA by,

$$\lambda^j = Vk^j \prod_{i=1}^{N} \frac{n_i(n_i - 1)\cdots(n_i - \nu_i^j + 1)}{V^{\nu_i^j}}.$$

In the limit of system's size going to infinity, it has been proven that the solution to the CME is precisely the solution to the corresponding deterministic solution given by the LMA [144]. Therefore, the CME is a more general model than the LMA, just as quantum mechanics is more general than classical mechanics. For more details on the general formulation of the CME, the reader is referred to [205, 207].

Writing a general CME for a general reaction can be a little confusing at first, so instead, we will obtain the CME step by step for the chemical reaction (2.1). The probabilistic transition rates are illustrated in Figure 2.1. The number of C molecules is given by $n_C = j$,

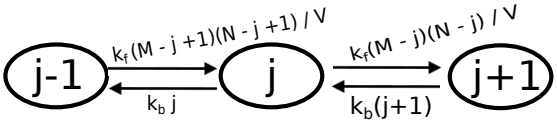

Figure 2.1: CME rate diagram: j denotes the number of C molecules.

so $P_j(t)$ is the probability of finding j C molecules at time t. At this state, there are j C molecules each of which transitions to $A + B$ with rate k_b. Therefore, the rate of transition from $n_C = j$ to $n_c = j - 1$ is $k_b j$. Analogously, at this state there are $M - j$ A molecules and $N - j$ B molecules. The rate of transition from state $n_C = j$ to $n_C = j + 1$ is k_f/V. Note that dividing by the volume is crucial, since if the molecules are confined in a small volume, they will react faster. Consequently, the rate of transition from $n_C = j$ to $n_C = j + 1$ is $\frac{k_f}{V}(M - j)(N - j)$. The rest of the transition rates are given in Figure 2.1. The resulting

CME is

$$\begin{aligned}\frac{dP_j(t)}{dt} =& \frac{k_f}{V}(M-j+1)(N-j+1)P_{j-1}(t) \\ &- \left(\frac{k_f}{V}((M-j)(N-j)+k_b j\right) P_j(t) + k_b(j+1)P_{j+1}(t). \end{aligned} \tag{2.4}$$

Lets find the steady state solution of this equation. We want the number of molecules to remain constant; therefore, what leaves the state with j molecules, should also enter to it. In mathematical language, this means

$$\begin{aligned} & P_j \frac{k_f}{V}(M-j)(N-j) = P_{j+1}k_b(j+1), \\ \Rightarrow \quad & \frac{P_{j+1}}{P_j} = \frac{\frac{k_f}{V}(M-j)(N-j)}{k_b(j+1)}. \end{aligned}$$

At position j the steady state probability distribution should be given by

$$\begin{aligned} & P_j^{ss}(t) = \frac{P_j}{P_{j-1}}\frac{P_{j-1}}{P_{j-2}}\cdots\frac{P_1}{P_0}P_0, \\ \Rightarrow \quad & P_j^{ss}(t) = P_0 \prod_{l=0}^{j-1} \frac{k_f}{V k_b}\frac{(M-l)(N-l)}{l+1}. \end{aligned}$$

This is the steady state probability distribution we were looking for; its form is similar to a binomial distribution except for the factor $(M-l)$. It can be normalized adjusting P_0 such that $\sum_j P_j^{ss} = 1$, where $z = 1/P_0$ is the partition function.

2.1.3 The Fokker Planck equation (FPE)

The CME (Eq. 2.4) looks like a finite difference scheme, so it can be rewritten as its corresponding equivalent partial differential equation (PDE). The PDE we will derive from the CME is called the FPE. Although it is the same equation as the one derived in Section 3.1, here it should be interpreted as a continuous approximation to the discrete CME. The accuracy of such an approximation, therefore, deserves careful mathematical scrutinies.

Let $z = j/V$ be a continuous variable and $m = M/V$, $n = M/V$ so that $P_j(t) \to P(z,t) = f_c(z,t)$, i.e. the discrete probability distribution as a function of j becomes continuous in z. To simplify notation, also define the following two functions,

$$\begin{aligned} g_1(z) =& k_f(m-z)(n-z)f_c(z,t), \\ g_2(z) =& k_b z f_c(z,t), \end{aligned}$$

where we already introduced the change of variable to z, m and n. This allow us to write the CME as

$$\frac{df_c(z,t)}{dt} = V(g_1(z-h) - g_1(z) - g_2(z) + g_2(z+h)).$$

In this form, $Vh \to 1$ is equivalent to $V \to 1/h$, then as $h \to 0$ the volume $V \to \infty$. Taylor expanding $g_1(z-h)$ and $g_2(z+h)$ up to second order for $h << 1$ we obtain

$$\begin{aligned}
\frac{\partial f_c(z,t)}{\partial t} =& V\left(-hg_1'(z) + \frac{h^2}{2}g_1''(z) + hg_2'(z) + \frac{h^2}{2}g_2''(z)\right), \\
\text{as} \quad h \approx \frac{1}{V} \quad \Rightarrow \quad \frac{df_c(z,t)}{dt} =& -g_1'(z) + \frac{1}{2V}g_1''(z) + g_2'(z) + \frac{1}{2V}g_2''(z), \\
\Rightarrow \quad \frac{df_c(z,t)}{dt} =& \frac{\partial}{\partial z}\left[-g_1(z) + g_1(z) + \frac{1}{2V}\frac{\partial}{\partial z}(g_1(z) + g_2(z))\right].
\end{aligned}$$

Substituting the functions g_1 and g_2 we obtain

$$\begin{aligned}
\frac{\partial f_c(z,t)}{\partial t} =& \frac{\partial}{\partial z}\left[(-k_f(m-z)(n-z) + k_b z)f_c(z,t) + \frac{1}{2V}\frac{\partial}{\partial z}((k_f(m-z)(n-z) + k_b z)f_c(z,t))\right] \\
=& \frac{\partial}{\partial z}\left[\left(-k_f(m-z)(n-z) + k_b z + \frac{1}{2V}\frac{\partial}{\partial z}(k_f(m-z)(n-z) + k_b z)\right)f_c(z,t) \quad \dots \right. \\
& \left. + \frac{1}{2V}(k_f(m-z)(n-z) + k_b z)\frac{\partial f_c(z,t)}{\partial z}\right].
\end{aligned}$$

The second term in the factor multiplying $f_c(z,t)$ is divided by V, so as $V \to \infty$, the second term is much smaller than the first one, so we can neglect it obtaining the non-linear Fokker-Planck equation,

$$\frac{\partial f_c(z,t)}{\partial t} = \frac{\partial}{\partial z}\left[(-k_f(m-z)(n-z) + k_b z)\, f_c(z,t) + \frac{1}{2V}(k_f(m-z)(n-z) + k_b z)\frac{\partial f_c(z,t)}{\partial z}\right]. \tag{2.5}$$

To obtain a meaningful linear version of the equation, lets consider linear fluctuations around the equilibrium, i.e. $z = z_0 + \epsilon z_1$ and $f_c(z,t) = f_0 + \epsilon f_1$, with $f_0 = f_c(z^*, t)$ and $z_0 = z^*$ the

corresponding constant values at equilibrium. Substituting in the recently obtained equation,

$$\frac{\partial(f_0+\epsilon f_1)}{\partial t} = \frac{\partial}{\partial z}\Bigg[\left(-k_f(m-z_0-\epsilon z_1)(n-z_0-\epsilon z_1)+k_b(z_0+\epsilon z_1)\right)(f_0+\epsilon f_1) \quad \dots$$
$$+\frac{1}{2V}(k_f(m-z_0-\epsilon z_1)(n-z_0-\epsilon z_1)+k_b(z_0+\epsilon z_1))\frac{\partial(f_0+\epsilon f_1)}{\partial z}\Bigg].$$

As f_0 is constant since its the value at equilibrium and $\partial/\partial z = \partial/\partial z_1$,

$$\epsilon\frac{\partial f_1}{\partial t} = \frac{\partial}{\partial z_1}\Bigg[\left(-k_f(m-z_0-\epsilon z_1)(n-z_0-\epsilon z_1)+k_b(z_0+\epsilon z_1)\right)(f_0+\epsilon f_1) \quad \dots$$
$$+\frac{1}{2V}(k_f(m-z_0-\epsilon z_1)(n-z_0-\epsilon z_1)+k_b(z_0+\epsilon z_1))\epsilon\frac{\partial(f_1)}{\partial z_1}\Bigg]$$

$$\epsilon^0: \qquad 0 = \frac{\partial}{\partial z_1}\left[(-k_f(m-z_0)(n-z_0)+k_b z_0)\, f_1\right].$$

$$\epsilon^1: \qquad \epsilon\frac{\partial f_1}{\partial t} = \epsilon\frac{\partial}{\partial z_1}\left[z(k_f(m+n-2z_0)+k_b)f_1 + \frac{k_f(m-z_0)(n-z_0)+k_b z_0}{2V}\frac{\partial f_1}{\partial z_1}\right].$$

From the equation obtained with the Law of Mass action (Eq. 2.2), we can immediately deduce that at equilibrium $c = z_0$ then $dc/dt = 0$, and therefore $-k_f(m-z_0)(n-z_0)+k_b z_0 = 0$. This confirms our result at order ϵ^0, and allows to simplify our result at order ϵ^1 as

$$\epsilon\frac{\partial f_1}{\partial t} = \epsilon\frac{\partial}{\partial z_1}\left[z(k_f(m+n-2z_0)+k_b)f_1 + \frac{k_b z_0}{V}\frac{\partial f_1}{\partial z_1}\right].$$

Diving by ϵ, dropping the subscript in z and f, and using that $z_0 = z^*$, we can rewrite this equation as

$$\frac{\partial f(z,t)}{\partial t} = \frac{\partial}{\partial z}\left[\frac{z}{\tau}f(z,t) + \frac{k_b z^*}{V}\frac{\partial f(z,t)}{\partial z}\right], \tag{2.6}$$

with $\tau = [k_f(m+n-2z^*)+k_b]^{-1}$. This is the linearized version of the Fokker-Planck equation, whose (stochastic process) solution is known as Ornstein-Uhlenbeck process.

Taking the limit as $V \to \infty$ we obtain

$$\frac{\partial f(z,t)}{\partial t} = \frac{1}{\tau}\frac{\partial}{\partial z}\left(z f(z,t)\right),$$

which can be easily solved by the method of characteristics. The solution is given by,

$$z = z_0 e^{-t/\tau},$$
$$f(z,t) = f_0\left(z e^{t/\tau}\right) e^{t/\tau},$$

where z_0 is the characteristic and $f_0(z_0) = f(z,0)$ is the initial condition. Note that the solution for the concentration z is the same as in Eq. 2.3 with $\tau = [k_f(m+n-2z^*)+k_b]^{-1}$. This means that in the limit $V \to \infty$, the CME recovers the results obtained by the LMA for the fluctuations around equilibrium. Furthermore, we also obtained how the probability distribution function evolves with time. For instance, if $f_0(z) = e^{-z^2}$ is a simple Gaussian, the limit as $t \to \infty$ is $f(z,t) \to \delta(z)$. In general, this will be true for any initial condition $f_0(z)$ that is zero at infinity, which is always the case since probability needs to vanish at infinity. This is the complete deterministic result; the probability of finding it in the steady state of the LMA is one and zero elsewhere.

We can also find the steady state from Eq. 2.6, where $V >> 1$ but not quite infinite, by solving

$$\frac{D}{V}\frac{\partial^2 f_{ss}(z)}{\partial z^2} + \frac{1}{\tau}\frac{\partial}{\partial z}\left(z f_{ss}(z)\right) = 0$$

where $D = k_b z^*$. Integrating once, using the boundary condition that $f_{ss}(z) \to 0$ as $z \to \infty$ and solving it, we obtain a simple Gaussian

$$f_{ss}(z) = \sqrt{\frac{V}{\pi D \tau}} e^{-\frac{V}{\tau D} z^2}. \tag{2.7}$$

All the results in this section can be summarized in the diagram in Figure 2.2. It clearly shows the chemical master equation is the most fundamental model of all. Although this was done for a particular example, it is a general statement, see [206, 207, 258].

2.2 Random time-change Poisson representation

In the previous section, we showed the CME is an appropriate mathematical model for chemical kinetics at mesoscopic scales; it recovers the deterministic dynamics in the large volume/ large number of particles limit. The CME is actually describing a continuous-time Markov chain [267]. This means that the dynamics of chemical reactions constitute a stochastic process where the state at time t is the number of molecules of each species at time t. This number is of course a random variable, whose probability distribution function (pdf) dynamics are given by the Markov chain, which in this case is the CME.

The CME provides the probability distribution dynamics; however, it does not directly relate to sample paths of the stochastic process. An alternative representation of the same

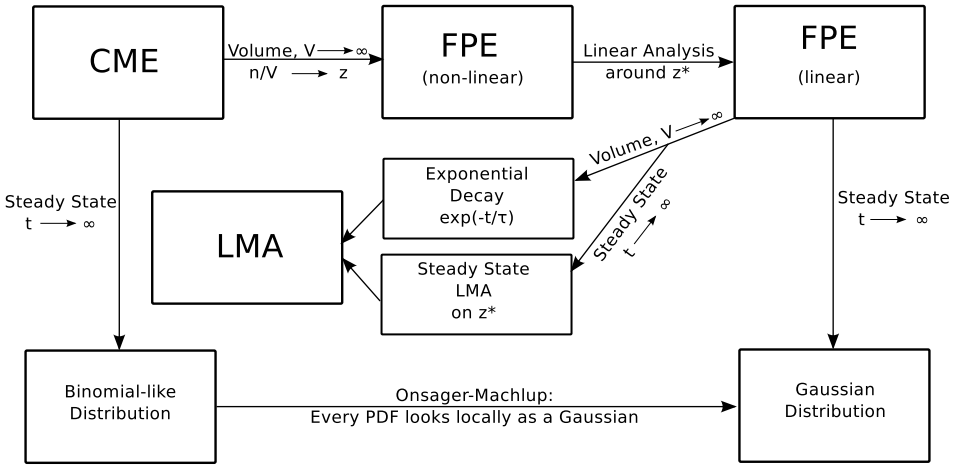

Figure 2.2: Connection between LMA,CME and FPE

Markov process can be constructed; this representation is called the random time-change representation [144], and it allows a straightforward relation to the sample paths of the stochastic process.

In this section, we will introduce this representation for a simple model and extend it to a more general context. In order to determine the state of a Markov chain, we need to know how many molecules of each chemical species are at time t. These quantities will be determined by the initial condition, the number of molecules at the beginning, and the number of reactions of each type that occurred up to time t. As the number of reactions of each type is a random variable, it can be understood as a counting process. We will assume reactions occur one at a time, and reactions are independent if they occur in different time intervals. More concisely, we will assume the reaction counting process is a Poisson process. We will first provide a brief overview of Poisson processes.

2.2.1 Poisson process

The Poisson process is a counting process that counts the number of random observations of an event in time. Consider the Figure 2.3, which shows a time line and the x indicate an event happened at that point in time. We define a variable

$$Y(t) := \text{number of observations up to time } t$$

For $t < s$, $Y(s) - Y(t) :=$ number of observations in time interval $(t, s]$. We assume this counting process has the following properties:

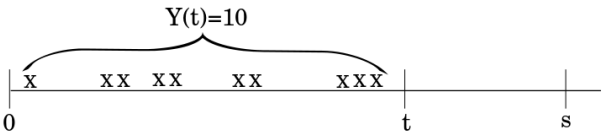

Figure 2.3: Representation of the events occured during a Poisson process up until time t.

- Observations occur one at a time;
- Observations in disjoint time intervals are independent random variables, i.e.

$$Y(t_k) - Y(t_{k-1}) \qquad \text{with} \qquad t_0 < t_1 < t_2 \cdots < t_m$$

  as m independent random variables;
- The distribution for $Y(t+a) - Y(t)$ does not depend on t.

It can be shown that the probability of having k events in the time interval $(t, s]$ is given by a Poisson distribution [254],

$$P\{Y(s) - Y(t) = k\} = \frac{[\lambda(s-t)]^k}{k!} e^{-\lambda(s-t)},$$

for some constant λ. Therefore, each Poisson process has a rate λ associated to it; we denote $Y_\lambda(t)$ a Poisson process with rate λ. For $\lambda = 1$, we obtain a unit rate Poisson process $Y(t)$. Note that the structure of of the Poisson distribution allows us to write $Y_\lambda(t)$ as a unit rate Poisson process by incorporating the rate into the time variable. This is called the random time-change representation

$$Y_\lambda(t) = Y(\lambda t).$$

Furthermore, we can generalize this result to the case where the λ parameter is a function of time,

$$Y_\lambda(t) = Y\left(\int_0^t \lambda(s) ds\right). \tag{2.8}$$

When we employ Poisson processes in practical applications, we are usually concerned in the probability of an event happening in a Δt interval,

$$P\{Y_\lambda(t + \Delta t) - Y_\lambda(t) > 0 | \mathcal{F}_t\} = P\{Y_\lambda(t + \Delta t) - Y(t) > 0\}, \tag{2.9}$$

where $\mathcal{F}_t$ is all the previous history of the process[1] up to time t. However, as it is a Poisson process, we know the random variable $Y_\lambda(t+\Delta t)-Y_\lambda(t)$ is independent, so $\mathcal{F}_t$ is not relevant. Furthermore, this probability can be written in terms of the cumulative distribution function $F_y(t)$, which is given by

$$F_y(k) = P\{Y_\lambda(t+\Delta t) - Y_\lambda(t) \leq k\} = e^{-\lambda\Delta t}\sum_{i=0}^{k}\frac{[\lambda\Delta t]^i}{i!}.$$

Note that if $\Delta t = 0$ then $k = 0$ since events cannnot happen in a zero time interval. Using this relation we can write Eq. 2.9 in terms of the cumulative distribution function as

$$P\{Y_\lambda(t+\Delta t) - Y(t) > 0\} = 1 - F_y(0) = 1 - e^{-\lambda\Delta t} \approx \lambda\Delta t. \tag{2.10}$$

The approximation in the right hand side is valid for small time steps.

2.2.2 Random time-change representation for chemical kinetics

In this section, we will show the time-change Poisson representation for the sample path of the stochastic processes of chemical reactions. As mentioned before, the dyanmics of the probability density is given by the CME. This representation will give an alternate formulation to the CME that represents the sample paths of the stochastic process. We will begin with a simple example and then extend it to a more general case. Consider the reaction

$$A + B \to C,$$

with $X_A(t)$, $X_B(t)$ and $X_C(t)$ the number of molecules at time of A, B and C respectively at time t. The vector $\overline{X}(t) = (X_A(t), X_B(t), X_C(t))^T$ denotes the state of the whole system at any given time. This can be written as

$$\overline{X}(t) = \overline{X}(0) + R(t)\begin{bmatrix} -1 \\ -1 \\ 1 \end{bmatrix},$$

where $R(t)$ denotes the number of reaction that have occured up to time t and the vector $\xi = (-1, -1, 1)^T$ serves to point out that every time a reaction happens an A and a B lose one molecule each and C gains one. The question we face now is how to write $R(t)$?

The number of reactions $R(t)$ is a stochastic counting process. As the probability of a reaction in the interval $(t, t+\Delta t]$ should be proportional to the number of A and B particles

[1] In probability theory, the history of the process, $\mathcal{F}_t$, is a σ-algebra.

and to the time interval, we can write

$$P\{ \text{ Reaction occurs in } (t, t+\Delta t]\} \approx \kappa X_A(t) X_B(t) \Delta t.$$

This equation is very similar to Eq. 2.10. As a matter of fact, we can be more precise and rewrite it as

$$P\{ \ R(t+\Delta t) - R(t) > 0\} \approx \kappa X_A(t) X_B(t) \Delta t.$$

Comparing to Eq. 2.10, we can say $R(t) = Y_{\lambda^*}(t)$ with $\lambda^* = \kappa X_A(t) X_B(t) \Delta t$. Using the time-change representation in Eq. 2.8, we can write this in terms of a unit-rate Poisson process,

$$R(t) = Y_{\lambda^*}(t) = Y\left(\int_0^t \lambda(s)^* ds\right) = Y\left(\int_0^t \kappa X_A(s) X_B(s) ds\right).$$

We can now write the random time-change Poisson representation of the stochastic process for $A + B \to C$ as,

$$\overline{X}(t) = \overline{X}(0) + Y\left(\int_0^t \kappa X_A(s) X_B(s) ds\right) \begin{bmatrix} -1 \\ -1 \\ 1 \end{bmatrix}.$$

This result can be easily generalized to a complicated reaction scheme with m reactions. Instead of having only one reaction gven by the vector $\xi = (-1, -1, 1)^T$, we can have a set of reactions ξ_l, with $l =, 1 \ldots, m$ that each can involve different chemical species. Each of these reactions will be specified by independent Poisson processes; therefore, we can write

$$\overline{X}(t) = \overline{X}(0) + \sum_{l=1}^{m} \xi_l Y_{(l)}\left(\int_0^t \lambda_l\left(\overline{X}(s)\right) ds\right), \tag{2.11}$$

where $Y_{(l)}(\ldots)$ are independent unit-rate Poisson processes and the rate of each reaction is given by some function of the state vector $\lambda_l\left(\overline{X}(s)\right)$, which has to be determined on a case by case basis.

2.3 Numerical methods for stochastic chemical kinetics

Any stochastic Markov process has two different mathematical representations: its stochastic trajectory and its time-dependent probability distribution following a Kolmogorov forward equation. In the present context, this will correspond to the Gillespie algorithm and the CME respectively. The Gillespie algorithm is a mathematical algorithm that allows calculating

stochastic sample trajectories for chemical kinetics. As one could expect there will also be two type of numerical methods; the first kind would be to obtain the probability distribution function and the second one to obtain the stochastic trajectories.

We should first explore how can we obtain the full probability distribution. The CME, as in Eq. 2.4, is in the form of a difference equation, which means it can be written in the form,

$$\frac{d\mathbf{P}(t)}{dt} = \mathbf{A}\mathbf{P}(t),$$

where $\mathbf{A}$ is a matrix that will depend on the rates. We can think of solving this equation as a Laplace equation like in [156]. In general, we can implement a simple Crank-Nicholson method to numerically solve this equation,

$$\mathbf{P}(t)^{n+1} = \mathbf{P}(t)^n + \frac{dt}{2}\left[\mathbf{A}\mathbf{P}(t)^n + \mathbf{A}\mathbf{P}(t)^{n+1}\right].$$

We can also do a better job by implementing a TR-BDF2 method to ensure better stability [156],

$$\mathbf{P}(t)^* = \mathbf{P}(t)^n + \frac{dt}{4}\left[\mathbf{A}\mathbf{P}(t)^n + \mathbf{A}\mathbf{P}(t)^*\right], \tag{2.12}$$

$$\mathbf{P}(t)^{n+1} = \frac{1}{3}\left[4\mathbf{P}(t)^* - \mathbf{P}(t)^n + dt\mathbf{A}\mathbf{P}(t)^{n+1}\right]. \tag{2.13}$$

However, the dimension of the grid will grow as fast as the particles in your systems. A CME with one chemical species and 500 molecules will require a one dimensional grid with 500 cells; a CME with two chemical species and 1000 molecules of each will require a two dimensional grid with 1000×1000 cells and so on. Furthermore, what is the appropriate initial probability distribution function for the system? One could try a set of Dirac's deltas or even try a uniform distribution. The system, if complex enough, might even be chaotic, so it would be wise to solve trajectories for each different initial condition; it becomes a very complex high dimensional dynamical system, and it might be expensive and inefficient to solve each trajectory with a method like the one in Eq. 2.13. However, solving it for certain initial conditions might still bring great insight into what could be the qualitative behavior of the system, if it is stable, if it reaches equilibrium, and so on. Other possible numerical method's to solve the CME is discussed in [258].

2.3.1 Gillespie Algorithm

On the other hand, the stochastic trajectory representation of the process is given by the Gillespie algorithm. This algorithm, first developed in [94] and further explained in [90], is concerned with answering two questions:

- When will next reaction occur?
- Which reaction will occur?

The answer should be given in terms of probability, so let introduce the reaction probability density function,

$$P(\tau,\mu)d\tau := \begin{array}{l}\text{probability that, given a state } (x_1, x_2, \cdots, x_n)\\ \text{at time } t\text{, the reaction } \mu \text{ occurs in the time}\\ \text{interval } (t+\tau, \mathrm{t}+\tau+\mathrm{d}\tau),\end{array}$$

where τ and μ are random variables and provide the answers to the two questions above respectively. Lets also call

$$\lambda_\mu dt := \begin{array}{l}\text{probability that reaction } \mu \text{ occurs in } V\\ \text{in } (t, t+dt) \text{ given the system is at}\\ (x_1, x_2, \cdots, x_n) \text{ at time } t,\end{array}$$

$$P_0(\tau) := \begin{array}{l}\text{the probability that, given the state } (x_1, x_2, \cdots, x_n)\\ \text{at time } t\text{, no reaction will occur in } (t, t+\tau).\end{array}$$

The coefficients λ_μ are obtained from the rate constants of each reaction in the CME, see [94]. As the probability that no reaction will occur in time $d\tau$ is approximately given by $1 - \sum_{\nu=1}^{\mu} \lambda_\nu d\tau$, we can write

$$P_0(\tau + d\tau) = P_0(\tau)\left[1 - \sum_{\nu=1}^{\mu} \lambda_\nu d\tau\right].$$

This can be easily written as ODE with solution

$$P_0(\tau) = \exp\left[-\sum_{\nu=1}^{\mu} \lambda_\nu \tau\right].$$

From the definitions just stated, it's straightforward to obtain the following expression for the reaction probability density function,

$$\begin{aligned} & P(\tau,\mu)d\tau = P_0(\tau)\lambda_\mu d\tau, \\ \Rightarrow \quad & P(\tau,\mu) = \lambda_\mu \exp\left[-\sum_{\nu=1}^{\mu} \lambda_\nu \tau\right] = \lambda_\mu e^{-\lambda_0 \tau}, \end{aligned}$$

where $\lambda_0 = \sum_{\nu=1}^{\mu} \lambda_\nu$. If two random numbers μ and τ were generated following this probability distribution, we could do a numerical simulation of the chemical process. This can be

done approximately by choosing

$$\tau = \frac{1}{\lambda_0}\ln\left[\frac{1}{r_1}\right] \quad \text{with PDF:} \quad P_1(\tau) = \lambda_0 e^{-\lambda_0 \tau},$$
$$\mu = \text{Integer for which:} \quad \sum_{\nu=1}^{\mu-1}\lambda_\nu < r_2\lambda_0 \leq \sum_{\nu=1}^{\mu}\lambda_\nu \quad \text{with PDF:} \quad P_2(\mu) = \frac{\lambda_\mu}{\lambda_0},$$

with r_1 and r_2 uniformly distributed random numbers between 0 and 1, $P_1(\tau)$ is the probability for the next reaction time to be τ and $P_2(\mu)$ is the probability for the next reaction to be the μ reaction. Note that in this case $P(\tau, \mu) = P_t(\tau)P_r(\mu)$, for more details see [94]. The last calculation answers our two initial questions and allows to do a Monte Carlo numerical simulation of the process by choosing two random numbers on each time step. Although the algorithm might be simple, it is the conceptual basis of much more complicated methods. It is important to notice it doesn't rely on the CME; therefore, it is considered a different mathematical representation of the same stochastic process described by the CME.

2.3.2 First reaction method

An equivalent algorithm to Gillespie's algorithm can be obtained directly from the random time change representation of Eq. 2.11. It is also shown in [90]. The algorithm is as follows:

1. Initialize the time and the species concentration vector, $t = 0$, $\bar{X}(0) = \bar{X}_0$.

2. Sample the first event of m unit rate Poisson processes. This is equivalent to sample m independent unitary exponential waiting times, $\Delta_1, \Delta_2, \cdots, \Delta_m$.

3. Apply the time-change to the m unitary exponential times by solving for t in the integrals

$$\Delta_l = \int_0^\tau \lambda_l(s)ds.$$

   This yields the reaction times for all the possible reactions $\tau_1, \tau_2, \cdots, \tau_m$. Note the rates λ_l will depend on a reaction rate and on the chemical species involved in the corresponding reaction. Also, in general, λ_l will remain constant between reaction events, so solving the integral should be straightforward.

4. Choose the first reaction to happen, which corresponds to the smallest possible time $\min(\tau_1, \tau_2, \cdots, \tau_m)$.

5. Apply the reaction corresponding to the smallest time, i.e. if $\tau_i = \min(\tau_1, \tau_2, \cdots, \tau_m)$, apply the i^{th} reaction following Eq. 2.11.

6. Update the time and number of molecules and recalculate the rates λ_l. Then, go back to step 2 and repeat.

The algorithm we just described is completely equivalent to the first reaction method. The main difference is that in this algorithm we employed the time-change representation. The original first reaction method is as follow,

1. Initialize the time and the species concentration vector, $t = 0$, $\bar{X}(0) = \bar{X}_0$.

2. For each reaction i sample exponentially distributed times following

$$Pr(\tau_i = \tau) = \lambda_l e^{-\tau\lambda_l}.$$

3. Choose the time for the first reaction as $\min(\tau_1, \tau_2, \cdots, \tau_m)$.

4. Apply the reaction corresponding to the smallest time, i.e. if $\tau_i = \min(\tau_1, \tau_2, \cdots, \tau_m)$, apply the i^{th} reaction.

5. Update number of molecules and recalculate λ_i, then go to 2.

More complicated algorithms, like the next reaction method [8, 9], take advantage of the times already calculated, so only one random number has to be computed per time step. This algorithm is straightforward to obtain following the random time-change approach from Eq. 2.11, as shown in [8, 9].

It's also worth showing that Gillespie's algorithm is equivalent to the first reaction method. We want to find the probabilities of having the first reaction occuring in time τ_F and the probability of it being the k^{th} reaction, i.e. $\Pr[\tau_F = t]$ and $\Pr[\mu = k]$ respectively, where τ_F and μ are the random variables. In the first reaction method, we obtain these probabilities as the minimum of all the sampled τ_i and its corresponding reaction, which is equivalent to sample directly from the probability $\Pr[\tau_F \geq x, \mu = k]$. We can begin by writing this probability as

$$\Pr[\tau_F \geq x, \mu = k] = \Pr[\tau_F \geq x, \{\tau_i \geq \tau_k\}, i \neq k].$$

Note this probability requires that the times of all the other reactions to be greater than the one for the k^{th} reaction. Using Bayes rule and the fact that this is a cumulative distribution fucntion for τ_F, this can be written as

$$\int_x^\infty \Pr[\{\tau_i \geq \tau_k\}, i \neq k | \tau_k = \tau] \underbrace{\lambda_k e^{-\lambda_k \tau} d\tau}_{Pr[\tau < \tau_k < \tau + d\tau]}.$$

However, note that the random variables τ_i for the times for each reaction i^{th} to happen are independent, so we can write $\Pr[\tau_1 > \tau, \tau_2 > \tau, \cdots] = \Pr[\tau_1 > \tau]\Pr[\tau_2 > \tau]\cdots$, where each one of those is exponentially distributed; therefore,

$$\int_x^\infty \Pr\left[\{\tau_i \geq \tau_k\}, i \neq k | \, \tau_k = \tau\right] \lambda_k e^{-\lambda_k \tau} d\tau = \int_x^\infty \prod_{\substack{i=1 \\ i \neq k}}^{m} \left(e^{-\lambda_i \tau}\right) \lambda_k e^{-\lambda_k \tau} d\tau$$

$$= \lambda_k \int_x^\infty e^{-\sum_{i=1}^m \lambda_i \tau} d\tau = \frac{-\lambda_k}{\sum_{i=1}^m \lambda_i} e^{-\tau} \Big|_x^\infty = \frac{\lambda_k}{\lambda_0} e^{-x\lambda_0},$$

where $\lambda_0 = \sum_{i=1}^m \lambda_i$. This yields the joint probability distribution function as

$$\Pr\left[\tau_F \geq x, \mu = k\right] = \frac{\lambda_k}{\lambda_0} e^{-\tau\lambda_0}.$$

The corresponding marginal distributions are obtained in a straightforward way,

$$\Pr[\tau_F \geq \tau] = \sum_{k=1}^{m} \frac{\lambda_k}{\lambda_0} e^{-\tau\lambda_0} = e^{-\tau\lambda_0},$$

$$\Pr[\mu = k] = \Pr[\tau_F \geq 0, \mu = k] = \frac{\lambda_k}{\lambda_0}.$$

Note the probability for τ_F is the cumulative of an exponential distribution; therefore,

$$\Pr[\tau_F = \tau] = \lambda_0 e^{-\tau\lambda_0}.$$

Note this is exactly the same probability distributions that were obtained with the Gillespie algorithm; therefore, sampling using the first reaction method is completely equivalent to sampling using Gillespie's direct method. This result is equivalent to a classic result probability. It essentially proves that for m independent exponentially random variables $X_1, X_2, \cdots, X_m$ with parameters $\lambda_1, \lambda_2, \cdots, \lambda_m$, then $\min(X_1, X_2, \cdots, X_n)$ is exponentially distributed with parameter $\lambda_{\min} = \lambda_1 + \lambda_2 + \cdots + \lambda_m$, and $\Pr[k | X_k = \min(X_1, X_2, \cdots, X_m)] = \lambda_k/(\lambda_1 + \cdots + \lambda_m)$.

2.3.3 τ-leaping

The τ-leaping method follows a similar logic to the previous method we just described. The main difference is that it allows longer time steps. Consequently, the method is considerably faster than the Gillespie algorithm or any of its variants. However, this comes with a price; the method is no longer exact.

The method is derived from the same conceptual basis as Gillespie's and the random

time change representation. One of the most simple ways to intuitevly derive the method is to use the random time-change representation from Eq. 2.11. Forcing the time step to be equal to τ, we can rewrite the equation as

$$\overline{X}(\tau) = \overline{X}(0) + \sum_{l=1}^{m} \xi_l Y_{(l)} \left(\int_0^\tau \lambda_l \left(\overline{X}(s) \right) ds \right).$$

Additionally, we can provide an Euler approximation to the integrals inside the Poisson processes,

$$\int_0^\tau \lambda_l \left(\overline{X}(s) \right) ds \approx \lambda_l \left(\overline{X}(s) \right) \tau. \tag{2.14}$$

This yields the main formulation of the τ-leaping method,

$$\overline{X}(\tau) = \overline{X}(0) + \sum_{l=1}^{m} \xi_l Y_{(l)} \left(\lambda_l \left(\overline{X}(s) \right) \tau \right).$$

As the time step is now fixed, we are no longer interested in when will the first reaction happened. Instead, we need to know how many reactions of a given type happened in the time interval $[0, \tau)$. Therefore, we need to sample $Y_{(l)} \left(\lambda_l \left(\overline{X}(s) \right) \tau \right)$ from

$$\Pr[Y(t+\tau) - Y(t) = k] = \frac{[\lambda_l \tau]^k}{k!} e^{-\lambda_l \tau},$$

to obtain the numbers of reactions k for every lth reaction type. The main issue is that this method cannot guarantee non-negative value for the number of molecules. This requires additional adjustments that will be not addressed here but the reader is referred to [7, 8, 9, 35, 36, 91].

It should also be noted that different approximations to the integral from Eq. 2.14 yield different version of the τ-leaping method. For instance, we could try a mid-point approximation and obtain an implicit τ-leaping method.

Another type of numerical methods worth to be mentioned are the kinetic Monte Carlo methods (KMC). This method will be explored in more detail in next chapter when dealing with stochastic reaction-diffusion systems.

2.4 Delbrück-Gillespie processes

The dynamics models we just studied for mesoscopic, homogeneous chemical reaction system is a birth and death stochastic process. Any stochastic Markov process can be represented mathematically using two different descriptions: stochastic trajectories and a time-dependent

probability distribution following a Kolmogorov forward equation. For diffusion processes, these would correspond to SDE's and the FPE respectively. In the context of homogeneous chemical reaction systems, these representations correspond to the random time-changed Poisson process on the one hand and the CME on the other, see [206]. The stochastic process of these two mathematical representations for homogeneous chemical reaction systems was named the Delbrück-Gillespie process by [206]. This convention is important to note that the process is the same regardless of which representation is chosen the random time-change Poisson representation or the CME.

The Delbrück-Gillespie process is more than either the random time-change representation or the CME alone. It is a full range analytical theory of dynamics of homogeneous chemical reaction systems. It has emergent nonlinear differential equations (deterministic case limits) and emerging stochastic jump dynamics on evolutionary time scales.

2.5 Bistability: The Schlögl model

Schlögl model is a simple example of a chemical reaction system that exhibits bistability. Bistable behavior can be found in many biological networks including heart models, the visual perception, and gene networks [258]; therefore, it is important to have comprehensive mathematical models of the bistable chemical reaction systems. The Schlögl model is also a good example to study the differences between the deterministic and the stochastic modeling techniques applied to bistability.

One very relevant application comes from cell biology. A living cell operates in an environment with open biochemical reaction systems. That means, there is a flux of material or energy acting on the system; therefore, equilibrium thermodynamics are no longer applicable, and we have to rely on non-equilibrium theory, which allows the possibility of multiple steady state states and non-zero steady state flux. In addition, there is a non-zero entropy production which characterizes the non-equilibrium steady state (NESS). A relevant question is if entropy production can predict the relative stability of the functional cellular attractors (FCA)? The Schlögl model gives some insight into this and other matters.

In the deterministic model, each stable steady state peak corresponds to a peak in the stationary probability distribution. These states are referred as Functional Cellular Attractors (FCA). This is the state in which the system (the cell) is most likely to be found and in which it performs its functions.In addition, the Schlögl model exhibits multiple time scales: a fast scale where the system relaxes to one of the FCA, and a slow scale over which the system transitions from one FCA to another. A key question is how long the system remains in each FCA. The CME and the Fokker-Planck approximations of the model yield conflicting answers to this question. Furthermore, spatial considerations should be considered in the future, since they are fundamental in intracellular modeling. For a more detailed exposition, see [258].

To understand in detail these matters, we present here the Schlögl model, which is a trimolecular autocatalytic reaction scheme,

$$A + 2X \underset{k_2}{\overset{k_1}{\rightleftharpoons}} 3X$$
$$B \underset{k_4}{\overset{k_3}{\rightleftharpoons}} X.$$

Let a, b, x denote the concentrations of each chemical species, with a, b fixed as parameters. Note in general this makes the system open since it has an external flux of a and b to keep their concentrations constant. The system is assumed homogeneous in space, and its volume is denoted by V. When the chemical potentials of the two baths are equal, the system reaches chemical equilibrium, as predicted by Gibbs Grand canonical theory. When they are unequal, the system is driven.

The deterministic version of the model is given by the LMA,

$$\frac{dx}{dt} = k_1 a x^2 - k_2 x^3 - k_4 x + k_3 b. \tag{2.15}$$

As it's a cubic, depending on the parameters, it can have up to three steady states. The bistable case is given when the cubic intersects zero three times, and they are two stable steady states separated by one unstable steady state.

The stochastic version of the model is given by the CME,

$$\frac{dP_0(t)}{dt} = \mu P_1 - \lambda_0 P_0$$
$$\frac{dP_n(t)}{dt} = \lambda_{n-1} P_{n-1} + \mu_{n+1} P_{n+1} - (\lambda_n + \mu_n) P_n,$$

for $n = 1...\infty$, where the random variable $n_X(t)$ is the number of X molecules at time t and n_A, n_B the number of A and B molecules that are fixed for a given V. The quantity $P_n(t)$ denotes the probability of having nX molecules at time t: $P_n(t) = Prn_X(t) = n$, and the birth and death rates are given by $\lambda_n = \hat{k_3} n_B + \hat{k_1} n_A n(n-1)$ and $\mu_n = \hat{k_4} n + \hat{k_2} n(n-1)(n-2)$. The rates $\hat{k_i}$ are related to the deterministic model by $\hat{k_i} = k_i / V^{m-1}$, where m is the number of reactants in the corresponding reaction. This can be deducted from dimensional analysis of the LMA. Thus, the rates in terms of ODE parameters are,

$$\lambda_n = b k_3 V + \frac{a k_1 n(n-1)}{V}$$
$$\mu_n = n k_4 + \frac{k_2 n(n-1)(n-2)}{V^2}. \tag{2.16}$$

The steady state probability distribution is found by mathematical detailed balance, $\lambda_{n-1} P^{ss}_{n-1} =$

$\mu_n P_n^{ss}$ (note this guarantees $\frac{dP_n(t)}{dt}$), in which the probability flux in the forward direction equals the one in the backward direction. This leads to the stationary probability

$$\frac{P_n^{ss}}{P_0^{ss}} = \frac{P_n^{ss}}{P_{n-1}^{ss}} ... \frac{P_1^{ss}}{P_0^{ss}} P_0^{ss} = \prod_{i=0}^{n-1} \frac{\lambda_i}{\mu_{i+1}} \tag{2.17}$$

$$P_0^{ss} = 1 - \sum_{j=1}^{\infty} P_j^{ss}. \tag{2.18}$$

Note the last equation means that the probability of being on any other state with $j \neq 0$ is one minus the probability of being on state $j = 0$.

Now, we will study the stochastic and deterministic models under equilibrium conditions. The condition for chemical detailed balance says that in equilibrium each elementary process in the chemical reaction should be equilibrated by its reverse process. In the case of the Schlögl model this translates into,

$$\frac{k_1 a x^2}{k_2 x^3} = 1 \quad \text{and} \quad \frac{k_3 b}{k_4 x} = 1 \tag{2.19}$$

$$\Rightarrow \qquad \frac{k_1 k_4 a}{k_2 k_3} = 1. \tag{2.20}$$

In this case, the deterministic system will tend to only one equilibrium steady state x_{ss} easily obtained from the previous equations as,

$$x_{ss} = \frac{k_1 a}{k_2} = \frac{k_3 b}{k_4}.$$

The probability distribution function for the detailed balance can also be obtained using Eq. 2.19, Eq. 2.17 and Eq. 2.16, which yields

$$\frac{P_n^{ss}}{P_0^{ss}} = \prod_{i=0}^{n-1} \frac{\theta}{i+1} = \frac{\theta^n}{n!}$$

$$\text{with:} \quad \theta = \frac{a k_1 V}{k_2}.$$

Furthermore, with this result and Eq. 2.18, we can write

$$P_0^{ss} = 1 - \sum_{j=1}^{\infty} P_j^{ss} = 1 - P_0^{ss} \sum_{j=1}^{\infty} \frac{\theta^j}{j!} = 1 - P_0^{ss} \left(e^{\theta} - 1\right)$$

$$\Rightarrow \qquad P_0^{ss} = e^{-\theta}.$$

As predicted by Gibbs' theory, these results yield a Poisson distribution given by

$$P_n^{ss} = \frac{\theta^n}{n!} e^{-\theta} \quad \text{with:} \quad \theta = \frac{ak_1 V}{k_2}.$$

The peak and expected value of a Poisson distribution is given by it's parameter, in this case θ. As the value of θ is the mean number of molecules, given by the deterministic concentration x_{ss} multiplied by the volume, we note the number of molecules at the peak of the distribution corresponds to the steady state concentration in the deterministic model.

When the parameters do not satisfy the chemical detailed balance (Eq. 2.20), the system will reach a non-equilibrium steady state (NESS). Unlike equilibrium conditions, multiple NESS may exist for a given set of parameters. As these parameters move away from the chemical detailed balance condition (Eq. 2.20), the probability density function will deform from its Poisson shape. Assuming only the concentrations of A and B change, as it's more likely the case in a biological setting, we can observe how the probability distribution is affected, for example, see Figure 2.4.

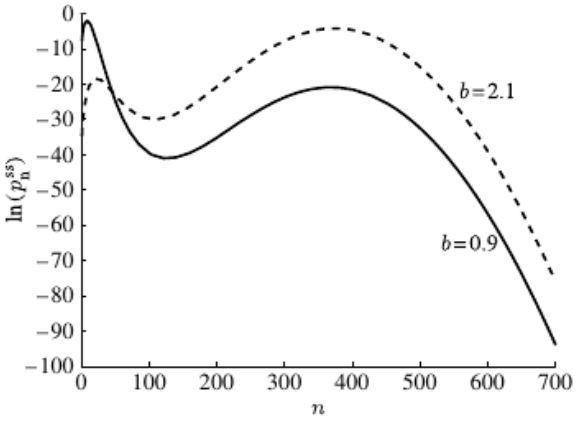

Figure 2.4: Probability density function of the steady state model as b changes with reaction rates fixed at $k_1 = 3$, $k_2 = 0.6$, $k_3 = 0.25$, $k_4 = 2.95$ and $a = 1$. This figure was obtained from [258]

.

Note that the shape of the probability distribution function in Figure 2.4 has two peaks now. When does the probability distribution bifurcate from one NESS to two NESS's, can be answered by analyzing the discriminant of Eq. 2.15 as a function of a and b. For a more detailed exposition, see [258].

Under bistable conditions, the deterministic and stochastic models yield different predictions. In the deterministic model, the system will tend towards one of the two stable fixed

points depending only on the initial condition. On the stochastic model the system will also relax towards one stable point; however, it will randomly switch between the two FCA on a timescale that depends on the system size. This means that, in a small volume system, jumping from on FCA to another is an event that may happen on a reasonable time scale.

In addition, the two peaks in the distribution can exchange their relative heights under changes in a, b and V, see [258]. The proportion of time spent on each peak is dictated by the ratio of the transition rates between them, which depends on the relative height of the peaks. Since the relative height differences are amplified in the large system limit, the time spent in the more stable FCA (highest peak) increases as the volume increases. Thus, for a large but finite volume system, the system ultimate fate, regardless of it's starting point, depends on which is the most stable FCA, which is dictated only by the model parameters.

We have shown the phenomenological accuracy and detail in open chemical reaction systems that can be obtained from the probability distribution function of the CME, especially when dealing with small volume systems in NESS. We showed this richness cannot be described by any of the deterministic models (LMA) nor continuous approximations (FPE) that assume large volumes. For a more detailed exposition, the reader is again referred to [258].

Chapter 3

BIOCHEMICAL STOCHASTIC REACTION-DIFFUSION SYSTEMS

In this chapter, we will introduce stochastic reaction-diffusion processes. In order to do so, we will first need to do a brief overview of diffusion processes within the context of this work. This will allow us to introduce the theory of diffusion-influenced reaction, which is the key ingredient for almost all the stochastic reaction-diffusion algorithms. Unlike macroscopic reaction-diffusion, this theory recognizes that at microscopic and mesoscopic scales[1] the diffusion and reaction processes are coupled. We will later explore different aspects within this theory, like partially reflected Brownian Motion, mean first passage times and diffusion under a force field. This chapter will conclude with an overview of current numerical approaches to model stochastic reaction-diffusion.

The key references in this chapter are [73, 88, 111, 184, 140, 225, 240, 254] for diffusion processes and stochastic differential equations. For a complete overview of the theory of diffusion-influenced reactions the reader is referred to [3, 4, 28, 46, 47, 57, 62, 105, 224, 227, 230, 235]. Partially reflected Brownian motion was studied in [101, 32], first passage time theory in [88, 225, 236, 254] and diffusion under a field of force in [88, 141, 254]. For some of the main software and algorithms available for stochastic reaction-diffusion, the reader is referred to [13, 57, 63, 64, 71, 77, 106, 108, 125, 223, 244, 256, 257, 268].

3.1 Diffusion Processes

A diffusion process is a continuous-time Markov process that has continuous sample paths (trajectories) for which the Kolmogorov forward equation is the Fokker-Planck equation. It can be understood as a Markov process with no jumps, and it can be defined by specifying its first two moments, which correspond to the drift and diffusion coefficient in the Fokker Planck equation. These processes are solutions to stochastic differential equations (SDEs) and require stochastic calculus to be rigorously defined. Some examples of diffusion processes are Brownian motion, reflected Brownian motion and OrnsteinUhlenbeck processes. In order to study these processes, we will begin with an overview of Brownian motion. As it was initially inspired by a problem in Physics, it provides an intuitive starting point to study more general diffusion processes. Furthermore, the solution to a general SDE is defined via

[1] In this work, we are mostly interested in chemical dynamics at cellular and sub-cellular scales.

integrals that involve Brownian motions, just as the trajectoy of a Delbrück-Gillespie process is defined via integrals that involve Poisson processes, as we showed in the previous chapter.

We will further develop some of the main results that are necessary to understand biochemical stochastic reaction-diffusion systems. For more detailed development of diffusion processes and stochastic differential equations, the reader is referred to [73, 88, 111, 184, 140, 225, 240, 254, 267]

3.1.1 Brownian motion

The theory of Brownian motion [68, 208, 253], as developed by Einstein, Smoluchowski, and Langevin, describes the random motion of a particle immersed in a fluid resulting from its collisions with the atoms or molecules of the fluid. There are two distinct physical effects from the collisions: A mean frictional force that resists a macroscopic motion and a random fluctuating force, with zero mean, that rapidly changes the directions of movements.

Consider a heavy particle immersed in a fluid of lighter molecules, whose motion is described by Newtonian mechanics. As a consequence, the velocity of the heavy particle varies by small and supposedly uncorrelated jumps. We assume the probability for a certain change in velocity ΔV depends on V at the current time but not on earlier values. This is the Markovian assumption, and it is only an approximation to reality since collisions are not really instantaneous. At equilibrium we obtain a stationary process, where the autocorrelation time is the time for an initial given velocity to damp out, see [254] for a more complete discussion.

However, this damping was not observed experimentally. Einstein and Smoluchowski realized why [68, 230]. Between two successive observations of the position of the Brownian particle, the velocity has grown and decayed several times. In other words, the interval between two experimental observations is much larger than the autocorrelation time of the velocity. Therefore, we only observe the net displacement after many changes in the velocity, i.e. a set of observations of the position $x_1, x_2, \ldots, x_n, \ldots$, where x_i is the position at time $t = i\Delta t$. Additionally, in this coarser case, the position becomes Markovian as well. In mathematical terms, in the limit of infinitesimally small time steps Δt, this process is referred as standard Brownian motion or Wiener process. It should be noted that this limit is not trivial, and it requires Ito's stochastic calculus.

This discussion already shows that there are two main descriptions of a Brownian particle. The full theory that includes the velocity and the position of the particle and an approximate theory where the time-scale of the damping of the velocity is much faster than the time-scale of the process we are interested in (observations). We will refer to the former as the Langevin approach and to the latter as standard Brownian motion or over-damped Brownian motion.

As with any model, the theory itself is a mathematical idealization of the physical reality. For instance, as a continuous function of time, standard Brownian motion has a fractal geometry, i.e. between any two instants in time, there is an infinite amount of fluctuations and

changes of direction of the particle. However, any physical process that follows Newtonian mechanics always has two times sufficiently close that a particle only moved on a straight line, known as mean free path.

In this section, we will show the mathematical definition of standard Brownian motion as a stochastic process. In Section 3.1.4, we will present the more physically intuitive Langevin approach and show how the standard Brownian motion is recovered from it.

Consider a stochastic process W_t, in order for this process to be considered standard Brownian motion or a Wiener process, it has to obey the following:

- the position at initial time is at the origin, $W_0 = 0$;
- the trajectory described by W_t is continuous [2];
- it has independent increments, $W_t - W_s$, for non-overlapping time intervals [3] $0 \leq s \leq t$;
- the increments are normally distributed with mean zero and variance $\delta t = t - s$, $W_t - W_s \sim \mathcal{N}(0, t\delta t)$.

It is possible to interpret each of these conditions from a Physics perspective. We can think of W_t as the position $x(t)$ of the immersed particle at time t. The conditions can be interpreted as follows: the particle is set at the origin at time 0; the trajectory of the particle should be continuous; the future position of the particle only depends on its current position; in average, the particle should remain close to its starting point, and its separation distance is proportional to the elapsed time.

Note W_t plays the role of the random fluctuating force with zero mean, that rapidly changes the directions of movements, mentioned in the first paragraph. The mean frictional force appears in the Langevin approach; however, it can also appear in other stochastic processes as we will study in the next section.

3.1.2 Stochastic differential equations (SDE)

A stochastic differential equation is a differential equation in which one or more of the terms is a stochastic process. This results in a solution that is also an stochastic process. Most SDEs contain a variable which represents white noise, which is calculated as the derivative of the Wiener process or the standard Brownian we just studied. Other types of random behavior are also possible, like jump processes as we will begin to study in Chapter 6 [4]. A

[2] More rigorously, it is referred as almost surely continuous in probability theory.

[3] In probability theory, it is independent of the sigma-field, $\sigma(W_m, m \leq s)$.

[4] Another good reference in stochastic differential equations with Markovian switching [165].

small survey on specific solutions of SDEs and integration issues is presented in the Appendix A.

We will begin with a non-rigorous heuristic and intuitive approach [73]. Consider the ODE for some particle following a trajectory $x(t)$,

$$\frac{dX(t)}{dt} = \mu(X(t)) \quad X(0) = x_0.$$

This equation yields a smooth trajectory. However, in many relevant physical, biological, engineering and finance applications, we observe noisy trajectories. How to model them? We want to include the possibility of random perturbations into the ODE,

$$\frac{dX(t)}{dt} = \mu(X(t) + \sigma(X(t))\xi(t) \quad X(0) = x_0,$$

where σ is a function and $\xi(t)$ represents the white noise. This white noise can be thought of as the time derivative of the Wiener process in the previous section, so $\frac{dX(t)}{dt} = \mu X(t) + \sigma(X(t))\frac{dW_t}{dt}$. "Multiplying by dt", we obtain

$$dX(t) = \mu X(t)dt + \sigma(X(t))dW_t.$$

This equation, properly interpreted, is a stochastic differential equation. The solution should be given in terms of an integral,

$$X(t) = x_0 + \int_0^t \mu X(s)ds + \int_0^t \sigma(X(t))dW.$$

However, to truly define this process, we need to construct the Wiener process correctly; we need to define the stochastic integral $\int_0^t \dots dW$ and show the solution exists, see [73, 225] and also the Appendix A for some more details. Here we will not study all these issues, but we will show some relevant derivations. The properties of the Wiener process were already established in the previous section. However, we still need to define the stochastic integral (also see Appendix A). In order to do so, we will first need to study the quadratic variation of the Wiener process.

Quadratic variation for the Wiener process

The quadratic variation of a function $f(t)$ in a given time interval $[0, T]$ is given by

$$Q_v = \lim_{n\to\infty} \sum_{i=0}^{n-1} \left[f(t_{i+1}) - f(t_i)\right]^2,$$

where $t_k = \frac{k}{n}T$. Assuming $f(x)$ is differentiable, we can use the mean value theorem

$$\sum_{i=0}^{n-1} \left[f(t_{i+1}) - f(t_i)\right]^2 \leq \sum_{i=1}^{n-1} \left[f'(s_i)(t_{i+1} - t_i)\right]^2,$$

with $t_i \leq s_i \leq t_{i+1}$. However,

$$\begin{aligned}
\sum_{i=1}^{n-1} \left[f'(s_i)(t_{i+1} - t_i)\right]^2 &\leq \max_i [f'(s_i)^2] \sum_{i=0}^{n-1} (t_{i+1} - t_i)^2 \\
&= \max_i [f'(s_i)^2] \sum_{i=0}^{n-1} \left(\frac{T}{n}\right)^2 \\
&= \max_i [f'(s_i)^2] \left(\frac{T^2}{n}\right),
\end{aligned}$$

and as $n \to \infty$, $Q_v \to 0$, continuous differentiable functions have zero quadratic variation. However, as the Wiener process is continuous but nowhere differentiable, this will no longer be true. To show this, instead of using $f(t)$, let's use the Wiener process $W(t) = W_t$. The quadratic variation is then

$$Q_v = \lim_{n\to\infty} \sum_{i=0}^{n-1} \underbrace{\left[W(t_{i+1}) - W(t_i)\right]}_{\sim N(0,T/n)}^2,$$

where, as mentioned in the previous section, has normally distributed and independent increments $W(t_{i+1}) - W(t_i)$ with mean zero and variance $t_{i+1} - t_i = T/n$. The sum can be written in terms of a more simple random variable,

$$\sum_{i=0}^{n-1} \left[W(t_{i+1}) - W(t_i)\right]^2 = \sum_{i=0}^{n-1} X_i^2 = \sum_{i=0}^{n-1} Y_i,$$

with $X_i \sim N(0, T/n)$. Note, since the mean of X_i is zero, $\mathbb{E}[X_i^2] = T/n$ and $\mathbb{E}[Y_i] = T/n$. The sum can be rewritten as

$$\sum_{i=0}^{n-1} Y_i = n \left(\frac{1}{n} \sum_{i=0}^{n-1} Y_i\right).$$

By the law of large numbers, the quantity inside the parenthesis converges to its mean T/n, so $\sum_{i=0}^{n-1} Y_i \sim T$ for large n. In the limit as $n \to \infty$,

$$\lim_{n\to\infty} \sum_{i=0}^{n-1} \left[W(t_{i+1}) - W(t_i)\right]^2 = T. \tag{3.1}$$

The quadratic variation of the Wiener process is non-zero. This has consequences in how simple calculations work, like integrals and the chain rule. For instance, without too much rigor, the equality just derived can be extended to its infitesimal limit where the sum becomes an integral [111],

$$\int_0^t dW_s^2 = \int_0^t ds.$$

Other way to understand this is for very small δt, the quantity $\sum_{i=0}^{n-1} \left[W(t_{i+1}) - W(t_i)\right]^2$ has expected value T and variance $O(\delta t)$, see [111]. Therefore, we obtain the infinitesimal quadratic variation of the Wiener process goes like $dW_t^2 \sim dt$.

Ito's lemma

Ito's lemma is one of the main results from stochastic calculus, and it will be very helpful to derive some of the equations we will need in this chapter. We can begin by considering a twice differentiable function $f(x)$; however, instead of using x as the independent variable, we will use a random variable, or more generally, a stochastic process X_t. The most simple stochastic process we can think of is a Wiener process W_t. Applying a Taylor expansion to such a function, we obtain

$$F(W_t + dW_t) = F(W_t) + \frac{\partial F}{\partial x} dW_t + \frac{1}{2}\frac{\partial^2 F}{\partial x^2} dW_t^2 + O(dW_t^3).$$

However, we know the quadratic varaition of a Wiener process goes $dW_t^2 = dt$. Therefore, we can non-rigorously obtain the chain rule for a stochastic process under the Ito integration,

$$dF = \frac{\partial F}{\partial x} dW_t + \frac{1}{2}\frac{\partial^2 F}{\partial x^2} dt.$$

The first term correspond to the classical part and the second term emerges from the fact that the quadratic variation of a stochastic process under Ito's integral is non-zero. A more general version of this result is easy to obtain. Instead of simply applying this to a function of a Wiener process, we can use a general stochastic process that obeys the SDE,

$$dX_t = \mu(X_t, t)dt + \sigma(X_t, t)dW_t.$$

The Taylor expansion of $F(X_t)$ is given by

$$\begin{aligned} F(X_t + dX_t, t + dt) &= F(X_t, t) + \frac{\partial F}{\partial t}dt + \frac{\partial F}{\partial x}dX_t + \frac{1}{2}\frac{\partial^2 F}{\partial x^2}dX_t^2 + O(dX_t^3, dt^3) \\ &= F(X_t, t) + \frac{\partial F}{\partial t}dt + \frac{\partial F}{\partial x}\left(\mu(x,t)dt + \sigma(x,t)dW_t\right) \\ &\quad + \frac{1}{2}\frac{\partial^2 F}{\partial x^2}\left(\sigma(x,t)^2 dW_t^2\right) + O(dX_t^3, dt^3). \end{aligned}$$

Therefore, a general version of Ito's lemma or Ito's chain rule is

$$dF = \left(\frac{\partial F}{\partial t} + \mu(x,t)\frac{\partial F}{\partial x} + \frac{\sigma(x,t)^2}{2}\frac{\partial^2 F}{\partial x^2}\right)dt + \sigma(x,t)\frac{\partial F}{\partial x}dW_t. \tag{3.2}$$

3.1.3 Fokker-Planck equations (FPE)

We can derive an equation for the probability density function dynamics from the stochastic differential equation. Let's begin with a general one-dimensional SDE

$$dX_t = \mu(X_t, t)dt + \sigma(X_t, t)dW_t, \tag{3.3}$$

and apply Ito's chain rule from Eq. 3.2 (see also [225]) for an arbitrary twice differentiable scalar function $f(x)$,

$$f(X_t + dX_t) - f(X_t) = f'(X_t)dX_t^2 + \frac{f''(X_t)}{2}dX_t^2$$

$$= f'(X_t)\left[\mu(X_t,t)dt + \sigma(X_t,t)dW_t\right] + \frac{f''(X_t)}{2}\left[\mu(X_t,t)^2dt^2 + 2\mu(X_t,t)dtdW_t + \sigma(X_t,t)^2dW_t^2\right].$$

Since $dW_t^2 \sim dt$, the only first order terms in the coefficient of $f''(X_t)$ is the last one, so

$$df(X_t) = f'(X_t)\left[\mu(X_t,t)dt + \sigma(X_t,t)dW_t\right] + \frac{f''(X_t)}{2}\sigma(X_t,t)^2dt.$$

Taking the expected value of this equation and using the fact that $\langle dW_t \rangle = 0$,

$$\frac{d}{dt}\langle f(X_t)\rangle = \left\langle f'(X_t)\mu(X_t,t) + \frac{f''(X_t)}{2}\sigma(X_t,t)^2 \right\rangle. \tag{3.4}$$

As we know X_t is an stochastic process, it has a conditional probability $p(x,t|x_0,t_0)$, then the expected value of $f(X_t)$ is given by the corresponding integral. Taking the time derivative

of this integral,

$$\frac{d}{dt}\langle f(X_t)\rangle = \frac{d}{dt}\int_\Omega f(x)p(x,t|x_0,t_0)dx = \int_\Omega f(x)\frac{\partial p(x,t|x_0,t_0)}{\partial t}dx, \tag{3.5}$$

where Ω is the whole spatial domain in x. Note the derivative was shifted into the integral as a partial derivative, so it only acts on $p(x,t|x_0,t_0)$. On the other hand, we can also write the right hand side of Eq. 3.4 as an integral using the definition of expected value and $p(x,t|x_0,t_0)$,

$$\frac{d}{dt}\langle f(X_t)\rangle = \int_\Omega \left[f'(x)\mu(x,t) + \frac{f''(x)}{2}\sigma(x,t)^2\right] p(x,t|x_0,t_0)dx.$$

We will now integrate by parts once the first term and twice the second term. We will also use the fact that in this case $\Omega \in (-\infty,\infty)$, so that $p(x,t|x_0,t_0)$ and its derivative should vanish at infinity. After the integration, we obtain

$$\frac{d}{dt}\langle f(X_t)\rangle = \int_\Omega \left[-f(x)\frac{\partial}{\partial x}\left(\mu(x,t)p(x,t|x_0,t_0)\right) + \frac{f(x)}{2}\frac{\partial^2}{\partial x^2}\left(\sigma(x,t)^2 p(x,t|x_0,t_0)\right)\right] dx.$$

Equating this equation to Eq. 3.5,

$$\int_\Omega f(x)\frac{dp(x,t|x_0,t_0)}{dt} = \int_\Omega f(x)\left[-\frac{\partial}{\partial x}\left(\mu(x,t)p(x,t|x_0,t_0)\right) + \frac{1}{2}\frac{\partial^2}{\partial x^2}\left(\sigma(x,t)^2 p(x,t|x_0,t_0)\right)\right] dx.$$

As this is true for an arbitrary function $f(x)$, then the equality holds without the need of having the integral,

$$\frac{dp(x,t|x_0,t_0)}{dt} = -\frac{\partial}{\partial x}\left(\mu(x,t)p(x,t|x_0,t_0)\right) + \frac{1}{2}\frac{\partial^2}{\partial x^2}\left(\sigma(x,t)^2 p(x,t|x_0,t_0)\right).$$

We can rewrite the conditional part as an initial condition for the PDE as,

$$\begin{aligned}\frac{dp(x,t)}{dt} &= -\frac{\partial}{\partial x}\left(\mu(x,t)p(x,t)\right) + \frac{1}{2}\frac{\partial^2}{\partial x^2}\left(\sigma(x,t)^2 p(x,t)\right),\\ p(x,t_0) &= \delta(x-x_0).\end{aligned}$$

However, there is no reason that the initial condition is uniquely a delta. It can be any function as long as it integrates to one, so it remains being a probability; therefore,

$$\begin{aligned}\frac{dp(x,t)}{dt} &= -\frac{\partial}{\partial x}\left(\mu(x,t)p(x,t)\right) + \frac{1}{2}\frac{\partial^2}{\partial x^2}\left(\sigma(x,t)^2 p(x,t)\right),\\ p(x,t_0) &= p_0(x).\end{aligned}$$

This is the Fokker-Planck equation corresponding to the stochastic process given by the SDE in Eq. 3.3. It describes the dynamics of the probability distribution function $p(x,t)$ that the trajectories of the SDE from Eq. 3.3 follow.

Multi-dimensional case

This result can be extended to a general system of SDE's. Consider the system of SDE's

$$d\overline{X}_t = \overline{A}(\overline{X}_t, t)dt + \overline{\overline{B}}(\overline{X}_t, t)d\overline{W}_t,$$

where the over-bar represents an $N-$dimensional vector and the double over-bar a NxN matrix. The corresponding Fokker-Planck equation for this system can be derived in a similar manner to obtain

$$\frac{df(\overline{x},t)}{dt} = -\sum_{i=1}^{N} \frac{\partial}{\partial x}\left[A_i(\overline{x},t)f(\overline{x},t)\right] + \frac{1}{2}\sum_{i,j=1}^{N} \frac{\partial^2}{\partial x^2}\left[D_{ij}(\overline{x},t)f(x,t)\right]. \tag{3.6}$$

where

$$D_{ij}(\overline{x},t) = \sum_{k=1}^{M} B_{ik}(\overline{x},t)B_{kj}(\overline{x},t).$$

For a detailed derivation of the multi-dimensional case the reader is referred to [225, 254].

3.1.4 Langevin equation and Klein-Kramers equation

With the discussion above in mind, we begin with a general approach in the spirit of Langevin [145]. Consider the stochastic dynamic equations for an immersed particle of mass m,

$$dX_t = V_t dt, \quad mdV_t = \big(-\eta V_t\big)dt + \sqrt{2k_B T\eta}\; dW_t; \tag{3.7}$$

where X_t is the position, V_t the velocity, η the damping coefficient, $\xi(t)dt = \sqrt{2k_BT\eta}\; dW_t$ is the white noise term with W_t the standard Brownian motion or Wiener process [5], k_B the Boltzmann constant and T the temperature. The Wiener process satisfies $E[W_t] = 0$ and $E[W_tW_s] = \min(t,s)$, which implies $E[\xi(t)\xi(s)] = 2k_BT\eta\delta(t-s)$. The stochastic trajectory in its integral form is given by

$$X(t) = X(0) + \int_0^t e^{-\eta s/m}\left(V(0) + \frac{1}{m}\int_0^s e^{\eta\tau/m}\sqrt{2k_BT\eta}\; dW_\tau\right)ds, \tag{3.8}$$

[5]The notation using $\xi(t)$ is introduced since it might be more familiar to readers with a Physics background.

see the Appendix A for a derivation. Its probability distribution dynamics is described by the multivariate Fokker-Planck equation, as shown in Eq. 3.6. In this specific case, this equation is usually referred as the Klein-Kramers equation,

$$\frac{\partial f(x,v,t)}{\partial t} = \frac{\partial}{\partial v}\left[\left(\frac{k_B T\eta}{m^2}\right)\frac{\partial f}{\partial v} + \frac{\eta v}{m} f\right] - v\frac{\partial f}{\partial x}. \tag{3.9}$$

Klein-Kramers equation is mathematically very problematic since it has zero diffusion in the position variable. This problem has only been carefully studied in recent years using a degenerated diffusion coefficient. Klein-Kramers equation has not been widely discussed in the mathematics literature because of this reason. However, this is not an issue in the certain limits. In the over-damping limit of Eq. 3.7, we obtain $dx = \frac{1}{\eta}\xi(t)dt$, which yields a simpler Fokker-Planck equation

$$\frac{\partial f(x,t)}{\partial t} = D\frac{\partial^2 f(x,t)}{\partial x^2}, \tag{3.10}$$

with the diffusion coefficient given by the Einstein relation: $D = k_B T/\eta$. This equation describes the probability distribution dynamics of standard Brownian Motion or Wiener process with no drift. Note it can be extended to varying damping coefficient $\eta(x)$, which would make the diffusion coefficient not constant, and it will change the form of the equation. In particular, the issue of Itō vs. Stratonovich or divergence form of the diffusion term matters [14].

Although Eq. 5.4 has an identical form as the classical diffusion equation for a density of particles, it has a much fundamental character; it does not rely on Fick's law. The classical equation should be understood as the equation of *mean density* of a large number of identical, independent Brownian particles. Fick's law then is an emergent statistical phenomenon.

The theory of chemical reaction in aqueous solution, mediated by diffusion encounter, is based on a three-dimensional version of the standard Brownian motion we just presented, with the addition of an absorbing or partially absorbing boundary condition to model the "event of encounter" in a reaction; it is the core of Smoluchowski's theory [46, 230]. However, as Brownian Motion is such a powerful and useful mathematical idealization, it is easy to assume that it is a first principle. For instance, we tend to think of random walks as approximations to standard Brownian motion (or more accurately to a Wiener Process), immediately assuming Brownian motion is the best description of the physical world. In reality, the theory of Brownian motion is a mathematical limit, and one could even argue Random Walks might provide models closer to what one observes in reality than Brownian motion theory. With computational tasks in mind, why shouldn't we think standard Brownian motion theory is the one providing an approximation to some specific kind of Random walks?

For relatively simple processes, as in diffusion-influenced irreversible reactions, standard

Brownian motion provides a robust theoretical framework. However, when dealing with more complex processes like reversible reactions, a great deal of subtleties arise [3, 13, 28, 136, 199]. Many of the issues one encounters while trying to model more and more complex processes are intrinsic to the fact that one had adopted a specific mathematical idealization, especially when dealing with such an abstract idealization like Brownian Motion. For instance, it has been shown that the continuous diffusion approximation of discrete reaction networks can fail to represent correctly the mesoscopically interesting steady-state behavior of bistable systems [258], an issue of utter relevance in biochemical cell dynamics. The purpose of this paper is to convince the reader that an alternate discrete approach to reversible stochastic reaction-diffusion might provide a simpler, more robust, and computation-friendly framework where these subtleties are no longer an issue. It also unifies previous theoretical approaches with more recent simulation algorithms, contributing to a better understanding of reversible stochastic reaction-diffusion. Although the model here presented is for a relatively simple problem, it provides the guidelines for a different line of research that could address fundamental issues in stochastic reaction-diffusion theory and simulations.

3.2 Diffusion-influenced reaction models

A quantitative mathematical description of biochemical systems at a cellular scale is complex involving many cell types and/or molecular species. Furthermore, these are small-scale thermodynamic systems, such that a quantitative mathematical description must be inherently stochastic and often involve a small but significant number of diffusing species that interact and react with each other.

Initially developed by Smoluchowski [230], the diffusion-influenced reaction theory [105, 236] states that the rate of certain bimolecular reaction $A + B \to C$ depends on the rate of diffusion encounter— i.e. diffusion-influenced. Furthermore, the theory allows a stochastic interpretation in terms of Brownian Motion[6] and first passage times [236], so it is valid at mesoscopic scales. As at cellular scales many bimolecular reactions are diffusion-influenced, this theory is the key element to model more complicated mesoscopic biochemical systems. Therefore, most of the current research and algorithms for mesoscopic reaction-diffusion are built on top of diffusion-influenced reaction theory [13, 63, 71, 237].

There has been a recent significant effort to produce accurate models and stochastic simulation algorithms for complex biochemical reaction-diffusion systems; however, even at the theoretical level, there are several aspects yet to be understood and improved. In this section, we give an introduction to the main aspects of the diffusion-influenced reaction theory, so in the next chapters, we can show how to apply it and how it can be improved to help us better model and simulate more complex biochemical systems.

---

[6]This is not obvious in the reversible case, as shown in Chapter 5

3.2.1 Smoluchowski's model

Consider the reaction $A + B \xrightarrow{k_S} C$, where A and B are two reactive spheres diffusing in space. Fix the frame of reference at the center of A and assume many B particles diffuse around A with a diffusion coefficient given by the sum of A and B diffusion coefficients, $D = D_A + D_B$, following standard Brownian motion. Whenever the B molecules reach by diffusion the boundary σ given by the sum of the radii of A and B, $\sigma = R_A + R_B$, we assume a reaction occurs. We call this reaction a purely diffusion-controlled reaction. Smoluchowski classical work, given in detail in [46, 227, 230], calculates the association rate constant k_S.[7]

In Smoluchowski's original work, the concentration of molecule B surrounding the A is denoted by $c(r,t)$. It obeys a simple three-dimensional diffusion equation,

$$\frac{\partial c(r,t)}{\partial t} = \nabla \cdot \big[D(r)\nabla c(r,t)\big], \quad r \in [\sigma, R] \tag{3.11a}$$

$$c(\sigma,t) = 0, \quad c(R,t) = c_0. \tag{3.11b}$$

As the problem is spherically symmetric, we obtain $\frac{\partial c(r,t)}{\partial t} = \frac{D}{r^2}\frac{\partial}{\partial r}\left(r^2 \frac{\partial}{\partial r} c(r,t)\right)$, for constant D. The absorbing boundary condition at σ represents the purely diffusion-controlled reaction with 100% reaction for each and every encounter; the boundary condition at R provides a bath of B molecules that guarantees a constant concentration, c_0, at a distance $R \gg \sigma$. The quantity c_0 is identified as the "bulk concentration" in an aqueous solution containing many A's and B's. In the limit of $R \to \infty$, the time-dependent and stationary solutions to this equation are given respectively by

$$c(r,t) = c_0\left[1 - \frac{\sigma}{r}\mathrm{erfc}\left(\frac{r-\sigma}{\sqrt{4Dt}}\right)\right], \qquad c_{ss}(r) = c_0\left[1 - \frac{\sigma}{r}\right].$$

The steady state diffusion controlled association rate constant is then obtained from the flux at the reaction radius, σ, as

$$k_S = \frac{4\pi D\sigma^2 c'_{ss}(\sigma)}{c_0} = 4\pi D\sigma.$$

In the one and two dimensional case, it is worth mentioning that it is not possible to obtain reaction rates in the same manner since the mean first passage times diverge as $R \to \infty$. There is a large literature on how to deal with this physically very different and mathematically

[7] In fact, how to define the association rate constant k_S is itself an important issue. Ideally, if the waiting time distribution for successive reactions is exponential, then a single rate parameter k_S suffices. When the distribution is non-exponential, usually one takes the reciprocal of the mean time as the k_S, which can be shown to agree with an appropriate steady-state flux. The spatial dimension has a crucial role in this problem, which is certainly related to Pólya's recurrence theorem.

challenging problem [199, 200, 201, 219]. Also, as pointed out in [46], the time-dependent flux becomes infinite at $t = 0$, which is unacceptable when the initial rate may be very significant. These issues, among others pointed out in [46], are weaknesses of the theory.

3.2.2 Collins and Kimball's model

Collins and Kimball gave an improvement over Smoluchowski's theory [46], in which the absorbing boundary at σ is replaced with a partially absorbing boundary condition. This is obtained by making the flux equal to the concentration at the reaction radius,

$$4\pi\sigma^2 D \frac{\partial c(r,t)}{\partial r}\bigg|_{r=\sigma} = \kappa c(\sigma, t), \tag{3.12}$$

where κ controls the degree of diffusion-influence in the reaction ($\kappa = 0$ means no reaction, while $\kappa \to \infty$ means the reaction is diffusion limited). In stochastic simulations, κ is intimately related to the probability of being absorbed (p) or being reflected. But the relation is non-trivial as signified by the dimension of κ: $[\text{length}]^3[\text{time}]^{-1}$. In fact, both D and κ are best understood in terms of a discrete setting: $D = \frac{\Delta x^2}{6\Delta t}$ and $\frac{\kappa}{4\pi\sigma^2} = \frac{\Delta x}{\Delta t}p$, see Section 3.3.

Solving Eq. 3.11a with $\frac{\partial c(r,t)}{\partial t} = 0$ and with this boundary condition yields the steady state, and the partially absorbing reaction rate of Collins and Kimball,

$$c_{ss}(r) = c_0\left[1 - \frac{\kappa\sigma}{4\pi D\sigma + \kappa}\left(\frac{1}{r}\right)\right], \tag{3.13}$$

$$k_{CK} = \frac{\kappa k_S}{\kappa + k_S}. \tag{3.14}$$

Note that if $\kappa \to \infty$ we recover the purely diffusion limited reaction rate k_S. Furthermore, in the full time dependent solution with the new boundary condition, the flux will no longer be singular at $t = 0$ [46].

The reaction rates defined through steady-state flux, given in Eq. 3.14, have a clear probabilistic interpretation in terms of the mean passage times, τ [227, 236]. We can assume $\tau_{CK} = \tau_S + \tau_\kappa$, where τ_{CK} is the mean passage time until the first reaction occurs in the Collins and Kimball model, τ_S is Smoluchowski's mean first passage time from a uniform distribution outside the absorbing boundary to the absorbing boundary, and $\tau_\kappa \sim \kappa^{-1}$ is the mean passage time starting from the absorbing boundary until the molecule is bound, this is illustrated in Figure 3.1. Note Eq. 3.14 is immediately recovered by using the inverse relation $\tau_{CK} \sim 1/k_{CK}$. A reaction is reaction-probability limited if $k_S \gg \kappa$, such that $k_{CK} \approx \kappa$. Therefore, Collins and Kimball's theory is applicable to cases ranging from diffusion-limited scenario $k_S \ll \kappa$ to reaction-probability-limited scenario.

The reaction diffusion problems framed as above can equivalently be described in terms

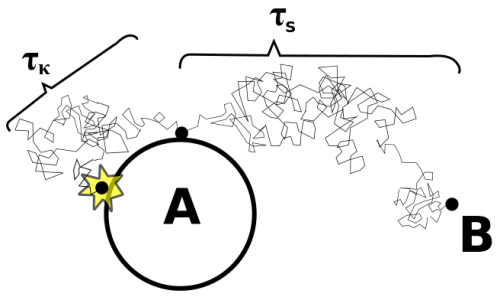

Figure 3.1: Interpretation of the times corresponding to the inverse of the reaction rates in the Collins and Kimball model. Note that after a time τ_S when particle B collides with A, the reaction might not happen; it still has to wait a time τ_κ. This is the stochastic trajectory interpretation of a partially absorbing boundary. In a more formal interpretation PRBM should be understood as purely reflective Brownian Motion conditioned to stop at a random time [32, 101], see Section 3.3.

of the Green's functions for an isolated pair of A and B molecules [256, 257]. Consider again one molecule A fixed in the origin. We will denote $f(r,t|r_0)$ the probability of a particle B being a distance r from A at time t given that it was at r_0 at time 0. This transition probability will obey the diffusion equation, initial condition and boundary condition,

$$\frac{\partial f(r,t|r_0)}{\partial t} = \nabla \cdot \big[D(r)\nabla f(r,t|r_0)\big]. \tag{3.15a}$$

$$f(r,0|r_0) = \frac{\delta(r-r_0)}{4\pi r_0^2}. \tag{3.15b}$$

$$\lim_{r\to\infty} f(r,t|r_0) = 0, \tag{3.15c}$$

and an extra boundary condition at $r=\sigma$, which can be Eq. 3.11b or Eq. 3.12 written in terms of $f(r,t|r_0)$. Note this is an equation for the probability $f(r,t|r_0)$, which is the "remaining" probability density function in the presence of an absorbing or partially absorbing boundary (diffusion with killing). Then

$$-\frac{d}{dt}\int_\sigma^\infty 4\pi r^2 f(r,t|r_0)dr$$

is the probability density function for the absorbing time.

3.2.3 Reversible bimolecular reaction via diffusion encounter.

The Green's function formulation for an isolated pair has been extended to modeling reversible reactions in one, two and three dimensions [3, 136, 199]. For spherical symmetry and constant $D(r) = D$, these extensions consist of augmenting the boundary condition in Eq. 3.12 with a "back-reaction" with rate μ:

$$4\pi\sigma^2 D \frac{\partial f(r,t|r_0)}{\partial r}\bigg|_{r=\sigma} = \kappa f(\sigma,t|r_0) - \mu\big[1 - S(t|r_0)\big], \tag{3.16}$$

$$\text{where } S(t|r_0) = 1 - \int_0^t 4\pi\sigma^2 D \left.\frac{\partial f(r,\tau|r_0)}{\partial r}\right|_{r=\sigma} d\tau,$$

and $S(t|r_0)$ is referred as the survival probability in the literature. An analogous version of the boundary condition in Eq. 3.16 first appeared in [224], which also made an important statement that in a chemical reaction equilibrium, the $\lim_{t\to\infty} f(r,t|r_0)$ should be uniform in space independent of r.

The notion of survival probability doesn't really make sense when talking about reversible reactions. A more appropriate name for $S(t|r_0)$ is the probability of B not being bound at time t given it initially was a distance r_0 from A, regardless if the particle was bounded at some time between 0 and t. This is clear from the fact that

$$\begin{aligned} S(t|r_0) =& 1 - \int_0^t 4\pi\sigma^2 D \left.\frac{\partial f(r,\tau|r_0)}{\partial r}\right|_{r=\sigma} d\tau \\ =& \int_\sigma^\infty 4\pi r^2 f(r,t|r_0) dr, \end{aligned} \tag{3.17}$$

which is easily proved by differentiating Eq. 3.17 by t, then using Eq. 3.15a and the boundary conditions, then repeat the inverse process and evaluate at $t = 0$ to find the integration constant to be one. The second integral is clearly the probability of being unbound as we mentioned before. The exact solution of this problem is given in [136]. In [198, 197], the authors implemented numerical simulations using this model as a starting point.

If one restricts the diffusion of B in a finite space and replaces Eq. 3.15c with a reflecting boundary at R, then the stationary equilibrium solution to Eq. 3.15a with boundary condition Eq. 3.16 gives $f_{eq}(r) \equiv f_{eq}(\sigma) = (\mu/\kappa)p_C$ in which p_C is the equilibrium probability of C: $p_C = 1 - f_{eq}(\sigma)V_B$, where $V_B = \frac{4\pi}{3}\big(R^3 - \sigma^3\big)$ is the volume available to the diffusing B [224]. Therefore, the theory provides a rigorous *equilibrium constant* for the reversible association reaction

$$K_{eq} \equiv \left(\frac{p_C}{1 - p_C}\right) V_B = \frac{\kappa}{\mu}. \tag{3.18}$$

This implies that if the bimolecular association rate constant is κ, then the unimolecular

dissociation rate constant has to be μ. On the other hand, if we choose Eq. 3.14 as the on-rate constant $k_{\text{on}} = \kappa k_S/(k_S + \kappa)$, as suggested by Fig. 3.1, then the off-rate constant has to be $k_{\text{off}} = \mu k_S/(k_S + \kappa)$. The validity of Eq. 3.18 assumes two well-defined states, $A + B$ and $AB \equiv C$, with Markov transition in between. Strictly speaking, this requires the dynamics within each of the two states to be sufficiently rapid while the transitions between the two states as relatively rare events. "Diffusion finally manages to separate the reaction partners." [28]. Additionally, these rates can be interpreted as

$$k_{\text{on}} = k_S \frac{\kappa}{k_S + \kappa} = k_S \phi, \tag{3.19}$$

where $\phi = \kappa/(k_S + \kappa)$ can be understood as the fraction of geminate recombinations that lead to association or also as the probability of association at the boundary. Then the off rate is

$$k_{\text{off}} = \mu \frac{k_S}{k_S + \kappa} = \mu(1 - \phi), \tag{3.20}$$

where the probability of dissociation at the boundary is $\big(1 - \phi\big)$. The reverse reaction rate constant k_{off} has the property that it is diffusion controlled if, and only if, k_{on} is diffusion controlled, quite irrespective of the value of μ. "[A]ny description of the reaction process that divides the initial bimolecular event into a diffusive association step $[\cdots]$ and a subsequent unimolecular transformation is logically incorrect." [224]. This means that in the case of reversible bimolecular reactions, we should not treat association and dissociation as independent processes [8].

For simplicity, all the models presented in this section assumed there is no force field. However, all the models have generalizations that introduce a force field through a potential; they can all be found in the literature cited.

3.3 Partially reflective Brownian Motion (PRBM)

Consider a random walk moving in one dimensional space. This can be described as a discrete time Markov chain, where the state i refers to its position $x_i = i\delta x$. Let the probability of jumping from state i to $i + 1$ be q_i and from state i to $i - 1$ be p_i, such that $p_i + q_i \leq 1$ and $1 - (p_i + q_i)$ is the probability of not jumping. For a purely reflective boundary at $i = 0$, the

[8] We should note this is not strictly true in the case of particle-based simulations. The collective mean behavior of a reaction-diffusion particle-based simulation that models association and dissociation independently can have an emergent global coupled behavior. Therefore, particle-based simulations that model association and dissociation independently could in theory still reproduce the results established by [224]. As a matter of fact, the model presented in Chapter 5 validates previous particle-based algorithms in the back-reaction boundary condition context from [224]

only possibility is that the probability from jumping from state $i = 0$ to the absorbed state is $p_0 = 0$. Analogously, for the purely absorbing boundary at $i = 0$, it is required that $p_0 = 1$. In the same manner, we can easily think of the partially absorbing boundary condition at $i = 0$, where the probability of being absorbed is $p_0 = \epsilon$, with $\epsilon \in (0, 1)$.

In order to study this random walk, lets assume δx is fixed, so in order to satisfy that $p_i + q_i \leq 1$, we need $\delta t \leq \delta x^2/(2D)$. We would like to relate this random walk to Brownian Motion, so we need to assign correct values to q_i and p_i. This is analogous to what we will do in Section 5.3. The jump probabilities elsewhere outside the boundary should be $q_i = p_i = D\delta t/\delta x^2$. Following the same structure of the Markov chain from Eq. 5.5 with Eq. 5.14, the i^{th} equation yields

$$\frac{\pi_i^{n+1} - \pi_i^n}{\delta t} = D\left[\frac{\pi_{i+1}^n - 2\pi_i^n + \pi_{i-1}^n}{\delta x^2}\right], \tag{3.21}$$

which in the continuous limit recovers the one dimensional Brownian Motion $\partial\Pi/\partial x = D\partial^2\Pi/\partial x^2$. We also would like to recover the partially absorbing boundary condition, so we write the first equation in the Markov chain,

$$\frac{\pi_0^{n+1} - \pi_0^n}{\delta t} = \frac{D}{\delta x^2}\pi_1^n - \frac{D}{\delta x^2}\pi_0^n - \frac{\epsilon}{\delta t}\pi_0^n,$$

where we used that the probability of staying at shell $i = 0$ is $1-(q_0+p_0) = 1-(D\delta t/\delta x^2+\epsilon)$. In order for this equation to have the same form as Eq. 3.21, we need to introduce the ghost shell π_{-1} (as explained in Section 5.3.1), which satisfies

$$\epsilon\pi_0^n = D\delta t\frac{\pi_0^n - \pi_{-1}^n}{\delta x^2}.$$

In order to be able to recover the partially absorbing boundary condition $D\partial\Pi/\partial x|_{x=x_0} = \kappa\Pi(x_0, t)$, we need to set $\epsilon = \kappa\delta t/\delta x$. It is now straightforward to write κ and the Diffusion coefficient in terms of the jump probabilities in the discrete model by summing p_i and q_i,

$$D = \frac{\delta x^2}{2\delta t}, \quad \kappa = \frac{\delta x}{\delta t}\epsilon. \tag{3.22}$$

Note $\epsilon = 0$ corresponds to a purely reflective boundary, which means $\kappa = 0$, so $\partial\Pi/\partial x|_{x=x_0} = 0$. The purely absorbing boundary corresponds to $\epsilon \to 1$. As shown in Section 5.3.1, $\delta t \leq \delta x^2/(2D)$, so $\kappa = \delta x\epsilon/\delta t \geq 2D\epsilon/\delta x$. Then, as $\delta x \to 0 \Rightarrow \kappa \to \infty$, and the boundary condition becomes $\Pi(x_0, t) = 0$. As expected, this matches the limiting behavior from Collins and Kimball's original work [46].

A very subtle issue is in the continuous limit of the probability of partial absorption $\epsilon = \kappa\delta t/\delta x$ with κ constant. Again as $\delta t \leq \delta x^2/(2D)$, then $\epsilon \leq \kappa\delta x/(2D)$. This means that

in the continuous limit $\delta x \to 0$, the probability of partial absorption goes to zero, $\epsilon \to 0$. However, $\epsilon = 0$ means a purely reflective boundary, not a partially absorbing one, so the continuous limit of partially absorbing boundaries can be confusing, especially when trying to interpret them in particle-based simulations. The works [101, 32] elaborate on this issue and state that partially reflected Brownian Motion (PRBM) should be understood as purely reflective Brownian Motion conditioned to stop at a random moment given in terms of the local time process. In more intuitive terms, given a counting process $\mathcal{L}_t$ that counts the number of hits of a particle to the reflective boundary, the particle is killed (absorbed) when $\mathcal{L}_t \geq \chi$, where χ is an independent exponentially distributed random variable. In this sense, PRBM is best understood as the limit of a random walk. Furthermore, the parameters D and κ have a clear interpretation in terms of the jump and partial absorption probabilities. This result provides a more insightful understanding of the parameters even in the continuous model.

Also note the probability of absorption is a function of δt, $\epsilon = \kappa\delta t/\delta x$. Assuming we chose the largest possible value of $\delta t = \delta x^2/(2D)$, we have $\epsilon = \kappa\delta x/(2D)$. However, the fact that $0 \leq \epsilon \leq 1$ limits our choice of δx. This bring into light that this choice of ϵ might not be the most appropriate one for a Markovian model. On the other hand, the probability $\epsilon = \kappa\delta t/\delta x$ could be understood as a first order approximation when sampling from an exponential waiting time,

$$1 - e^{-\kappa\frac{\delta t}{\delta x}} \approx \kappa\frac{\delta t}{\delta x}. \tag{3.23}$$

This is basically emphasizing the fact that the reaction process at the boundary is Poissonian. Using $\epsilon = 1 - e^{-\kappa\delta t/\delta x}$ allows a more accurate choice for the discrete partial reaction probability since it always satisfy $0 \leq \epsilon \leq 1$. In this case, the discrete parameter κ is given by $\kappa = -\frac{\delta x}{\delta t}\log[1-\epsilon]$. It also gives the upper bound for the κ parameter in a given discretization of the diffusion process. As $p_0+q_0 \leq 1$, then $\epsilon+D\delta t/\delta x^2 \leq 1$, so $\kappa \leq -\frac{\delta x}{\delta t}\log\left[D\frac{\delta t}{\delta x^2}\right]$; the equality corresponds to the purely absorbing case. Note that using the result from Eq. 3.23 in the Markov model does not affect any of the previous limiting results. As a matter of fact, all the models in Section 5.3 can use this result without affecting the continuous limit behavior. It should also be noted this result would have never been obtained by looking for an accurate discretization of the continuous models; it is only obtained by looking for consistency with the underlying stochastic process.

3.4 The mean first passage time (MFPT)

The mean first passage time (MFPT) theory deals with the problem of calculating the mean average time required for a particle undergoing Brownian motion starting at r to reach a boundary for the first time. We say this boundary is an absorbing boundary since once

the particle reaches the boundary, the process ends. There happens to exist a connection between the MFPT and the diffusion-controlled rates we just calculated. This connection was first pointed out in [227, 236]. We will begin with a general derivation of the equations for the MFPT; we will solve the problem for a general one-dimensional problem, and we will solve it for Smoluchowski-type models.

3.4.1 MFPT for a general Fokker-Planck equation

In this section, we will derive the equations satisifed by the MPFT for a general one dimensional Fokker-Planck equation. The MFPT τ is related to the probability $S(t)$ that the system has not yet reacted or that the particle has not yet reached the absorbing boundary. The average MFPT can be defined through an approximate realtion with the survival probability [236] given by

$$S(t) \approx \exp\left(-\frac{t}{\tau}\right),$$

which is equivalent to the more common definition of τ as

$$\tau = \int_0^\infty S(t)dt.$$

On the other hand, the survival probability can also be defined through the probability $p(r,t|r_0,0)dr$ of finding the particle at position r and time t if it was initially at r_0. The integral over the whole spatial domain Ω is by definition of the survival probability,

$$S(t) = \int_\Omega p(r,t)dr.$$

The dynamics of this probability have to be given by a Fokker-Planck equation since this is a simple diffusion process. A general Fokker-Planck equation that describes the dynamics of the probability can be written in terms of a linear differential operator $L(r)$,

$$\frac{\partial p(r,t|r_0,0)}{\partial t} = L(r)p(r,t|r_0,t).$$

Instead of solving this equation, we will try to rewrite it as an equation for $S(t)$, so we can relate it to the MFPT, τ.In order to do so, we can rewrite the adjoint of this equation,

$$\frac{\partial p(r,t|r_0,0)}{\partial t} = L^*(r_0)p(r,t|r_0,t),$$

where $L^*(r_0)$ is the adjoint operator of $L(r)$. We can now integrate the whole equation over r to obtain an equation for $S(t)$

$$\frac{\partial S(t|r_0)}{\partial t} = L^*(r_0)S(t|r_0),$$

where we emphasized the fact that the survival probability for a given sample in general depends on the initial position. Furthermore, by the previous definition, we know $\tau = \int_0^\infty S(t)dt$, so we can integrate over time now

$$S(t|r_0)\Big|_0^\infty = L^*(r_0)\tau.$$

As the survival probability at inifinity is zero and at $t = 0$ is one, we finally obtain a general equation for the MFPT,

$$L^*(r_0)\tau = -1.$$

Note the boundary conditions of the problem also need to be traduced to the adjoint language. This process is actually more difficult than for the equation. Nonetheless, for most of the problems we are interested in, the resulting adjoint boundary conditions for the Dirichlet, Neumann and Robin boundary conditions are exactly the same ones as for the original equation. An example of the derivation of such can be consulted in [236].

For the sake of completeness, we will give some examples of the operator $L(r)$. In spherical coordinates for the classical Smoluchowski type problems, like those of Section 3.2, we usually have

$$L(r) = \nabla \cdot D(r)\nabla + \beta\nabla \cdot D(r)(\nabla U(x)),$$

where $D(r)$ is the diffusion coefficient, β is a damping constant and $U(x)$ a potential. The adjoint is obtained by integrating by parts,

$$L^*(r_0) = \nabla \cdot D(r)\nabla - \beta D(r)(\nabla U(x)) \cdot \nabla.$$

This linear operator is a slightly more complicated version that the one used in Eq. 3.29; this one includes a potential function $U(x)$.

Another case that will be useful in future endeavors is the general one-dimensional Fokker-Planck equation. Consider the Fokker-Planck equation, as derived in Section 3.1,

$$\frac{\partial P(y,t|y_0,0)}{\partial t} = -\frac{\partial}{\partial y}\left(A(y)P(y,t|y_0,0)\right) + \frac{\partial^2}{\partial y^2}\left(\frac{B(y)}{2}P(y,t|y_0,0)\right),$$

where $L(y) = -\frac{\partial}{\partial y}A(y) + \frac{\partial^2}{\partial y^2}\frac{B(y)}{2}$. The adjoint operator is given then by $L^*(y_0) = A(y_0)\frac{\partial}{\partial y_0} + \frac{B(y_0)}{2}\frac{\partial^2}{\partial y_0^2}$, so the equation for the MFPT is,

$$A(y_0)\frac{\partial \tau(y_0)}{\partial y_0} + \frac{B(y_0)}{2}\frac{\partial^2 \tau(y_0)}{\partial y_0^2} = -1. \tag{3.24}$$

Assuiming a reflecting boundary on the left at $y = L$ and an absorbing one on the right at $y = R$, the corresponding boudary conditions are

$$\left.\frac{\partial \tau}{\partial y_0}\right|_{y=L} = 0 \qquad \tau(R) = 0.$$

This boundary value problem can be easily solved using an integrating factor to obtain

$$\tau(y) = \int_0^R \frac{1}{\mu(y')}\left[\int_L^{y'} \frac{2\mu(y'')}{B(y'')}dy''\right]dy' \tag{3.25}$$

$$\text{with :} \quad \mu(y) = \exp\left[\int \frac{2A(y')}{B(y')}dy'\right], \tag{3.26}$$

where $\mu(y)$ is the integrating factor. This is the solution for the MFPT for a general one-dimensional Fokker-Planck equation, and it cannot be explicitly solved until $A(y)$, $B(y)$, L and R are specified.

3.4.2 MFPT for Smoluchoski-type models

In this section, we will solve the MFPT problem for a d-dimensional Smoluchowski problem. The MFPT for this problem can be solved using the adjoint equation, as derived in Section 3.4.1. The original problem can be found in Section 3.2.1; its corresponding adjoint equation for the MFPT τ_d is given by

$$\frac{1}{r^{d-1}}\left(\frac{\partial}{\partial r}r^{d-1}D\frac{\partial}{\partial r}\tau_d(r)\right) = -1, \tag{3.27}$$

with its corresponding boundary condition. The left hand side is the d-dimensional Laplacian in radial coordinates and $\tau_d(r)$ is the MFPT, for a diffusion d-dimensional Brownian motion, started at r. Emulating Smoluchowski's model, lets assume an absorbing Boundary condition at R_0 and a reflective boundary condition at R_1, i.e.

$$\tau_d(R_0) = 0, \quad \left[\frac{d\tau_d(y)}{dy}\right]_{y=R_1} = 0. \tag{3.28}$$

The solution to the Eq. 3.27 with the boundary condition from Eq. 3.28 is given by,

$$\tau_d(r) = \frac{R_1^d}{dD}\left[\frac{r^{2-d}}{2-d} - \frac{R_0^{2-d}}{2-d}\right] + \frac{1}{2dD}(R_0^2 - r^2). \tag{3.29}$$

Note this equation seems to be not well defined for the two dimensional case $d = 2$. In this case, we have to write $d = 2 + a$ and take the limit when $a \to 0$. This process yields the solution for $d = 2$ given by

$$\tau_2(r) = \frac{R_1^2}{2D}\left[\ln(r) - \ln(R_0)\right] + \frac{1}{4D}(R_0^2 - r^2). \tag{3.30}$$

In order to relate the first passage time to the reaction rate of Smoluchowski theory, lets write the solution for $d = 3$,

$$\tau_3(r) = \frac{R_1^3}{3D}\left[\frac{1}{R_0} - \frac{1}{r}\right] + \frac{1}{6D}(R_0^2 - r^2). \tag{3.31}$$

We want to look at the limit when $R_1 \to \infty$. As r is the initial condition, it satisfies $R_0 < r < R_1$, i.e. $1/R_0 > 1/r$; therefore the leading order term as $R_1 \to \infty$ is

$$\tau_3(r) \sim \frac{R_1^3}{3D}\frac{1}{R_0} = \frac{4\pi R_1^3}{3}\frac{1}{4\pi R_0 D}. \tag{3.32}$$

Note we have the volume of the sphere $V = \frac{4\pi R_1^3}{3}$ multiplied by the inverse of Smoluchowski's reaction rate, $k_S = 4\pi R_0 D$, so it can be simplified to

$$\tau_3(r) \sim \frac{1}{c_0 k_S}, \tag{3.33}$$

where the concentration of the molecule is almost exactly $c_0 = 1/V$. The same result was obtained for the model by Collins and Kimball on [227] by using the boundary conditions

$$4\pi D R_0^2 \tau_d'(R_0), \quad \tau_d'(r_1) = 0$$

instead of the ones in Eq. 3.28, obtaining

$$\tau_{3CK}(r) \sim \frac{1}{c_0 k_{CK}}. \tag{3.34}$$

These results relate the reaction association rates as the inverse of the mean first passage

times. It also allows a new interpretation of Eq. 5.18 as a sum of first passage times

$$\frac{1}{k_{CK}} = \frac{1}{\kappa} + \frac{1}{k_S},$$

where κ^{-1} is the elapsed time one has to wait for the reaction to occur after the diffusion-limited reaction. This extra parameter is very helpful since reactions are not intrinsically diffusion-limited.

Is it possible to obtain a similar result for 1,2 or even 4 dimensions? The solutions for $d = 1, 2, 3, 4$ dimensions for Smoluchowski's problem are given by,

$$\tau_1(r) = \frac{R_1}{D}\left[r - R_0\right] + \frac{1}{2D}(R_0^2 - r^2), \tag{3.35}$$

$$\tau_2(r) = \frac{R_1^2}{2D}\left[\ln(r) - \ln(R_0)\right] + \frac{1}{4D}(R_0^2 - r^2), \tag{3.36}$$

$$\tau_3(r) = \frac{R_1^3}{3D}\left[\frac{1}{R_0} - \frac{1}{r}\right] + \frac{1}{6D}(R_0^2 - r^2), \tag{3.37}$$

$$\tau_4(r) = \frac{R_1^4}{4D}\left[\frac{1}{2R_0^2} - \frac{1}{2r^2}\right] + \frac{1}{8D}(R_0^2 - r^2). \tag{3.38}$$

As $R_1 \to \infty$, the leading orders are given by

$$\tau_1(r) = \frac{R_1}{D}r = V_1\frac{r}{D}, \tag{3.39}$$

$$\tau_2(r) = \frac{R_1^2}{2D}\ln(r) = V_2\frac{\ln(r)}{2D}, \tag{3.40}$$

$$\tau_3(r) = \frac{R_1^3}{3D}\frac{1}{R_0} = V_3\frac{1}{4\pi R_0 D} \tag{3.41}$$

$$\tau_4(r) = \frac{R_1^4}{4D}\frac{1}{2R_0^2} = V_4\frac{1}{4\pi^2 D R_0^2}, \tag{3.42}$$

since $R_0 < r < R_1$, and V_n is the volume of the n-sphere. The quantities multiplying the volumes V_n are the inverse of the reaction rate. As we can see in the three and four dimensional case, we have $1/k_S$ and $1/4\pi^2 D R_0^2$ respectively. Both rates are constant; however, for the first and second dimensional case we observe the reaction rate depends on r. The fact we cannot derive a constant Smoluchowski reaction rate in one and two dimensions is intimately related to the nature of Brownian motion. In one and two dimensions, the probability of a particle undergoing Brownian motion to come back to it's starting point is one, while for three or more dimensions it's finite.

Notice we don't only know the first passage times are the inverse of the reaction rates; these results also establish a connection between the stochastic theory of the first passage time

of one Brownian particle with Smoluchowski's bulk concentration theory. This distinction will be relevant in our future studies.

3.5 Kramers' theory

Kramer theory was first developed by Kramers' in his seminal paper [141]. Kramers' model for a chemical reaction consists of a Newtonian particle of mass M immersed in a lighter fluid subject to a force-field given by the potential $U(x)$. The coordinate x correspond to the reaction coordinate, and its values at the minima of the potential, $x = a$ and $x = c$, denote the reactant and product states respectively [9]. The local maximum of $U(x)$, $x = b$, which is between $x = a$ and $x = c$ corresponds to the transition state, see Figure 3.2. The remaining degrees of freedom constitute a heat bath at temperature T (contact with lighter fluid) [105]. Therefore, the dynamics of this particle can be described by the Langevin equation (Eq. 3.7) with the addition of a potential [254],

$$dX_t = V_t dt, \tag{3.43}$$

$$dV_t = -\gamma V_t dt - \frac{\partial U(x)}{\partial x} dt + \sqrt{2k_B T\gamma} dW_t, \tag{3.44}$$

where, without loss of generality, the mass is assumed 1, $M = 1$, γ is the damping coefficient, k_B the Boltzmann constant, X_t denotes the position in the reaction coordinate space and V_t its velocity in this space.

Following Section 3.2, we can write the Fokker-Planck equation for this process,

$$\frac{\partial P(x,v,t)}{\partial t} = -\frac{\partial}{\partial x}\left(vP\right) - \frac{\partial}{\partial v}\left(-\gamma v P - \frac{\partial U(x)}{\partial x}\right) + \frac{1}{2}\frac{\partial^2}{\partial x^2}\left(2k_B T\gamma P\right),$$

where $P(x,v,t)dxdvdt$ is the probability of finding the particle at position x with velocity v at time t. In more compact form, this can be rewritten as,

$$\frac{\partial P(x,v,t)}{\partial t} = -v\frac{\partial P}{\partial x} + U'(x)\frac{\partial P}{\partial v} + \gamma\left(\frac{\partial(vP}{\partial v} + k_B T\frac{\partial^2 P}{\partial v^2}\right). \tag{3.45}$$

Note this equation is also known as Klein-Kramers equation.

Let's assume the potential $U(x)$ has the form shown in Figure 3.2. The question the theory wants to address is what is the average time (inverse rate) that a particle initially at $x = a$ takes to escape the potential barrier at $x = b$.

Solving this problem is not an easy task, and in most cases approximations are required. We will solve this problem with three different approaches: a physically intuitive and ap-

[9] This can be interpreted in several different ways as shown later in Section 5.2

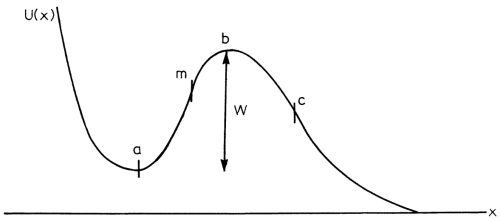

Figure 3.2: Kramers' potential for a chemical reaction. Note the potential is effectively bistable if a cutoff is assumed, for the time being assume the cutoff is at $x = c$, where $x = c$ is the second minimum. This figure was taken from [254].

proximated approach, the overdamped case where $\gamma \gg 1$ and for an intermediate value of γ. The case for very small γ can be studied in [254].

3.5.1 Physically intuitive approach

Here we will present an approach to solving Kramers' problem using many approximations and physical intuition following [254]. Hopefully, it will give the reader a better intuition on the problem when we move to the more rigorous cases.

Assuming the height of the potential W at $x = b$, given by $W = U(b) - U(a)$, is big enough such that the thermal fluctuations mostly move the particle around its initial position at the minimum at $x = a$, we can obtain a lot of information from the steady state behavior.

We begin by assuming $U'(x) = 0$ in Eq. 3.45 and solve the steady state. Using separation of variables is easy to obtain the solution as,

$$P^0_{ss} = C_0 \exp\left[-\frac{v^2}{2k_BT}\right].$$

We will now use this results as an ansatz for the steady state of the general case when $U'(x) \neq 0$, Eq. 3.45. Assume $P_ss(x, v) = h(x)e^{-v^2/k_BT}$. Substituting in Eq. 3.45, many terms cancel, and we obtain an equation for $h(x)$

$$\frac{dh(x)}{dx} = -\frac{U'(x)}{k_BT}h(x) \qquad \Rightarrow \qquad h(x) = A_0 e^{-U(x)/k_BT}.$$

The full solution for the steady state is then given by,

$$P_{ss}(x, v) = A_0 \exp - \left[\frac{U(x) + v^2/2}{k_BT}\right], \tag{3.46}$$

where A_0 is a normalization constant. Note this distribution is exactly what we expected

since it is the Boltzmann distribution. To obtain the normalization constant, we need the probability to intergate to one, so

$$\int_{-\infty}^{b}\int_{-\infty}^{\infty} P_{ss}(x,v)dvdx = 1 \quad \Rightarrow$$
$$A_0^{-1} = \int_{-\infty}^{b} e^{-U(x)/k_BT} \underbrace{\left(\int_{-\infty}^{\infty} e^{-v^2/2k_BT}dv\right)}_{\sqrt{2\pi k_BT}} dx = \sqrt{2\pi k_BT}\int_{-\infty}^{b} e^{-U(x)/k_BT}. \tag{3.47}$$

Note the integration was assume until $x = b$ since assuming the steady state was equivalent to assume the particle is very unlikely to reach $x = b$ since the potential height W is too large. For this same reason the probability of being at $x = b$ is very small $P_{ss}(b, v) \ll 1$ and $P_{ss}(x, v)$ is approximately zero for $x > b$. This will allow us to use the method of Laplace to approximate the integral. The method of Laplace to approximate integrals with exponential functions states that,

$$\int_a^b e^{Mf(x_0)} \approx \sqrt{\frac{2\pi}{M|f''(x_0|}} e^{Mf(x_0)}, \tag{3.48}$$

when $M \gg 1$ and $f(x)$ is twice differentiable, has a unique maximum at $x_0 \in (a, b)$ and is concave, $f''(x_0) < 0$. Applying this method to the integral in Eq. 3.47, we obtain,

$$A_0^{-1} = \frac{2\pi k_BT}{\sqrt{U''(a)}} \exp - \left[\frac{U(a)}{k_BT}\right]. \tag{3.49}$$

With the normalization factor A_0, we have written a full approximate solution for the steady state. We will use this to calculate the average time τ or rate for the particle to escape the potential barrier. The rate of escape at $x = b$ should be given by the flux of particles at $x = b$,

$$\frac{1}{\tau} \propto \int_0^{\infty} vP(b, v)dv = A_0 e^{-U(b)/k_BT}\int_0^{\infty} ve^{-v^2/2k_BT}dv = A_0 k_BT \exp\left[-\frac{U(b)}{k_BT}\right],$$

where we only consider the case when $v > 0$ since the particle needs positive velocity to escape. Substituting A_0 from Eq. 3.49, we obtain the rate of escape is,

$$\frac{1}{\tau} \propto \frac{\sqrt{U''(a)}}{2\pi} \exp\left[-\frac{U(b) - U(a)}{k_BT}\right], \tag{3.50}$$

where $W = U(b) - U(a)$ is the height of the barrier in reference to the starting point. Note we do not really need to know the whole function $U(x)$; the only highly relevant information

is the height of the potential barrier W and the curvature at the minimum $U''(a)$. A rough interpretation of Eq. 3.50 is the particle oscillates in a potential $w_a^2 x^2/2$, where $w_a = \sqrt{U''(a)}$, so it hits the wall at $x = b$ $w_a/2\pi$ per second, and each time it hits it, it has the probability $e^{-W/k_B T}$ to cross it.

3.5.2 Overdamped case

In order to provide a more rigorous result, we will need to focus different ranges given by the level of damping. In this section, we will explore the overdamped case following [254]. Consider Eq. 3.44, when $\gamma \ll 1$ (or $M \approx 0$), the velocity relaxes to a steady state so fast that $dV_t \approx 0$, then $-\gamma V_t dt - \frac{\partial U}{\partial x} dt + \sqrt{2k_B T \gamma} dW_t = 0$. As $V_t dt = dX_t$, we immediately obtain

$$dX_t = -\frac{1}{\gamma}\frac{\partial U}{\partial x} dt + \sqrt{\frac{2k_B t}{\gamma}} dW_t,$$

with its corresponding Fokker-Planck equation,

$$\frac{\partial P(x,t)}{\partial t} = \frac{\partial}{\partial x}\left(\frac{1}{\gamma} U'(x) P\right) + \sqrt{\frac{k_B T}{\gamma}} \frac{\partial^2 P}{\partial x^2}.$$

Note this is the same result as in Eq. 3.10, but taking into account the potential $U(x)$. Again we have to look for the average time for a particle initially at $x = a$ to escape past the barrier at $x = b$. This could be re-framed as the problem of a one-dimensional diffusion with absorbing boundary at $x = b$. As we are looking for the mean first passage time, we can use the formula for the MFPT of a general one-dimensional Fokker-Planck equation, see Eq. 3.24 derived earlier. The equation is

$$\frac{1}{\gamma}\frac{\partial U}{\partial x_0}\frac{\partial \tau(x_0)}{\partial x_0} + \frac{k_B T}{\gamma}\frac{\partial^2 \tau(x_0)}{\partial x_0^2} = -1,$$

where x_0 is the initial position of the particle. We can use the results from Eq. 3.26 in Section 3.4; we only need to determine the $A(x_0), B(x_0), R$ and L. For the equation we just stated,

$$A(x) = -\frac{1}{\gamma}\frac{\partial U}{\partial x} \qquad \frac{B(x)}{2} = \frac{k_B T}{\gamma}.$$

The boundary condition on the left will be a reflecting boundary condition at $x = a$, and the boundary condition to the right will be an absorbing boundary at $x = c$, see Figure 3.2.

These are given by

$$\left.\frac{\partial \tau}{\partial x}\right|_{x=L} = 0 \qquad \tau(c) = 0.$$

We can take the limit as $L \to -\infty$; however, it will not be that relevant because the particle can never really escape the potential for $x < a$, see Figure 3.2. Also note the absorbing boundary can be at $x = b$ or $x = c$. However, it will again not very relevant because the time it takes the particle to reach from $x = a$ to $x = b$ is much longer than the times it takes to drop from $x = b$ to $x = c$. Following Eq. 3.26, the integrating factor will be

$$\mu(x_0) = \exp\left[-\frac{1}{k_B T}\int^x U'(x')dx'\right] = \exp\left[-\frac{U(x)}{k_B T}\right],$$

so we can write the MFPT as

$$\tau(x_0) = \int_{x_0}^{c} e^{\frac{U(x')}{k_B T}}\left[\int_L^{x'} \frac{\gamma}{k_B T} e^{\left(-\frac{U(x'')}{k_B T}\right)dx'}\right]dx'.$$

We also know the initial condition is set at $x_0 = a$, and that we can take the limit of $L \to -\infty$ so

$$\tau(a) = \frac{\gamma}{k_B T}\int_a^{c} e^{\frac{U(x')}{k_B T}}\left[\int_{-\infty}^{x'} e^{\left(-\frac{U(x'')}{k_B T}\right)}dx'\right]dx'.$$

We can approximate the inside integral using the method of Laplace, see Eq. 3.48. As the particle is absorbed at $x = c$ and it is difficult for it to even get close to $x = b$, the main contribution to the inside integral is around $x = a$ (see sign of exponential). Applying the method of Laplace around $x = a$ to the inside integral, we obtain

$$\int_{-\infty}^{x'} e^{\left(-\frac{U(x'')}{k_B T}\right)}dx' \approx \sqrt{\frac{2\pi k_B T}{|U''(a)|}}e^{-\frac{U(a)}{k_B T}}.$$

Substituting in the equation for $\tau(a)$,

$$\tau(a) \approx \sqrt{\frac{2\pi k_B T}{|U''(a)|}}e^{-\frac{U(a)}{k_B T}}\frac{\gamma}{k_B T}\int_a^{c} e^{\frac{U(x')}{k_B T}}dx'.$$

This integral has a different sign, so its main contribution will be around $x = b$. Applying once again the method of Laplace, we get

$$\int_a^c e^{\frac{U(x')}{k_B T}} \approx \sqrt{\frac{2\pi k_B T}{|U''(b)|}} e^{\frac{U(b)}{k_B T}}.$$

Substituting it into the equation above, we obtain the final expression for the MFPT

$$\tau(a) \approx \frac{\gamma}{k_B T} \frac{2\pi k_B T}{\sqrt{|U''(a)||U''(b)|}} \exp\left[\frac{U(b) - U(a)}{k_B T}\right].$$

Note $D = \gamma/k_B T$ will match the diffusion coefficient. Using the notation $w_a = \sqrt{|U''(a)|}$ and $w_b = \sqrt{|U''(b)|}$ we can write the rate at which the particle initially at $x = a$ escapes the potential barrier at $x = b$ as

$$\frac{1}{\tau(a)} \approx \frac{w_a w_b}{2\pi\gamma} \exp\left[-\frac{U(b) - U(a)}{k_B T}\right], \tag{3.51}$$

where the relative height of the barrier is $W = U(b) - U(a)$. This is the final result for the overdamped case.

3.5.3 Intermediate damping case

In this section, we will show the results of Kramers' theory for an intermediate value of the damping, γ following again [254]. In this case, we will have two main assumptions:

- (i) for $x < m$ in Figure 3.2, the stationary solution is the Boltzmann distribution from Eq. 3.46, with A_0 given by Eq. 3.49,

$$P_{ss}^{-}(x, v) = \frac{w_a}{2\pi k_B T} \exp\left[-\frac{U(x) - U(a) + v^2/2}{k_B T}\right]; \tag{3.52}$$

- (ii) for $x > m$ one can approximate the potential with a parabola,

$$U(x) \approx U(b) - \frac{w_b^2}{2}(x - b)^2. \tag{3.53}$$

Note the quantities w_k denote $w_k = \sqrt{|U''(k)|}$. A value $x = m$ between $x = a$ and $x = b$ for which this is a good approximation exists as long as γ is not too small. If γ is too small, the particle would move more freely making the stationary solution for $x < m$ inaccurate and requiring the full shape of the potential to calculate the solution for $x > m$.

We already have the solution for $x < m$, so in order to solve this problem, we need the solution for $x > m$. Then, we need to match these two expressions to obtain a solution for the whole domain and use it to calculate the escape rate. We will use the superscript $-$, $+$ and m to denote the solution at $x < m$, $x > m$ and $x \approx m$ respectively.

Solution for $x > m$

Set the origin of the frame of reference at $x = b$ and assume an ansatz of the form,

$$P_{ss}^{+}(x, v) = Q(x, v) \exp\left[\frac{w_b^2 x^2 - v^2}{2k_B T}\right],$$

where $Q(x, v)$ is unknown. Note this has the form of a Boltzmann distribution too, where $-w_b^2 x^2$ is the harmonic potential expected from the fact we approximated the potential in this region by a parabola. We can substitute this into the original Klein-Kramers' equation, see Eq. 3.45. After some simple algebra, we obtain an equation for $Q(x, v)$

$$-v\frac{\partial Q}{\partial x} - w_b^2 x^2 \frac{\partial Q}{\partial v} - v\gamma\frac{\partial Q}{\partial v} + \gamma T \frac{\partial^2 Q}{\partial v^2}.$$

In order to solve this equation, we try a characteristic solution of the form $Q(x, v) = f(z) = f(v - \alpha x)$, with α an unknown. Substituting into the equation yields,

$$(\alpha v - w_b^2 - \gamma v) f'(z) = -\gamma k_B T f''(z). \tag{3.54}$$

If the coefficient of $f'(z)$ is a function of z alone, i.e. $(\alpha v - w_b^2 - \gamma v) = \lambda z$ with λ unknown, we can solve this equation. To do so, we will equate the coefficients in x and v of

$$\alpha v - w_b^2 - \gamma v = \lambda z, \qquad \Rightarrow \qquad \alpha - \gamma = \lambda \quad \text{and} \quad -w_b^2 = -\lambda\alpha. \tag{3.55}$$

By combining the latter two, we can obtain an equation for α, $-w_b^2 = -(\alpha - \gamma)\alpha$. This yields a quadratic equation on α, $\alpha^2 - \gamma\alpha - w_b^2 = 0$, so

$$\alpha_{\pm} = \frac{\gamma}{2} \pm \frac{1}{2}\sqrt{\gamma^2 + 4w_b^2}. \tag{3.56}$$

Furthermore, as $\lambda = \alpha - \gamma$, we obtain $\lambda_{\pm} = -\alpha_{\mp}$. With this, we just found α, but we are still missing $f(z)$. The equation to obtain $f(z)$ can be obtained from Eq. 3.54, which we assumed is equal to $\lambda z f'(z)$, so

$$-\gamma k_B T f''(z) = \lambda z f'(z).$$

This is a simple ODE whose solution is,

$$f(z) = B_0 + C_0 \int_{M_0}^{z} \exp\left[-\frac{\lambda z'2}{2\gamma k_B T} dz'\right],$$

where M_0, B_0 and C_0 need to be determined. The steady state solution to our problem can now be written by noting that $z = v - \alpha x$ and $f(v - \alpha x) = Q(x, v)$, so

$$P^{+}_{ss}(x, v) = \exp\left[\frac{w_b^2 x^2 - v^2}{2k_B T}\right]\left[B_0 + C_0 \int_{M_0}^{v-\alpha x} \exp\left[-\frac{\lambda z'2}{2\gamma k_B T} dz'\right]\right].$$

As $P(\xi, v)^{+}_{ss} \to 0$ as $\xi \to \infty$, then $B_0 = 0$, $M_0 = -\infty$, $\alpha > 0 \Rightarrow \alpha = \alpha_+$ and $\lambda = -\alpha_-$. Inputting these values into the equation and noting from Eq. 3.53 that $w_b^2 x2/2 = U(b) - U(a)$ and from Eq. 3.55 that $\lambda_- = w_b^2/\alpha_+$, we can rewrite it as

$$P^{+}_{ss}(x, v) = \exp\left[-\frac{U(x) - U(b) + v^2/2}{k_B T}\right]\left[C_0 \int_{-\infty}^{v-\alpha_+ x} \exp\left[-\frac{w_b^2 z'2}{2\gamma\alpha_+ k_B T} dz'\right]\right]. \tag{3.57}$$

The value of C_0 will be chosen to match the solution from $x < m$.

Extending the solution to the whole domain

In this part, we will match the solutions for $x < m$ and $x > m$ to match at $x = m$ to obtain a solution in the whole domain. Let's extend this equation into the well where $x < m$ ($x < 0$ since we moved the origin at $x = b$). In this region, the integral of Eq. 3.57 will cover the main contributions around $x = b$, so it can be approximated through the method of Laplace,

$$P_{ss}(x < m, v) = \exp\left[-\frac{U(x) - U(b) + v^2/2}{k_B T}\right]\left[C_0 \sqrt{\frac{2\pi\gamma\alpha_+ k_B T}{w_b^2}}\right].$$

This should match exactly with solution at $x < m$ from Eq. 3.52, so

$$\exp\left[-\frac{U(x) - U(b) + v^2/2}{k_B T}\right]\left[C_0 \sqrt{\frac{2\pi\gamma\alpha_+ k_B T}{w_b^2}}\right] = \frac{w_a}{2\pi k_B T} \exp\left[-\frac{U(x) - U(a) + v^2/2}{k_B T}\right],$$

$$\Rightarrow \qquad C_0 = e^{-W/k_B T} (2\pi T)^{3/2} \frac{w_a w_b}{\sqrt{\gamma\alpha_+}},$$

with $W = U(b) - U(a)$. Therefore the solution in the whole domain will be given by Eq. 3.57 with C_0 given by the expression above,

$$P_{ss}(x,v) = (2\pi T)^{3/2}\frac{w_a w_b}{\sqrt{\gamma\alpha_+}}e^{-W/k_BT}\exp\left[-\frac{U(x)-U(b)+v^2/2}{k_BT}\right]\left[\int_{-\infty}^{v-\alpha_+ x}\exp\left(-\frac{w_b^2 z'^2}{2\gamma\alpha_+ k_BT}dz'\right)\right].$$

This is the solution in the whole domain.

Rate for intermediate damping

The rate will be given by the expected value of the velocity at $x = b$, so

$$\frac{1}{\tau} = \int_{-\infty}^{\infty} vP(b,v)dv = \underbrace{(2\pi T)^{3/2}\frac{w_a w_b}{\sqrt{\gamma\alpha_+}}e^{-W/k_BT}}_{C_0}\int_{-\infty}^{\infty} ve^{-v^2/2k_BT}\left[\int_{-\infty}^{v-\alpha_+ x} e^{\left(-\frac{w_b^2 z'^2}{2\gamma\alpha_+ k_BT}\right)}dz'\right]dv.$$

Integrating by parts doing $df = ve^{-v^2/2k_BT}$ and g the whole other integral, the first term outside the integral vanishes, and we are left with

$$\frac{1}{\tau} = C_0 k_BT\int_{-\infty}^{\infty}\exp\left[-\frac{v^2}{k_BT} - \frac{w_b^2(v-\alpha_+ b)}{2\gamma\alpha_+ k_BT}\right]dv.$$

This integral can be integrated exactly to yield,

$$\frac{1}{\tau} = C_0 k_BT\exp\left[-\frac{(\alpha_+ b)^2 w_b^2}{2k_BT(\gamma\alpha_+ + w_b^2)}\right]\sqrt{\frac{2\pi\gamma\alpha_+ k_BT}{\gamma\alpha_+ + w_b^2}}$$

Substituting again C_0 and noting $x = b$ is the origin, so $b = 0$, then

$$\frac{1}{\tau} = \int_{-\infty}^{\infty} vP(b,v)dv = \frac{w_a w_b}{2\pi}e^{-W/k_BT}\left(\gamma\alpha_+ + w_b^2\right)^{-1/2}.$$

Using the appropriate value of α_+ from Eq. 3.56, we can substitute into the equation. After some simple algebra, we find the main result of this section,

$$\frac{1}{\tau} = \frac{w_a w_b}{\pi}e^{-W/k_BT}\left[\gamma + \sqrt{\gamma^2 + 4w_b^2}\right]^{-1},$$

with $W = U(a) - U(b)$ and $w_k = \sqrt{|U''(k)|}$. This is the rate for which a particle initially at $x = a$ escapes the potential barrier at $x = b$. Note that in the limit $\gamma \gg w_b$, we immediately

recover Eq. 3.51 for the overdamped limit,

$$\frac{1}{\tau} \approx \frac{w_a w_b}{2\pi\gamma} e^{-W/k_B T}.$$

When $\gamma \ll w_b$, the equation simplifies to the result obtained with the physical intuitive approach from Eq. 3.50,

$$\frac{1}{\tau} \approx \frac{w_a}{2\pi} e^{-W/k_B T}.$$

Note for very small γ the parabola approximation breaks down and we need another approach, see [254] for a detailed approach in that case.

Chapter 4

APPLICATIONS TO FLUORESCENCE CORRELATION SPECTROSCOPY

In this chapter, we will use the theory reviewed in Chapters 2 and 3 to study fluorescence correlation spectroscopy (FCS) theory using computational experiments. FCS is a well-established and widely used experimental method to determine chemical rate constants, diffusion coefficients and other properties of stochastic reaction-diffusion systems. The currently existing theory of FCS is based on the linear fluctuation theory originally developed by Einstein, Onsager, Lax, and others as a phenomenological approach to equilibrium fluctuations in bulk solutions. For mesoscopic reaction-diffusion systems with nonlinear chemical reactions among a small number of molecules, a situation often encountered in single-cell biochemistry, it is expected that FCS time correlation functions of a reaction-diffusion system can deviate from the classic results of Elson and Magde [69].

We will begin by discussing the nonlinear effect for reaction systems without diffusion. For nonlinear stochastic reaction-diffusion systems there are no closed solutions; therefore, we carry out stochastic Monte-Carlo simulations to study the system. We show that the deviation is small for a simple bimolecular reaction; the most significant deviations occur when the number of molecules is small and of the same order. Our results show that current linear FCS theory could be adequate for measurements on biological systems that contain many other sources of uncertainties. At the same time, it provides a framework for future measurements of nonlinear, fluctuating chemical reactions with high-precision FCS. The work on this chapter is based on our journal publication [56].

4.1 Fluorescence correlation spectroscopy (FCS)

Single-molecule studies of biological macromolecules focus on conformational states of individual molecules and transitions between states [33, 100, 208, 271]. Concentration fluctuation spectroscopy, on the other hand, measures the molecular number fluctuations associated with linear, and nonlinear, biochemical reactions [70, 266]. For unimolecular reactions, these two approaches are conceptually equivalent, in statistical terms, via the multi-nomial distribution: If a single molecule has K states with $p_k(t)$ being the probability for the molecule in state k at time t, then for M independent copies of the same molecule, one has the probability

distribution for m_ℓ number of molecules in ℓ state following [112, 113]

$$\frac{M!}{m_1!m_2!\cdots m_K!}\,(p_1(t))^{m_1}\,(p_2(t))^{m_2}\cdots(p_K(t))^{m_K}\,, \tag{4.1}$$

where $m_1+m_2+\cdots+m_K=M$. In fact more specifically, if the first-order rate constant for transition $k\to j$ is q_{kj}, then in the concentration fluctuation measurements of a system with M independent copies of the molecule, the temporal correlation function is simply M times the correlation function derived from a single-molecule measurement. If we denote the "state of the reaction system" by $\{m_1,m_2,\cdots,m_K\}$, the rate constant for transition from $\{m_1,\cdots,m_j,\cdots,m_\ell,\cdots,m_K\}$ to $\{m_1,\cdots,m_j-1,\cdots,m_\ell+1,\cdots,m_K\}$ is $m_jq_{j\ell}$. Experimentally, single-molecule measurements on state fluctuations have a much more superior signal-to-noise characteristics than the concentration fluctuation.

However, for reaction systems with nonlinear reactions such as $A+B\rightleftharpoons C$, the two approaches no longer provide equivalent information; they are in fact complementary. This distinction has not been widely appreciated. Corresponding to chemistry reaction theories, the single-molecule approach parallels nicely with Kramers' reaction rate theory [105], while the concentration fluctuation measurements is intimately related to Delbrück's chemical master equation, or Gillespie's stochastic kinetics, for chemical reaction systems with reaction networks [59, 93, 205]. In the latter systems, rate constants for individual reactions are supposedly known a priori; complex chemical or biochemical behavior arises as a consequence of a nonlinear reaction network [208].

Fluorescence correlation spectroscopy (FCS) is one of the leading physiochemical techniques to experimentally measure concentration fluctuations of nonlinear chemical reactions with stochastic fluctuations in mesoscopic systems [214]. Other methods include conductance fluctuations for electrochemical reaction [79]. With the newfound perspective given above, especially with nonlinear chemical reactions in mind, we re-visit the original theory of FCS developed by Elson and Magde (EM) [69]. We show that the EM theory is based on the universally valid phenomenological linear approximation approach to macroscopic fluctuations, developed by Einstein for Brownian motion, Onsager and Machlup for linear Gaussian fluctuations [186], and Lax for nonequilibrium steady state [146]. A systematic exposition is given by Keizer[134]. The original EM theory was motivated by Eigen's linear relaxation kinetics [264] and Onsager's regression hypothesis [185]. It has been experimentally verified for concentration fluctuations in bulk solutions [66, 162].

There is a growing interest in the concentration (or copy-number) fluctuation studies on single live cells, both experimental [270] and theoretical [205]. In this Letter, we show that for some systems the linear, phenomenological fluctuation theory breaks down, and a mechanistic nonlinear stochastic reaction theory is necessary.

Nonlinear chemical reaction. The nonlinear effect we discuss for FCS is also present in

chemical relaxation kinetics. To illustrate this, consider the bimolecular reaction $A+B \underset{k_b}{\overset{k_f}{\rightleftharpoons}} C$. According to Eigen's theory, linear relaxation kinetics gives a single time constant τ_r:

$$\tau_r^{-1} = k_f\Big(c_A^{eq} + c_B^{eq}\Big) + k_b = k_f\Big(c_A^{tot} + c_B^{tot} - 2c_C^{eq}\Big) + k_b. \tag{4.2}$$

The relaxation kinetics then is a single exponential for the concentration of C: $\big(c_C(t) - c_C^{eq}\big) = \big(c_C(0) - c_C^{eq}\big)e^{-t/\tau_r}$. However, the nonlinear kinetics based on the Law of Mass Action is

$$c_C(t) - c_C^{eq} = \left\{\frac{1}{1 - k_f\tau_r\delta_0\big(1 - e^{-t/\tau_r}\big)}\right\}\delta_0 e^{-t/\tau_r}, \tag{4.3}$$

with

$$\delta_0 = c_C(0) - c_C^{eq}.$$

The term in the $\{\cdots\}$ is due to the nonlinear effect. When the amplitude δ_0 is sufficiently small, this term is negligible. Figure 4.1 shows the fractional difference between the fully nonlinear relaxation kinetics given in Eq. 4.3 and the single exponential from the linear case. If the amplitude δ_0 is small, the fractional difference will also be small and the linear approximation is valid; otherwise, there will be a significant difference between the linear and nonlinear case.

It is important to note that for nonlinear reactions the relaxation time not only depends on the individual rate constants but also on the concentrations at equilibrium. Furthermore, for nonlinear reactions, the reaction rates depend on diffusion, as it's clearly established in the theory of diffusion limited reactions [28, 46, 236]. Although not apparent in the Law of Mass Action, the diffusion is necessary to determine the macroscopic reaction rate. The coupling between the diffusion and the reaction rates is the actual source of the nonlinearity, and it is also the reason why the relaxation time depends on the composition at equilibrium. With this realization in mind, it becomes clear that the bimolecular association rate constant k_f, and the diffusion constants for A and B used in EM theory are not independent parameters, see Section 4.5. It is worth to mention that in the MesoRD approach to stochastic reaction-diffusion, these parameters are treated as independent [106].

For stochastic reaction-diffusion kinetics, the difference between the linear and nonlinear systems can also be significant; however, the FCS systems are sufficiently complex and no analytical results are available. In order to address this issue, the present study will rely on Monte Carlo simulations to study nonlinear reaction-diffusion systems.

In Section 4.2, the implementation of an stochastic Monte Carlo method is explained. The parameters employed in the simulations are shown to be consistent with the ones used in EM theory. Section 4.3 shows the comparisons between the mesoscopic, nonlinear correlations

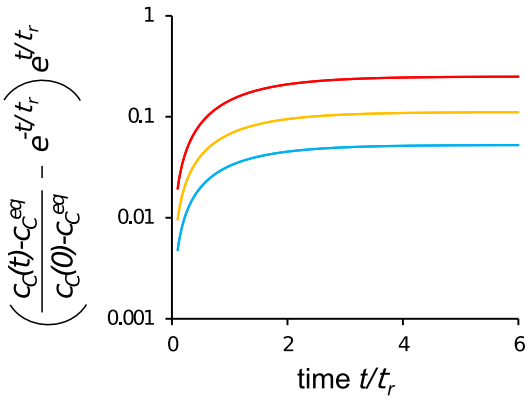

Figure 4.1: The fractional difference between linear and fully nonlinear kinetics for various $k_f\tau_r\big(c_C(0) - c_C^{eq}\big) = 0.2$ (red), 0.1 (orange) and 0.05 (blue).

obtained from Monte Carlo simulations and the EM theory. The discrepancies between these two are further discussed in Section 4.4. For completeness, the analytical results of EM theory are included in Section 4.5.

4.2 Simulation methods

The results of the simulations performed in the present work will be compared to the results from EM theory [69]. Since some of the key molecular parameters used in the simulations are different from the "macroscopic" rate constants and diffusion coefficients in the EM theory, it is important that the parameters employed in the simulation are consistent with those from EM theory. We explain how the simulation was performed and show that the parameters are consistent.

Three-dimensional diffusion is simulated in terms of 3D random walk with time step, Δt, and length step, ϵ_ξ. These parameters are related to the 3D diffusion constants used in EM theory $D_\xi = \epsilon_\xi^2/\big(6\Delta t\big)$ with $\xi = A, B$ or C. The reason for different step sizes is to keep all the particles moving with a single frequency, which means, same time step and different diffusion coefficients. Initially, particles are positioned randomly with uniform distribution in a cubic box of dimensionless length 2×2×2 with periodic boundary conditions. There are three molecular species represented by particles, A, B, and C. At every time step, each particle moves with a distance of ϵ_ξ in one of the $\pm x$, $\pm y$ and $\pm z$ directions at equal probability of 1/6. Depending on if a reaction is involved, we have three cases to be discussed below in detail.

Pure diffusion. In this case, since reactions are not involved, there is only one specie

(say A) of particles moving in a 3D random walk. In order to emulate FCS in simulation, we introduce a laser beam in the transverse plane with a cylindrical Gaussian intensity profile[70],

$$I(\mathbf{r}) = I_0 e^{-2(x^2+y^2)/w^2}, \tag{4.4}$$

where $I(\mathbf{r})$ is the intensity of the incident laser light at position $\mathbf{r} = (x, y)$, I_0 is the maximum intensity at the center of the beam and the focal volume w is given by the radius at which $I/I_0 = e^{-2} \ll 1$. In the pure diffusion, as well as in all the other cases, the focal volume w needs to be much smaller than the simulation box and considerably larger than the length step. In this case, setting the value of w to the length step (ϵ_A) as $w = 10\epsilon_A$ is sufficient for good accuracy. The fluctuation in the photocurrent is caused by the concentration fluctuation through

$$\delta I(t) = I(t) - \langle I(t) \rangle, \tag{4.5}$$

with,

$$I(t) = I_0 \sum_{i=1}^{N_A} e^{-2(x_i^2+y_i^2)/w^2}.$$

Here, N_A is the total number of A particles and x_i, y_i their positions. Therefore, the correlation of concentration fluctuations is just the temporal autocorrelation of the photocurrent, $G(\tau)$, calculated in the simulation as

$$G(\tau) = \frac{1}{N_t - j} \sum_{k=1}^{N_t - j} \delta I\big(k\Delta t\big) \delta I\big((k+j)\Delta t\big), \tag{4.6}$$

where $\tau = j\Delta t$, j starts from 0, and N_t is the total number of time steps. $G(\tau)$ is further normalized dividing by $G(0)$. Note we are treating the molecules as point-like light sources; however, the molecular radii will be relevant when calculating the binding radius for the bimolecular reaction case.

Unimolecular isomerization. In this case, we consider a reaction of type $A \underset{k_b}{\overset{k_f}{\rightleftharpoons}} B$ with rate constants k_f and k_b, and an equilibrium constant $K_{eq} = k_f/k_b$. In the simulation, we set k_f and k_b as rate parameters of exponentially distributed waiting times. These are related to the probability of the reactions occurring via

$$P_{A\to B} = 1 - \exp\left(-k_f \Delta t\right),$$
$$P_{B\to A} = 1 - \exp\left(-k_b \Delta t\right),$$

respectively [93]. Without loss of generality, we assume particle A and B have the same diffusion coefficient and thereby the same characteristic length step ϵ. Once again, it's suffi-

cient to choose the focal volume $\omega = 10\epsilon$. At each time step, besides of performing a random walk, particle A can become B with probability $P_{A\to B}$, and particle B can become A with probability $P_{B\to A}$. Concentration fluctuations for A or B are measured analogously to the pure diffusion case.

Bimolecular reaction. Some very effective and accurate methods have been developed for the bimolecular reaction with diffusion when the number of ligands is large [198, 197]. These are based on the analytical solution for the reversible diffusion-influenced reaction for an isolated pair in 1D and 3D [3, 98, 136, 137]. Unfortunately, the current work will require simulations in the nonlinear regime where we have a small number of ligands where these methods might not be appropriate. There are also other popular tools like the MesoRD and Smoldyn software to simulate these and other type of reactions [13, 106]; however, the simplicity of the simulations required allowed us to produce our own code employing a similar approach to Smoldyn [13].

Before addressing how to perform the simulations for bimolecular reactions, note EM theory calculates the final autocorrelation function for the bimolecular case as the sum of all the correlations weighted accordingly,

$$G(\tau) = \sum_{j=1}^{m} \sum_{l\leq j} (2 - \delta_{jl}) G_{jl}(\tau),$$

where G_{jl} is the correlation between molecule j and l, and j, l can be A, B or C. The function $G(\tau)$ contains the resulting photocurrent correlations from all the fluorescent molecules A, B and C, including coupling effects. The autocorrelation function $G(\tau)$ is the one that is actually compared to real experiments because it's not experimentally possible to isolate the fluorescence of A from that of the reaction product C. However, in our computational setting, we can allow ourselves to concentrate on only one of these correlation curves, $G_{CC}(\tau)$. This curve obtained from only the photocurrent fluctuations of molecule C contains all the information we need, including both reaction rates. As EM theory should remain consistent, the error made when calculating the reaction rates by fitting the simulation correlation curve with the theoretical $G_{CC}(\tau)$ are equivalent to those made when fitting the experimental curve with the theoretical $G(\tau)$, with the exception of additional experimental errors. How to obtain the autocorrelation function $G_{CC}(\tau)$ that we will compare to our simulations is shown in Section 4.5.

For the bimolecular simulations, the reaction is assumed to be $A + B \underset{k_b}{\overset{k_f}{\rightleftharpoons}} C$ with second-order rate constant k_f (forward reaction rate), first-order rate constant k_b (backward reaction rate) and equilibrium constant $K_{eq} = k_f/k_b = c_c^{eq}/\left(c_A^{eq} c_B^{eq}\right)$. Here, c_ξ^{eq} is the equilibrium concentration of specie ξ. We assumed the diffusion coefficients to be $D_A = D_C = D$ and $D_B \geq D$, since usually A and C are considered macromolecules and B plays the role of a

small ligand. Consequently, the lengths steps will obey $\epsilon_A = \epsilon_C \leq \epsilon_B$, and a sufficiently accurate focal volume is found to be $\omega = 25\epsilon_B$. Note the diffusion constant of a particle is not determined by its molecular weight **per se** but by its hydrodynamic radius. We set the probability of a backward reaction to occur in terms of the parameter κ_b as,

$$P_{C\to AB} = 1 - \exp\left(-\kappa_b \Delta t\right). \tag{4.7}$$

At every Δt we check if any reaction occurs. For the forward reaction, we assume it's diffusion limited. When the distance between molecules A and B is less than the binding radius R, they react with probability one. The binding radius is given by the sum of the radii of A and B. Note that the binding radius should be much smaller than the focal volume ω, this condition is imposed in all the simulations. In the backward reaction, particle C becomes A and B simply with probability $P_{C\to AB}$. The newly formed A molecule is placed where the C molecule was, and the B particle is placed a distance R_u away from it in a random direction, with $R_u > R$. If the B particle happens to be placed inside the binding radius of another A molecule, another random direction is chosen to avoid an artificial binding. The introduction of an unbinding radius R_u is a possible solution to simulate the many-particle reaction accurately and address the issue of geminate recombinations in the diffusion limited model [13].

Note we called the backward rate κ_b and not k_b. As particles A and B need to collide first before reacting, the effective forward rate k_f required to compare to EM theory is unknown. Consequently, it is not clear if κ_b should be the effective backward rate k_b either. Also note that for the bimolecular case, we do not expect the macroscopic concentrations relaxation to be exponential but a power law [99], this confirms that κ_b from Eq. 4.7 might not correspond to the effective backward rate k_b. This is a subtle matter that will be treated in more detail in Chapter 5. For the purpose of the current work, understanding some of the dynamics of geminate recombinations[4, 135] will help us address this issue.

Geminate recombinations. Geminate recombinations occur when a particle B that just dissociated from a certain A, associates again with it[4, 13, 135]. At first sight, it is not evident how this phenomenon alters the reaction rates. One way to understand it is in terms of the waiting times. For the first reaction, the B molecule is positioned randomly with a uniform distribution outside of the reaction sphere of radius R. The mean first passage waiting time for the reaction to occur is the one given by Collins and Kimball's or Smoluchowski's theory[46, 227]. However, whenever a dissociation occurs, the B particle is always positioned very near A. As a result, the distribution of the initial position of the B molecule should not be uniform, and the average waiting time for the forward reaction to occur again will no longer be the one given by Collins and Kimball or Smoluchowski's theory. As the average waiting times and the rates are inversely proportional, the effective forward rate cannot be expected to be the same either [227, 236]. In other words, the just

dissociated B has a higher chance to bind to the same A. This is conceptually prevented in the classical Law of Mass Action, and Delbrück-Gillespie theory, which requires a rapid stirring reaction vessel [93].

So how to map the correct forward rate to EM theory? Let us focus on the Smoluchowski approach and call ϕ the probability of a geminate recombination to occur. In a system in equilibrium with several molecules, the law of large numbers tells us that a fraction ϕ of all the forward reactions are due to geminate recombinations. Therefore, we expect that the remaining fraction $1-\phi$ follows the forward reaction rate for irreversible reactions given by Smoluchowski's theory. This yields the relation between the irreversible rate of Smoluchowski [46], $k_D = 4\pi R D_*$ with $D_* = D + D_B$, and the reversible effective forward rate k_f as[13]

$$k_f = \frac{k_D}{1-\phi}. \tag{4.8}$$

In order to calculate the backward rate, we only need to know the equilibrium constant K_{eq}. From our simulation, we can calculate it in terms of the average concentrations as $K_{eq} = c_c^{eq}/\left(c_A^{eq} c_B^{eq}\right)$. However, we also know $K_{eq} = k_f/k_b$, so the effective backward rate can be calculated as

$$k_b = k_f/K_{eq}. \tag{4.9}$$

The only question left to answer is how to calculate the probability of geminate recombinations ϕ. As geminate recombinations are actually a stochastic process, there are many issues to deal with in order to fully address that question. This will be addressed in more detail in Chapter 5. However, a simple approach using Smoluchowski's original solution with an unbinding radius will be sufficient for our current purpose[13]. We can solve Smoluchowski's steady state equation for a reversible reaction in equilibrium using an absorbing boundary condition at R and a constant B concentration at R_u [13]. These boundary conditions mean that the flux at the source R_u equals the flux at the sink in R, as it's expected from a reversible reaction at equilibrium. The solution to this boundary problem is given by

$$\rho(r) = c_0 \frac{R_u(R-r)}{r(R-R_u)},$$

where $\rho(r)$ can be understood as the concentration of B or as the radial distribution function if it's normalized. The reaction rate is given by the flux,$4\pi R^2 D_* \rho'(R)$ per average concentration of B molecules, c_0,

$$k_f = \frac{4\pi R D_*}{1-\frac{R}{R_u}} = \frac{k_D}{1-\frac{R}{R_u}}. \tag{4.10}$$

Note that as $R_u \to \infty$ the original Smoluchowski's irreversible rate is recovered. Comparing this result with Eq. 4.8 yields that $\phi = R/R_u$ [13]. It's important to note this analytic result is only fully valid in the limit of infinitely accurate Brownian Motion. In our simulation, we'll employ random walks with very small characteristic length step, so Eq. 4.10 is a good approximation of the forward rate. If the characteristic step is increased, the simulations become faster; however, a more complicated approach is necessary to calculate the correct reaction rates, as the one used by Smoldyn software[13]. For the purpose of this work, computational efficiency is not an immediate issue, so we employ characteristic length steps that are small enough to use the forward rate given in Eq. 4.10 accurately.

It is still not evident how to choose the appropriate unbinding radius R_u. An initial guess satisfying $R_u > R$ is made. Since every different unbinding radius yields different values of the forward rate, the final concentrations at equilibrium and the equilibrium constant K_{eq}, the simulation is executed to yield these for the initial guess. Afterward, the unbinding radius is recalculated in terms of the final concentrations, and the process is repeated until the unbinding radius remains practically constant between iterations. The unbinding radius in each iteration is recalculated as,

$$R_u = \left[\frac{3}{4\pi}\left(\frac{V_{box}}{nA}\right)\right]^{1/3} \tag{4.11}$$

where V_{box} is the volume of the cubic box and nA is the number of A particles at equilibrium. This expression is obtained by assuming each A molecule has it's own mini-sphere with volume V_{box}/nA. In this sphere, we can assume the behavior is the same as in Smoluchoski's theory which involves only one copy of the A molecule. Assuming A is positioned at the center of the sphere, the appropriate unbinding radius would correspond to the distance between A and the border of the sphere. This value is clearly given in Eq. 4.11.

Once the unbinding radius is calculated, ϕ is determined as well as the forward rate k_f. The effective backward rate k_b is obtained with k_f and the equilibrium constant K_{eq} using Eq. 4.9. These last three parameters are precisely the ones used in EM theory [69]. In order to validate the simulation, we tested the case with one A molecule fixed at the center. The forward rate was calculated using the average first passage time after each forward reaction [227, 236] $k_f = 1/(c_0\tau)$ from the simulation and the Smoluchowski equation for reversible reaction (Eq. 4.10). The relative error between the two calculated forward rates was less than five percent for 100 runs with 5×10^7 time iterations. These results provide consistency between the parameters used in our simulation and the parameters from EM theory.

4.3 FCS and nonlinear stochastic reaction-diffusion

As controls, both pure diffusion and unimolecular reaction with diffusion are carried out first. The EM theory for both these linear stochastic dynamics is exact; hence, it is expected

to agree completely with the simulations, aside from statistical uncertainties. This is indeed the case as shown in Figures (4.2a) and (4.3a).

For the nonlinear reaction with diffusion, EM theory has no exact solution; however, linearization around equilibrium yields a correlation curve in the form of an integral. This integral can be approximated asymptotically for certain range of parameters, or it can be solved numerically. For details on the analytic solutions, see Section 4.5. For certain values of the equilibrium concentration, the simulation deviates from these solutions. We account this deviation to the non-linear effects that are present in the simulation but not in EM theory. The maximum errors are calculated with the maximum norm, which for the error between $\mathbf{x} = (x_1, \cdots, x_n)$ and $\mathbf{y} = (y_1, \cdots, y_n)$ is given by $||\mathbf{x}-\mathbf{y}||_{\max} = \max\{|x_1-y_1|, \cdots, |x_n-y_n|\}$.

To ensure the validity of the results, two asymptotic limits, where the nonlinear effects are known to be negligible, are employed as a third and fourth control. In order to provide a quantification of the non-linear deviation, its magnitude is studied as a function of the forward reaction rate and the number of molecules. All these will be further discussed in detail.

Control I: pure diffusion. The calculated $G_{AA}(\tau)$, normalized autocorrelation function, from simulations with the number of particles, $N_A = 25$, and total measurement time, $T = 10^5$, is plotted along the analytical solution in Figure (4.2a). Aside from statistical errors, the simulation results agree completely with the analytical solution from Eq. 4.12 as expected. We further calculate the difference between the analytical solution and the simulation results with different total measurement time, as depicted in Figure (4.2b). Consistently, it shows that this difference is decreasing with increasing total measurement time $T = N_t\Delta t$. Note that since particles are treated independently, an increase in the total measurement time is equivalent to increasing the number of particles.

Control II: unimolecular reaction with diffusion. Analogously to the pure diffusion case, we calculate the temporal autocorrelation of the photocurrent, $G(\tau)$, for either species of particles. Without loss of generality, we choose the initial number of A and B particles equal, i.e. $N_A = N_B$. We calculate the photocurrent for particle B along with the analytic solution (Eq. 4.14), as plotted in Figure (4.3a). The simulation results are again in good agreement with the analytic solution. In addition, we calculate the difference between the analytical solution and simulation results of $G_{BB}(\tau)$ for different total measurement times. As depicted in Figure (4.3b), the error between the analytical result and the simulation decreases as the total measurement time increases. Once more, as the particles react independently of each other, an increase in the total measurement time is equivalent to increasing the number of particles evenly.

Nonlinear reaction with diffusion. We choose N_A, N_B and N_C small and of the same

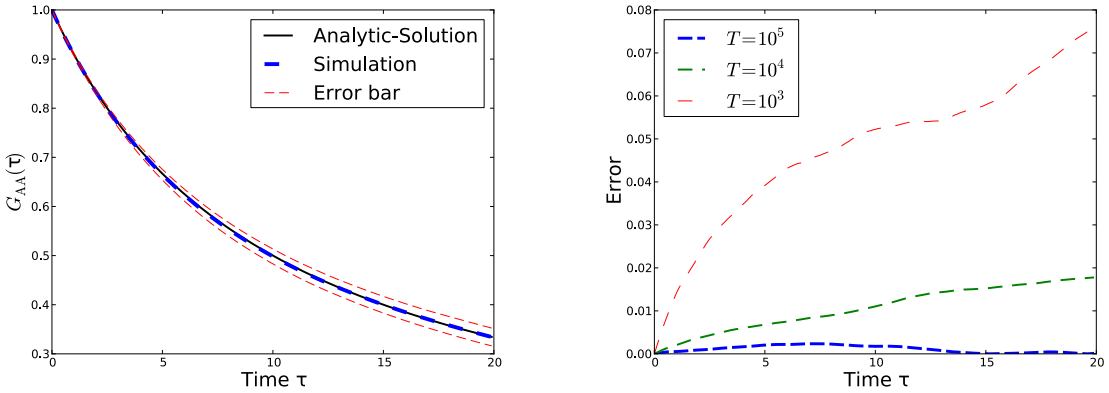

(a) (b)

Figure 4.2: (a) The autocorrelation of the simulated fluorescent signal, $G_{AA}(\tau)$, for pure 3D diffusion with twenty five A particles. The motions of all these particles are completely statistically independent. Here, $\epsilon = 0.1$, $\omega = 10\epsilon_A$ $\Delta t = 0.1$, and total time steps in the simulations are $T = 10^5$ (blue dash). The black solid line is EM's analytical result[69] (Eq. 4.12); the thick dashed line (blue) is the simulation result, and the thin dashed lines (red) are the simulation error bars calculated from the standard deviation calculated over 30 realizations. (b) The absolute value of the difference between the simulated $G_{AA}(\tau)$ and the EM's results for different total time steps: $T = 10^3$ (red dash), 10^4 (green dash), and 10^5 (blue dash). The maximum error for $T = 10^5$ is 2.3×10^{-3} and for $T = 10^3$ is 7.6×10^{-2}.

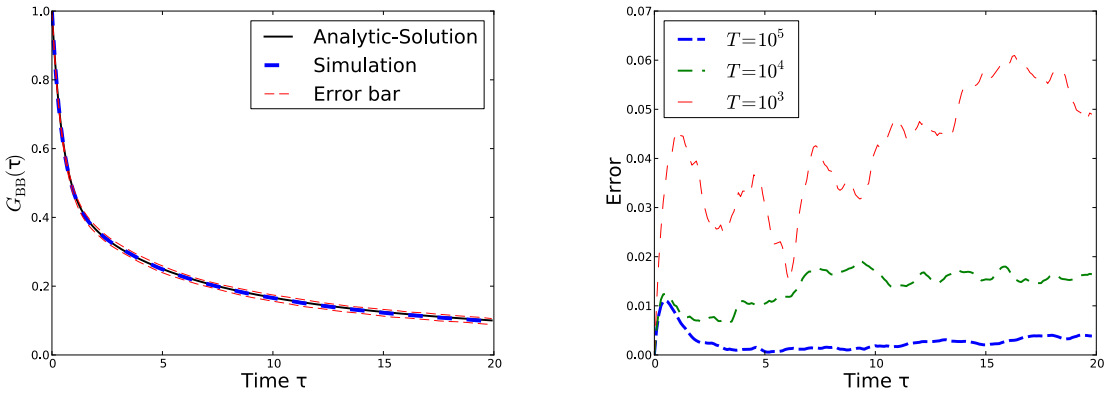

(a) (b)

Figure 4.3: (a) The temporal autocorrelation of the photocurrent $G_{BB}(\tau)$ for particle B in the unimolecular isomerization, $A \underset{k_b}{\overset{k_f}{\rightleftharpoons}} B$. Here, $\epsilon_A = \epsilon_B = 0.1$, $\omega = 10\epsilon_A$, $\Delta t = 0.1$, $T = 10^5$ and $k_f = k_b$. The black solid line is EM's analytical result[69] (Eq. 4.14); the thick dashed line (blue) is the simulation result, and the thin dashed lines (red) are the error bars from standard deviation calculated over 30 realizations. (b) The difference between the analytical solution and simulation results of the unimolecular isomerization for $G_{BB}(\tau)$ at different total measurement times, $T = 10^5$, $T = 10^4$ and $T = 10^3$. The maximum error for $T = 10^5$ is 1.1×10^{-2} and for $T = 10^3$ is 6.0×10^{-2}.

order. We calculate the temporal autocorrelation of the photocurrent $G(\tau)$ for particle C and compare it against the analytical solution. In Figure (4.4a) two solutions for the correlation curve are shown: the simulation curve and the numerical approximation of the analytic solution integral (Eq. 4.15). As N_A, N_B and N_C are of the same order, the asymptotic approximation of the integral is outside its range of validity (see Section 4.5), and it's not included in the plot. A noticeable disagreement between the simulation and the numerical analytic integration result is observed as depicted in Figure (4.4a). The maximum error between the simulation and the analytic solution is around 0.04, and the theory will produce an error of 11.5% in the forward reaction rate if fitted to the central tendency in the simulation curve. The plots in Figs. (4.4b) and (4.4c) correspond to the two asymptotic limits where the nonlinear effects are negligible and the simulation converges to the analytic linear theory. These two limits will be discussed next.

Asymptotic limit I: large number of ligands. In the case where $N_B \gg N_A, N_C$, the concentration of B molecules barely fluctuates. Consequently, the nonlinear reaction with diffusion approaches asymptotically a linear unimolecular reaction with diffusion, i.e. the nonlinear effects are negligible. A simple example is given by the law of mass action for $A + B \underset{k_b}{\overset{k_f}{\rightleftharpoons}} C$. If b barely fluctuates around b_0, the concentration of C follows

$$\frac{dc}{dt} = K_f a - k_b c, \quad \text{with :} \quad K_f = k_f b_0,$$

with a, b, c the concentrations of A, B, C and k_f the second order rate constant. The last equation is clearly linear and EM theory provides an exact result for it. In Figure 4.5, besides the same two solutions as plotted before, the exact analytic solution approached as N_B becomes $N_B \gg N_A, N_C$ is also included. Since it's in its range of validity and the non-linear effects are negligible, the asymptotic approximation of the linear analytic solution (Eq. 4.15) is also plotted. The four solutions, including the simulation and the numerical integration of Eq. 4.15, converge to the same correlation curve, as expected. This result is clearly depicted in Figure 4.5. It also shows consistency with our two controls, since the error decreases when increasing the number of particles. Recovering the correct asymptotic limit when $N_B \gg N_A, N_C$ serves as a third control to validate our simulation.

Asymptotic limit II: large number of all molecules. If the number of all the molecules is increased, i.e. $N_A, N_B, N_C \gg 1$, the concentration of any of the species barely fluctuates around equilibrium. Analogously to the previous case, the nonlinear effects become second order and the system approaches a linear solution, which is plotted as the exact analytic solution in Figure 4.6. Additionally, the numerical analytic solution and the simulation curves are plotted as before. In this case, the asymptotic approximation of the linear analytic

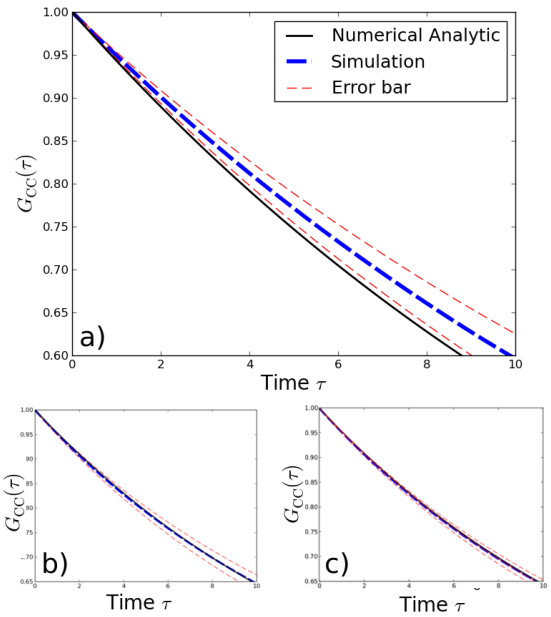

Figure 4.4: a) The temporal autocorrelation of the photocurrent, $G_{CC}(\tau)$, for particle C in the bimolecular reaction with N_A, N_B and N_C small and of the same order (around 35 each). The thick dashed line (blue) is the simulation result, and the thin dashed lines (red) are the error bars given by the standard deviation calculated over 30 realizations. Here $\epsilon_A = \epsilon_C = 0.0033$, $\epsilon_B = 0.0066$, $\omega = 25\epsilon_B$, $\Delta t = 0.1$, $T = 2 \times 10^6$ and $R = 0.05$. The calculated unbinding radius for this case was in average $R_u = 0.302$. The maximum error between the simulation and the analytic solution is around 0.04. b) Same parameters as in a) but with the asymptotic limit of many ligands N_B. c) Same parameters as in a) for the asymptotic limit of large number of molecules $N_A, N_B, N_C \gg 1$. The full plots of the asymptotic limits plots b) and c) are shown in Figs 4.5 and 4.6.

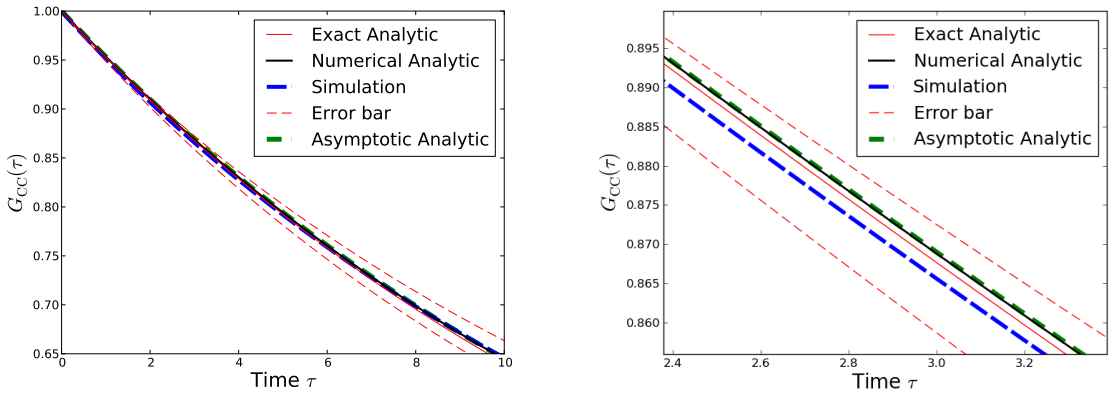

(a) (b)

Figure 4.5: a) The temporal autocorrelation of the photocurrent, $G_{CC}(\tau)$, for particle C in the bimolecular reaction with $N_B \gg N_A, N_C$; $N_B \sim 2000$, $N_A, N_C \sim 20$. The error bars are once again given by the standard deviation calculated over 30 realizations. Here $\epsilon_A = \epsilon_C = 0.0033$, $\epsilon_B = 0.0066$, $\omega = 25\epsilon_B$, $\Delta t = 0.1$, $T = 2 \times 10^6$ and $R = 0.05$. The calculated unbinding radius for this case was in average $R_u = 0.414$. The maximum error between the numerical analytic solution and the simulation is 3.2×10^{-3}. b) Zoomed in version of a).

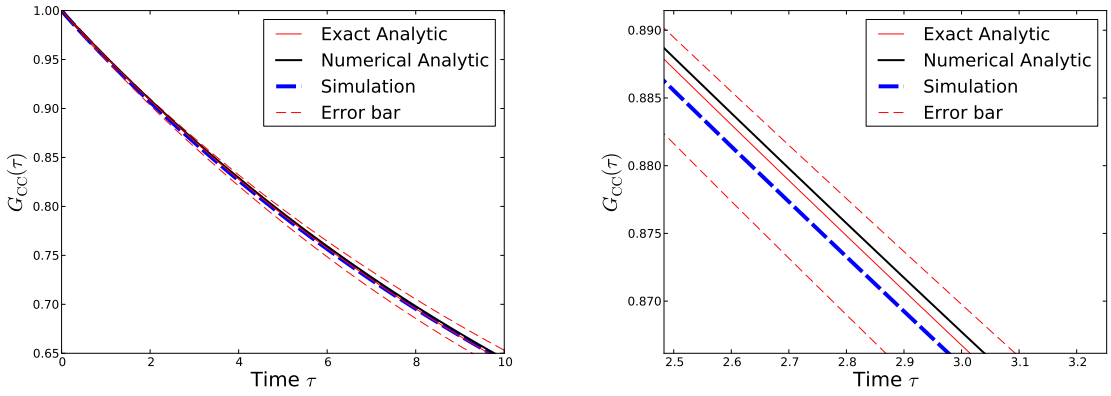

(a) (b)

Figure 4.6: a) The temporal autocorrelation of the photocurrent, $G_{CC}(\tau)$, for particle C in the bimolecular reaction with $N_B, N_A, N_C \gg 1$; $N_A, N_B, N_C \sim 500$. The error bars are once again given by the standard deviation calculated over 30 realizations. Once again the parameters are $\epsilon_A = \epsilon_C = 0.0033$, $\epsilon_B = 0.0066$, $\omega = 25\epsilon_B$, $\Delta t = 0.1$, $T = 2 \times 10^6$ and $R = 0.05$. The calculated unbinding radius for this case was in average $R_u = 0.132$. The maximum error between the numerical analytic solution and the simulation is 2.8×10^{-3}. b) Zoomed in version of a).

solution (Eq. 4.15) is not in its range of validity, so it is not included. As we can see in Figure 4.6, the simulation, the numerical analytic solution and the exact linear unimolecular solution are all converging, i.e. the non-linear effects are becoming negligible as the number N_A, N_B and N_C is increased. This asymptotic limit serves as a fourth control to validate the simulation.

Nonlinear deviation variation. In order to better quantify the deviation for the nonlinear reaction case shown in Figure 4.4. We calculated how this deviation varies in term of the relative change in the forward reaction rate (Figure 4.7(a)) and with the uniform increase in the number of all molecules (Figure 4.7(b)).

The plot shown in Figure 4.7(b) shows the convergence to the asymptotic limit II: Large number of all molecules. As expected from our previous result, the error is gradually reduced as the number of all molecules is increased. Furthermore, on the plot in Figure 4.7(a), we manipulated the forward reaction rates k_f. As these rates are related to the diffusion coefficients $D_\xi = \epsilon_\xi / 6\Delta t$ by Eq. 4.10, the best way to manipulate the reaction rate is to modify the characteristic length step ϵ_ξ. In this case, we multiplied ϵ_ξ (with $\xi = A, B, C$) by a constant between one and two, which yields a percentage variation of the forward reaction

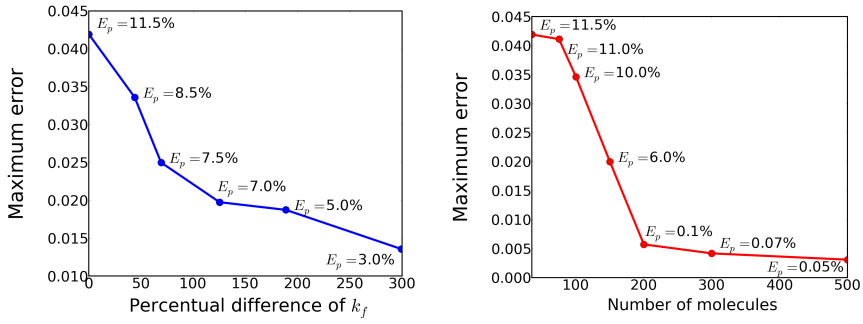

(a) (b)

Figure 4.7: Plot of the maximum error between the numerical analytical correlation curve and the simulated one as a function of: a) Percentage deviation between forward reaction rates, b) Number of molecules $N = N_A, N_B, N_C$. The first point on the left of both plots corresponds to the simulation with N_A, N_B and $N_C \sim 35$ plotted in Figure 4.4. The percentage deviation in a) is in reference to this point. The last point to the right in b) corresponds to the case plotted in Figure 4.6. Each point in the curves has an E_p, corresponding to the percentage error when predicting the forward rate k_f by fitting the theory to the simulation central tendency.

rate up to 300%.

The deviation in Figure 4.7(a) is reduced as the reaction rate is increased. This is expected from the law of mass action for $A + B \underset{k_b}{\overset{k_f}{\rightleftharpoons}} C$, where their concentrations a, b and c satisfy $(ab)k_f/k_b = c$ in the steady state. In this expression, it is clear how an increase in the forward rate k_f can be equivalent to an increase of b. Consequently this case is equivalent to the asymptotic limit I: large number of ligands. As the characteristic length step is increased, the error by approximating diffusion by a random walk is also increased. However, this error is still not relevant since the overall error shown in Figure 4.7(a) decays as the reaction rate is increased.

Also note each point in Figure 4.7 has an associated percentual error, E_p. This was obtained by testing slightly different values for the forward rate k_f in the analytic curve until the maximum error against the simulation was below 0.002. Ideally, a least squares fitting could be employed. However, it is left as future work to develop a faster and more robust simulation to illustrate a complete landscape of the deviations as a function of two or more parameters. This could include a least square fitting to obtain the percentual error.

4.4 Discussion

We showed that our simulation recovers the correct reaction rates of the Smoluchowski's model for reversible reactions providing consistency between the simulation parameters and the parameters used by EM theory. As first controls, the exact solutions of EM theory for the pure diffusion and the unimolecular reaction with diffusion were recovered by our simulation. In addition, to further validate the simulation, two asymptotic limits were tested. In the asymptotic limits of a large number of ligands and a large number of molecules, the simulation and the theoretical correlation curves converge as expected. This confirms that in these limits the nonlinear effects become negligible and linear EM theory is very accurate. However, in the case where N_A, N_B and N_C are not very big and have similar values (around 35 each), we showed the simulation results deviate from those of linear EM theory. As the simulation proved to be an accurate model, we account the deviations due to nonlinear effects that are depreciated in linear EM theory[70], as briefly shown in Section 4.5.

The dependence of the deviation in the number of molecules and the reaction rates was analyzed. When employing an increasing number of all of the molecules, we observe the deviation is reduced and the system gradually reaches the asymptotic limit II, as expected. When the forward reaction rate was gradually increased to 300% its original value, we again observe the error is reduced. This is due the fact that increasing the reaction rate produces a similar effect to that of the increase in the number of ligands, which corresponds to the asymptotic limit I, where the error is also reduced.

For most experimental scenarios the assumptions $N_B \gg N_A$, N_C or N_A, N_B, $N_C \gg 1$ are appropriate, and the results provided by EM theory are very accurate. Nonetheless, this work showed that when the number of molecules is small, nonlinear effects are not negligible showing a deviation between the simulation of the nonlinear model and linear EM theory. However, experimental FCS correlation curves usually involve other sources of noise not considered in the simulated fluctuations, like the mismatch of refractive indexes and photobleaching of fluorophores amongst others. As we found the deviation to be small with a 11.5% error in the reaction rates, it is likely that the error produced by the nonlinearity is still within the experimental uncertainty of current laboratory measurements, so it might require a more carefully designed setup and clean system to test our theory.

In particular, we do not believe the nonlinear effect will be relevant in the current cellular biophysical investigations. Rather, the significance of the present work is to bring quantitative experimental measurements on nanometric, nonlinear chemical reactions a step closer to a stochastic theoretical framework. It also intends to call attention to nonlinear kinetics in the fluctuation chemistry setting. Certainly, we hope this work paves the way to study more complex nonlinear reactions with concentration fluctuations. We are certain for other more complex reaction systems the nonlinear effect can be larger. Furthermore, on the practical side, nonlinear chemical reactions in biology are widely present; so being able to show, at least in the simplest case, the EM theory works well, even in a context where nonlinearities

are significant, is a relevant contribution for current practice of FCS in biochemistry.

With the increasing accuracy and ability of single-molecule techniques, results like the ones obtained herein will become experimentally accessible. We also believe FCS will grow more and more into an analytical tool. In a clear analytical chemistry setting, an 11% deviation would be significant. It is true that such level of quantification is still in development, but we hope results like ours provide additional motivation. Developing nonlinear chemical reaction theory with fluctuations, in terms of FCS or more generally speaking, remains a challenge.

4.5 Elson and Magde FCS theory

Three main results from EM theory [70] are incorporated in this Section. For the three cases, pure diffusion, unimolecular isomerization and nonlinear reaction with diffusion, the full expressions for the correlation curves are given. Additional details are given to explain why EM theory is a linear theory for the bimolecular reaction.

The parameters used are Δt the time step, ϵ_ξ with $\xi = A, B$ or C the diffusion length step for every time step taken, D_ξ the diffusion coefficient of ξ and ω focal volume given by the radius of the Gaussian laser.

Pure diffusion. The normalized auto correlation curve for purely diffusive A molecules is given by,

$$G_{AA}(\tau) = \frac{1}{1+\tau/\tau_{D_A}} \tag{4.12}$$

$$\text{with} \quad \tau_{D_A} = \frac{\omega^2}{4D_A} \quad \text{and} \quad D_A = \frac{\epsilon_A^2}{6\Delta t}. \tag{4.13}$$

Unimolecular reaction with diffusion. The normalized autocorrelation curve of B for the diffusive reaction $A \underset{k_b}{\overset{k_f}{\rightleftharpoons}} B$ with $D_A = D_B$ is given by,

$$G_{BB}(\tau) = \frac{1}{1+K_{eq}}\left(\frac{K+\exp\left(-R\tau\right)}{1+\tau/\tau_{D_B}}\right), \tag{4.14}$$

with $R = k_f + k_b$, $K_{eq} = k_f/k_b$ and,

$$\tau_{D_B} = \frac{\omega^2}{4D_B} \quad \text{and} \quad D_B = \frac{\epsilon_B^2}{6\Delta t}.$$

Nonlinear reaction with diffusion. The normalized autocorrelation curve of C for the

diffusive reaction $A + B \underset{k_b}{\overset{k_f}{\rightleftharpoons}} C$ with $D_A = D_C = D$ is given by the integral,

$$G_{CC}(\tau) = \frac{\omega^2}{4\pi} \int_{-\infty}^{\infty} \int_{-\infty}^{\infty} \mathcal{F}(\tau, \nu_x, \nu_y) d\nu_x d\nu_y, \tag{4.15}$$

with

$$\mathcal{F}(\tau, \nu_x, \nu_y) = \exp\left[-(\nu_x^2 + \nu_y^2)\frac{\omega^2}{4}\right] Z_{CC}(\tau, \nu_x, \nu_y),$$

where ν_x and ν_y are the Fourier frequency variables corresponding to the spatial variables x and y. The integral cannot be solved exactly; nonetheless, we have two possible approaches: provide an asymptotic approximation or solve it numerically. The former, as done in EM theory[70], requires that $D_B \gg D$ and $C_A^{eq} \sim C_C^{eq} \ll C_B^{eq} \sim K_{eq}^{-1}$. The numerical solution doesn't require any of these conditions. In Section (4.3), we employ both approaches to compare the theory against our simulation.

In Eq. 4.15, $Z_{CC}(\tau, \nu_x, \nu_y)$ is given by

$$Z_{jl}(\tau, \nu_x, \nu_y) = \sum_s X_l^{(s)} Y_j^{(s)} \exp\left(\lambda^{(s)}\tau\right), \tag{4.16}$$

with $j, l = A, B$ or C. The quantities $X^{(s)}$ for $s = 1, 2, 3$ are the right eigenvectors, $Y^{(s)}$ are the left eigenvectors and $\lambda^{(s)}$ are the three eigenvalues of matrix $\mathbf{M_0}$ from Eq. 4.18. The matrix $\mathbf{M_0}$ is obtained from the reaction diffusion equation for the concentration of the three molecules at position $\mathbf{r}$ and time τ. The concentration for the three molecules will be given by the vector $\mathbf{C}(\mathbf{r}, \tau)$ with components $C_j(\mathbf{r}, \tau)$ and $j = A, B$ or C. The full **nonlinear** reaction diffusion equation is given by

$$\frac{\partial \mathbf{C}(\mathbf{r}, \tau)}{\partial \tau} = \mathbf{D} \cdot \nabla^2 \mathbf{C}(\mathbf{r}, \tau) + \mathbf{M}(\mathbf{C}(\mathbf{r}, \tau)) \cdot \mathbf{C}(\mathbf{r}, \tau), \tag{4.17}$$

where $\mathbf{D}$ is a diagonal matrix with the j^{th} chemical diffusion coefficients D_j, and $\mathbf{M}$ is the stoichiometry matrix[1]. Note that $\mathbf{M}$ is not a constant coefficient matrix, since this is a nonlinear reaction, it depends on the concentration vector $\mathbf{C}(\mathbf{r}, \tau)$. Supposing the system is stationary, the chemical concentrations $\mathbf{C}(\mathbf{r}, \tau)$ will reach a thermodynamic equilibrium; therefore, the mean concentration of each component will be given by the ensemble average of the concentration, i.e. $\mathbf{C}^{eq} = \langle \mathbf{C}(\mathbf{r}, \tau) \rangle$. The ensemble average can be understood as the averaged quantity over many identical systems at a certain time. Although the partial differential equation (PDE) (Eq. 4.17) is deterministic, another **linear** PDE can be derived for the fluctuations of the system around equilibrium. This fluctuations will be given by $\boldsymbol{\delta C}(\mathbf{r}, \tau) = \mathbf{C}(\mathbf{r}, \tau) - \mathbf{C}^{eq}$. Substituting into Eq. 4.17 and dropping the **nonlinear** terms we

[1]Matrix of reaction coefficients based on the Law of Mass action.

obtain the PDE for the fluctuations

$$\frac{\partial \delta \mathbf{C}(\mathbf{r},\tau)}{\partial \tau} = \mathbf{D} \cdot \nabla^2 \delta \mathbf{C}(\mathbf{r},\tau) + \mathbf{M_0} \cdot \delta \mathbf{C}(\mathbf{r},\tau), \tag{4.18}$$

where the constant coefficient matrix $\mathbf{M_0} =$

$$\begin{bmatrix} -(\nu^2 D + k_f C_B^{eq}) & -k_f C_A^{eq} & kb \\ -k_f C_B^{eq} & -(\nu^2 D_b + k_f C_A^{eq}) & kb \\ k_f C_B^{eq} & k_f C_A^{eq} & -(\nu^2 D + k_b) \end{bmatrix},$$

with $\nu^2 = \nu_x^2 + \nu_y^2$.

The expression for the auto correlation curve (Eq. 4.15) is not trivially obtained from the calculations just shown, for a full treatment consult EM theory[70]. What is to be noted is that Eq. 4.15 is based on Eq. 4.18, which is the linearized version of the PDE in Eq. 4.17 around equilibrium.

Chapter 5

MARKOV CHAINS FOR REVERSIBLE BIMOLECULAR REACTIONS

Chemical kinetics involving diffusion of reactants and subsequent chemical reaction are described by diffusion-influenced reaction theory. This theory is the fundamental building block of most of the current algorithms to simulate biochemical reaction-diffusion systems at cellular or sub-cellular scales [13, 57, 63, 64, 71, 77, 106, 108, 125, 223, 244, 256, 257, 268]. The classical models for irreversible diffusion-influenced reactions [46, 47, 105, 227, 230, 235] can be derived by introducing absorbing boundary conditions to over-damped continuous Brownian motion (BM) theory. As there is a clear corresponding stochastic process, the mathematical description takes both Kolmogorov forward equation for the evolution of the probability distribution function and the stochastic sample trajectories. This dual description is a fundamental characteristic of stochastic processes and allows simple particle based simulations to accurately match the expected statistical behavior. However, in the traditional theory using the back-reaction boundary condition to model reversible reactions with geminate recombinations, several subtleties arise: it is unclear what the underlying stochastic process is, which causes complications in producing accurate simulations; and it is non-trivial how to perform an appropriate discretization for numerical computations.

In this chapter, we derive a discrete stochastic model for diffusion-influenced reactions that recovers the classical models and their boundary conditions in the continuous limit. In the case of reversible reactions, we recover the back-reaction boundary condition, unifying the back-reaction approach with those of current simulation packages. Furthermore, all the complications encountered in the continuous models become trivial in the discrete model. The work on this chapter is based on the journal publication [57].

5.1 Introduction

The theory of Brownian motion [68, 208, 253], as developed by Einstein, Smoluchowski, and Langevin, describes the random motion of a particle immersed in a fluid resulting from its collisions with the atoms or molecules of the fluid. There are two distinct physical effects from the collisions: A mean frictional force that resists a macroscopic motion and a random fluctuating force, with zero mean, that rapidly changes the directions of movements. As with any model, the theory itself is a mathematical idealization of the physical reality. For instance, as a continuous function of time, overdamped Brownian motion has a fractal ge-

ometry, i.e. between any two instants in time, there is an infinite amount of fluctuations and changes of direction of the particle. However, any physical process that follows Newtonian mechanics always has two times sufficiently close that a particle only moved on a straight line, known as mean free path.

In the current work, we deal with reversible chemical reactions mediated by diffusion in aqueous solution, which is a complex problem built over the Brownian Motion framework. Historically, Smoluchowski, and Collins and Kimball [46, 230] formulated a macroscopic theory for the irreversible formation of a chemical species C from separated A and B compounds in terms of diffusive motions of the reactants, leading to their encounter and chancy transformation. Interestingly, the stochastic process underlying the same diffusion equation and boundary condition, known as *partially reflected Brownian motion* (PRBM) [101], predetermines an associated process of repeated futile encounter known as a gemination process [4, 13, 28, 56], which plays a central role in both association and dissociation processes. The rigorous mathematical problem of PRBM, however, is non-trivial [23]. It is best understood as the limit of a discrete random walk [32], as explained in detail in Section 3.3.

In practice, most complex problems in applied mathematics are inevitably solved computationally. The continuous mathematical descriptions of Brownian motion problems like the above are eventually discretized into algorithms that are appropriate for numerical computations. One therefore naturally seeks a formulation of applied "Brownian motion" problems directly in terms of a discrete representation. Such an approach, without loss of accuracy and rigor, bypasses two difficult mathematical subjects altogether: continuous stochastic path as the limit of a discrete Markov process and numerical accuracy of high-order discrete algorithm for a continuous problem. The objective of the present work is to follow this approach to develop a discrete stochastic model for reversible bimolecular reactions via diffusion encounter.

It is important to mention that at this point we are not concerned in making a judgment of whether the physical reality is Newtonian or not but on a more computationally accessible approach. Our premise is that all phenomena we observe as the physical reality at some time and space scales, in applied mathematics, can be formulated and implemented as discrete models, which is not necessarily the same as implementing discretization of continuous physical laws. In 1960s computational fluid dynamics (CFD) had a similar problem emerged that was first solved by Godunov in his 1959 revolutionary paper [95]. Before Godunov's work, the CFD numerical methods for compressible flow were plagued with difficulties. His approach to solve these issues was to provide a discrete conservation law instead of a discretization of a conservation law solely [95, 155, 210, 248]. The model presented herein shares that inspirational spirit; we will formulate a discrete stochastic process instead of a discretization of a continuous stochastic process.

Additional motivation lies in the growing need for quantitative mathematical models, and fast algorithms, of small biological systems like cells or subcellular compartments of the cell.

Most of these systems are non-homogeneous in space and have a low number of molecules, so its modeling is based on stochastic reaction-diffusion theory at mesoscopic scales. However, unlike the case of homogeneous reaction theory [22, 206], the connection between the reaction-diffusion phenomena at different microscopic, mesoscopic and macroscopic scales is still a matter of recent research [15, 80, 108, 124, 125]. Our model contribution in this front is to unify the theory of reversible diffusion-influenced reactions [3, 136, 224] with the different approaches to model reversible reactions taken by several simulation packages , like Smoldyn, FPKMC, eGFRD [13, 63, 237] and others [64, 106, 223, 244, 257, 268]. We also note that in a macroscopic phenomenological reaction-diffusion theory the diffusion coefficients of A and B and their association rate constant are three independent parameters [162, 177]. Mechanistically, however, the last is a function of the former two [56, 230]. Our discrete model could also provide a guideline on how to establish these connections for nonlinear reversible reactions.

With the discussion above in mind, we begin with a general approach in the spirit of Langevin [145]. Consider the stochastic dynamic equations for an immersed particle of mass m,

$$dx = vdt, \quad mdv = \big(-\eta v + \xi(t)\big)dt; \tag{5.1}$$

where x is the position, v the velocity, η the damping coefficient, $\xi(t)$ the white noise term that satisfies $\xi(t)dt = \sqrt{2k_BT\eta}\ dW_t$ with W_t the standard Brownian motion or Wiener process, k_B the Boltzmann constant and T the temperature. The Wiener process satisfies $E[W_t] = 0$ and $E[W_tW_s] = \min(t, s)$, which implies $E[\xi(t)\xi(s)] = 2k_BT\eta\delta(t - s)$. The stochastic trajectory in its integral form is given by

$$x(t) = x(0) + \int_0^t e^{-\eta s/m}\left(v(0) + \frac{1}{m}\int_0^s e^{\eta\tau/m}\xi(\tau)d\tau\right)ds, \tag{5.2}$$

which is derived in the Appendix A. Its probability distribution dynamics is described by the multivariate Fokker-Planck equation, which in this specific case, it is usually referred as the Klein-Kramers equation,

$$\frac{\partial f(x,v,t)}{\partial t} = \frac{\partial}{\partial v}\left[\left(\frac{k_BT\eta}{m^2}\right)\frac{\partial f}{\partial v} + \frac{\eta v}{m}f\right] - v\frac{\partial f}{\partial x}. \tag{5.3}$$

In the overdamping limit of Eq. 5.1, we obtain $dx = \frac{1}{\eta}\xi(t)dt$, which yields a simpler Fokker-Planck equation

$$\frac{\partial f(x,t)}{\partial t} = D\frac{\partial^2 f(x,t)}{\partial x^2}, \tag{5.4}$$

with the diffusion coefficient given by the Einstein relation: $D = k_BT/\eta$. This equation describes the probability distribution dynamics of standard Brownian Motion or Wiener

process with no drift. Note it can be extended to varying damping coefficient $\eta(x)$, which would make the diffusion coefficient not constant, and it will change the form of the equation. In particular, the issue of Itō vs. Stratonovich or divergence form of the diffusion term matters [14].

Although Eq. 5.4 has an identical form as the classical diffusion equation for a density of particles, it has a much fundamental character; it does not rely on Fick's law. The classical equation should be understood as the equation of *mean density* of a large number of identical, independent Brownian particles. Fick's law then is an emergent statistical phenomenon.

The theory of chemical reaction in aqueous solution, mediated by diffusion encounter, is based on a three-dimensional version of the standard Brownian motion we just presented, with the addition of an absorbing or partially absorbing boundary condition to model the "event of encounter" in a reaction; it is the core of Smoluchowski's theory [46, 230]. However, as Brownian Motion is such a powerful and useful mathematical idealization, it is easy to assume that it is a first principle. For instance, we tend to think of random walks as approximations to standard Brownian motion (or more accurately to a Wiener Process), immediately assuming Brownian motion is the best description of the physical world. In reality, the theory of Brownian motion is a mathematical limit, and one could even argue Random Walks might provide models closer to what one observes in reality than Brownian motion theory. With computational tasks in mind, why shouldn't we think standard Brownian motion theory is the one providing an approximation to some specific kind of Random walks?

For relatively simple processes, as in diffusion-influenced irreversible reactions, standard Brownian motion provides a robust theoretical framework. However, when dealing with more complex processes like reversible reactions, a great deal of subtleties arise [3, 13, 28, 136, 199]. Many of the issues one encounters while trying to model more and more complex processes are intrinsic to the fact that one had adopted a specific mathematical idealization, especially when dealing with such an abstract idealization like Brownian Motion. For instance, it has been shown that the continuous diffusion approximation of discrete reaction networks can fail to represent correctly the mesoscopically interesting steady-state behavior of bistable systems [258], an issue of utter relevance in biochemical cell dynamics. The purpose of this work is to convince the reader that an alternate discrete approach to reversible stochastic reaction-diffusion might provide a simpler, more robust, and computation-friendly framework where these subtleties are no longer an issue. It also unifies previous theoretical approaches with more recent simulation algorithms, contributing to a better understanding of reversible stochastic reaction-diffusion. Although the model here presented is for a relatively simple problem, it provides the guidelines for a different line of research that could address fundamental issues in stochastic reaction-diffusion theory and simulations. A condensed review of some of the classical models for bimolecular reactions that are mediated by diffusion encounter was presented in Chapter 3, in particular Section 3.2.

5.2 Reaction-diffusion as a discrete stochastic process

In this section, we will present the theoretical basis and motivation to model reaction-diffusion as a discrete stochastic process. As mentioned in the previous section, all the subtle issues that cause confusion among the existing theories of reversible reactions with diffusion become trivial when moving to an appropriate discrete time/space stochastic description. This will shed some light in the advantages of the discrete stochastic models presented in the next section. It should be noted that similar successful attempts have been made to write one and two dimensional irreversible Smoluchowski type models as discrete stochastic processes [246, 247, 265]. We will break down our attention into three different aspects:

1. Reactions as stochastic processes and their two descriptions, e.g., ensemble distribution and sample trajectories.

2. Definition of bound/unbound in $A + B \rightleftharpoons C$.

3. Simulations with geminate recombinations. Gemination is the process described by τ_κ in Fig. 3.1.

Although these three aspects are closely related to each other, the sequential presentation illustrates some of the advantages of our discrete stochastic model from slightly different angles. Some of the subtle issues that come up in the classical models will be discussed in the different sections, and it will be addressed how the discrete stochastic description helps solving them. Each of these aspects will be covered in detail in the following subsections.

5.2.1 Chemical reactions as stochastic processes

Well stirred chemical reactions where there is no spatial component in the equations have been successfully modeled with deterministic models based on the Law of Mass Action (LMA). However, for cellular biochemical processes inside individual cells, the number of molecules might not be large enough for an accurate continuous description. In this case, there is a unifying stochastic mathematical framework known as the Delbrück-Gillespie process, whose Kolmogorov forward equation (KFE) has been known as the Chemical Master Equation (CME), and whose stochastic trajectories can be computed with the Gillespie, or Doob-Bortz-Kalos-Lebowitz, algorithm [205, 206]. Although spatial homogeneity is still assumed in this theory, its depth and richness lie in Kurtz's theorem, stochastic nonlinear bistability [207], and stochastic oscillations. This theory has provided a better understanding of biochemical bistability, as shown by a deterministic and stochastic comparison of the Schlögl model [258], and in the separation between the dynamics at short and long time scales.

The Delbrück-Gillespie process is a landmark example, at least in chemical reaction dynamics, of the two parallel descriptions of a stochastic process. Its CME describes the time-evolution of the probability distribution while the Gillespie algorithm describes the stochastic trajectory of the system, one reaction at a time, whose statistical ensemble properties will satisfy such probability distribution. The same dual description is of key importance when it comes to producing particle-based numerical simulations. One may know (or think to know) the KFE of a diffusion process; however, if we cannot obtain the stochastic trajectories from it, it becomes very difficult to produce accurate particle-based numerical simulations. In theoretical mathematics, this is the task of constructing a Markov process from its infinitesimal generator [184]. This is precisely the case of the continuous reversible diffusion-influenced reactions modeled with the back-reaction boundary condition from Eq. 3.16. The boundary condition obscures the underlying stochastic process and consequently complicates any particle-based simulation. This is the reason why we need a more transparent formulation as the one presented here, where the nature of the stochastic process is simple from the beginning. On the theoretical side, we have also noted that while Kurtz's theorem provides a rigorous and satisfying mathematical foundation, in probabilistic terms, for the LMA, the theory of hydrodynamic limit as the foundation of nonlinear partial differential equations of reaction-diffusion type is far from complete and still only accessible to experts [15, 80].

5.2.2 Bound/unbound states in bimolecular reactions

Chemical reactions are considered as discrete events. But at an atomic scale, in a bimolecular reaction like $A + B \rightleftharpoons C$, the very definition of a B that is bound (C state) or unbound to an A molecule is not unequivocal. This is particularly the case for diffusion-influenced reaction [203], which can yield significantly different quantitative descriptions due to different laboratory measurements. We give two such possibilities, both have been used in experiments that define C:

- **Distance**: FRET (Förster resonance energy transfer) method directly measures the distance between two optical markers that are attached on A and B respectively. Therefore, for this type of data, we say molecule B is bound to A if the distance between the two molecules is less or equal to σ. We call $r = \sigma$ the absorption or reaction boundary.

- **State**: Spectroscopic methods differentiate atomic structures of a particular chemical group inside a molecule. If an optically active chemical group (OACG) in B normally adopts a structure b but a very different structure b^* near A, then the spectroscopic signals become a definition for B versus C. Therefore, we say molecule B is bound to A if the OACG inside B is in the b^* state; the molecule is unbound if the OACG is in the b state. However, all atomic structures in a molecule fluctuate. In a stochastic setting, the group in B still has a finite probability of adopting the b^* structure, while

also having a non-zero probability of being in state b when very near A. Note in biochemistry, the biological function of a molecule is usually associated with the state of a chemical group within.

In a well-defined bimolecular reaction, the small probabilities of a B with its OACG in the b^* state, and a B bound to A with its OACG in the b state, are negligibly small. Therefore, the two definitions above are usually equivalent.

As a simple example, consider a molecule B diffusing in three dimensions with particle A fixed at the origin $r = 0$. Assume the intra-molecular potential is described by a Lennard-Jones potential. In this case, it is possible to choose the location of the absorption boundary in the separatrix of the effective potential, so the *state* and *distance* definition match each other, as shown in Fig. 5.1a. However, there are many other possibilities. For instance, in Fig. 5.1b, we chose the absorption boundary arbitrarily, so it is necessary to decide if B is bound to A when it crosses the absorption boundary (*distance*) or when it is close to the local minima of $U_{eff}(r)$ (*state*). In the latter case, it is not even clear the absorbing boundary can model the reaction accurately, so we have to ask the question: does it even make sense to have an absorbing boundary?

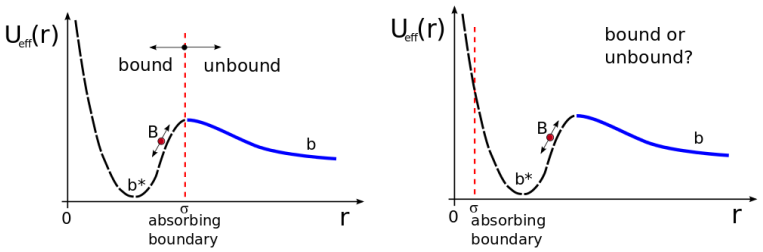

Figure 5.1: Plots of the effective interaction potential $U_{eff}(r) = V\left[\left(\frac{r_m}{r}\right)^{12} - 2\left(\frac{r_m}{r}\right)^{6}\right] - \ln 4\pi r^2$ that molecule B undergoes, where r is the inter-particle distance, V is the depth of the local minima and r_m the local minima position. The effective potential takes into account a Lennard-Jones potential and the three dimensional geometrical drift terms. The corresponding b^* and b states of the OACG are marked in the potential. The left plot (a) shows when the absorbing boundary location matches the expected behavior under the interaction potential. The plot on the right (b) shows an example that the absorbing boundary location can be chosen arbitrarily. In the latter case, it is not clear that the absorbing boundary models the reaction correctly.

The answer is: it depends on the physics one is trying to model. For instance, in the context of diffusion under an interaction potential, all irreversible reaction models need an absorbing boundary. Without it, there is always a nonzero probability of the full reverse reaction to occur. In this case, the choice of the boundary location cannot be completely

arbitrary; it needs to be chosen based on experimental data or obtained via more fundamental interactions, such as the Lennard-Jones interaction. One approach that could provide a solution would relate Kramers' theory [105, 141] applied to the diffusion under a Lennard-Jones potential with Smoluchowski's type models. A similar attempt has been studied before for a double well potential elsewhere [227].

In the case of reversible reactions, a similar reasoning can be applied, though the concept of absorbing boundary needs to be replaced by a reaction boundary. However, it is also possible to model reversible reactions without employing a reaction boundary at all. They can be modeled as a diffusion process under a bistable effective interaction potential, like the one shown in Figs. 5.1, where one state corresponds to B being bound and the other to B being unbound. As a matter of fact, any model that employs a reaction boundary should be fitted to this more general view of a reversible reaction. Although there has been some work in this direction [227], it is still not yet fully understood how to establish the connection between Kramers' theory applied to reversible unimolecular reaction [105, 141] and the theory of reversible bimolecular reaction mediated by diffusion.

A more complicated example is given in Fig. 5.2a, where the state of the OACG can oscillate stochastically independent of the distance r. In this case, the effective potential is much more complicated than just a Lennard-Jones potential. As a matter of fact, it is a potential landscape that can depend on more variables than just r. In this scenario, the state definition can be extended, at least conceptually, to very complicated potential landscapes that could even be stochastic and dynamic. For instance, in Fig. 5.2b, the two OACG states are given in terms of two Gibbs free energy potentials (G) as a function of the reaction coordinate q, like in Marcus theory of electron transfer [166]. In these cases, the state description could become completely detached from the distance description.

Following this analysis, we can say that describing a reversible bimolecular reaction solely through diffusion within its multivariate potential landscape is a more general approach, which corresponds to the *state* definition. Conversely, the models with a reaction boundary are an approximation to this more general description, which would correspond to the *distance* definition. This two definitions can be matched if the potential only depends on the inter-particle distance r, and we choose a distance close to the separatrix of the potential. It should be noted there is always the possibility that the potential corresponds to an external forcing, or that the absorbing/reacting boundary is actually modeling an absorbing membrane.

These results bring attention to the fact that reaction boundaries are in some sense "artificial". From a continuous mathematical point of view, a Brownian particle could cross a spatial boundary an infinite amount of times in a finite time, which provides a very non-intuitive description of what is physically happening at the reaction boundary and how to implement a discrete particle-based simulation. This is also intimately related to the issue of geminate recombinations, and it is partly the reason why particle-based modeling

of reaction boundaries is non-trivial. In order to do so, one needs to discretize continuous Brownian Motion into a random walk, then somehow provide a discrete model of the reaction boundary, such that in the continuous limit the ensemble average over many identical systems satisfies the continuous equation and the reaction boundary condition. One can come up with multiple ideas on how to do this, but providing one with mathematical rigor is not trivial [32], especially when the reaction boundaries are complex like in Eq. 3.16.

5.2.3 Geminate recombinations

Geminate recombinations occur when a particle B that just dissociated from a certain A, immediately associates again with it. They have been a subject of extensive research [4, 13, 135, 198, 199], and they are fundamental in providing accurate stochastic reaction-diffusion models and algorithms at cellular and sub-cellular level. They are also intimately related to the definition of bound and unbound we discussed in the previous subsection.

In order to gain a better physical insight, we can observe them in the context of irreversible reactions with partially absorbing boundaries and Kramers' theory [105, 141]. Consider three-dimensional diffusion of a B molecule under a double well potential $U^*_{eff}(r)$, like shown in Fig. 5.2c. Two models will be considered. The first one uses a fully absorbing boundary at the first well $r = \sigma_1$ and the second one a partially absorbing boundary at the second well $r = \sigma_2$. It has been shown that in the steady state the κ parameter of the partially absorbing boundary can be calculated using Kramers' theory, allowing the two models reaction rate to match each other [227]. This result shows that the partially absorbing boundary at $r = \sigma_2$ is equivalent to a fully absorbing one at $r = \sigma_1$ [1]. As we know from [28, 32, 101, 224], partially absorbing boundary conditions can be understood as a model for geminate recombinations. The picture just presented favors this view, since the partially absorbing boundary at σ_2 can effectively model the back and forth diffusion in the interval (σ_1,σ_2) before the reaction is finally completed. This back and forth diffusion is also represented by the rebinding diffusion process previously observed in Fig. 3.1, and it is what we understand as geminate recombinations.

The previous result states that our partially absorbing models of irreversible reactions do take into account geminate recombinations. However, there is still an absorbing boundary, so the dissociation process is not fully modeled. In order to do so, we need to introduce the back-reaction boundary condition at the reaction boundary, which is given by a partially absorbing boundary condition with the addition of the back-reaction term, as in Eq. 3.16. This model was first solved exactly in one dimension and later on in two and three dimensions [3, 136, 199]. However, the solution is not simple, and it's hard to grasp some physical

[1] The density profile of both approaches is expected to have at least the same shape, although they might integrate to a slightly different value due to small differences between the time-dependent rates of the two approaches.

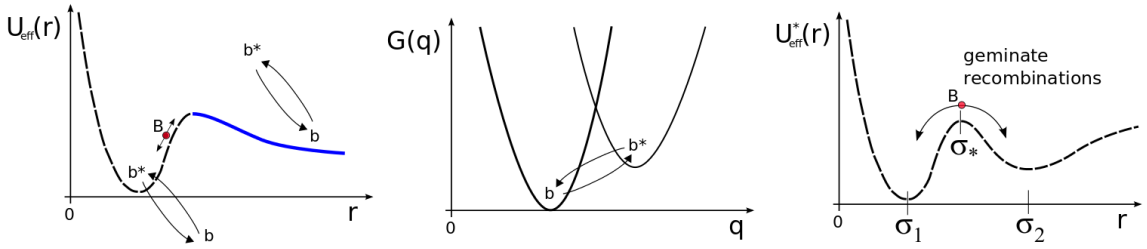

Figure 5.2: The left plot (a) is the same than Fig. 5.1 with the addition of stochastic oscillations of the OACG that are independent of r. The center plot (b) shows the Gibbs free energy potential for the two possible states of the B molecule as a function of the reaction coordinate. The right plot (c), shows how geminate recombinations can be interpreted in the context of diffusion under the interaction potential $U^*_{eff}(r)$, where r is the inter-particle distance. This effective potential takes into account a double well potential and the three dimensional geometrical drift terms.

intuition out of it. It is also based on a non-local boundary condition, and it is not clear, from a rigorous mathematical point of view, what is the corresponding stochastic process behind the partial differential equation (PDE) for the probability. This last issue is relevant because it doesn't allow us to accurately derive a particle-based stochastic simulation of the trajectories that in average will satisfy the probability described by the PDE. Algorithms like eGFRD [237] and FPKMC [63] are used to simulate reversible reactions using exact solutions for reactions between an isolated pair. However, they do not use solutions for the back-reaction boundary; they use the solution for the partially absorbing boundary and model the dissociation process with an exponential waiting time. It is not obvious nor trivial to show that these two approaches are equivalent.

The model presented in the next section bypasses these issues by framing the problem as a discrete Markov chain. Its Markovian nature allows simple and accurate particle-based simulations that obey the expected statistical behavior given by the KFE. The events occurring at the reaction boundary, including geminate recombinations, are intuitive and easily obtained from the jump probabilities. It also provides a robust and consistent stochastic description that can model reactions using a *distance* or *state* approach. In the continuous limit, it recovers the classical models along with the different boundary conditions. It also works as a unifying model since it shows other approaches to model reversible reactions like eGFRD and FPKMC are consistent with the stochastic trajectories of the PDE with the back-reaction boundary condition. It provides further validation for the continuous back-reaction model for diffusion-influenced reactions since the more intuitive discrete reversible reaction particle-based algorithm converges to it. The discrete model's robustness and particle-based simulations simplicity lie in its rigorous formulation as a discrete

stochastic process and its consequent intrinsic relation between the probability distribution dynamics and its individual stochastic trajectories.

5.3 Stochastic model for reversible diffusion-influenced reactions

The main idea is to create an intuitive Markov jump process, that can be interpreted as a discretization of Eq. 3.15a that conserves probability. The reaction process at the reaction boundaries is intuitively modeled adding association and/or dissociation jump probabilities. On the continuous limit, the continuous equation and the different boundary conditions are recovered, specifically providing additional validation for Eq. 5.22. As it is a discrete time and space stochastic model (Markov chain), it is easy to implement a numerical simulation for the probability mass function as well as a particle based simulation for the individual stochastic trajectories of the reaction process. We will begin by deriving the framework of the model with a radial random walk, and we will add complexity as we recover the different classical diffusion-influenced reaction models. It should be noted that in all the next models we can take the limit $dt \to 0$ to obtain a master equation and use a variant of the Gillespie Algorithm to solve it numerically. However, we believe the discrete time approach is educational since it provides a clear connection between the parameters in diffusion-influenced theory and their probabilistic meaning in particle-based simulations, see Eqs. 3.22 in Section 3.3.

5.3.1 Radial random walk with spherical symmetry

We would like to construct a random walk with spherical symmetry that recovers the Brownian motion diffusion equation in the continuous limit. We will start by considering a particle following a random walk in spherical coordinates. We will only be interested in the jumps between different spherical shells in the r direction separated a distance δ_r and not along the angular directions. If the particle is in shell i with radius $r_i = \sigma + i\delta r$ and σ a constant, the probabilities to jump to the smaller and bigger shells are p_i and q_i respectively. The process is partially illustrated in Fig. 5.3.

We can write this process as a discrete time Markov chain. Let the position in the radial direction be denoted by $\mathcal{R}_t$, a random variable for every given t constituting a discrete state and time stochastic process. We will call $\pi_i^t = \Pr[\mathcal{R}_t = r_i]$ the probability of being at spherical shell i at time t. The state of the whole system at time t is given by the vector of all states $\boldsymbol{\pi}^t = [\pi_0^t, \pi_1^t, \cdots, \pi_i^t, \cdots]$. The dynamics of our random walk are given in terms of the stochastic matrix $\mathbb{P}$ and the Kolmogorov forward equation,

$$\boldsymbol{\pi}^{t+1} = \boldsymbol{\pi}^t \mathbb{P}. \tag{5.5}$$

Note the stochastic matrix should depend on the probabilities p_i and q_i. The resulting

stochastic matrix is

$$\mathbb{P} = \begin{bmatrix} 1-q_0 & q_0 & 0 & \cdots & \cdots \\ p_1 & 1-(p_1+q_1) & q_1 & 0 & \\ \vdots & & \ddots & & \\ & 0 & p_i & 1-(p_i+q_i) & q_i & \cdots \\ \vdots & & & \vdots & \ddots & \end{bmatrix} \tag{5.6}$$

Note the rows sum to one as expected. For practical purposes, the matrix can be truncated using a finite number of shells N. In all theses models, we will assume no-flux boundary conditions in the outermost shell, unless stated otherwise. In order to recover Brownian diffusion, we need to adjust the jump probabilities in the random walk in spherical coordinates with

$$p_i = \delta t \left(\frac{D}{\delta r^2} - \frac{D}{r_{i-1}\delta r} \right), \qquad q_i = \delta t \left(\frac{D}{\delta r^2} + \frac{D}{r_{i+1}\delta r} \right), \tag{5.7}$$

where D is the constant diffusion coefficient. Note the probability of staying in the shell i given by $1-(p_i+q_i)$ grows approaching $1-2\delta t D/\delta r^2$ as r_i is increased. Using these values we can rewrite the i^{th} equation of (5.5) as,

$$\pi_i^{t+1} = \pi_i^t + \delta t D \left[\frac{\pi_{i-1}^t - 2\pi_i^t + \pi_{i+1}^t}{\delta r^2} \right] - \delta t \frac{2D}{r_i} \left[\frac{\pi_{i+1}^t - \pi_{i-1}^t}{2\delta r} \right] + \delta t \frac{D}{\delta r} \left[\frac{\pi_i^t}{r_i - \delta r} - \frac{\pi_i^t}{r_i + \delta r} \right].$$

We would like to recover a continuous equation for the probability. The discrete probability π_i^t is related to the continuous probability distribution function $\Pi(r_i,t)$ by $\pi_i^t = \Pi(r_i,t)\delta r$, so we need to divide π_k^t by δr for all k first. However this doesn't make any difference in structure of the equation, so now we can take the limit as $\delta_t \to 0$ and $\delta_r \to 0$ following standard finite difference theory [156], which yields second order accuracy in space and first order in time. We obtain,

$$\frac{\partial \Pi(r,t)}{\partial t} = D\frac{\partial^2 \Pi(r,t)}{\partial r^2} - \frac{2D}{r}\frac{\partial \Pi(r,t)}{\partial r} + \frac{2D}{r^2}\Pi(r,t), \tag{5.8}$$

where $\Pi(r,t)$ is a probability distirbution function in r. This equation can be written in the form of a Fokker Planck equation with drift,

$$\frac{\partial \Pi(r,t)}{\partial t} = D\frac{\partial^2 \Pi(r,t)}{\partial r^2} - \frac{\partial}{\partial r}\left(\frac{2D}{r}\Pi(r,t) \right). \tag{5.9}$$

The probability of being a distance r from the origin at time t is $\Pr\{r < \tilde{\mathcal{R}}_t \leq r + \delta r\} = \Pi(r,t)dr$, where $\tilde{\mathcal{R}}_t$ is now a stochastic process with continuous state and time. However, this is the probability of being at any point in the sphere with radius r, so we cannot yet compare

it with the Smoluchowski diffusion equation. In order to do so, we need the equation for the probability of being at any point in space given by $f(r,\theta,\phi,t)r^2\sin(\theta)drd\theta d\phi$. Integrating this equation in the angular coordinates yield the probability $\Pi(r,t)$. As we have spherical symmetry in f, this yields

$$\Pi(r,t)dr = 4\pi r^2 f(r,t)dr. \tag{5.10}$$

Substituting this result into Eq. 5.9 and doing some algebra, we recover the Smoluchowski equation (Eq. 3.11a) for constant D as expected,

$$\frac{\partial f(r,t)}{\partial t} = \frac{D}{r^2}\frac{\partial}{\partial r}\left(r^2\frac{\partial f(r,t)}{\partial r}\right) = \nabla\cdot[D\nabla f(r,t)], \tag{5.11}$$

where ∇ operates in spherical coordinates with symmetry in the polar and azimuthal angle; therefore, the discrete time Markov chain models the discrete analog to overdamped Brownian motion in spherical coordinates. However, we haven't yet discussed the continuous limit in the discrete boundary of the innermost shell r_0. We can also write the first equation of (5.5) as,

$${\pi_0}^{t+1} = \pi_0^t + \delta t D\left[\frac{\pi_1^t - \pi_0^t}{\delta r^2}\right] - \delta t\left[\frac{D}{r_0}\frac{\pi_1^t}{\delta r} + \frac{D}{\delta r}\left(\frac{\pi_0^t}{r_0+\delta r}\right)\right].$$

In order to find what boundary condition this discretization satisfies, we will follow standard finite difference techniques [156]. We will introduce the ghost cell π_{-1}^t, so we can rewrite this equation as,

$${\pi_0}^{t+1} = \pi_0^t + \delta t D\left[\frac{\pi_1^t - 2\pi_0^t + \pi_{-1}^t}{\delta r^2}\right] - \delta t\frac{2D}{r_0}\left[\frac{\pi_1^t - \pi_{-1}^t}{2\delta r}\right] + \delta t\frac{D}{\delta r}\left[\frac{\pi_0^t}{r_0-\delta r} - \frac{\pi_0^t}{r_0+\delta r}\right],$$

where

$$\pi_{-1}^t = \pi_0^t\frac{\left(\frac{1}{\delta r} - \frac{1}{r_{-1}}\right)}{\left(\frac{1}{r_0} + \frac{1}{\delta r}\right)}. \tag{5.12}$$

Dividing by δr and taking the limit $\delta_t \to 0$, $\delta_r \to 0$, we again recover Eq. 5.8 with second order accuracy in space and Eq. 5.12 becomes the zero flux condition for the Fokker-Planck

equation (see Section 5.4.1),

$$\left.\frac{\partial \Pi(r,t)}{\partial r}\right|_{r=r_0} = \frac{2\Pi(r_0,t)}{r_0}.$$

Using this result and employing Eq. 5.10, the reflective boundary condition for Eq. 5.11 can be rewritten as $\left.\frac{\partial f(r,t)}{\partial r}\right|_{r=r_0} = 0$, as expected. Note we $r_0 - \delta r > 0$. Unless stated otherwise, in this and all of the subsequent models we will also employ a zero flux boundary on the outermost spherical shell $r = r_{max}$. As we have an irreducible and aperiodic Markov chain with a finite number of states, we know it has a steady state. Moreover, as the flux is zero on both boundaries, the detailed balance condition must be satisfied everywhere. Detailed balance will be mentioned in more detail on Section 5.3.4. In order to recover the Smoluchowski diffusion equation (Eq. 3.11a) in the whole space, we can take the limit as $r_0 \to 0$ and $r_{max} \to \infty$.

It should be noted that the limit $\delta_t \to 0$, $\delta_r \to 0$ will only guarantee our discretization is consistent with the continuous model. In order for the method to be convergent in the finite difference sense, we also need to satisfy a CFL condition that we can obtain through stability analysis [156]. However, this discretization is also a Markov chain, so we can also obtain a stability condition by making sure that all the rows of the matrix from Eq. 5.6 sum to one and that all the entries are in the interval $[0, 1]$. This analysis yields the condition that $\frac{\Delta t}{\Delta r^2} < \frac{1}{2D}$, which happens to be the same as the CFL condition for the one-dimensional diffusion equation. When we add more complexity in the next sections, like boundary reaction terms and potentials, we need to be careful that our matrix still satisfies these Markov conditions.

On the discrete model, we can also write the diffusion coefficient in terms of the jump probabilities by summing up Eqs. 5.7 to yield Einstein's relation,

$$D = \frac{\delta r^2}{2\delta t}(p_{i+1} + q_{i-1}). \tag{5.13}$$

This is a more general expression than the obtained in random walks on Cartesian coordinates. On a Cartesian random walk, if the probability of staying in the same spot is zero, we obtain $p_{i+1} + q_{i-1} = 1, 1/2, 1/3$, in one, two and three dimensions respectively, recovering the well known expression $D = \delta r^2/(2n\delta t)$ with n the number of dimensions.

In the next section, we will use this spherical random walk to construct a discrete model for irreversible diffusion-influenced reactions.

5.3.2 Discrete model for irreversible diffusion-influenced reactions

The random walk derived in the previous model does not yet include any reaction. In order to study the reaction $A + B \to C$, consider again a particle B diffusing under the spherical symmetric random walk in the previous section. In addition, there will be a particle A fixed

at the origin. If we define the shell $r_0 = \sigma$ as the reaction boundary or the binding radius, then we can incorporate the probability of a reaction $P_b = \tilde{\kappa}(r)\delta t$. An illustrated description of the process is shown in Fig. (5.3), and a detailed one-dimensional symmetric version of this model is presented in Section 3.3. The stochastic matrix will now look like

$$\mathbb{P} = \begin{bmatrix} 1-(q_0+P_b) & q_0 & 0 & \cdots & \\ p_1 & 1-(p_1+q_1) & q_1 & 0 & \\ \vdots & & \ddots & & \\ & 0 & p_i & 1-(p_i+q_i) & q_i \\ & & & \vdots & \ddots \end{bmatrix}. \tag{5.14}$$

Note the first row doesn't sum up to one, since there is a probability of being absorbed, P_b. In order to recover the total probability, we need to sum this probability to the first row of the stochastic matrix. Furthermore, the association rate $\tilde{\kappa}(r)$ will scale depending on where we chose our reaction boundary to be. A physically reasonable assumption is that the rate $\tilde{\kappa}(r)$ scales inversely to the infinitesimal volume of the reaction spherical shell, $\tilde{\kappa}(r) = \kappa/(4\pi r^2\delta_r)$, where κ is the constant rate in the boundary condition of Eq. 3.16 and has units of volume over time. The bigger the shell, the smaller we need $\tilde{\kappa}(r)$ to be in order to keep the model consistent. Furthermore, note the probability of being absorbed at shell $r_0 = \sigma$ is $P_b = \tilde{\kappa}(r_0)\delta t$, so we can solve for κ to obtain $\kappa = 4\pi\sigma^2 P_b \delta r/\delta t$. This equation, along with Eq. 5.13, provide the diffusion-influenced theory parameters D and κ in terms of the jump probabilities. As shown in Section 3.3, the probability of being absorbed could be replaced by a more accurate value $P_b = 1 - e^{-\tilde{\kappa}(r_0)\delta t}$, in which case $\kappa = -4\pi\sigma^2\delta r \log[1-P_b]/\delta t$. However, this is not relevant in the continuous limit analysis we will now carry out.

Employing this stochastic matrix on the system (5.5) yields the same result as in the spherical random walk except for the first equation in the boundary r_0 which yields,

$$\pi_0{}^{t+1} = \pi_0^t + \frac{\delta t D}{\delta r^2}\left[\pi_1^t - 2\pi_0^t + \pi_0^t\left(1 - \frac{\delta r^2}{D}\frac{\kappa}{4\pi r_0^2 \delta r}\right)\right] - \delta t\left[\frac{D}{r_0}\frac{\pi_1^t}{\delta r} + \frac{D}{\delta r}\left(\frac{\pi_0^t}{r_0+\delta r}\right)\right].$$

$$\Rightarrow \quad \pi_0{}^{t+1} = \pi_0^t + \delta t D\left[\frac{\pi_1^t - 2\pi_0^t + \pi_{-1}^t}{\delta r^2}\right] - \delta t\frac{2D}{r_0}\left[\frac{\pi_1^t - \pi_{-1}^t}{2\delta r}\right] + \delta t\frac{D}{\delta r}\left[\frac{\pi_0^t}{r_0-\delta r} - \frac{\pi_0^t}{r_0+\delta r}\right],$$

where π_{-1}^t satisfies

$$\pi_0^t - \frac{\delta r\kappa}{4\pi D r_0^2}\pi_0^t = \pi_{-1}^t + \delta r\frac{\pi_0^t}{r_{-1}} + \delta r\frac{\pi_{-1}^t}{r_0} \tag{5.15}$$

Dividing by δr and taking the limit as $\delta_t \to 0$, $\delta_r \to 0$ again satisfies the Fokker-Planck

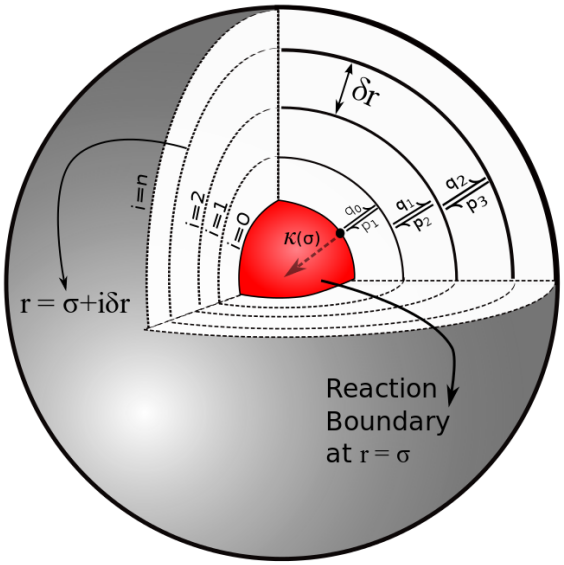

Figure 5.3: Concentric shells for the discrete model for irreversible diffusion-influenced reactions. This figures illustrates a random walk in spherical coordinates and the reaction occurring at the reaction boundary at shell $i = 0$.

equation (Eq. 5.9) with second order accuracy in space; however, Eq. 5.15 now becomes

$$\left.\frac{\partial \Pi(r,t)}{\partial r}\right|_{r=\sigma} = \frac{\kappa}{4\pi\sigma^2 D}\Pi(\sigma,t) + \frac{2\Pi(\sigma,t)}{\sigma}$$

with first order accuracy, where $\Pi(r,t)$ is the continuous analog of π_i^t. Employing once again the change of variables in Eq. 5.10, we recover the well known boundary condition of Collins and Kimball (see Eq. 3.12),

$$4\pi\sigma^2 D \left.\frac{\partial f(r,t)}{\partial r}\right|_{r=\sigma} = \kappa f(\sigma,t).$$

We would like to provide a comparison between Collins and Kimball solution (Eq. 3.13) and our Markov approach; however, our equations model the dynamics for the probability mass function and Collins and Kimball models the concentration gradient. A possible probabilistic interpretation of Collins and Kimball model is given by the Green,s function for an isolated pair, like in the GFRD approach [231, 257, 256]; however, the steady state will yield zero. The main difficulty in providing a better probabilistic interpretation is the far-field boundary condition with constant value at infinity. In order to address this issue, we will take an alternate approach to compare the steady state solution. We will solve the

Fokker-Planck equation (Eq. 3.11a) with the boundary conditions,

$$4\pi\sigma^2 D\frac{\partial f(r,t)}{\partial r}\bigg|_{r=\sigma} = 4\pi R^2 D\frac{\partial f(r,t)}{\partial r}\bigg|_{r=R} = \kappa f(\sigma,t), \tag{5.16}$$

and $\int_\sigma^R 4\pi r^2 f(r,t)dr = 1$. These conditions mean that the probability flux at $r=\sigma$ is the same as the flux at $r=R$, which is, from a probabilistic point of view, a periodic boundary condition. The steady state solution is exactly of the same form as Eq. 3.13, but with a fixed constant $c_0 = A_0$,

$$f_{ss}(r) = A_0\left[1-\frac{\kappa\sigma}{4\pi D\sigma+\kappa}\left(\frac{1}{r}\right)\right], \tag{5.17}$$

$$A_0 = \left[4\pi\left(\frac{R^3-\sigma^3}{3}\right)-\frac{4\pi\sigma\kappa}{4\pi\sigma D+\kappa}\left(\frac{R^2-\sigma^2}{2}\right)\right]^{-1}. \tag{5.18}$$

This result provides a mathematical connection with the original gradient concentration approach and the probability approach. As a matter of fact, from a mathematical point of view, the boundary condition in Eq. 5.16 is also satisfied in the original Collins & Kimball formulation at steady state. In the probabilistic interpretation, the free parameter A_0 will give the normalization constant for the probability. In this case, we fixed it so the probability integrates to one. Nonetheless, we could have chosen it to integrate to any other value between 0 and 1. For instance, if we want the probability to integrate to 0.7, we can obtain the corresponding value of A_0. In the concentration interpretation and scaled accordingly, this value will correspond to the concentration of the material/chemical bath in the far-field in order to get 30% of absorbtion before reaching the steady state. For our current comparison and without loss of generality, we chose it so the probability integrates to one. Although this might seem odd given we have an absorbing boundary condition, the far-field boundary condition is a source compensates for the absorption.

In order to do the comparison, we modify the stochastic matrix (5.14) in our Markov model to model this periodicity by adding a $\tilde{\kappa}(\sigma)\delta t$ term in the last column and first row of the truncated stochastic matrix. We can compute the probability mass function from the Markov chain at time $t = n\delta t$ with $\boldsymbol{\pi}^n = \boldsymbol{\pi}^0\mathbb{P}^n$ until reaching the steady state $\boldsymbol{\pi}^{ss} = \boldsymbol{\pi}^{ss}\mathbb{P}$, and we can also do a particle based simulation using the jump probabilities. A comparison of the three approaches for uniform initial distributions is shown in Figure 5.4. The quantity plotted in this and every other figure in this section is $\pi_i^t/(4\pi r_i^2\delta r)$, which uses the first order equation that the probability between the point-continuous and spherical-discrete setting is $\pi_i^t = 4\pi r_i^2 f(r_i,t)\delta r$. Note the agreement between the ensemble behavior of stochastic trajectories and the probability mass function is expected from the stochastic theory. This stochastic formulation of our model is what allows trivial particle-based simulations that accurately match the expected statistical behavior given by probability mass function dynamics. It

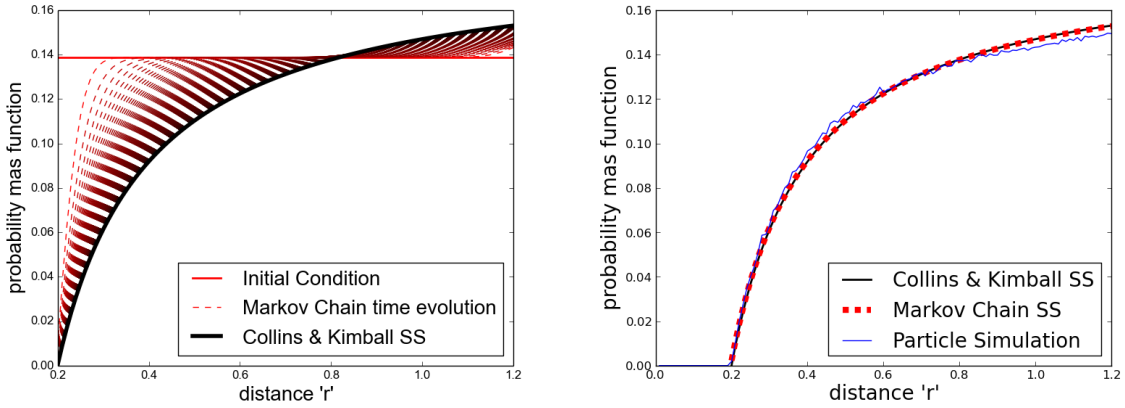

Figure 5.4: Model verification: (a) The steady state of Collins and Kimball's solution of Eq. 3.13 (or Eq. 6.8) with $c_0 = A_0$ from Eq. 5.18 is plotted with a thick black line. The initial condition (uniform distribution) for the discrete Markov model is plotted as an horizontal red line. The dashed lines represent the convergence in time to the steady state of the Markov chain from $t = 0$ to $t = 1$ taken every 100 time steps; the darker lines correspond to longer times. (b) The steady state of the periodic solution to Collins and Kimball (Eq. 6.8) is compared to the Markov chain steady state and to a particle based simulation with 3E6 particles and 1E4 time iterations. The parameters used were: $\delta r = 0.01$, $\delta t = 0.0001$, $D = 0.1$, $\tilde{\kappa}(\sigma) = 4000.0$, $\sigma = 0.2$, and 100 shells for the discrete models.

should also be noted this is an open system in non-equilibrium steady state (NESS) driven by the flux from the sink and source at the inner and outer boundary, so it will not satisfy detailed balance [204].

In order to provide an even more complete connection to the meaning of the Collins and Kimball rate in the discrete model, consider a particle in the shell in the reaction boundary $r_0 = \sigma$. The particle has three possible movements: it can diffuse to level $i = 1$ with probability $q_0 \approx \delta t D/\delta r^2$ (first order); it can react with probability $\tilde{\kappa}(\sigma)\delta_t$; or it can diffuse along the spherical shell with probability ξ. Lets assume that if the particle diffuses out to shell $n = 1$ then the particle is fully dissociated without any geminate recombinations; therefore, the probability of reaction while diffusing in the shell r_0 is given by

$$\phi = \tilde{\kappa}(\sigma)\delta_t \sum_{n=0}^{\infty} \xi^n = \frac{\tilde{\kappa}(\sigma)\delta_t}{1-\xi} = \frac{\tilde{\kappa}(\sigma)\delta_t}{\tilde{\kappa}(\sigma)\delta_t + \delta t D/\delta r^2}$$

where we used that $1 = \xi + \tilde{\kappa}(\sigma)\delta_t + q_0$. As we already obtained that $\tilde{\kappa}(r) = \kappa/(4\pi r^2 \delta_r)$, we

can substitute $\tilde{\kappa}(\sigma)$, which yields

$$\phi = \frac{\kappa}{4\pi\sigma^2 D/\delta_r + \kappa}.$$

This is the discrete approximation of the fraction of reactions due to geminations of the Collins and Kimball reaction rate [13, 28, 224]. Its continuous counterpart is shown in Eq. 3.19 and Eq. 3.20. Note we do not expect convergence as $\delta r \to 0$, since this approximate derivation will no longer make sense from a continuous perspective. Nonetheless, it provides a clear physical picture of how the gemination process work.

5.3.3 Extension to reversible diffusion-influenced reactions

In this section, we will extend the previous model to deal with reversible reactions. We will begin by adding one more state π_b^t at the beginning of the state vector: $\boldsymbol{\pi}^t = [\pi_b^t, \pi_0^t, \pi_1^t, \cdots, \pi_i^t, \cdots]$. This new state means the probability of the B molecule to be bound to A. The stochastic matrix will naturally require an additional first row and column

$$\mathbb{P} = \begin{bmatrix} 1-P_u & P_u & 0 & 0 & \cdots \\ P_b & 1-(q_0+P_b) & q_0 & 0 & \cdots \\ 0 & p_1 & 1-(p_1+q_1) & q_1 & \cdots \\ \vdots & & & \ddots & \end{bmatrix}, \tag{5.19}$$

where $P_b = \tilde{\kappa}(r)\delta t$ and $P_u = \tilde{\mu}(r_0)\delta t$ is the probability for dissociation to occur at the corresponding shell. The dissociation parameter $\tilde{\mu}(r)$ is trivially related to the constant dissociation rate μ in Eq. 3.16 by $\tilde{\mu}(r) = \mu$ with units of time^{-1}. Once again P_b and P_u could be replaced with more accurate exponential expressions, see Section 3.3.

Note that now all the rows of the stochastic matrix sum to zero since we are taking into account the particles that have already reacted. Also note π_b^t is the probability of B being bound to A, so it can be written as $\pi_b^t = [1 - S_d(t)]$, where $S_d(t) = \sum_{i=0}^{N} \pi_i^t$ is the probability of being unbound at time t. The first equation now yields,

$$\pi_b^{t+1} = \pi_b^t \left[1 - \tilde{\mu}(r_0)\delta t\right] + \pi_0^t \tilde{\kappa}(r_0)\delta t.$$

Dividing by δr and taking the limit, we can arrange the left hand side to yield $\Pi_b(t) \approx (\pi_b^{t+1} - \pi_b^t)/\delta t$. On the right hand side it might seem this equation might not converge, since $\tilde{\kappa}(r_0)$ scale as $1/\delta r$. However, using Eq. 5.10 we know $\pi_0^t = 4\pi r^2 f(r_0, t)\delta r$ at first order, so in the limit we immediately obtain,

$$\frac{df_b(t)}{dt} = \kappa f(r_0, t) - \mu f_b(t), \tag{5.20}$$

where $f_b(t) = \Pi_b(t)$, so μ has units of time^{-1} and κ of volume over time as expected. This

equation only involves reaction, since we didn't allow any diffusion to happen when B is in the bound state. The second equation will yield even more interesting results, the equation is

$$\pi_0^{t+1} = \pi_0^t + \frac{\delta t D}{\delta r^2}\left[\pi_1^t - 2\pi_0^t + \pi_0^t\left(1 - \frac{\delta r^2}{D}\frac{\kappa}{4\pi r_0^2 \delta r}\right)\right] - \delta t\left[\frac{D}{r_0}\frac{\pi_1^t}{\delta r} + \frac{D}{\delta r}\left(\frac{\pi_0^t}{r_0 + \delta r}\right)\right] + \delta t \mu \pi_b^t.$$

$$\Rightarrow \quad \pi_0^{t+1} = \pi_0^t + \delta t D\left[\frac{\pi_1^t - 2\pi_0^t + \pi_{-1}^t}{\delta r^2}\right] - \delta t \frac{2D}{r_0}\left[\frac{\pi_1^t - \pi_{-1}^t}{2\delta r}\right] + \delta t \frac{D}{\delta r}\left[\frac{\pi_0^t}{r_0 - \delta r} - \frac{\pi_0^t}{r_0 + \delta r}\right],$$

where π_{-1}^t satisfies

$$\pi_0^t - \frac{\delta r \kappa}{4\pi D r_0^2}\pi_0^t + \mu\frac{\delta r^2}{D}\pi_b^t = \pi_{-1}^t + \delta r \frac{\pi_0^t}{r_{-1}} + \delta r \frac{\pi_{-1}^t}{r_0}. \tag{5.21}$$

Dividing by δr and taking the limit as $\delta_t \to 0$, $\delta_r \to 0$ again satisfies the Fokker-Planck equation (Eq. 5.9). For Eq. 5.21, we use again Eq. 5.10 and the fact that $\pi_i^t = 4\pi r^2 f(r_i, t)\delta r$ at first order to obtain

$$4\pi\sigma^2 D \left.\frac{\partial f(r,t)}{\partial r}\right|_{r=\sigma} = \kappa f(\sigma, t) - \mu f_b(t),$$

where $f_b(t) = \Pi_b(t)$ and $\sigma = r_0$. Now note that $f_b(t) = [1 - S(t)]$, where $S(t) = \int_\sigma^\infty 4\pi r^2 f(r,t) dr$ is the probability of being unbound, i.e. the continuous version of $S_d(t)$, so we can write

$$4\pi\sigma^2 D \left.\frac{\partial f(r,t)}{\partial r}\right|_{r=\sigma} = \kappa f(\sigma, t) - \mu[1 - S(t)], \tag{5.22}$$

This is the back-reaction boundary condition (Eq. 3.16) found in the exact solution for the reversible reaction [3, 136, 199]. Note this boundary condition couples the Fokker-Planck equation (Eq. 5.9) with the Eq. 5.20. The probability of being unbound can be represented in terms of the integral from Eq. 3.17, which yields a non-local boundary condition and sheds light in the fact that some non-local boundary conditions might be only a condensed technique to write complicated coupled systems. The time evolution of the probability mass function given by our Markov approach is shown for two set of parameters in Figure 5.5. The initial condition is given as uniform for the unbound state and zero for the bound one. The probability is conserved following,

$$\pi_b^t + \sum_{i=0}^{N} \pi_i^t = 1,$$

for all times t, where π_i^t is equal to $4\pi r_i^2 f(r_i, t)\delta r$ at first order, and π_b is the probability of

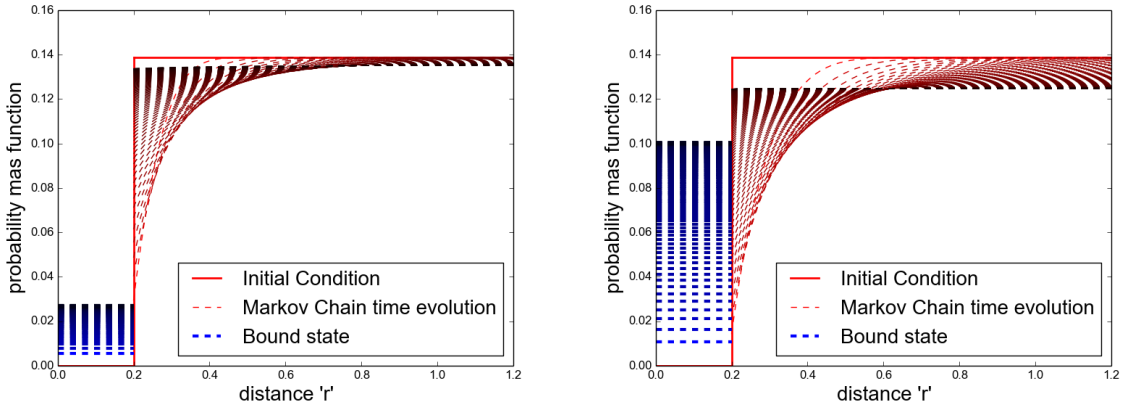

Figure 5.5: Convergence of the discrete model to steady state for the reversible case for two sets of parameters. The initial condition is a uniform distribution in the unbound state and zero on the bound state, and it is plotted as a red line. The dashed lines represent the convergence in time to the steady state of the Markov chain from $t = 0$ to $t = 1$ taken every 400 and 1000 time steps respectively; the darker lines correspond to longer times. (a) Parameters used were: $\delta r = 0.01$, $\delta t = 0.0001$, $D = 0.1$, $\tilde{\kappa}(\sigma) = 8000.0$, $\mu = 200$ $\sigma = 0.2$, and 100 shells. The bound state π_b value at different time steps is shown as an horizontal line from $r = [0, \sigma]$ (b) Same parameters with rates exaggerated to better show the convergence to the steady state.

being bound—its value is represented by the height of the blue dashed bar on the plots in Figure 5.5. On both plots we can observe convergence towards a flat steady state. As we included the bound state as part of the irreducible and aperiodic Markov chain as well as no-flux boundaires elsewhere, the system is closed and has a steady state, so detailed balance must be satisifed. The probability lost in the unbound region is balanced by the probability gained in the bound one. Since the model is a Markov chain, particle-based simulation of this discrete stochastic reversible diffusion-influenced model is trivial by employing the jump probabilities.

Note the continuous limit we just derived of the discrete model provides a more simple form of the model than the original back-reaction continuous model as two coupled partial/ordinary differential equations,

$$\frac{df_b(t)}{dt} = \kappa f(r_0, t) - \mu f_b(t), \tag{5.23}$$

$$\frac{\partial f(r,t)}{\partial t} = \nabla \cdot [D(r) \nabla f(r,t)] \tag{5.24}$$

with the back-reaction boundary condition

$$4\pi\sigma^2 D \left.\frac{\partial f(r,t)}{\partial r}\right|_{r=\sigma} = \kappa f(\sigma,t) - \underbrace{\mu f_b(t)}_{\mu[1-S(t|r_0)]} . \tag{5.25}$$

Although this equation can be derived from the original model, we recovered it naturally from the discrete model limit. As the association and dissociation were intuitively implemented in the discrete model, its convergence to the original continuous model, provides additional validation that it is appropriate to model reversible bimolecular reactions via diffusion encounter. It should be mentioned a similar model was developed using a Master Equation to derive modified reaction rates for simulations of the reaction diffusion master equation (RDME) [77]. Nonetheless, the methodology follows a different logic; they assume the reaction rate in the Master Equation as unknown, and they use the continuous theory to derive an appropriate rate for some specific discretization. In our work, we chose fixed reaction probability, and we showed the condition under which this recovers the continuous theory. We also provide the parameters of the continuous model in terms of the discrete probabilities, which provides insight into the meaning of these quantities. In addition, the relation we obtained between the rate and the discretization parameters is simpler, and they don't extend their model to the cases discussed in the following Sections.

5.3.4 The unbinding radius

In the previous model with reversible reaction, we assumed the B particles are associated and dissociated in the same reaction shell corresponding to $r = \sigma$. However, the probability of reacting/dissociating can be distributed along different spatial points and not only on a specific boundary. In the stochastic matrix (5.19), the term P_u can be placed in any of the columns in the first row. For instance, if this term is collocated in the n^{th} column of the matrix, when the B molecule is dissociated, it would be placed in the sphere $i = n$ with unbinding radius $\sigma_u = \sigma + n\delta r$ (see Figure 5.3). The binding process occurs in the boundary $i = 0$ with $r = \sigma$, so we could say there is a binding radius $r = \sigma$ and an unbinding radius at $r = \sigma_u$. A new question now arises: if we consider an ensemble of these systems at thermodynamic equilibrium, is detailed balance satisfied?

Detailed balance tells us that in a chemical kinetic system at equilibrium every elementary reaction is balanced by its reverse reaction $\pi_i P_{i\to j} = \pi_j P_{j\to i}$ [158], where $P_{a\to b}$ is the transition probability from state a to b. At equilibrium, detailed balanced will not be satisfied inside the shells $i = 0$ and $i = n$ since we have an open system with a source and a skin. In these shells, we actually observe a NESS, like the one from Section 5.3.2. Nonetheless, we scaled the unbinding rate so the net flux coming out of shell $i = n$ is zero, so detailed balance will be satisfied everywhere else between shell $i = n$ and the outermost shell. This might seem at first confusing since detailed balance is based on chemical kinetics; however, the concept

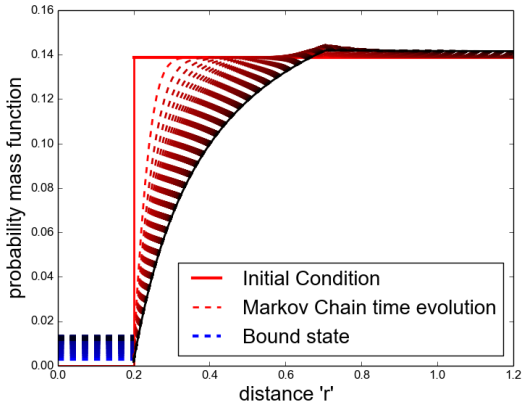

Figure 5.6: Convergence of the discrete model to its steady state for the reversible case with an unbinding radius. The initial condition is a uniform distribution in the unbound state and zero on the bound state, and it is plotted as a red line. The dashed lines represent the convergence in time to the steady state of the Markov chain from $t = 0$ to $t = 1$ taken every 100 time steps; the darker lines correspond to longer times. (a) Parameters used were: $\delta r = 0.01$, $\delta t = 0.0001$, $D = 0.1$, $\tilde{\kappa}(\sigma) = 6000.0$, $\mu = 50$, $\sigma = 0.2$, $\sigma_u = 0.7$, and 100 shells. The bound state π_b value at different time steps is shown as an horizontal dashed line from $r = [0, \sigma]$. The final steady state is emphasized as a black continuous curve; as the slope from the right of $r = \sigma_u$ is zero, we know the net flux for $r > \sigma_u$ is zero, as expected. Detailed balance is not satisfied between $r = \sigma$ and $r = \sigma_u$

can be easily extended to diffusion and random walks. As we know that as long as there are no flux conditions in the boundaries of a system in steady state, detailed balance must be satisfied everywhere. As there is no flux condition at shell $i = n$ and at infinity (or at the outermost shell), detailed balance is satisfied between those two boundaries. This is indeed the reason why the particle-based stochastic reaction-diffusion algorithms that introduce an unbinding radius work. Introducing the unbinding radius sacrifices accuracy in the local region around $r = \sigma$, but it allows fast and accurate simulations [13, 56] on slightly larger scales. In Figure 5.6, we can observe the time convergence of the probability mass function to the steady stated for this case. In contrast with Figure 5.5, we can see between $r = \sigma$ and $r = \sigma_u$ the solution has non-zero flux; this is the region where detailed balance will not be satisfied. However, the solution will be accurate everywhere else, where detailed balance is satisfied.

5.3.5 Radial random walk under a force-field

Assuming the random walk is symmetric and influenced by a smooth interaction potential $U(r)$, we can modify the original transition probabilities in Eq. 5.7 by including the interaction potential term as

$$\begin{aligned} p_i &= \delta t \left(\frac{D}{\delta r^2} - \frac{D}{r_{i-1}\delta r} + \frac{\beta D}{4\delta r^2} \left[U_{i+1} - U_{i-1} \right] \right), \\ q_i &= \delta t \left(\frac{D}{\delta r^2} + \frac{D}{r_{i+1}\delta r} - \frac{\beta D}{4\delta r^2} \left[U_{i+1} - U_{i-1} \right] \right), \end{aligned} \tag{5.26}$$

where $\beta = 1/k_B T$, with k_B the Boltzmann constant and T the temperature. With these new values of p_i and q_i in the matrix 5.14, we can rewrite the i^{th} equation of (5.5) as,

$$\begin{aligned} {\pi_i}^{t+1} = \pi_i^t &+ \delta t D \left[\frac{\pi_{i-1}^t - 2\pi_i^t + \pi_{i+1}^t}{\delta r^2} \right] - \delta t \frac{2D}{r_i} \left[\frac{\pi_{i+1}^t - \pi_{i-1}^t}{2\delta r} \right] \\ &+ \delta t \frac{D}{\delta r} \left[\frac{\pi_i^t}{r_i - \delta r} - \frac{\pi_i^t}{r_i + \delta r} \right] + \delta t \frac{\beta D}{2\delta r} \left[\pi_{i+1}^t \left(\frac{U_{i+2} - U_i}{2\delta r} \right) - \pi_{i-1}^t \left(\frac{U_i - U_{i-2}}{2\delta r} \right) \right]. \end{aligned} \tag{5.27}$$

Dividing by δr and taking the limit as before we obtain

$$\frac{\partial \Pi(r,t)}{\partial t} = D \frac{\partial^2 \Pi(r,t)}{\partial r^2} - \frac{\partial}{\partial r} \left(\frac{2D}{r} \Pi(r,t) \right) + \beta D \frac{\partial}{\partial r} \left[\Pi(r,t) \frac{\partial U(r)}{\partial r} \right], \tag{5.28}$$

with second order accuracy in space. Employing once again the fact that $\Pi(r,t) = 4\pi r^2 f(r,t)$, we recover the Smoluchowski equation under a potential [235],

$$\frac{\partial f(r,t)}{\partial t} = \frac{D}{r^2} \frac{\partial}{\partial r} \left(r^2 \left[\frac{\partial f(r,t)}{\partial r} + \beta f(r,t) \frac{\partial U(r)}{\partial r} \right] \right) \tag{5.29}$$

$$= \frac{D}{r^2} \frac{\partial}{\partial r} \left(r^2 e^{-\beta U(r)} \frac{\partial}{\partial r} e^{\beta U(r)} f(r,t) \right). \tag{5.30}$$

We have not talked about the boundary yet. This will be a very subtle issue as we will comment on further. For the time being, lets assume the boundary is given as that of the matrix (5.14). In such case the first difference equation of the Kolmogorov forward equation

yields,

$$\pi_0^{t+1} = \pi_0^t + \frac{\delta t D}{\delta r^2}\left[\pi_1^t - 2\pi_0^t + \pi_0^t\left(1 - \frac{\delta r^2}{D}\frac{\kappa}{4\pi r_0^2 \delta r}\right)\right] - \delta t\left[\frac{D}{r_0}\frac{\pi_1^t}{\delta r} + \frac{D}{\delta r}\left(\frac{\pi_0^t}{r_0 + \delta r}\right)\right] + \frac{\delta t \beta D}{2\delta r}\left[\pi_1^t\left(\frac{U_2 - U_0}{2\delta r}\right) + \pi_0^t\left(\frac{U_1 - U_{-1}}{2\delta r}\right)\right].$$

Once again, in order to find the boudary condition, we rewrite this equation in the same form than Eq. 5.27 by introducing the ghost cell π_{-1}^{t+1}. This will require introducing values for the potential at two ghost cells U_{-1} and U_{-2},

$$\pi_0^{t+1} = \pi_0^t + \delta t D\left[\frac{\pi_1^t - 2\pi_0^t + \pi_{-1}^t}{\delta r^2}\right] - \delta t\frac{2D}{r_0}\left[\frac{\pi_1^t - \pi_{-1}^t}{2\delta r}\right] + \delta t\frac{D}{\delta r}\left[\frac{\pi_0^t}{r_0 - \delta r} - \frac{\pi_0^t}{r_0 + \delta r}\right] + \delta t\frac{\beta D}{2\delta r}\left[\pi_1^t\left(\frac{U_2 - U_0}{2\delta r}\right) - \pi_{-1}^t\left(\frac{U_0 - U_{-2}}{2\delta r}\right)\right],$$

where U_{-1} and U_{-2} are usually well defined since the boundary where $i = 0$ corresponds to $\sigma > 0$ and δr is small. In the case where these are undefined, we can always use articial values to match the right derivative and curvature of the potential at the boundary. This equation divided by δr in the limit $\delta_t \to 0$ and $\delta_r \to 0$ is again reduced to the appropriate Fokker-Planck equation, given by Eq. 5.28. However, analogously as before, π_{-1}^t needs to satisfy,

$$\pi_0^t - \frac{\delta r \kappa}{4\pi D r_0^2}\pi_0^t + \frac{\beta}{4}\pi_0^t(U_1 - U_{-1}) = \pi_{-1}^t + \delta r\frac{\pi_0^t}{r_{-1}} + \delta r\frac{\pi_{-1}^t}{r_0} - \frac{\beta}{4}\pi_{-1}^t(U_0 - U_{-2}),$$

which in the continuous limit becomes

$$\left.\frac{\partial \Pi(r,t)}{\partial r}\right|_{r=\sigma} = \frac{\kappa}{4\pi\sigma^2 D}\Pi(\sigma,t) + \frac{2\Pi(\sigma,t)}{\sigma} - \beta\left.\frac{\partial U(r)}{\partial r}\right|_{r=\sigma}\Pi(r,t),$$

with first order accuracy in space. Using again Eq. 5.10, we can rewrite it as

$$4\pi\sigma^2 D\left.\frac{\partial f(r,t)}{\partial r}\right|_{r=\sigma} = \kappa f(\sigma,t) - 4\pi\sigma^2 D\beta\left.\frac{\partial U(r)}{\partial r}\right|_{r=\sigma} f(\sigma,t)$$

$$\Rightarrow \quad 4\pi\sigma^2 D e^{-\beta U(\sigma)}\left[\frac{\partial e^{\beta U(r)} f(r,t)}{\partial r}\right]_{r=\sigma} = \kappa f(\sigma,t),$$

which is the Collins-Kimball-Debye boundary condition [227]. If we would have used matrix (5.19) instead, we would have obtained the back-reaction boundary condition in Eq. 5.22

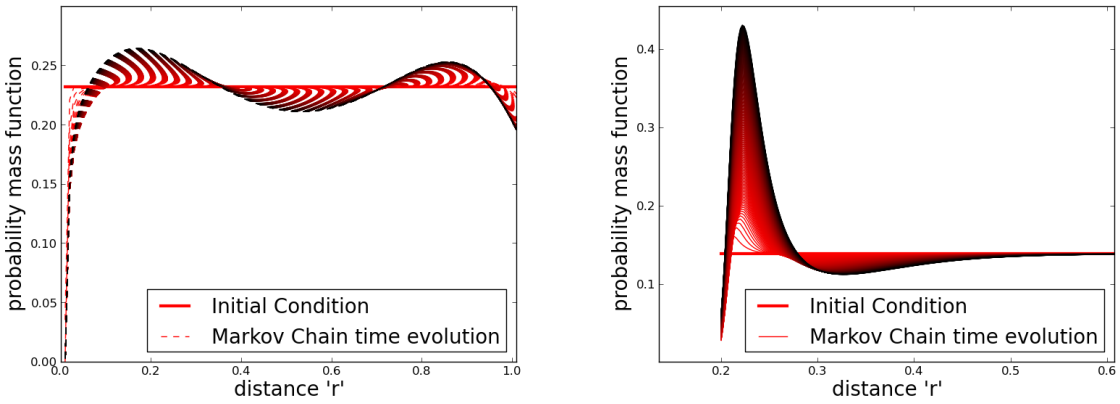

Figure 5.7: Convergence to steady state for the diffusion under a force field case for two potentials. The initial condition for the discrete Markov model, which is a uniform distribution, is plotted as a thick red line. The thin lines represent the convergence in time to the steady state of the Markov chain from $t = 0$ to $t = 0.2$ taken every 10 time steps; the darker lines correspond to longer times. (a) Plot using potential $U_{(r)} = U_K(r)$. The parameters used were $V_0 = 0.0001$, $r_m = 0.5$, $A = 2.0$, $\delta r = 0.01$, $\delta t = 0.0001$, $D = 0.1$, 100 shells and $r_0 = 0$.(b) Plot using a Lennard-Jonnes type potential $U(r) = U_{LJ}(r)$. The parameters were $V_0 = 0.00005$, $r_m = 0.22$ $\delta r = 0.002$, $\delta t = 2E - 5$, $D = 0.1$, 500 shells and $r_0 = 0.2$.

with the addition of the potential factors. However, there is the subtlety of how to define the bound state that we discussed in Section 5.2.2. Does it depend on the distance between A and B molecules, or does it depend on the state? According to our previous discussion, it will depend on the physical problem at task.

In Figure 5.7, we plot the convergence to the steady state for the two potential functions,

$$U_K(r) = V_0 \left[(A(r - r_m))^4 - (A(r - r_m))^2 \right], \quad \text{and}$$
$$U_{LJ}(r) = V_0 \left[\left(\frac{r_m}{r} \right)^{12} - 2 \left(\frac{r_m}{r} \right)^6 \right].$$

These correspond to the potential in Kramers original work and a Lennard-Jonnes potential. We observe the steady state distribution exhibits bistability, even when using the Lennard-Jonnes potential due to the geometrical drift. In this case, the reversible reaction can be modeled without the need of a boundary, and the state of B can be stated as bound or unbound depending on which side of the separatrix of the potential it is. Note this still matches both the distance and state definition mentioned in Section 5.2.2. However, if the potential doesn't only depend on r but on more variables, the distance and state definition might not provide the same answer.

Once again, as we have a steady state and zero flux boundaries, detailed balance must be satisfied, and the equilibrium state satisfies the Gibbs-Boltzmann distribution. We should also mention an alternative discretization for discontinuous potentials was introduced in [262]. Their discretization is only performed in one dimension and does not implement reversible reacting boundaries. In the future, it would be interesting to explore how to extended their to include reversible reaction boundaries. Another very relevant work was done in [142, 195], where a similar discretization as a Markov chain is given; however, the emphasis is on providing a numerical solution of the Smoluchowski equation instead of a stochastic framework that allows particle based simulations in conjunction with probability mass function dynamics.

5.4 Advantages, disadvantages and future directions

We developed a discrete time/space stochastic model for bimolecular chemical reaction via diffusion encounter. The model converges to all the well known classical results of continuous irreversible diffusion-influenced reaction theory. It also allows diffusion under a force field, like in the theories of Debye and Kramers.

The significance of this formulation is for the case of reversible reactions, where there have been extensive discussions on the best approach to model the process. One of the main models is given by the usual diffusion equation, Eq. 3.15a, coupled with the back-reaction boundary condition from Eq. 5.22. The main issue with this model, however, is that the back-reaction boundary condition is so complicated that it obscures the underlying stochastic process and consequently an accurate and transparent particle-based simulation. The discrete model presented here was inherently constructed as a stochastic process using simple notions of discrete association and dissociation reactions. In the continuous limit, it recovers the reversible diffusion-influenced theory, providing a clear description of the underlying stochastic process, which is hard to grasp in the continuous limit due to the nature of PRBM as shown in Section 3.3. In addition, it provides the continuous model parameters as a function of the jump and reaction probabilites, which elucidates the probabilistic interpretation of the parameters in the classical theory. It also allows straightforward simple Markovian algorithms to compute particle-based simulations and to compute the probability distribution, ensuring consistency between the two as well as conservation of probability.

In the continuous limit, we recover a more extensive version of the original back-reaction model, as in the Eq. 5.23, Eq. 5.24 and Eq. 5.25. This result unifies the back-reaction boundary approach for reversible diffusion-influenced reactions with our discrete model. Furthermore, as we modeled the dissociation process following an exponential waiting time, the previous result also shows consistency between the reversible diffusion-influenced reaction theory and the approaches taken by other simulation algorithms, like eGFRD and FPKMC [237, 63].

The model also allows an immediate implementation of an unbinding radius for the dissociation process, and it provides the correct scaling for the dissociation rate in terms of the diffusion controlled association rate. This approach can be used by other simulation algorithms to speed up simulations in a similar manner as done in Smoldyn [13]. However, high accuracy and detailed balance are lost in the region inside the unbinding radius.

One disadvantage is the high accuracy of the discrete model causes numerical computations to be slow. Additionally, the model currently only works for one A and one or multiple B's; however, we provided a guideline for possible implementations with multiple A's. These are left as future work. Other future directions are to implement extensions for volume reactivity models [62] and more complicated scenarios where a reaction is not only weighted as a function of space but also other variables. Regardless of its computation capabilities, the model itself provides a lot of insight on the modeling of reversible reactions, and it unifies different approaches by providing an underlying common stochastic framework. The discrete stochastic nature of this model establishes a research guideline that could lead to more robust computational solutions of complex models, where else continuous models might become increasingly convoluted, obscure or even intractable.

5.4.1 Second order accuracy in no-flux boundaries

In the discretization of Section 5.3.1, we mentioned that we have second order accuracy in all the inner points. However, the boundary condition we obtain from Eq. 5.12 is only first order accurate. Lets check this, subtracting Eq. 5.12 from π_0^t and dividing by δr we obtain,

$$\begin{aligned}\frac{\pi_0^t - \pi_{-1}^t}{\delta r} &= \pi_0^t \frac{1}{\delta r}\left[1 - \frac{\left(\frac{1}{\delta r} - \frac{1}{r_{-1}}\right)}{\left(\frac{1}{r_0} + \frac{1}{\delta r}\right)}\right] = \frac{\pi_0^t}{r_0^2}\frac{2r_0 - \delta r}{1 - (\delta r/r_0)^2} \\ &= \pi_0^t \frac{2r_0 - \delta r}{r_0^2}\sum_{i=0}^{\infty}\left(\frac{\delta r}{r_0}\right)^{2i} = \frac{2\pi_0^t}{r_0}\left[1 + O(\delta r)\right].\end{aligned}$$

Following standard finite difference theory [156], we take the limit as $\delta r \to 0$ and recover the zero flux boundary condition $\left.\frac{\partial \Pi(r,t)}{\partial r}\right|_{r=r_0} = \frac{2\Pi(r_0,t)}{r_0}$ to first order. In general, this would not be desirable when discretizing a partial differential equation for simulation since the first order error would be propagated to the rest of the solution. Nonetheless, it is not clear how relevant the accuracy at the boundaries is when interpreting the discretization as jump probabilities in a Markov chain. Once again, the actual stochastic process is very clear in the discrete scenario since we are modeling a discrete stochastic process instead of the discretization of a continuous stochastic process. We also know that the reactions and the no-flux boundaries are modeled appropriately in the discrete process. How relevant is that we recover the continuous version of the boundary conditions with high accuracy is up for

debate. The important part is that we do recover them showing consistency between the discrete and continuous models. In theory, we could try to modify the rates to obtain a second order discretization. However, it seems it would not be possible to write this discretization as a Markov chain anymore.

In the case of no-flux boundary conditions, there is an alternative approach that will yield second order accuracy. Lets concentrate on the steady state π^{ss}, which we know satisfies detailed balance in the boundary $\pi_0^{ss} q_0 = \pi_1^{ss} p_1$. The detailed balance condition for the problem in Section 5.3.1 can be written as,

$$\pi_0^{ss}\left(\frac{1}{r_0}+\frac{1}{\delta r}\right) = \pi_1^{ss}\left(\frac{1}{\delta r}-\frac{1}{r_{-1}}\right). \tag{5.31}$$

Subtracting Eq. 5.12 from π_1^{ss} and dividing the result by $2\delta r$, we obtain

$$\frac{\pi_1^{ss}-\pi_{-1}^{ss}}{2\delta r} = \frac{1}{2\delta r}\left[\pi_1^{ss} - \pi_0^{ss}\frac{\left(\frac{1}{\delta r}-\frac{1}{r_{-1}}\right)}{\left(\frac{1}{r_0}+\frac{1}{\delta r}\right)}\right].$$

Using the detailed balance condition of Eq. 5.31, we can write the right hand side in terms of π_0^{ss}, which yields

$$\begin{aligned}\frac{\pi_1^{ss}-\pi_{-1}^{ss}}{2\delta r} &= \frac{\pi_0^{ss}}{2\delta r}\left[\frac{\left(\frac{1}{\delta r}+\frac{1}{r_1}\right)}{\left(\frac{1}{\delta r}-\frac{1}{r_0}\right)} - \frac{\left(\frac{1}{\delta r}-\frac{1}{r_{-1}}\right)}{\left(\frac{1}{r_0}+\frac{1}{\delta r}\right)}\right] \\ &= \frac{2r_0\pi_0^{ss}}{r_0^2-\delta r^2} = \frac{2\pi_0^{ss}}{r_0}\sum_{i=0}^{\infty}\left(\frac{\delta r}{r_0}\right)^{2i} = \frac{2\pi_0^{ss}}{r_0}\left[1+O(\delta r^2)\right].\end{aligned}$$

In the limit $\delta r \to 0$, it satisfies the no flux boundary condition with second order accuracy. This result is a consequence of the fact that our discretization can be interpreted as a Markov chain with detailed balance. The downsides are that this level of accuracy is only attained in the steady state solution and that it is not applicable for reactive boundaries.

5.4.2 Extension to multiple molecules

The aim of the present work is to unify theories and algorithms and to provide a deeper understanding of stochastic reaction-diffusion processes, by using a simple intuitive model. Nonetheless, we will offer some suggestions on its value in computations, in particular, its extension to multiple-molecule simulations. One of the key advantages of this formulation, in comparison to other algorithms, is that it can handle multiple B's in particle-based simulations naturally on the same grid, and it doesn't need to decouple a system into multiple two-body problems. Of course, once a B has been absorbed a new B cannot be absorbed

until the previous one is dissociated. In this sense, our model already handles multiple molecules.

The real challenge is when one also has multiple A's. If we assume A's are diluted macromolecules, there are several possibilities to extend this model that would be worthwhile to explore. One possibility is to create non-overlapping truncated spherical grids around each A molecule. Each one of this molecules diffuses along with its grid following a random walk with diffusion coefficient D_A. In the same manner, B molecules diffuse on open space following a random walk with coefficient D_B, unless they diffuse into one of the outermost spherical shells or if they are already inside one. If a B molecule diffuses into one of the outer shells, it will undergo diffusion inside the spherical shells following the model from the previous sections. If the molecule escapes the outermost shell of the grid, it will return to diffuse freely with the direction of exit chosen randomly from a uniform distribution. Complications will arise if at some time step two grids of A overlap. In this case, we would need to calculate new non-overlapping grids for the two A's, which will force a smaller time step. However, as A is dilute this should not happen very often. In the case where A molecules are binding sites fixed in space, this could be an efficient and accurate approach.

Another possible implementation is to precompute the probability distribution function in a large and high-resolution grid and save these into a lookup table. The table could then be used as the reference solution to compute the probabilities in simulation algorithms like eGFRD or FPKMC. The difference is that this solution uses the back-reaction boundary condition and not the partially absorbing one. This could speed up existing algorithms since the partially absorbing boundary requires modeling every dissociation event while the back-reaction boundary does not. This model provides an easy and intuitive alternative to compute lookup tables for third-parties interested in developing their own simulations, and it also encourages reproducibility. It would be interesting to compare the lookup tables obtained in our discrete model with those of other simulation packages. Implementation of these extensions and the comparison studies between different algorithms is left as future work.

Chapter 6

COUPLED DIFFUSION PROCESSES AND MESOSCOPIC TRANSITION THEORY

In this chapter, we will use the ideas from Chapter 5 as the building block of a more comprehensive theory for reversible bimolecular reactions via diffusion encounter. The content of this chapter is still a work in progress, so instead of providing an unpolished version of the theory, we introduce three main areas that constitute the core of our new theory. Each of these areas emerges from complications with the classical diffusion-influenced reaction theory. The first area (Sections 6.1 and 6.2) concerns establishing a probabilistic interpretation of the original concentration-based Smoluchowski model. We will establish this interpretation by showing the concentration-based model can be derived as the hydrodynamic limit of a nonequilibrium statistical mechanical model for a large number of particles obeying the Smoluchowski master equation (SME) –a spherical random walk with reactive boundaries and continuous time. Establishing this interpretation is fundamental to accurately develop a nonequilibrium thermodynamic theory for bimolecular diffusion-influenced reactions, which is extremely relevant to describe biological processes at cell scales. This issue corresponds to the second area, nonequilibrium thermodynamics (Section 6.3), where we will introduce some areas of nonequilibrium thermodynamics and mesoscopic nonequilibrium thermodynamics relevant to our theory. The idea is to supply the blueprints needed to accurately relate the original concentration-based Smoluchowski's theory and its probabilistic interpretation with nonequilibrium thermodynamics. The third area (Sections 6.4 and 6.5) introduces coupled diffusion processes as a novel model for reversible diffusion-influenced reactions that blends smoothly with concentration-based models and nonequilibrium thermodynamics. In this part, we extend the SME model into a stochastic model that allows conformational changes and the removal of reaction boundaries by using coupled-diffusion processes. Despite the fact that the theory partially introduced through in the following sections is a work in progress, it should be noted that parts of this chapter are already being prepared for publication.

6.1 The Smoluchowski Master equation

In Chapter 5 (also see [57]), we derived a discrete time and discrete state Markov chain model that recovers the Smoluchowski equation. In this section, we will use this model to write its corresponding Master equation (continuous time Markov chain). This equation will be fundamental to establish the probabilistic interpretation of the original concentration-based

Smoluchowski model.

Consider an A particle in the origin and a B molecule diffusing in the space around it. Partition the space around A in spherical shells of width δ_r. Assume particle B diffuses in spherical coordinates, so we are only interested in the jumps between different spherical shells in the r direction. If the particle is in shell i with radius $r_i = \sigma + i\delta r$ and σ a constant, the probabilities to jump to the smaller and bigger shells are $\tilde{q}_{i,i-1}$ and $\tilde{q}_{i,i+1}$ respectively. We can write this process as a discrete time Markov chain. Let the position in the radial direction be denoted by $\mathcal{R}_t$, a random variable for every given t constituting a discrete state and time stochastic process. We will call $\pi_i^t = \Pr[\mathcal{R}_t = r_i]$ the probability of being at spherical shell i at time t. The state of the whole system at time t is given by the vector of all states $\boldsymbol{\pi}^t = [\pi_0^t, \pi_1^t, \cdots, \pi_i^t, \cdots]$. The dynamics are given in terms of the Markov chain

$$\boldsymbol{\pi}^{t+1} = \boldsymbol{\pi}^t \mathbb{P},$$

where $\mathbb{P}$ is the stochastic matrix. If we define the shell $r_0 = \sigma$ as the reaction boundary or the binding radius, then we can incorporate the probability of a reaction $q_{0,b} = \tilde{\kappa}(r)\delta t$. Following Eq. 5.14 and [57], the stochastic matrix is given by,

$$\mathbb{P} = \begin{bmatrix} 1-(\tilde{q}_{0,1}+q_{0,b}) & \tilde{q}_{0,1} & 0 & \cdots & \cdots & q_{0,b} \\ \tilde{q}_{1,0} & 1-(\tilde{q}_{1,0}+\tilde{q}_{1,2}) & \tilde{q}_{1,2} & 0 & & \\ \vdots & & \ddots & & & \\ & 0 & \tilde{q}_{i,i-1} & 1-(\tilde{q}_{i,i-1}+\tilde{q}_{i,i+1}) & \tilde{q}_{i,i+1} & \\ \vdots & & & \vdots & \ddots & \end{bmatrix}. \tag{6.1}$$

where the probabilities of jumping from shell i to shell $i+1$ or $i-1$ are given by $\tilde{q}_{i,i\pm1}$,

$$\tilde{q}_{i,i\pm1} = \delta t \left(\frac{D}{\delta r^2} \pm \frac{D}{r_{i\pm1}\delta r} \right). \tag{6.2}$$

Note we are truncating the system up to shell N (the $(N+1)^{th}$ column of matrix $\mathbb{P}$). The last term $q_{0,b}$ in the first row of the matrix, corresponds to a periodic boundary condition. This means every time a particle is absorbed at the absorbing boundary $r_0 = \sigma$, a new one is placed at the outermost shell r_N. This periodic condition will be consistent with the Smoluchowski model as we will explain below and as it is shown in [57].

Furthermore, as there is always a positive one in the diagonal, we can subtract the vector $\boldsymbol{\pi}^t$ on both sides, divide every equation in the system by δt and take the limit $\delta t \to 0$ to obtain the Smoluchowski Master equation (SME),

$$\frac{d\boldsymbol{\pi}(t)}{dt} = \boldsymbol{\pi}(t)\mathbb{Q}, \tag{6.3}$$

where $\boldsymbol{\pi}(t)$ is the continuous time analog of $\boldsymbol{\pi}^t$ and the matrix $\mathbb{Q}$ is given by

$$\mathbb{Q} = \begin{bmatrix} -(q_{0,1}+q_{0,b}) & q_{0,1} & 0 & \cdots & \cdots & q_{0,b} \\ q_{1,0} & -(q_{1,0}+q_{1,2}) & q_{1,2} & 0 & & \\ \vdots & & \ddots & & & \\ & 0 & q_{i,i-1} & -(q_{i,i-1}+q_{i,i+1}) & q_{i,i+1} & \\ \vdots & & & \vdots & \ddots & \end{bmatrix}. \tag{6.4}$$

The transition probabilities $q_{i,i\pm1}$ are given by,

$$q_{i,i\pm1} = \frac{D}{\delta r^2} \pm \frac{D}{r_{i\pm1}\delta r}, \tag{6.5}$$

and $q_{0,b} = \tilde{\kappa}(r)$. Note the rows of $\mathbb{Q}$ now sum to zero as we should expect from a continuous time Markov chain. The i^{th} equation has the form,

$$\frac{d\pi_i(t)}{dt} = q_{i-1,i}\pi_{i-1}(t) - (q_{i,i-1}+q_{i,i+1})\pi_i(t) + q_{i+1,i}\pi_{i+1}(t). \tag{6.6}$$

6.2 Probabilistic interpretation of Smoluchowski's model

In this section, we will develop a nonequilibrium statistical mechanical approach for diffusion-influenced reactions based on the probabilistic dynamics of an isolated interacting pair. We will show Smoluchowski's original model emerges as a thermodynamic mean-field limit of this model. This result will show the relation between the probabilistic model and the concentration-based model. It will also provide an unequivocal physical interpretation of Smoluchowski's original concentration-based model. This result is relevant because it will help to establish an accurate nonequilibrium thermodynamic theory for diffusion-influenced reactions.

6.2.1 Smoluchowski's model with periodic flux

The original Smoluchowski approach models the concentration gradient with an absorbing boundary. This model was later generalized by Collins and Kimball to a partially absorbing boundary. The main difficulty in providing a connection between the concentration based model and the probabilistic one is the far-field boundary condition with a constant value. In this paper, we will show that the original concentration based Smoluchowski model is nothing more that a nonequilibrium thermodynamic mean field limit for a large number of particles that each obey the probabilistic model. This will provide an accurate interpretation of the concentration based Smoluchowski model in terms of a thermodynamic limit of well defined stochastic processes.

A key first step to obtain this result is to study the Smoluchowski problem with a partially

absorbing boundary condition and periodic flux. We will begin by solving the Fokker-Planck equation (Eq. 3.11a) with the boundary conditions,

$$4\pi\sigma^2 D\frac{\partial f(r,t)}{\partial r}\bigg|_{r=\sigma} = 4\pi R^2 D\frac{\partial f(r,t)}{\partial r}\bigg|_{r=R} = \kappa f(\sigma,t), \tag{6.7}$$

and $\int_\sigma^R 4\pi r^2 f(r,t)dr = 1$. These conditions mean that the probability flux at $r=\sigma$ is the same as the flux at $r=R$, so we have a periodic boundary condition. The steady state solution is exactly of the same form as Eq. 3.13, but with a fixed constant $c_0 = A_0$,

$$f_{ss}(r) = A_0\left[1 - \frac{\kappa\sigma}{4\pi D\sigma + \kappa}\left(\frac{1}{r}\right)\right], \tag{6.8}$$

$$A_0 = \left[4\pi\left(\frac{R^3-\sigma^3}{3}\right) - \frac{4\pi\sigma\kappa}{4\pi\sigma D+\kappa}\left(\frac{R^2-\sigma^2}{2}\right)\right]^{-1}. \tag{6.9}$$

This result will help provide a mathematical connection with the original gradient concentration approach and the probability approach. It can be easily interpreted as a concentration gradient for a large number of B molecules, where the absorption flux at σ is exactly the same as the incoming flux of particle at $r=R$. However, it can also be understood as the probability distribution for one B molecule, which every time it is absorbed at $r=\sigma$, it is placed back again at $r=R$.

We should note that the boundary condition in Eq. 5.16 is also satisfied in the original Collins and Kimball formulation at steady state from Eq. 3.13. In the probabilistic interpretation, the free parameter A_0 will give the normalization constant for the probability, which we can fix so the probability integrates to one. Nonetheless, we could have chosen it to integrate to any other value between 0 and 1. For instance, for the steady state probability to integrate to $p \in [0,1]$, we can obtain the corresponding value of A_0. In the concentration interpretation, we need to scale this parameter accordingly, so it corresponds to the concentration of the material/chemical bath in the far-field required to get $100(1-p)\%$ of net absorption before reaching the steady state.

6.2.2 Canonical ensemble interpretation of Smoluchowski's model

The SME we just derived gives us the dynamics of the probability of one B molecule in this system. The quantity $\pi_i(t)$ is the probability of finding one B molecule in shell i at time t.

In order to provide a picture closer to original Smoluchowski's concentration-based model consider m independent and identical B molecules that obey Eq. 6.3. The number of ways to arrange m independent B molecules in the system, such that n_i are in state i (shell i) while maintaining the total number constant $m = n_1 + n_2 + \ldots + n_N$, is given by the multinomial distribution [110]. Therefore, we can write the joint probability of having n_i molecules on

each state as

$$P(n_0, n_1, \ldots, n_N, t) = \frac{m!}{n_0! n_1! \ldots n_N!} \pi_0(t)^{n_0} \pi_1(t)^{n_1} \ldots \pi_N(t)^{n_N}. \tag{6.10}$$

Therefore, the expected value of having n_k molecules in shell k at time t is given by the expected value of the multinomial,

$$\mathbb{E}[\mathcal{N}_k = n_k] = m\pi_k(t),$$

where $\mathcal{N}_k$ refers to the random variable of the value of number of particles in shell k. In the interest of minimizing notation, we will refer to this expected value as $F_i(t) = m\pi_k(t)$. We want to relate this result with the original SME from Eq. 6.3. In order to do so, we only need to multiply by m the equation for the i^{th} shell given by Eq. 6.6. This yields

$$\frac{dF_i(t)}{dt} = q_{i+1,i}F_{i+1}(t) - (q_{i,i-1} + q_{1,i+1})F_i(t) + q_{i-1,i}F_{i-1}(t). \tag{6.11}$$

We will now follow a similar procedure to that of [57]. Substituting the corresponding values for the transition rates given in Eq. 6.5, we obtain the following equation

$$\frac{dF_i(t)}{dt} = D\left[\frac{F_{i+1}(t) - 2F_i(t) + F_{i-1}(t)}{\delta r^2}\right] - \frac{2D}{r_i}\left[\frac{F_{i+1}(t) - F_{i-1}(t)}{2\delta r}\right] + \frac{D}{\delta r}\left[\frac{F_i(t)}{r_i - \delta r} - \frac{F_i(t)}{r_i + \delta r}\right]. \tag{6.12}$$

We can now take th limit as $\delta r \to 0$ to obtain

$$\begin{aligned}\frac{\partial F(r,t)}{\partial t} &= D\frac{\partial^2 F(r,t)}{\partial r^2} - \frac{2D}{r}\frac{\partial F(r,t)}{\partial r} + \frac{2D}{r^2}F(r,t), \\ &= \frac{\partial F(r,t)}{\partial t} = D\frac{\partial^2 F(r,t)}{\partial r^2} - \frac{\partial}{\partial r}\left(\frac{2D}{r}F(r,t)\right),\end{aligned} \tag{6.13}$$

where $F(r,t)dr$ is the continuous analog of $F_i(t)$, i.e. the expected value for the number of B particles in a shell of width δr in position r and at time t.

This is the expected value computed at any point in the shell with radius r, so we cannot yet compare it with the Smoluchowski diffusion equation. In order to do so, we need the equation for the expected value at any point in space given by $f(r,\theta,\phi,t)r^2\sin(\theta)drd\theta d\phi$. Integrating this equation in the angular coordinates due to symmetry yields the expected value we just obtained, $F(r,t)$,

$$F(r,t)dr = 4\pi r^2 f(r,t)dr. \tag{6.14}$$

Substituting this result into Eq. 6.13 and doing some algebra, we recover the Smoluchowski original equation (Eq. 3.11a),

$$\frac{\partial f(r,t)}{\partial t} = \frac{D}{r^2}\frac{\partial}{\partial r}\left(r^2\frac{\partial f(r,t)}{\partial r}\right) = \nabla\cdot[D\nabla f(r,t)].$$

Note that, in this case, the equation has a very precise meaning. The quantity $4\pi r^2 f(r,t)dr$ is the expected number of particles at the shell of radius r and width δr at time t. More precisely, the quantity $f(r,t)$ has units of number of particles per unit volume, so it is the expected value for the concentration at a given point with position r at time t.

Although we almost stated the result of this section, we still need to deal with the boundary conditions. We can also obtain the equations at the boundaries by again multiplying by m the first and last equation of the system of Eqs. 6.3. The resulting equations for the inner and outer boundaries are the following,

$$\frac{dF_0(t)}{dt} = -(q_{0,1}+q_{0,b})F_0(t) + q_{1,0}F_1(t) \tag{6.15}$$

$$\frac{dF_N(t)}{dt} = F_0(t)q_{0,b} + F_{N-1}(t)q_{N-1,N} - F_N(t)q_{N,N-1} \tag{6.16}$$

Note $q_{0,b} = \tilde{\kappa}(r)$, where the physically reasonable assumption is that the rate $\tilde{\kappa}(r)$ scales inversely to the infinitesimal volume of the reaction spherical shell, i.e. $\tilde{\kappa}(r) = \kappa/(4\pi r^2\delta_r)$, where κ will be the constant rate in the boundary condition [57].

Substituting the rates into the two equations at the inner and outer boundary at shells $i = 0$ and $i = n$ and doing some algebra, we obtain the following equations,

$$\frac{dF_0}{dt} = \frac{D}{\delta r^2}\left[F_1 - 2F_0 + F_0\left(1 - \frac{\delta r^2}{D}\frac{\kappa}{4\pi r_0^2\delta r}\right)\right] - \left[\frac{D}{r_0}\frac{F_1}{\delta r} + \frac{D}{\delta r}\left(\frac{F_0}{r_0+\delta r}\right)\right]. \tag{6.17}$$

$$\Rightarrow \quad \frac{dF_0}{dt} = D\left[\frac{F_1 - 2F_0 + F_{-1}}{\delta r^2}\right] - \frac{2D}{r_0}\left[\frac{F_1 - F_{-1}}{2\delta r}\right] + \frac{D}{\delta r}\left[\frac{F_0}{r_0-\delta r} - \frac{F_0}{r_0+\delta r}\right], \tag{6.18}$$

for the inner boundary and

$$\frac{dF_N}{dt} = \frac{D}{\delta r^2}\left[F_{N-1} - 2F_N + F_N\right] + \left[\frac{D}{r_N}\frac{F_{N-1}}{\delta r} + \frac{D}{\delta r}\left(\frac{F_N}{r_N-\delta r}\right)\right] - F_0\frac{\kappa}{4\pi r_0^2\delta r}, \tag{6.19}$$

$$\Rightarrow \quad \frac{dF_N}{dt} = D\left[\frac{F_{N-1} - 2F_N + F_{N+1}}{\delta r^2}\right] - \frac{2D}{r_N}\left[\frac{F_{N+1} - F_{N-1}}{2\delta r}\right] + \frac{D}{\delta r}\left[\frac{F_N}{r_N-\delta r} - \frac{F_0}{r_N+\delta r}\right], \tag{6.20}$$

for the outer boundary. Note we omitted the time dependence of $F_i(t)$ to simplify notation. In both cases, Eq. 6.18 and Eq. 6.20, we introduced the ghost cells F_{-1} and F_{N+1} respectively

to force the equation to satisfy Eq. 6.12 (the equation satisfied inside the boundaries). In order for Eq. 6.18 and Eq. 6.20 to be satisfied, the ghost cells need to satisfy the equations

$$F_0 - F_0\frac{\kappa\delta r}{4\pi D r_0^2} = F_{-1} + \frac{\delta r}{r_0}F_{-1} + \frac{\delta r}{r_0 - \delta r}F_0,$$
$$F_N - F_0\frac{\kappa\delta r}{4\pi D r_0^2} = F_{N+1} - \frac{\delta r}{r_N}F_{N+1} - \frac{\delta r}{r_N + \delta r}F_N,$$

which will yield the boundary conditions. Arranging terms, dividing by δr and taking the limit as $\delta r \to 0$, we obtain

$$\left.\frac{\partial F(r,t)}{\partial r}\right|_{r=\sigma} = \frac{\kappa}{4\pi D\sigma^2}F(\sigma,t) + \frac{F(\sigma,t)}{\sigma},$$
$$\left.\frac{\partial F(r,t)}{\partial r}\right|_{r=r_{\max}} = \frac{\kappa}{4\pi D\sigma^2}F(\sigma,t) + \frac{F(r_{\max},t)}{r_{\max}},$$

respectively, where $r_0 = \sigma$ is the innermost shell and $r_{\max}$ is the outermost shell. Applying once again the identity in Eq. 6.14, we obtain the boundary conditions for the Smoluchowski model with periodic flux from Section 6.2.1,

$$\left.4\pi D\sigma^2\frac{\partial f(r,t)}{\partial r}\right|_{r=\sigma} = \kappa f(\sigma,t),$$
$$\left.4\pi D r_{\max}^2\frac{\partial f(r,t)}{\partial r}\right|_{r=r_{\max}} = \kappa f(\sigma,t).$$

These are the boundary conditions for the expected value of the concentration at position r and time t. It should be noted that the process to obtain the continuous limit of these equations is analogous to the one we presented in [57].

The previous result shows that the Smoluchowski model with periodic flux from Section 6.2.1 is nothing more than the mean field thermodynamic limit of a large number of B molecules, each obeying Eq. 6.3. The model described by Eq. 6.10 is a statistical mechanical approach to model diffusion-influenced reactions. It not only yields the expected mean field but can also yield the full probability distribution for all particles. This provides a comprehensive framework to study fluctuations in the concentration-based model.

The steady state of the statistical mechanical model is a nonequilibrium steady state since it always has a constant flux from the outer boundary to the inner one. Note the number of particles in the system does not change or fluctuate over time. Therefore, following nonequilibrium statistical mechanics terminology, we say this system is in a canonical ensemble. However, Smoluchowski's original concentration model does not maintain a constant number of particles (or concentration), unless a very specific initial condition is chosen. For a general

case, we need to develop a more comprehensive statistical mechanical model.

6.2.3 Grand canonical ensemble interpretation of Smoluchowski's model

In the grand canonical ensemble, the number of particles m is not constant. Therefore, we cannot apply the same approach using the multinomial distribution. An alternative approach is to write down the Master equation for the probability of having n_i particles in shell i, $P(n_0, n_1, \dots n_N, t)$. The master equation has many terms,

$$\frac{dP(n_0, n_1, \dots, n_N, t)}{dt} = \tag{6.21}$$

$$\text{absorbing boundary} \begin{cases} P(n_0 - 1, n_1, \dots, n_N, t) q_{-1,0}(n_{-1}) \\ +P(n_0 + 1, n_1, \dots, n_N, t) q_{0,-1}(n_0 + 1) \end{cases} \tag{6.22}$$

$$\text{inner diffusion} \begin{cases} +P(n_0 + 1, n_1 - 1, \dots, n_N) q_{0,1}(n_0 + 1) \\ +P(n_0 - 1, n_1 + 1, \dots, n_N) q_{1,0}(n_1 + 1) \\ +P(n_0, n_1 + 1, n_2 - 1 \dots, n_N) q_{1,2}(n_1 + 1) \\ +P(n_0, n_1 - 1, n_2 + 1 \dots, n_N) q_{2,1}(n_2 + 1) \\ \vdots \\ +P(n_0, \dots, n_{N-1} + 1, n_N - 1) q_{N-1,N}(n_{N-1} + 1) \\ +P(n_0, \dots, n_{N-1} - 1, n_N + 1) q_{N,N-1}(n_N + 1) \end{cases} \tag{6.23}$$

$$\text{outer boundary} \begin{cases} +P(n_0, \dots, n_N + 1) q_{N,N+1}(n_N + 1) \\ +P(n_0, \dots, n_N - 1) q_{N+1,N}(n_{N+1}) \end{cases} \tag{6.24}$$

$$\text{leaving state} \begin{cases} -P(n_0, \dots, n_N) \sum_{k=0}^{N} \left[q_{k,k+1} + q_{k,k-1} \right] n_k. \end{cases} \tag{6.25}$$

In order to not confuse all the terms in the master equation, we divided them into four categories: the incoming transitions to the current state through the absorbing boundary, the incoming transitions to the current state through diffusion of particles in the inner shells, the incoming transitions to the current state through the outer boundary in contact with a material bath and the transitions leaving the current state through diffusion or escape through either of the boundaries.

This equation is really difficult to manipulate, and it contains too much information to be tractable. However, we can use it to obtain an equation for the expected number of molecules at shell i. Multiplying the equation by n_i, summing over all the possible number of molecules $\bar{n} = n_j$ for all $j = 0, 1, 2 \dots$, using that $\langle n_i \rangle = \mathbb{E}[\mathcal{N}_i = n_i]$ and doing some

algebra, we can obtain this equation

$$\sum_{\{\bar{n}\}} n_i \frac{dP(n_0, n_1, \ldots, n_N, t)}{dt} = \frac{d\langle n_i \rangle}{dt} =$$

$$\underbrace{\langle n_{i+1} \rangle q_{i+1,i} - \langle n_i \rangle [q_{i,i+1} + q_{i,i-1}] + \langle n_{i-1} \rangle q_{i-1,i} + \sum_{j=-1}^{N} [\langle n_i n_j \rangle q_{j,j+1} + \langle n_i n_{j+1} \rangle q_{j+1,j}]}_{\text{absorbing boundary + inner diffusion + outer boundary}}$$

$$\underbrace{- \sum_{j=0}^{N} \langle n_i n_j \rangle [q_{j,j+1} + q_{j,j-1}] - \langle n_i n_{N+1} \rangle q_{N+1,N}}_{\text{leaving state}} .$$

As $q_{-1,k} = 0$ for all k, and $q_{0,-1} = q_{0,b}$, we can join the two series together. All the terms in the series will cancel out except for one. This remaining term will also cancel out with the second term from the "leaving state". The only terms left over are

$$\frac{d\langle n_i \rangle}{dt} = \langle n_{i+1} \rangle q_{i+1,i} - \langle n_i \rangle [q_{i,i+1} + q_{i,i-1}] + \langle n_{i-1} \rangle q_{i-1,i}. \tag{6.26}$$

Renaming $F_i(t) = \langle n_i \rangle$, we have exactly the same equation as Eq. 6.11, so we will have the same limiting behavior. Using the transition rates from Eq. 6.5, taking the limit $\delta r \to 0$ and using Eq. 6.14 to scale the geometrical effects, we obtain again the Smoluchowski equation

$$\frac{\partial f(r,t)}{\partial t} = \frac{D}{r^2} \frac{\partial}{\partial r} \left(r^2 \frac{\partial f(r,t)}{\partial r} \right),$$

where the function $f(r,t)$ is the expected value for the concentration. However, in this case, the interesting behavior will be at the boundaries when $i = 0, N$ in Eq. 6.26. The resulting equations are

$$\frac{dF_0(t)}{dt} = -(q_{0,1} + q_{0,b})F_0(t) + q_{1,0}F_1(t),$$
$$\frac{dF_N(t)}{dt} = q_{N+1,N}n_{N+1} - (q_{N,N+1} + q_{N,N-1})F_N(t) + q_{N-1,N}F_{N-1}(t),$$

where we used the fact that the number of particles at $i = n + 1$ is fixed , $\langle n_{N+1} \rangle = n_{N+1}$. The first equations is exactly the same than Eq. 6.15. This will again yield the boundary condition for the inner absorbing boundary

$$4\pi D\sigma^2 \frac{\partial f(r,t)}{\partial r}\bigg|_{r=\sigma} = \kappa f(\sigma, t).$$

However, the second equation is new. We can apply the same methodology to figure out the corresponding boundary condition. We introduce a a ghost cell at $i = N + 1$, $\tilde{F}_{N+1}$, so we can obtain a difference equation that satisfies Eq. 6.12. Using the rates from Eq. 6.5, we can write the equation for the outer boundary as,

$$\frac{dF_N(t)}{dt} = D\left[\frac{\tilde{F}_{N+1}(t) - 2F_N(t) + F_{N-1}(t)}{\delta r^2}\right] - \frac{2D}{r_N}\left[\frac{F_{N+1}(t) - F_{N-1}(t)}{2\delta r}\right]$$
$$+\frac{D}{\delta r}\left[\frac{F_N(t)}{r_N - \delta r} - \frac{F_N(t)}{r_N + \delta r}\right] - \frac{D}{\delta r^2}\tilde{F}_{N+1}(t) + n_{N+1}q_{N+1,N} + \tilde{F}_{N+1}(t)\frac{D}{r_N\delta r}.$$

In order to satisfy Eq. 6.12, the ghost cell needs to satisfy,

$$n_{N+1}q_{N+1,N} = \left[\frac{D}{\delta r^2} - \frac{D}{r_N\delta r}\right]\tilde{F}_{N+1}(t).$$

We can directly apply the scaling from Eq. 6.14. However, in this case $F_i(t)$ is still discrete, so $F_i(t) = 4\pi r_i^2 f(r_i)\delta r$. Additionally, the concentration C_0 in the outermost shell is given by $C_0 = n_{N+1}/4\pi r_{N+1}^2\delta r$. We will also call the rate of incoming particles $\gamma = q_{N+1,N}$. Substituting these into the equation, we obtain

$$C_0 4\pi r_{N+1}^2\delta r\gamma = \left[\frac{D}{\delta r^2} - \frac{D}{r_N\delta r}\right]4\pi r_{N+1}^2\tilde{f}(r_{N+1})\delta r,$$
$$\Rightarrow \qquad C_0\delta r^2\gamma = \left[1 - \frac{\delta r}{r_N}\right]D\tilde{f}(r_{N+1}).$$

In order to obtain a convergent limit, we will set the transition rate γ to have the value $\gamma = D/\delta r^2$. The limit as $\delta r \to 0$ yields

$$f(r_{\max}, t) = C_0.$$

Other value of γ could be provided in the discrete model; however, they will be unlikely to produce an accurate continuous limit. This result allows us to provide numerical simulations (discrete) that are consistent with the continuous model.

There was a hidden assumption when we assumed $C_0 = n_{N+1}/4\pi r_{N+1}^2\delta r$. Actually, the state n_{N+1} is different to all the others since the number of particles does not change even though the system is continually absorbing particles from it. The only feasible way this could happen is if somehow the $N + 1$ state can access an infinite number of particles, and this is exactly what happens. When assuming a constant concentration $C_0 = n_{N+1}/4\pi r_{N+1}^2\delta r$, we

actually refer to the concentration of the whole bath

$$C_0 = \frac{n_{\text{bath}}}{4\pi(R_\infty^3 - r_N^3)}.$$

In order to have access to an infinite amount of particles, we also need to make the corresponding volume infinite, $R_\infty \to \infty$. When looking at the boundary layer of width δr around r_N, the concentration has to be $C_0 = n_{N+1}/4\pi r_{N+1}^2 \delta r$, where $n_{N+1} \to 0$ as $\delta r \to 0$. Although it might appear that this assumes that the number of particles of the bath goes to zero, it is actually the opposite; the number of particles and the volume in the bath goes to infinity at a fixed rate.

It is also important to point out that Eq. 6.26 is a particular case of the equation,

$$\frac{d\left\langle n_i(t)\right\rangle}{dt} = \sum_{\substack{j=-1 \\ j\neq i}}^{N+1} \left[\left\langle n_j(t)\right\rangle q_{j,i} - \left\langle n_i(t)\right\rangle q_{i,j}\right].$$

which corresponds to a generalized version of the master equation, Eq. 6.25, where all the states can interact with one another. In [110], it was shown that a solution to this general master equation satisfies the following Poisson probability distribution,

$$P(n_0, n_1, \ldots, n_N, t) = \prod_{i=0}^{N} \left[\frac{\left\langle n_i(t)\right\rangle^{n_i}}{n_i!} e^{-\left\langle n_i(t)\right\rangle}\right].$$

This can be proved by direct substitution. As our equation is of the same form, it also satisfies the same distribution. Also note the expected value for the number of particles at shell i of this distribution is of course $\langle n_i(t)\rangle$.

One other very important issue we need to point out is the relevance of moving into a discrete state setting. The statistical mechanical model from Eq. 6.25 is highly simplified by employing a discrete state approach. It is not even clear how one would write such a model with a continuous state spectrum. As overly emphasized in [57], moving to a discrete setting simplifies mathematical manipulations and computational implementations.

6.3 Nonequilibrium thermodynamics

In this section, we introduce some relevant areas of nonequilibrium thermodynamics and mesoscopic nonequilibrium thermodynamics relevant to our theory. These are mostly based on [26, 212]. Although we do not establish a direct relation to our previous results derived in the first part of the chapter, we think the overview presented in this section provides a guideline to accurately extend our previous results to a nonequilibrium thermodynamics context. It should be noted this endeavor is currently a work in progress.

Classical thermodynamics, which deals with system in equilibrium, is built upon two fundamental laws: the first law of thermodynamics (conservation of energy) and the second law of thermodynamics (entropy law). A consistent macroscopic framework to describe non-equilibrium processes (i.e. thermodynamics of irreversible processes) can also be built upon these two laws. This well established framework is the theory of Non-equilibrium thermodynamics [102, 212], and the two previous laws take the form of its two main hypothesis:

- **Local equilibrium** hypothesis assumes the thermodynamic variables of each subsystem of a conveniently partitioned system, admit the same interpretation as in equilibrium.

- **Entropy production** of an isolated system is always zero or positive.

In order to contextualize this hypothesis, consider a macroscopic system with entropy S. The variation of the entropy can be written as

$$dS = dS_s + dS_i, \tag{6.27}$$

where dS_s is the entropy supplied to the system by the surroundings and dS_i is the entropy produced inside the system—also called entropy production. For reversible systems (or in equilibrium), $dS_i = 0$ and for irreversible (or non-equilibrium) $dS_i > 0$, then

$$dS_i \geq 0. \tag{6.28}$$

For the entropy supplied by the surroundings , in the case of adiabatically isolated system (i.e. no exchange of heat nor matter) $dS_s = 0$. However, for open systems with exchange of heat and/or matter this is not always true, and this is why the second hypothesis only refers to the entropy production.

The deviations from equilibrium are due the presence of unbalanced forces that give rise to fluxes, whose relation is compatible with the second law of thermodynamics. An additional objective of non-equilibrium thermodynamics is to relate the entropy production dS_i to the irreversible phenomena that may occur inside the system. In order to do so, we need to write these statements in a more suitable way to describe the densities of extensive properties, as mass and energy. Consider a partition of the system using infinitesimal volumes dV, each

with surface are $d\Omega$, then

$$S = \int_V \rho s dV,$$
$$\frac{dS_s}{dt} = -\int_\omega Js_{tot} \cdot d\omega,$$
$$\frac{dS_i}{dt} = \int_V \sigma dV,$$

where ρ is the mass density, s is the entropy per unit mass, Js_{tot} the total entropy flow per unit area and time, and σ the entropy production per unit volume and time (entropy source term). Differentiating the first equation in time, we get $\frac{dS}{dt} = \int_V \frac{\partial \rho s}{\partial t} dV$, substituting it along with the second and third equation into Eq. 6.27 and using Gauss theorem, we obtain

$$\int_V \left(\frac{\partial \rho s}{\partial t} + \nabla \cdot Js_{tot} - \sigma \right) dV = 0.$$

Since this relation is true for any arbitrary volume and as $\sigma \geq 0$, then

$$\frac{\partial \rho s}{\partial t} = -\nabla \cdot Js_{tot} + \sigma. \tag{6.29}$$
$$\sigma \geq 0, \tag{6.30}$$

are the corresponding local forms of Eq. 6.27 and Eq. 6.28. In order to obtain these equations, we employed our first hypothesis: statements in Eq. 6.27 and Eq. 6.28 hold for infinitesimally small parts of the system. Although the infinitesimal limit might only make sense mathematically, the local equilibrium assumption makes sense at a scale where the small "infinitesimal" subsystems are still considered macroscopic.

It is sometimes more convenient to rewrite Eq. 6.29 as,

$$\rho \frac{\partial s}{\partial t} = -\nabla \cdot J_s + \sigma, \tag{6.31}$$

where we employed the conservation of mass, $\frac{\partial \rho}{\partial t} + \nabla \cdot (\rho u) = 0$, and $J_s = Js_{tot} - \rho s v$ is the total entropy flux minus the entropy convective term. The theory of non-equilibrium thermodynamics relates the change in entropy to the variations in density, momentum, and energy, which will allow explicit expressions for J_s and σ. The dynamics are obtained from the local conservation laws, where the fluxes are linear functions of the forces. For an extensive work on the development of this theory, the reader is referred to the classical work [102].

To illustrate the theory, we will concentrate on a simple scenario of mass diffusion in one dimension. The first step will be to compute the entropy production. At equilibrium, the

Gibbs equation for the entropy S is satisfied,

$$Tds = dE + pdV - \mu dM,$$

where the extensive variables are the energy E, the volume V and the mass M; and the intensive variables are the pressure p, temperature T and chemical potential μ. Assuming constant energy, temperature and volume: $TdS = -\mu dM$. As the local equilibrium assumption assure that Gibbs equation is satisified for slow changes in the variables, we can introduce the spatial component x through a density $\rho(x)$ and rewrite the equation as,

$$T\frac{dS}{dt} = -\int \mu[x, \rho(x)]\frac{\partial \rho(x)}{\partial t}dx, \tag{6.32}$$

which yields the entropy production. We can input the mass conservation, $\frac{\partial \rho}{\partial t} = -\frac{\partial J}{\partial x}$, and integrate by parts to obtain

$$T\frac{dS}{dt} = \mu J\Big|_{d\Omega} - \int J\frac{\partial \mu}{\partial x}dx, \tag{6.33}$$

$$\Rightarrow \quad T\frac{dS}{dt} = -\int J\frac{\partial \mu}{\partial x}dx, \tag{6.34}$$

where we assumed the flux is zero at the boundary $d\Omega$. The mass flux J has an associated force—the gradient of the chemical potential— given by the linear phenomenological law

$$J = -L\frac{\partial \mu}{\partial x},$$

where L is the Onsager coefficient. This relation is closely related to Fick's law. When the chemical potential doesn't depend on x, i.e. $\mu = \mu[\rho(x)]$, we can combine this equation with the mass conservation,

$$\frac{\partial \rho}{\partial t} = -\frac{\partial J}{\partial x} = \frac{\partial}{\partial x}\left(L\frac{\partial \mu}{\partial x}\right),$$

$$\Rightarrow \quad \frac{\partial \rho}{\partial t} = \frac{\partial}{\partial x}\left(D\frac{\partial \rho}{\partial x}\right),$$

with $D = L\frac{\partial \mu}{\partial \rho}$ the Fick's diffusion coefficient. We just recovered the well known diffusion equation that described the diffusion of the density of particles.

As non-equilibrium thermodynamics uses the same set of thermodynamic variables locally than globally, the applications are constrained to macroscopic length scales. However, in the mesoscopic scale, the inherent stochasticity of the small length scales cannot be ignored and

fluctuations become relevant. Moreover, the linear force-flux relations work well for transport process, though activation processes, like bi-molecular reactions, are genuinely non-linear and cannot be studied with non-equilibrium thermodynamics.

6.3.1 Mesoscopic non-equilibrium thermodynamics

Scaling down to the mesoscopic scale entails increasing the number of degrees of freedom. In statistical mechanics, a phase space of $6N$ dimensions , with N the number of particles, is reduced to a few macroscopic thermodynamic variables. In this case, following [26, 212], we will be doing the inverse approach, but only to a mesoscopic scale. Consider the non-equilibrated degrees of freedom $\gamma = \gamma_i$ that could represent the velocity of a particle, the orientation of a spin or any parameter or coordinate that may define the state in the phase space. Let Γ be the position in the phase space, so $P(\gamma, t)dt = \Pr[\gamma < \Gamma < \gamma + d\gamma]$. The entropy of the system according to the Gibbs-Shannon entropy postulate is

$$S = S_{eq} - k_B \int P(\gamma, t) \ln \left[\frac{P(\gamma, t)}{P_{eq}(\gamma)} \right], \tag{6.35}$$

where S_{eq} is the entropy of the system when the degrees of freedom γ are at equilibrium, and $P_{eq}(\gamma)$ is the corresponding equilibrium probability given by the Boltzmann distribution

$$P_{eq} \sim \exp\left(\frac{\Delta W(\gamma)}{k_B T} \right), \tag{6.36}$$

where k_B is the Boltzmann constant, T the temperature and $\Delta W(\gamma)$ is the reversible work required to create that state. In other words,

$$\Delta W = \Delta E - T\Delta S + p\Delta V - \mu \Delta M + ...,$$

which reduces to the different themodynamic potentials when imposing different constraints. For instance, when T, V and M are constant , ΔW becomes the Helmholtz free energy. This tell us that the most likely state will be that with the minimum ΔW, which under different physical constraints could be the Gibbs free energy, Helmholtz free energy, internal energy, enthalpy or others.

Note as entropy is the quantity that can be related to probability, i.e. to the fluctuations of a mesocopic system, it will be the key ingredient to connect thermodynamics with mesoscopic thermodynamics and stochastic dynamics. In order to derive mesoscopic non-equilibrium

thermodynamics, lets take variations in Eq. 6.35,

$$\delta S = \delta S_{eq} - k_B \int \delta P(\gamma,t) \ln\left[\frac{P(\gamma,t)}{P_{eq}(\gamma)}\right] d\gamma - k_B \int P(\gamma,t) \frac{P_{eq}(\gamma)}{P(\gamma,t)} \frac{\delta P(\gamma,t)}{P_{eq}(\gamma)} d\gamma \quad (6.37)$$

$$= \delta S_{eq} - k_B \int \delta P(\gamma,t) \ln\left[\frac{P(\gamma,t)}{P_{eq}(\gamma)}\right] d\gamma - k_B \int \delta P(\gamma,t) d\gamma \quad (6.38)$$

$$\Rightarrow \quad \delta S = -k_B \int \delta P(\gamma,t) \ln\left[\frac{P(\gamma,t)}{P_{eq}(\gamma)}\right] d\gamma. \quad (6.39)$$

Additionally, the probability evolution in the γ has to obey the continuity equation,

$$\frac{\partial P}{\partial t} = -\frac{\partial J(\gamma,t)}{\partial \gamma}. \quad (6.40)$$

In the same way we took variations, we can differentiate Eq. 6.35 with respect to t and substitute the continuity equation,

$$\frac{\partial S}{\partial t} = -k_B \int \frac{\partial P(\gamma,t)}{\partial t} \ln\left[\frac{P(\gamma,t)}{P_{eq}(\gamma)}\right] d\gamma,$$

$$\Rightarrow \quad \frac{\partial S}{\partial t} = k_B \int \frac{\partial J(\gamma,t)}{\partial \gamma} \ln\left[\frac{P(\gamma,t)}{P_{eq}(\gamma)}\right] d\gamma.$$

Integrating by parts,

$$\frac{\partial S}{\partial t} = \int \frac{\partial}{\partial \gamma}\left(k_B J(\gamma,t) \ln\left[\frac{P(\gamma,t)}{P_{eq}(\gamma)}\right]\right) d\gamma - k_B \int J(\gamma,t) \frac{\partial}{\partial \gamma}\left[\ln \frac{P(\gamma,t)}{P_{eq}(\gamma)}\right],$$

which can be rewritten as

$$\frac{\partial S}{\partial t} = \int \frac{\partial}{\partial \gamma} J_s d\gamma + \sigma, \quad (6.41)$$

$$\text{with} \quad J_s(\gamma,t) = k_B J(\gamma,t) \ln\left[\frac{P(\gamma,t)}{P_{eq}(\gamma)}\right], \quad (6.42)$$

$$\text{and} \quad \sigma = k_B \int J(\gamma,t) \frac{\partial}{\partial \gamma}\left[\ln \frac{P(\gamma,t)}{P_{eq}(\gamma)}\right], \quad (6.43)$$

where J_s is the entropy flux and σ the entropy production.The linear flux-force relation is nowgiven by

$$J(\gamma,t) = -k_B L(\gamma, P(\gamma)) \frac{\partial}{\partial \gamma}\left(\ln \frac{P(\gamma,t)}{P_{eq}(\gamma)}\right),$$

where $L(\gamma, P(\gamma))$ is the Onsager chemical potential. Although this seems slightly arbitrary, it makes sense intuitively, and, as we will see later, it is consistent with the generalized chemical potential. Substituting this equation into the continuity Eq. 6.40, we get

$$\frac{\partial P}{\partial t} = \frac{\partial}{\partial \gamma}\left(D P_{eq} \frac{\partial}{\partial \gamma} \frac{P}{P_{eq}} \right),$$

with the diffusion coefficient $D = k_B L(\gamma, P)/P$. Using Eq. 6.36, we can rewrite in a more familiar form

$$\frac{\partial P}{\partial t} = \frac{\partial}{\partial \gamma}\left(D \frac{\partial P}{\partial \gamma} + \frac{D}{k_B t} \frac{\partial \Delta W}{\partial \gamma} P \right).$$

In the case where ΔW is given by the Gibbs energy $\Delta W = \Delta G = \Delta H - T\Delta S$, with H the enthalpy, the equation becomes,

$$\frac{\partial P}{\partial t} = \frac{\partial}{\partial \gamma}\left(D \frac{\partial P}{\partial \gamma} + \frac{D}{k_B t} \frac{\partial \Delta G}{\partial \gamma} P \right),$$

which is the familiar Fokker-Planck equation that described the Brownian motion of a particle under a field of force with a potential given by ΔG. Other choices of potentials are of interest depending on the desired application.

This is a simple explanation of the core of mesoscopic nonequilibrium thermodynamics. Note that simply by knowing the thermodynamic equilibrium potential, one could derive the general form of its kinetics.

In order to establish a connection with non-equilibrium thermodynamics concepts, lets generalize the idea of chemical potential into the mesoscopic scale. We can do this by writing the Gibbs equation, analog to Eq. 6.32, as

$$\begin{aligned} \delta S &= -\frac{1}{T} \int \mu \gamma \delta P(\gamma, t) d\gamma \\ \Rightarrow \quad \delta S_{eq} &= -\frac{1}{T} \int \mu_{eq} \delta P(\gamma, t) d\gamma \end{aligned}$$

where $\mu(\gamma)$ plays the role of a generalized chemical potential conjugated to the distribution function $P(\gamma, t)$ and μ_{eq} is its value at equilibrium. Comparing this equation to Eq. 6.39, we obtain the expression for the generalized chemical potential

$$\mu(\gamma, t) = k_B T \ln \left[\frac{P(\gamma, t)}{P_{eq}(\gamma)} \right], \tag{6.44}$$

which can be rewritten using Eq. 6.36 as,

$$\mu(\gamma, t) = k_B T \ln [P(\gamma, t)] + \Delta W,$$

where an equilibrium constant was omitted for simplicity. The thermodynamic force in this case is $T^{-1}\partial\mu/\partial\gamma$ (the derivative of the flux). We can also obtain the entropy production by substituting Eq. 6.44 into Eq. 6.43, to yield

$$\sigma = -\frac{1}{T}\int J\frac{\partial\mu}{\partial\gamma}d\gamma,$$

which is mimicking the diffusion process we studied in Eq. 6.34. However, this time the diffusion is not in physical space but in a potential landscape in the space of mesoscopic variables. The treatment of a diffusion process in the framework of non-equilibrium thermodynamics can then be extended to the case in which the relevant quantity is the probability density instead of the mass density, i.e. to the case of mesoscopic thermodynamics or stochastic thermodynamics.

6.4 Coupled-diffusion processes

We will now introduce the backbone of our new and more general theory for reversible diffusion-influenced reactions. Our theory is based on coupled diffusion processes, which provide a robust theoretical framework since they have a clear definition and interpretation as a stochastic process. This allows our theory to blend smoothly with the concentration-based models and the nonequilibrium thermodynamics aspects explored in the previous sections of this chapter. The main contribution of the theory is that it extends the original model by allowing conformational changes and the removal of artificial reaction boundaries. We will explore the most simple formulation of the theory and show how it can easily recover the classical diffusion-influenced reaction models.

6.4.1 Coupled diffusion model for an isolated pair

In this section we will introduce the coupled diffusion model for an isolated pair A and B that undergo the reversible reaction $A + B \rightleftharpoons C$. Assume the A molecule is placed at the origin, and the B molecule diffuses in space with diffusion coefficient D_u, where D_u is the diffusion coefficient in the unbound state. The molecule B can switch for the unbound state u to the bound states b and vice-versa. If the B molecule binds to A, it will change to the bound state, and the B molecule will now diffuse with diffusion coefficient D_b. The reaction will not be modeled as a boundary as it is usually done in diffusion-influenced reaction theory

[4, 28, 46, 105, 224, 230], but as a region in space where the reaction might occur. [1] This will be done by using the rate functions $\alpha(r)$ for association and $\lambda(r)$ for dissociation. The Kolmogorov Forward Equation (KFE) for this diffusion process with Markovian switching will have the form,

$$\frac{\partial f_u(r,t|r_0,S_0)}{\partial t} = \frac{D_u}{r^2}\frac{\partial}{\partial r}\left(r^2\frac{\partial f_0(r,t|r_0,S_0)}{\partial r}\right) - \alpha(r)f_u(r,t|r_0,S_0) + \lambda(r)f_b(r,t|r_0,S_0), \tag{6.45}$$

$$\frac{\partial f_b(r,t|r_0,S_0)}{\partial t} = \frac{D_b}{r^2}\frac{\partial}{\partial r}\left(r^2\frac{\partial f_b(r,t|r_0,S_0)}{\partial r}\right) + \alpha(r)f_u(r,t|r_0,S_0) - \lambda(r)f_b(r,t|r_0,S_0), \tag{6.46}$$

where $f_u(r,t|r_0,S)$ is the probability distribution function (PDF) for the B particle in the unbound state $S=u$ and $f_b(r,t|r_0,S)$ the PDF for the B particle in the bound state $S=b$. Both PDFs are conditioned to the initial position of the B molecules $r_0 \in \mathbb{R}$ as well as its initial state $S_0 \in \{u,b\}$. Assuming the particle is initially at the unbound state u at $r=r_0$, we can write the initial conditions and boundary conditions as,

$$f_u(r,0|r_0,u) = \frac{\delta(r-r_0)}{4\pi r_0^2}, \quad f_b(r,0|r_0,u) = 0,$$

$$\lim_{r\to\infty} f_u(r,t|r_0,u) \to 0, \quad \lim_{r\to\infty} f_b(r,t|r_0,u) \to 0.$$

This simple model for an isolated pari will be enough to recover all the classic diffusion-influenced reaction models for irreversible and reversible reactions. This will be shown in the next Section and later we will show a general version of the model.

6.4.2 Recovery of irreversible diffusion-influenced models

A partially diffusion controlled association occurs with rate k_0 once particle B collides with particle A, i.e. when the relative distance from their centers is less or equal than σ_b (the sum of the two radii). In this case, the probabilistic association rate must be given by a Dirac delta at σ_b weighted by the rate k_0 and a geometrical constant

$$\alpha(r) = k_0\frac{\delta(r-\sigma_b)}{4\pi r^2}.$$

Note that $k_0 \to \infty$ should recover Smoluchoswki's completely diffusive limit. As in the original Smoluchoski's and Collins and Kimball theory, there is no dissociation, we will just

[1] This is in agreement to the more general state definition of the bound state studied in [57].

assume $\lambda(r) = 0$. With this assumption the system is uncoupled, and we only need to solve

$$\frac{\partial f_0(r,t)}{\partial t} = \frac{D_0}{r^2}\frac{\partial}{\partial r}\left(r^2\frac{\partial f_0(r,t)}{\partial r}\right) - k_0\frac{\delta(r-\sigma_b)}{4\pi r^2}f_0(r,t).$$

Integrating from the sphere at $\sigma_b - \epsilon$ to $\sigma_b + \epsilon$ we obtain

$$\int_{\sigma_b-\epsilon}^{\sigma_b+\epsilon}\frac{\partial f_0(r,t)}{\partial t}4\pi r^2 dr = 4\pi D_0\left[r^2\frac{\partial f_0(r,t)}{\partial r}\right]_{\sigma_b-\epsilon}^{\sigma_b+\epsilon} - k_0 f_0(\sigma_b,t),$$

Note that as F_0 and its time derivative are continuous then as $\epsilon \to 0$ the left hand side becomes zero leaving

$$4\pi D_0\sigma_b^2\left[\frac{\partial f_0(r,t)}{\partial r}\right]_{\sigma_b} = k_0 f_0(\sigma_b,t), \tag{6.47}$$

where $[g(r)]_{\sigma_b} = g(\sigma_b^+ - \sigma_b^-)$ means the jump of $g(r)$ across σ_b. This is almost Collins and Kimball boundary condition [46, 47, 227]; however, instead of the derivative evaluated at σ_b, we have the jump of the derivative. In order to resolve this issue, we'll have to actually solve the equation

$$\frac{\partial f_0(r,t)}{\partial t} = \frac{D_0}{r^2}\frac{\partial}{\partial r}\left(r^2\frac{\partial f_0(r,t)}{\partial r}\right)$$

with the interface condition from Eq. 6.47. Solving this system with the interface condition is analogous to solve the original system with the Dirac delta source term. The stationary solution in the limit of $R_{box} \to \infty$ is given by

$$f_0^{ss}(r) = \begin{cases} C_{box}\left[1 - \frac{k_0\sigma_b}{k_0+4\pi D_0\sigma_b}\frac{1}{r}\right] & \text{for } r > \sigma_b \\ C_{box}\left[1 - \frac{k_0}{k_0+4\pi D_0\sigma_b}\right] & \text{if } 0 \le r \le \sigma_b \end{cases} \tag{6.48}$$

The solution obtained for $r > \sigma_b$ is exactly the stationary solution obtained by Collins and Kimball [46, 47, 227]. The solution for $0 \le r \le \sigma_b$ is just a constant, i.e. its spatial derivative is zero. As long as we use the Neumann boundary condition and the initial condition in this region is also constant, as it is expected to be, the solution will have zero derivative in this region. This means that $\frac{\partial f_0(r,t)}{\partial r}\Big|_{\sigma_b^-} = 0$ and that the interface condition in Eq. 6.47 can be rewritten as

$$4\pi D_0\sigma_b^2\left.\frac{\partial f_0(r,t)}{\partial r}\right|_{\sigma_b^+} = k_0 f_0(\sigma_b,t),$$

which is exactly the Collins and Kimball original boundary condition.

6.4.3 Recovery of reversible diffusion-influenced models

We will start again from the coupled diffusion equations (Eqs. 6.46) with the same parameters but with different boundary conditions. Consider one A and one B molecule, with A centered at the origin. The B molecule is initially placed a distance r_0 from A in its free state, i.e. unbound state 0; however, it can react with the A molecule and switch to a bound state 1 (a C molecule is formed). The B molecule can switch back and forth between these two states. As we know, f_0 and f_1 will give the probability density function for the unbound and bound state. As the approach in [3, 136] uses a probabilistic Green's function approach for an isolated pair, we will need to set up our boundary and initial conditions accordingly. These are given by a Dirac delta initial condition and four Neumann boundary conditions,

$$f_0(r,0|r_0) = \frac{\delta(r-r_0)}{4\pi\sigma_b^2} \quad f_1(r,0|r_0) = 0 \tag{6.49}$$

$$\frac{\partial f_0(r,t|r_0)}{\partial r}\Big|_{r=0} = \frac{\partial f_0(r,t|r_0)}{\partial r}\Big|_{r=R_{box}} = 0, \tag{6.50}$$

$$\frac{\partial f_1(r,t|r_0)}{\partial r}\Big|_{r=R_0} = \frac{\partial f_1(r,t|r_0)}{\partial r}\Big|_{r=R_{box}} = 0. \tag{6.51}$$

The Dirac delta tell us that the probability of finding the B particle at a distance r_0 in state 0 (unbound) at time t is one as we should expect. We can choose the association rate and dissociation rate to be,

$$\alpha(r) = k_0 \frac{\delta(r-\sigma_b)}{4\pi r^2}, \tag{6.52}$$

$$\lambda(r) = k_1. \tag{6.53}$$

We can integrate the equation for f_0 from $\sigma_b - \epsilon$ to $\sigma_b + \epsilon$, which immediately yields

$$\begin{aligned}\int_{\sigma_b-\epsilon}^{\sigma_b+\epsilon} \frac{\partial f_0(r,t|r_0)}{\partial t} 4\pi r^2 dr = 4\pi D_0 \sigma_b^2 \left[\frac{\partial f_0(r,t|r_0)}{\partial r}\right]_{\sigma_b} \\ -k_0 f_0(\sigma_b,t|r_0) + k_1 \int_{\sigma_b-\epsilon}^{\sigma_b+\epsilon} f_1(r,t|r_0) 4\pi r^2 dr.\end{aligned} \tag{6.54}$$

As the probability of being on either state should sum to one,

$$\int_0^{R_{box}} \left(f_0(r,t|r_0) + f_(r,t|r_0)\right) 4\pi r^2 dr = 1.$$

However, in the classical approaches, when the B molecule is bound, it's not allowed to diffuse. so we should take the limit $D_1 \to 0$. As a consequence, we can see from the coupled diffusion equations (Eqs. 6.46), the initial conditions (Eqs. 6.49) and the association rate (Eq. 6.52) that the B molecule will only be able to switch to the bound state 1 when $r = \sigma_b$. Once in this state, the molecule will not be able to diffuse as $D_1 \to 0$; therefore, when $D_1 = 0$, f_1 will be zero everywhere except at σ_b. Now we can rewrite the last equation as

$$\int_{\sigma_b-\epsilon}^{\sigma_b+\epsilon} f_1(r,t|r_0)4\pi r^2 dr = 1 - \int_0^{R_{box}} f_0(r,t|r_0)4\pi r^2 dr.$$

We can substitute this result in Eq. 6.54 and let $\epsilon \to 0$ to obtain,

$$4\pi D_0 \sigma_b^2 \left[\frac{\partial f_0(r,t|r_0)}{\partial r}\right]_{\sigma_b} = k_0 f_0(\sigma_b,t|r_0) - k_1\left[1 - P_u(t|r_0)\right], \tag{6.55}$$

where $P_u(t|r_0)$ is the probability of being unbound at time t, and it is given by $P_u(t|r_0) = \int_0^{R_{box}} f_0(r,t)4\pi r^2 dr$. The quantity $[1 - P_u(t|r_0)]$ is the probability of being bound at time t. As pointed out in [3], $P_u(t|r_0)$ can be written in terms of the probabily flux at the binding radius σ_b as,

$$P_u(t|r_0) = \int_0^{R_{box}} f_0(r,t)4\pi r^2 dr = 1 - \int_0^t 4\pi\sigma^2 D_0 \left.\frac{\partial p(r,t'|r_0)}{\partial r}\right|_{\sigma_b} dt', \tag{6.56}$$

where the net probability flux from unbound state to bound state is $j = -4\pi\sigma^2 D_0 \left.\frac{\partial p(r,t'|r_0)}{\partial r}\right|_{\sigma_b}$. Note $P_u(t|r_0)$ has been incorrectly called the survival probability in previous studies. The survival probability will tell you what is the probability of B not being absorbed (for the first time) at time t. The quantity $P_u(t|r_0)$ will tell you the probability of being unbound at time t regardless if recombinations occurred, i.e. regardless if B was absorbed and then desorbed again.

With this last consideration, Eq. 6.55 we almost got the boundary condition employed in [3, 136]. However, we have the jump of the probability flux across σ_b instead of just the flux evaluated at σ_b. This is easily fixed by noting that the model in [3, 136] is only valid for $r \geq \sigma_b$. From an stochastic perspective, this means that if a B particle reaches the partially absorbing boundary σ_b and doesn't react, it will not diffuse into $r < \sigma_b$. Instead it will be reflected towards $r \geq \sigma_b$. In terms of probability, this reflection can be enforced by setting the flux from the left side to zero,

$$\left.\frac{\partial f_0(r,t|r_0)}{\partial r}\right|_{\sigma_b^-} = 0.$$

Now we can rewrite Eq. 6.55 as

$$4\pi D_0 \sigma_b^2 \left.\frac{\partial f_0(r,t|r_0)}{\partial r}\right|_{\sigma_b^+} = k_0 f_0(\sigma_b, t|r_0) - k_1 \left[1 - P_u(t|r_0)\right], \tag{6.57}$$

with the unbound probability $P_u(t|r_0)$ given by Eq. 6.56. This is exactly the boundary condition along with the equations described in [3, 136].

6.5 SDE and random time-change representation of coupled diffussion processes

In the previous section, we showed the partial differential equations that describe the probability distribution dynamics of coupled diffusion process. However, we did not provide the equations for the stochastic sample trajectories. In this section, we intuitively derive the equations for the stochastic sample trajectories of coupled diffusion processes.

Consider a diffusion process X_t given by a stochastic differential equation (SDE) where the diffusion and drift coefficients depend on a random variable ξ_t with two discrete states, like in the first coupled diffusion model from Section 6.4.1. The SDE is given by

$$dX_t = \mu(X_t, \xi_t, t)dt + \sigma(X_t, \xi_t, t)dW_t,$$

where W_t is a Wiener process and ξ_t can take only two values, 1 and 2. In order to establish the dynamics of the Markovian switching of ξ_t, we will use a slightly modified version of the random time-change representation [8, 9]. We will first define two new variables $\eta_1(t)$ and $\eta_2(t)$. This variables will be indicator functions, which can only take the value zero or one and the sum of both should always be one, so only one of them can be one at a given time. In this way, we can define our variable $\xi(t)$ as

$$\xi_t = 1\eta_1(t) + 2\eta_2(t),$$

so ξ_t can only take the values one or two. The functions $\eta_i(t)$ are one when the Markovian switch is in state i. Now we need to write this functions in terms of the random time-change representation. In order to do so, we need The Markovian rates of the jumps from state i to state j given by q_{ij}; these will be assumed to be Poissonian, and they also depend on the position X_t, so

$$\Pr\{\xi_{t+\delta t} = j | \xi_t = i, X_t = x\} = q_{ij}(x)\delta t + O(\delta t).$$

With these rates, we can write the random time-change representation for the η functions

as,

$$\eta_1(t) = \delta_{\xi_0,1} + Y_{21}\left(\int_0^t q_{21}(X_s,s)\eta_2(s)ds\right) - Y_{12}\left(\int_0^t q_{12}(X_s,s)\eta_1(s)ds\right),$$
$$\eta_2(t) = \delta_{\xi_0,2} - Y_{21}\left(\int_0^t q_{21}(X_s,s)\eta_2(s)ds\right) + Y_{12}\left(\int_0^t q_{12}(X_s,s)\eta_1(s)ds\right),$$

where Y_{12} and Y_{21} are independent unit rate Poisson processes. The first term in $\eta_1(t)$ given by the Kronecker delta $\delta_{\xi_0,1}$ will identify the current state of the Markov switch. If the Markov chain $\xi_t = 1$, then it will be one, else it will be zero. The next term will provide a switch from state 2 to state 1 only if its current state is 2 ($\eta_2(t) = 1$). This will be done by the Poissonian event Y_{21}. The last term will switch from the state 1 to state 2 given the switch is currently in state 1 ($\eta_1(t) = 1$) by the Poissonian event Y_{12}. The same argument applies for $\eta_2(t)$. In this manner, we will know the state of the chain ξ_t depending on which of the two variables η_1 or η_2 is one.

6.5.1 SDE random time-change representation for N states

The general SDE with random time-change representation for a coupled diffusion process with N states can be written as,

$$dX_t = \mu(X_t,\xi_t,t)dt + \sigma(X_t,\xi_t,t))dW_t$$
$$\xi_t = \sum_{j=1}^{N} j\eta_j(t)$$
$$\eta_j(t) = \delta_{\xi_0,j} + \sum_{\substack{l=1\\ l\neq j}}^{N}\left[Y_{lj}\left(\int_0^t q_{lj}(X_s,s)\eta_l(s)ds\right) - Y_{jl}\left(\int_0^t q_{jl}(X_s,s)\eta_j(s)ds\right)\right],$$

where ξ_t can take the values $\{1,2,\cdots,N\}$, $\eta_j(t)$ are indicator functions with values 0 or 1, and $\sum_{i=1}^{N}\eta_j = 1$

Part II

HIGH RESOLUTION SHOCK-CAPTURING METHODS FOR FLUID INTERFACE PROBLEMS

Chapter 7

FINITE VOLUME METHODS

In this chapter, we will provide a compact review of finite volume methods for hyperbolic conservation laws. This will provide the fundamental concepts in conservative numerical methods that will be used for the methods and applications developed in the Chapters 8, 9, 10 and 11. This includes the development of Godunov's original method [95], its wave propagation form [154], as well as its extensions to second order accuracy and total variation diminishing schemes [67, 147, 215, 234, 255], usually referred as high resolution methods. The material in this chapter has contributions from many sources. However, this has been very well summarized in three major references [153, 155, 248].

7.1 Conservation Laws and Riemann problems

The fundamental equations in Physics are usually stated in terms of conservation laws. This includes subject areas like acoustics, mechanics, fluid mechanics, elasticity, electromagnetism, magneto-hydrodynamics, relativity and many others. The finite volume methods employed in the present work and explained in this section are used to solve these conservation laws, which are an important class of homogeneous hyperbolic equations. A very important property of any homogeneous hyperbolic linear system of equations is that it can be decoupled into a system of advection equations. In essence, the finite volume method algorithms explained here are methods to solve these advection equations ensuring the quantities described are being conserved.

A simple example of a conservation law is a one-dimensional hyperbolic partial differential equation (PDE),

$$q_t(x,t) + f(q(x,t))_x = 0,$$

with $f(q)$ the flux function. It basically means the temporal change of q is equal to the spatial change of the flux. This equation can be written in its quasilinear form or its integral form,

$$q_t + f'(q)q_x = 0,$$
$$\frac{d}{dt}\int_{x_1}^{x_2} q(x,t)dx = f(q(x_1,t)) - f(q(x_2,t)),$$

respectively. If the flux is a linear function $f(q) = Aq$, we called it a linear conservation law. If the flux is a nonlinear function of q, it is a nonlinear conservation law. The nature of conservation is easily understood from the integral form. It also happens to be a more fundamental form of the conservation law, since it admits discontinuous solutions and the differential form can be easily obtained when q and $f(q)$ are sufficiently smooth.

This concept can be easily extended to a system of conservation laws where instead of having q and $f(q)$ being scalars, they become vectors, and the quasilinear form for a linear system is given by $f'(q) = A$, where A is a matrix independent of q. For more details, the reader is referred to [155].

The most basic finite volume methods ensure conservation by discretizing the domain into grid cells. Afterwards, the solution is also discretized into piecewise constant functions in each grid cell (reconstruct). Then, this solution is advected with its corresponding velocity (evolve), and it is averaged again in each of the discretized regions (average). This is called the reconstruct-evolve-average (REA) algorithm [155], and it is the idea behind many conservative wave propagation algorithms.

7.1.1 The Riemann problem

In order to be able to decouple a system of conservation into uncoupled advection equations and figure out their velocities, we need to solve the Riemann problem at each cell interface. Therefore, the key ingredient in many modern numerical methods for hyperbolic problems is the Riemann solver, which solves the Riemann problem. Although the Riemann problem might seem simple, it is the fundamental block in the numerical solution of hyperbolic problems.

The Riemann problem is simply the hyperbolic equation with piecewise constant data and a single jump discontinuity as the initial condition. For a general one-dimensional system of conservation laws, the Riemann problem is given by

$$\begin{aligned} &q_t(x,t) + f(q(x,t))_x = 0, \\ &q_o(x) = \begin{cases} q_l & \text{if } x < 0 \\ q_r & \text{if } x > 0, \end{cases} \end{aligned} \tag{7.1}$$

where q_l and q_r are constant state vectors. If the system is linear, the flux is given as a matrix $f'(q) = A$, and the solution is easily computed in terms of its eigenvalues and eigenvectors. Assuming that A has also constant coefficients, i.e. they don't depend on x, and that it is diagonalizable,

$$A = R\Lambda R^{-1}, \tag{7.2}$$

where R is the matrix of eigenvectors and Λ is the diagonal matrix of eigenvalues. With this

decomposition, we can introduce the change of variables

$$w = R^{-1}q,$$

so we can rewrite the original system as

$$w_t + \Lambda w_x = 0,$$

which is a set of decoupled advection equations. Note the ideas presented here will remain to be relevant for non-linear systems.

7.2 Hyperbolic systems of conservation laws

A system of m conservation laws in d dimensions is written as

$$\frac{\partial q}{\partial t} + \sum_{j=1}^{d} \frac{\partial f_j(q)}{\partial x_j} = 0, \tag{7.3}$$

where $\overline{x} = (x_1, x_2, \cdots, x_d)$ corresponds to the spatial dimension, $q = (q_1(\overline{x}, t), \cdots, q_m(\overline{x}, t))$ is the vector of state variables and $f_j(q) = (f_{1j}(q), \cdots, f_{mj}(q))$ are the flux functions.

We are interested in studying wave propagation phenomena in conservation laws of the form of Eq. 7.3 or Eq. 7.4. This type of behavior is observed when the system is hyperbolic. The simplest example of an hyperbolic equation would be the wave equation $u_{tt} - c^2 u_{xx}$; however, in order for this equation to display wave propagation, c has to be real, so the wave equation is said to be hyperbolic only for real c. The same concept of hyperbolicity can be defined in the context of hyperbolic systems of conservation laws. In order to do so, let us consider an arbitrary unitary vector $\hat{n} = (n_1, \cdots, n_d)$ in d dimensions and let

$$A(q, \hat{n}) = \sum_{j=1}^{d} n_j A_j(q)$$

$$\text{with:} \quad A_j(q) = \left(\frac{\partial f_j}{\partial q} \right),$$

where $A_j(q)$ is the Jacobian of the j^{th} dimension flux $f_j(q)$. The matrix $A(q, \hat{n})$ represents a linear combination of these Jacobians in terms of the unit vector $\hat{n}$.

The system given by Eq. 7.3 or Eq. 7.4 is hyperbolic provided that for any direction given by the unit vector $\hat{n}$, the matrix $A(q, n)$ is diagonalizable with m real eigenvalues $\lambda_1 \leq \cdots \leq \lambda_m$ and a complete set of m linearly independent eigenvectors. Additionally, if all the eigenvalues are distinct the system is called strictly hyperbolic. The eigenvalues

must be real because they represent the physical propagation velocities for plane waves in the direction of $\hat{n}$.

Another aspect we are interested to study is the propagation of shock-waves. This requires that our solutions have discontinuities; however, in the formulation of Eq. 7.3 q has to be smooth to satisfy the equation pointwise. In order to address this issue, the system in Eq. 7.3 can be written in its integral form by integrating over an arbitrary domain Ω in d-dimensional space. The outward unitary normal to Ω is given by $\hat{k} = (k_1, \cdots, k_d)$. Noting the term with the sum in Eq. 7.3 is a divergence, we can employ the divergence theorem after integrating, which yields

$$\frac{d}{dt}\int_{\Omega} q d\bar{x} + \sum_{j=1}^{d}\int_{\partial\Omega} f_j(q) k_j dS = 0. \tag{7.4}$$

Note the nature of conservation is better understood from this equation where the time variation of q within the volume Ω equals the inward flux of q through the boundary $\partial\Omega$. Additionally, this new formulation still holds for discontinuous solutions. Solutions to the system in Eq. 7.4 are called weak solutions [1]. This form of the equations will allow us to derive conditions that hold across discontinuities. Denoting $q_{\pm}$ the limits of q on each side of the discontinuity, the so called Rankine-Hugoniot condition is obtained as

$$s(q_+ - q_-) = \sum_{j=1}^{d} k_j (f_j(q_+) - f_j(q_-)),$$

where s is the speed of the propagation of the discontinuity.

It is important to note that weak solutions are not necessarily unique and will require an additional physical constraint to choose amongst them. This constraint is usually called the entropy condition by analogy to gas dynamics. The solution obtained by satisfying the entropy condition can be viewed as the limit of the viscous problem associated as the viscosity goes to zero.

7.3 Godunov method

A very important class of finite volume methods are the Godunov-type methods. Although they are only first order accurate, they are the basis to build higher resolution methods.

We begin by considering a time and space discretization with intervals Δt and Δx respectively. The discrete points (x_i, t^n) are given by $x_i = i\Delta x$, $t^n = n\Delta t$ with i and n integers and $n \geq 0$. In our finite volume approach, the numerical solution Q_i^n at (x_i, t^n) is an approximation of the average over the spatial cell $C^i = (x_{i-1/2}, x_{i+1/2})$ of the true solution $q(x, t)$

[1] For a more general and useful definition of weak solutions see [155]

at time t^n, i.e.

$$Q_i^n \approx \bar{Q}_i^n = \frac{1}{\Delta x}\int_{C_i} q(x,t^n)dx.$$

The integral form of the conservation law in Eq. 7.4 for a one dimensional problem can be written for the grid cell C_i as,

$$\frac{d}{dt}\int_{C_i} q(x,t)dx = f(q(x_{i-1,2},t)) - f(q(x_{i+1/2},t)), \tag{7.5}$$

where $f(q(x_{i-1,2},t))$ and $f(q(x_{i+1/2},t))$ are the fluxes to the left and right of the grid cell respectively. Discretization in time yields,

$$\int_{C_i} q(x,t^{n+1})dx = \int_{C_i} q(x,t^n)dx - \left[\int_{t^n}^{t^{n+1}} f(q(x_{i+1/2},t))dt - \int_{t^n}^{t^{n+1}} f(q(x_{i-1,2},t))dt\right].$$

Dividing by Δx and using the cell average from Eq. 7.5, we obtain

$$\bar{Q}_i^{n+1} = \bar{Q}_i^n - \frac{1}{\Delta x}\left[\int_{t^n}^{t^{n+1}} f(q(x_{i+1/2},t))dt - \int_{t^n}^{t^{n+1}} f(q(x_{i-1,2},t))dt\right]. \tag{7.6}$$

Rewriting this equation in terms of the numerical approximations yields Godunov's method:

$$Q_i^{n+1} = Q_i^n - \frac{\Delta t}{\Delta x}\left[F(Q_i^n, Q_{i+1}^n) - F(Q_{i-1}^n, Q_i^n)\right], \tag{7.7}$$

where the numerical flux function is a numerical approximation to the fluxes in Eq. 7.6, i.e.

$$F(Q_i^n, Q_{i+1}^n) \approx \frac{1}{\Delta t}\int_{t^n}^{t^{n+1}} f(q(x_{i+1/2},t))dt.$$

7.3.1 Wave propagation form

We can also state Godunov's algorithm in a wave propagation form. We first note that, for a linear system, the jump of the solution vector can be expressed as a linear combination of the m eigenvectors r^p of the matrix A of the conservation law (see Eq. 7.2),

$$Q_i - Q_{i-1} = \sum_{p=1}^{m} \alpha_{i-1/2}^p r^p = \sum_{p=1}^{m} \mathcal{W}_{i-1/2}^p,$$

which can be interpreted as a set of waves (since each of the waves $\mathcal{W}_{i-1/2}^p$ is advected at its corresponding velocity given by the eigenvalue). At time, 0 the REA algorithm will have a

piecewise constant solution in each cell. By solving the Riemann problem at each interface, we will obtain a set of m waves $\mathcal{W}^p_{i\pm1/2}$ at each edge that will contribute to the corresponding cell average at the end of the time step. As the wave moves a distance $s^p_{i\pm1/2}\Delta t$ in a time interval and the cell is of width Δx, the contribution to the cell average is

$$-\frac{s^p_{i\pm1/2}\Delta t}{\Delta x}\mathcal{W}^p_{i\pm1/2},$$

where the sign arises from the fact that the jump in Q is measured from right to left. Therefore, in order to obtain the cell average in cell i, we only need to sum all the contributions from the right going waves coming from the edge $i-1/2$ and all the left going waves coming from edge $i+1/2$ as seen in Figure 7.1,

$$Q_i^{n+1} = Q_i^n - \frac{\Delta t}{\Delta x}\left[\underbrace{\sum_{p=1}^{m}(s^p_{i-1/2})^+ W^p_{i-1/2}}_{\text{LeftEdge}} + \underbrace{\sum_{p=1}^{m}(s^p_{i+1/2})^- W^p_{i+1/2}}_{\text{RightEdge}}\right],$$

where $(s^p_{i\pm1/2})^+ = \max(s^p_{i\pm1/2}, 0)$ and $(s^p_{i\pm1/2})^- = \min(s^p_{i\pm1/2}, 0)$.

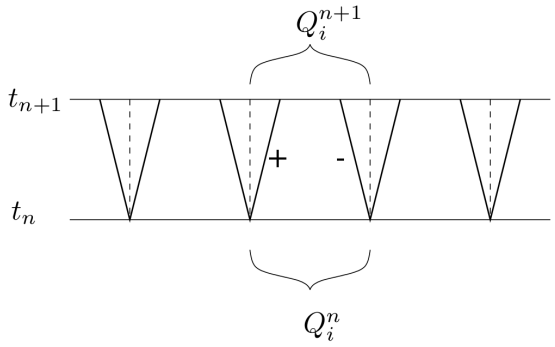

Figure 7.1: Representation of Godunov's algorithm in its wave propagation form. The central grid cell corresponds to cell i and the horizontal lines represent times t_n and t_{n+1}. The contributions to Q_i from waves coming from the left and right edges from time t_n to t_{n+1} are shown.

7.4 High resolution shock-capturing finite volume methods

The Clawpack software [44] uses the wave propagation form of Godunov's method [95] with the addition of high resolution corrections and limiters to better handle discontinuities[155].

We write the full numerical scheme in its wave propagation form. Consider a state vector $q(x,t)$ and a one dimensional system of conservation laws given by $q_t + f(q)_x = 0$. We partition the space in cells with index i and consider the cell average at time t to be $Q_i^n = \int_{x_{i-1/2}}^{x_{i+1/2}} q(x,t_n)dx$. Then the Godunov method is given by,

$$Q_i^{n+1} = Q_i^n - \frac{\Delta t}{\Delta x}\underbrace{\left[\sum_{p=1}^{m}(s_{i-1/2}^p)^+ W_{i-1/2}^p\right.}_{\text{LeftEdge}} + \underbrace{\left.\sum_{p=1}^{m}(s_{i+1/2}^p)^- W_{i+1/2}^p\right]}_{\text{RightEdge}} - \underbrace{\frac{\Delta t}{\Delta x}\left(\tilde{F}_{i+1/2} - \tilde{F}_{i-1/2}\right)}_{\text{HighResolution}} \quad (7.8)$$

with,

$$\tilde{F}_{i\pm1/2} = \frac{1}{2}\sum_{p=1}^{m}\left|s_{i\pm1/2}^p\right|\left(1 - \frac{\Delta t}{\Delta x}\left|s_{i\pm1/2}^p\right|\right)\underbrace{\widetilde{\mathcal{W}}_{i\pm1/2}^p}_{\text{Limiter}}, \quad (7.9)$$

which can be rewritten as

$$Q_i^{n+1} = Q_i^n - \frac{\Delta t}{\Delta x}(\mathcal{A}^-\Delta Q_{i+1/2} + \mathcal{A}^+\Delta Q_{i-1/2}) - \frac{\Delta t}{\Delta x}\left(\tilde{F}_{i+1/2} - \tilde{F}_{i-1/2}\right), \quad (7.10)$$

where $\mathcal{A}^-\Delta Q_{i\pm1/2} = \sum_{p=1}^m (s_{i\pm1/2}^p)^- \mathcal{W}_{i\pm1/2}^p$ and $\mathcal{A}^+\Delta Q_{i\pm1/2} = \sum_{p=1}^m (s_{i\pm1/2}^p)^+ \mathcal{W}_{i\pm1/2}^p$ are the left and right going fluctuations of the edge of cell $i \pm 1/2$ respectively, with $(s_{i\pm1/2}^p)^\pm$ indicating only those values of $s_{i\pm1/2}^p$ with sign $\pm$, m is the number of waves, $s_i^p \mp 1/2$ is the velocity of the p characteristic of the Riemann problem at edge $i \mp 1/2$, the wave $\mathcal{W}_{i\mp1/2}^p$ corresponds to the jump across that characteristic and $\widetilde{\mathcal{W}}_{i\pm1/2}^p$ is the limited version of the wave; we will explore this limited wave below, also see [155] for more details. The nonlinear version of the algorithm is completely analogous to this one [155].

There is a geometrical way to understand the higher order corrections. An equivalent formulation is to use a a piecewise linear reconstruction of the function instead of only piecewise constant. Consider the REA algorithm for the scalar advection equation with advecting velocity u. We can write Godunov's algorithm for the advection equation in terms of these slopes as [155],

$$Q_i^{n+1} = Q_i^n - \frac{u\Delta t}{\Delta x}(Q_i^n - Q_{i-1}^n) - \frac{1}{2}\frac{u\Delta t}{\Delta x}(\Delta x - u\Delta t)(\sigma_i^n - \sigma_{i-1}^n),$$

where σ_i^n is the slope at cell i time n. Note that if the slopes are zero, we recover the Godunov method for the advection equation, which is first order. However, other choices of slopes can recover second order methods like Lax-Wendroff, Beam-Warming and Fromm [155]. For instance, the slope $\sigma_i^n = (Q_{i+1}^n - Q_i^n)/\Delta x$, will recover the Lax-Wendroff method. The method from Eq. 8.26 is an extension of this method to a coupled one-dimensional

system of conservation laws. The choice of the slope goes into the selection of the limited wave $\widetilde{\mathcal{W}}^p_{i\pm1/2}$.

The limited waves $\widetilde{\mathcal{W}}^p_{i\pm1/2}$ will not only chose a slope to obtain a higher order correction, but they also decide when not to use higher order corrections to avoid oscillations. This is because close to discontinuities, like shock waves, the differential form of the equation is not valid, so neither its Taylor expansion nor the higher order solutions are well defined. In this case, it is more effective to use the Godunov's method without higher order corrections since it is still appropriate to deal with discontinuities. More generally, the limited waves $\widetilde{\mathcal{W}}^p_{i\pm1/2}$ are given by

$$\widetilde{\mathcal{W}}^p_{i\pm1/2} = \phi(\theta)^p_{i\pm1/2}\mathcal{W}^p_{i\pm1/2},$$

where $\phi(\theta)$ is the flux-limiter function [155] and θ is a measurement of the smoothness of the function. It can be shown that $\phi(\theta) = 0$ corresponds to the upwind method, $\phi(\theta) = 1$ to Lax-Wendroff, $\phi(\theta) = \theta$ to Beam-Warming and $\phi(\theta) = (1+\theta)/2$ to Fromm [155]. A combination is usually used to obtain the better balance between high-order accuracy and discontinuity handling[2], like the minmod limiter that chooses $\phi(\theta) = \text{minmod}(1, \theta)$, where the $\text{minmod}(a, b)$ chooses the smallest one between $|a|$ and $|b|$ if they have the same sign ($ab > 0$) or zero if they have different sign ($ab \leq 0$). Other high-resolution limiters are the superbee limiter $\phi(\theta) = \max(0, \min(1, 2\theta), \min(2, \theta))$, the MC limiter $\phi(\theta) = \max(0, \min((1+\theta)/2), 2, 2\theta)$ and the van Leer limiter $\phi(\theta) = (\theta+|\theta|)/(1+|\theta|)$, see [155]. It should be pointed out that some limiters do not reduce to Godunov's method at discontinuities since $\phi(theta)$ approaches 2 not 1 for limiters like the MC limiter.

There are several ways to choose the θ parameter to limit the waves coming out of the edges at $i - 1/2$. For a linear problem with two waves, where the 1-waves propagate to the left and the 2-waves to the right (like acoustics), we can measure the smoothness θ by comparing the magnitude of adjacent waves. The corresponding θ parameters can be obtained as $\theta^1_{i-1/2} = \|\mathcal{W}^1_{i+1/2}\|/\|\mathcal{W}^1_{i-1/2}\|$ and $\theta^2_{i-1/2} = \|\mathcal{W}^2_{i-3/2}\|/\|\mathcal{W}^2_{i-1/2}\|$, see [155]. In the case of nonlinear equations, the approach is similar; however, the eigenvectors of adjacent waves are no longer co-linear in phase space across adjacent cells, so we need to do a projection into the corresponding eigenvectors. For the nonlinear case, the θ parameter is given by

$$\theta^1_{i-1/2} = \frac{\mathcal{W}^1_{i+1/2}\cdot\mathcal{W}^1_{i-1/2}}{\mathcal{W}^1_{i-1/2}\cdot\mathcal{W}^1_{i-1/2}}, \qquad \theta^2_{i-1/2} = \frac{\mathcal{W}^2_{i-3/2}\cdot\mathcal{W}^2_{i-1/2}}{\mathcal{W}^2_{i-1/2}\cdot\mathcal{W}^2_{i-1/2}}.$$

This is the standard implementation in Clawpack [44], see [155].

The numerical solution requires solving a Riemann problem on each cell edge of our

[2]This requires introducing the concept of total variation diminishing (TVD) limiters, see [155] for more details.

partition in order to obtain the fluctuations. The solution to the Riemann problem usually provides the characteristic velocities s^p, and the waves $\mathcal{W}^p$, which can be calculated as the jump of q across the p characteristic. This information can be calculated for each cell edge, and it is the only information these algorithms require to solve the equations numerically. Of course one has to choose other things, like which limiter to use, the initial conditions or the grid size. Clawpack [44] provides an implementation of these algorithms.

7.5 Approximate Riemann solvers

The process of solving Riemann problem is often quite expensive; it is often true that it is not necessary to compute the exact solution of the Riemann problem to obtain good results, as pointed out in [155]. There are several kind of approximate Riemann solvers that are less expensive than exact ones and provide as good results when used with Godunov and high resolution methods. In this section, we will explore a couple of them. For a more complete account of this methods, see [155, 248].

The general structure of an approximate Riemann solver consists of m waves W^p propagating at speeds s^p, with $p = 1, \cdots m$. The vectors W^p represent the jump in q across each wave; therefore, its sum must recover the total jump

$$q_r - q_l = \sum_{p=1}^{m} W^p.$$

Also, the jump in the fluxes should be conservative,

$$f(q_r) - f(q_l) = \sum_{p=1}^{m} s^p W^p.$$

The flux function can then be rewritten as

$$\begin{aligned} f(Q_i, Q_{i+1}) &= f(Q_i) + \sum_{p=1}^{m} \left(s^p_{i+1/2}\right)^- W^p_{i+1/2} \\ &= f(Q_{i+1}) - \sum_{p=1}^{m} \left(s^p_{i-1/2}\right)^+ W^p_{i-1/2}, \end{aligned}$$

where $s^+ = \max(s, 0)$ and $s^- = \min(s, 0)$. Godunov's updating formula (Eq. 7.7) can then be written in its wave propagation form

$$Q_i^{n+1} = Q_i^n - \frac{\Delta t}{\Delta x}(A^+ \Delta Q_{i-1/2} + A^- \Delta Q_{i+1/2}), \tag{7.11}$$

with

$$A^+\Delta Q_{i-1/2} = \sum_{p=1}^{m} \left(s^p_{i+1/2}\right)^- W^p_{i+1/2}$$
$$A^-\Delta Q_{i-1/2} = \sum_{p=1}^{m} \left(s^p_{i-1/2}\right)^+ W^p_{i-1/2}.$$

From these equations, we expect that the distance the waves propagate doesn't exceed the length of the computational grid cell. This condition will make the numerical method stable and it's known as the CFL condition:

$$\frac{\Delta t}{\Delta x}\max|s^p| \leq 1, \quad 1 \leq p \leq m.$$

Note, as the waves W^p are defined as the jump in q across wave p, we can compute the solution q from the waves W^p and vice versa. As seen in the next sections, the HLL solvers will output the solution q and the speeds s^p, while the Roe solver will output the waves W^p and the speeds s^p. Also note the notation will change when dealing with HLL type solvers to keep it consistent with [248].

7.5.1 The HLL solver

We will start with the HLL solver, whose name arises from its developers Harten, Lax and van Lear. The main idea of HLL solvers is, given the wave speeds s_l and s_r by some algorithm, assume a wave configuration of two waves separating three constant states. A general one dimensional Riemann problem can be stated as,

$$q_t + f(q)_x = 0, \tag{7.12}$$
$$q(x,0) = \begin{cases} q_l & \text{if } x < 0 \\ q_r & \text{if } x > 0, \end{cases}$$

with q and $f(q)$ are the vectors of conserved variables and fluxes respectively. Employing an HLL solver, will yield a solution of the form

$$\tilde{q}(x,t) = \begin{cases} q_l & \text{if } \frac{x}{t} \leq s_l \\ q_{hll} & \text{if } s_l \leq \frac{x}{t} \leq s_r, \\ q_r & \text{if } \frac{x}{t} \geq s_r, \end{cases}$$

The main purpose is then to find the wave speed s_l and s_r and the intermediate state U_{hll}. In order to accomplish this, we can be write the integral form of conservation law (8.3) in

the control volume $[x_l, x_r] \times [0, T]$ as

$$\int_{x_l}^{x_r} q(x,T)dx = \int_{x_l}^{x_r} q(x,0)dx + \int_0^T f(q(x_l,t))dt - \int_0^T f(q(x_r,t))dt,$$
$$\Rightarrow \quad \int_{x_l}^{x_r} q(x,T)dx = x_r q_r - x_l q_l + T(f_l - f_r), \tag{7.13}$$

where we just evaluated the integrals and called $f_k = f(q_k)$. The integral on the left hand side can be split into three integrals from $[x_l, Ts_l]$, $[Ts_l, Ts_r]$ and $[Ts_r, x_r]$, where s_l and s_r are the fastest signal velocities arising from the Riemann problem in the left and right direction. We will show how to calculate them later on. As on the first interval $q(x,T) = q_l$ and the last interval $q(x,T) = q_r$, we can evaluate all except the integral in the middle state, i.e.

$$\int_{x_l}^{x_r} q(x,T)dx = \int_{Ts_l}^{Ts_r} q(x,T)dx + (Ts_l - x_l)q_l + (x_r - Ts_r)q_r. \tag{7.14}$$

Combining Eq. 7.13 and Eq. 7.14, we immediately have

$$\frac{1}{T(s_r - s_l)} \int_{Ts_l}^{Ts_r} q(x,T)dx = \frac{s_r q_r - s_l q_l + f_l - f_r}{s_r - s_l}. \tag{7.15}$$

The left hand side is nothing more than the average value of q in the middle state $[Ts_l, Ts_r]$; therefore,

$$q_{hll} = \frac{s_r q_r - s_l q_l + f_l - f_r}{s_r - s_l}. \tag{7.16}$$

Note the waves W^p $(p = 1, 2)$ for the Godunov updating formula (Eq. 7.11) can be easily computed as the jump in $\tilde{q}(x,t)$ across each one of the two waves. The corresponding HLL intercell flux can be easily calculated using the Rankine-Hugoniot conditions to yield,

$$f_{hll} = f_l + s_l(q_{hll} - q_l) = \frac{s_r f_l s_l f_r + s_l s_r (q_r - q_l)}{s_r - s_l}.$$

It was shown by Harten, Lax and van Leer that using the Godunov scheme with an HLL solver, if convergent, converges to the weak, physical entropy satisfying solution of the conservation laws. For a more detailed account in HLL solvers, see [248, 155].

7.5.2 The HLLC solver

Before showing how to calculate the wave speeds, we can improve the HLL solver by adding a third wave, a contact discontinuity. This is motivated from one dimensional Euler equa-

tions, since the solution consists of three waves, two shocks or rarefactions with a contact discontinuity in between. The name of this method is the HLLC solver since it is similar to the HLL solver, but it takes into account the contact discontinuity, so a C is added to the name. The solution for this method will be of the form

$$\tilde{q}(x,t) = \begin{cases} q_l & \text{if } \frac{x}{t} \leq s_l \\ q_{*l} & \text{if } s_l \leq \frac{x}{t} \leq s_*, \\ q_{*r} & \text{if } s_* \leq \frac{x}{t} \leq s_r, \\ q_r & \text{if } \frac{x}{t} \geq s_r, \end{cases}$$

where s_* is the wave speed of the contact discontinuity and the original middle state of the HLL solver, q_{hll}, was split into two new states, q_{*l}, q_{*r}, by the contact discontinuity. Assuming we can obtain s_l and s_r by some other algorithm, we only need to find q_{*l}, q_{*r} and s_* to solve the problem.

We will start by adding the middle wave speed s_* by splitting the right hand side of Eq. 7.15 as ,

$$\frac{1}{T(s_r - s_l)} \int_{Ts_l}^{Ts_r} q(x,T)dx = \frac{1}{T(s_r - s_l)} \int_{Ts_l}^{Ts_*} q(x,T)dx + \frac{1}{T(s_r - s_l)} \int_{Ts_*}^{Ts_r} q(x,T)dx. \tag{7.17}$$

The averages in the middle states left and right of the contact discontinuity will be given by

$$q_{*l} = \frac{1}{T(s_* - s_l)} \int_{Ts_l}^{Ts_*} q(x,T)dx, q_{*r} = \frac{1}{T(s_r - s_*)} \int_{Ts_*}^{Ts_r} q(x,T)dx.$$

Note these are quite similar to the ones in Eq. 7.17. Combining this result with Eq. 7.17 and Eq. 7.16, we obtain the consistency condition

$$q_{hll} = \frac{s_* - s_l}{s_r - s_l} q_{*l} + \frac{s_r - s_*}{s_r - s_l} q_{*r}. \tag{7.18}$$

Furthermore, we can apply the Rankine-Hugoniot conditions across each of the waves to obtain

$$f_{*l} = f_l + s_l(q_{*l} - q_l) \tag{7.19}$$

$$f_{*r} = f_{*l} + s_*(q_{*r} - q_{*l}) \tag{7.20}$$

$$f_{*r} = f_r + s_r(q_{*r} - q_r). \tag{7.21}$$

The expressions from Eq. 7.19, Eq. 7.20 and Eq. 7.21 can be combined to obtain the consistency condition (Eq. 7.18); therefore, these equation are sufficient to ensure consistency. Note these are three vectorial equations with four vector unknowns q_{*l}, q_{*r}, f_{*l} and f_{*r}. Also

note we still need to find s_*. In order to be able to solve this complications, we will need to make further assumptions in the particular problem we are dealing with. The most common assumptions are to assume equal pressure and normal velocity on both middle states, with the normal velocity also equal to the contact discontinuity speed, i.e.,

$$p_{*l} = p_{*r} = p_*,$$
$$u_{*l} = u_{*r} = u_* = s_*.$$

In the case of one dimensional Euler equations, these assumptions are adequate, and they allow us to solve the system to obtain the state vectors

$$q_{*k} = \frac{s_k q_k - f_k + p_* D}{s_l - s_*},$$

$$\text{with:} \quad D = [0, 1, s_*],$$

for $k = l, r$. Note the waves W^p $(p = 1, 2, 3)$ for Godunov's updating formula (Eq. 7.11) can be easily computed as the jump in $\tilde{q}(x, t)$ across each of the three waves. We can also obtain the fluxes as

$$f_{*k} = \frac{s_*(s_k q_k - f_k) + s_k(p_k + \rho_l(s_k - u_k)(s_* - u_k))D}{s_k - s_*}.$$

The contact discontinuity speed comes from equating the middle states pressures, and it's of the form

$$s_* = \frac{p_r - p_l + \rho_l u_l(s_l - u_l) - \rho_r u_r(s_r - u_r)}{\rho_l(s_l - u_l) - \rho_r(s_r - u_r)},$$

where ρ_k, u_k are the left or right density and speed in the Euler equations. These last results are straightforward from the equation we deduced, for detailed calculations the reader is referred to [248].

Finally, we just need to calculate the wave speeds s_l and s_r. In this calculation we will need to calculate the sound speed. This is where we require to employ the EOS. A simple estimate is the one given by Davis [248] as

$$s_l = \min\{u_l - c_l, u_r - c_r\} \qquad s_r = \max\{u_l + c_l, u_r + c_r\},$$

where u_k is the normal velocity and c_k is the sound speed on each side, $k = l, r$. Note that

the only way to calculate the speed of sound is using the EOS $p = p(\rho, e)$. It is given by,

$$c = \sqrt{\left.\frac{\partial p(\rho, e)}{\partial \rho}\right|_s},$$

where s is the entropy. A possible improvement is to employ Roe averages in wave speed estimates,

$$s_l = \min\{u_l - c_l, \tilde{u} - \tilde{c}\} \qquad s_r = \max\{\tilde{u} + \tilde{c}, u_r + c_r\},$$

where $\tilde{u}$ and $\tilde{c}$ are the Roe averages of the normal velocity and speed of sound respectively. These Roe averages are given by

$$\tilde{u} = \frac{\sqrt{\rho_l}u_l + \sqrt{\rho_r}u_r}{\sqrt{\rho_l} + \sqrt{\rho_r}}, \qquad \tilde{c} = \sqrt{(\gamma - 1)(\tilde{H} - \tilde{u}^2/2)},$$

$$\text{with:} \qquad \tilde{H} = \frac{\sqrt{\rho_l}H_l + \sqrt{\rho_r}H_r}{\sqrt{\rho_l} + \sqrt{\rho_r}},$$

where $H = (E + p)/\rho$ is the enthalpy, E is the total energy and p is the pressure. Variations of these might be more accurate when dealing with interfaces, like pointed out in [118]. For more details on how these averages are derived, the reader is referred to [67, 155, 248].

7.5.3 The Roe solver

Another extensively used Riemann approximate solver is the Roe solver [215]. The main idea is to determine an approximate solution to the Riemann problem by solving an approximate linear system with a constant coefficient matrix $\hat{A} = \hat{A}(q_l, q_r)$, which depends on the left and right state.

In order to have an hyperbolic conservation system that describes our problem accurately, the matrix $\hat{A}(q_l, q_r)$ has to satisfy the following conditions:

- The linearized system must be hyperbolic, i.e. $\hat{A}(q_l, q_r)$ has real eigenvalues and a complete set of eigenvectors.
- Consistency, $\hat{A}(q_l, q_r) \to f'(q^*)$ as $q_l, q_r \to q^*$.
- Conservation, $f(q_r) - f(q_l) = \hat{A}(q_l, q_r)(q_r - q_l)$.

One possibility is given by Roe [215] as

$$\hat{A}(q_l, q_r) = A(\tilde{q}), \qquad \tilde{q} = \tilde{q}(q_l, q_r),$$

where $A(q)$ is the original Jacobian of the system and $\tilde{q}$ is an average stated defined to fulfill these three conditions. In Roe's original paper, he derives $\hat{A}(q_l, q_r)$ for the Euler equations as shown in [155, 215]. A drawback of Roe solver is that it may compute entropy violating solutions, which occur when the real solution to the Riemann problem contains a transonic rarefaction where the eigenvalue changes sign through the rarefaction fan. The solver failure occurs when approximating this rarefaction as a single discontinuity. This error can be fixed using an entropy fix, see [155] for a detailed exposition.

Once we have the rank m matrix $\hat{A}(q_l, q_r)$ with eigenvalues $\hat{\lambda}_p$ and eigenvector $\hat{r}^p$, we can proceed as in the linear Riemann problem. First we need to compute the weights α^p of the projection of the jump $(q_r - q_l)$ onto the eigenvectors by solving $\hat{R}\alpha = q_r - q_l$, with $\hat{R}$ the matrix of eigenvectors $\hat{r}^p$. Afterwards, we can write the p waves W^p and speeds s^p as

$$W^p = \alpha^p \hat{r}^p, \qquad s^p = \hat{\lambda}^p \quad \text{with:} \quad p = 1, \cdots, m.$$

This results can be used as input for Godunov's updating formula (Eq. 7.11).

7.6 Operator-splitting for source terms

When we add a source term to a conservation law for $q(x,t)$, it is no longer conservative. A general one-dimensional conservation law with a source term $\psi(q,x,t)$ takes the form

$$q_t + f(q)_x = \psi(q,x,t).$$

The source terms can be solved using a fractional-step method [155] by alternating between the following set of equations

$$\begin{aligned} q_t + f(q)_x &= 0 \\ q_t &= \psi(q,x,y,t) \end{aligned}$$

The latter is an ordinary differential equation, which could have an exact solution, like in the case of Eqs. 10.1, as shown in Section 10.4 and in[55]. More complex source terms might require implementing another time stepping method like Runge-Kutta or TR-BDF2.

7.6.1 Geometrical source terms with TR-BDF2

This equation can be solved with any time integrator method like forward Euler or Runge-Kutta methods. However, in some cases with cylindrical or spherical symmetry the source terms are proportional to $1/r$ or $1/r^2$, so r can be close to zero; therefore, the problem can be stiff and the convergence might be too slow. In order to address this issue, we'll employ a mix between a trapezoidal method and a backward difference method called TR-BDF2. This method is very robust, stable and is second order accurate. The numerical method to

solve $\frac{dq}{dt} = f(q)$ can be written as,

$$q^* = q^n + \frac{\Delta t}{4}\left[f(q^n) + f(q^*)\right]$$
$$q^{n+1} = \frac{1}{3}\left[4q^* - q^n + \Delta t f(q^{n+1})\right].$$

Note this method is implicit, so it has to be solved numerically at each time step.

7.7 Multidimensional finite volume methods

In higher dimensions, the $d-$dimensional conservation law for $q(\bar{x}, t)$, with $\bar{x} = \{x_1, x_2, \cdots, x_d\}$, takes the form

$$q_t + \sum_{i=1}^{d} f_i(q)_{x_i} = 0.$$

In a similar manner to the previous section, the simplest way to solve this problem is to use dimensional splitting. This requires to use a split the operators acting in each of the possible directions x_i. Before presenting the splitting algorithm, it should be noted that the cell average in higher dimensions is given by

$$Q^n_{i_1,i_2,\cdots,i_d} = \frac{1}{\prod_{i=1}^{d}\Delta x_i}\int_{C_{i_1,i_2,\cdots,i_d}} q(\bar{x}, t_n)d\bar{x},$$

where $C_{i_1,i_2,\cdots,i_d}$ is the grid cell at $i_1, i_2, \cdots, i_d$, where the index i_k corresponds to the coordinate x_k. However, it will be unusual to encounter very high-dimensional problems since most of wave propagation concerns the physical space. In most cases, we will only have two or three dimensions. For instance, in two dimensions, we have an equation of the form $q_t + f(q)_x + g(q)_y = 0$ for $q(x, y, t)$ and the cell average is given by $Q^n_{i,j} = \frac{1}{\Delta y \Delta x}\int_{C_{i,j}} q(x, y, t_n)dx\,dy$. The dimensional splitting algorithm will split the two dimensional problem up into a sequence of one-dimensional problems alternating between solving $q_t + f(q)_x = 0$ and $q_t + g(q)_y = 0$.

Dimensional splitting works quite well in most cases, and it allows to easily extend the one-dimensional algorithms to higher dimensions. However, it limits the Courant number and it is only first order accurate. Other approaches to higher dimensional problems do not have these issues. This includes using transverse wave propagation by using transverse solvers, as we will do in Chapters 8, 10 and 11. For a detailed exposition on the derivation of these and other algorithms, the reader is referred to [155].

Chapter 8

NUMERICAL METHODS FOR INTERFACE PROBLEMS

In this chapter, we show how to extend the methods described in Chapter 7 to deal with interfaces. We start by providing intuitive derivations of the equations. As the numerical methods explored in Chapter 7 require the output of a Riemann solver, we concentrate on developing Riemann problems across interfaces. We begin with a simple example using one-dimensional linear acoustic equations, which later is extended to two dimensions and into mapped grids, as demonstrated in [34]. Most of this material can be found in [153, 155].

Later in this chapter, we use a similar approach for Euler equations with interfaces. However, we incorporate an additional difficulty, the interface coupling between a compressible and an almost incompressible fluid. The basic concepts of this part can be found in [153, 155, 248] while more advanced issues, like the interface coupling, are part of our journal publications [52, 55, 53]. but fit better in this introductory chapter. We also provide an exact solution for the Euler equations with a stiffened equation of state and jump in the material parameters. This is required by our Riemann solver, and it is fundamental to validate our method. This exact solution is also part of our journal publication [53]. In the last section of the chapter, we introduce elasticity equations. We show how to solve the Riemann problems with interfaces and with mapped grids. The main ideas developed in this last section can be found in [75, 151, 153, 155]. Other relevant methods to deal with interfaces that are not explored in this chapter can be found in [43, 75, 161, 220, 222, 229, 252, 260].

8.1 Acoustic equations with interfaces

In this section, we provide a brief intuitive derivation of the acoustics equations. We also derive the normal Riemann solver for one-dimensional acoustic equations with an interface. We proceed by extending the problem to two dimensions and introducing the transverse Riemann solver for two-dimensional acoustics in a Cartesian grid. These solvers are further extended for general quadrilateral mapped grids with an interface, and it is shown how to implement them into Clawpack [44]. Some of these methods and derivations can be found in [155].

8.1.1 Linear Acoustics equations

The linear acoustic equations can be obtained by linearizing the conservation of mass and momentum for an element of fluid. The conservation of mass and momentum are given by

$$\frac{\partial \rho}{\partial t} + \nabla \cdot (\rho \bar{u}) = 0, \qquad \frac{d(\rho \bar{u})}{dt} = -\nabla P,$$

where d/dt denotes the material derivative: $\frac{d}{dt} = \frac{\partial}{\partial t} + \bar{u} \cdot \nabla$. In one dimension, $\bar{u} = u$ and these can be easily rewritten as,

$$\begin{aligned} \rho_t + (\rho u)_x &= 0, \\ (\rho u)_t + (\rho u^2 + P(\rho))_x &= 0, \end{aligned}$$

where we assumed the pressure is a function of the density. Linearizing the equation around ρ_0 and $u_0 = 0$, we obtain the simpler system for the perturbations,

$$\begin{aligned} \rho_t + (\rho u)_x &= 0, \\ (\rho u)_t + P(\rho_0)\rho_x &= 0. \end{aligned}$$

where ρ and u are now the perturbations around ρ_0 and $u_0 = 0$. As perturbations on the pressure and density satisfy $p \approx P'(\rho_0)\rho$ and $\rho u \approx \rho_0 u$, we can rewrite the system of linear acoustic equations as

$$\begin{bmatrix} p \\ u \end{bmatrix}_t + \underbrace{\begin{bmatrix} 0 & K_0 \\ 1/\rho_0 & 0 \end{bmatrix}}_{A} \begin{bmatrix} p \\ u \end{bmatrix}_x = 0,$$

with $K_0 = \rho_0 P'(\rho_0)$ the bulk modulus of compressibility. This can be easily extended to two and three dimensions respectively,

$$\begin{bmatrix} p \\ u \\ v \end{bmatrix}_t + \underbrace{\begin{bmatrix} 0 & K_0 & 0 \\ 1/\rho_0 & 0 & 0 \\ 0 & 0 & 0 \end{bmatrix}}_{A} \begin{bmatrix} p \\ u \\ v \end{bmatrix}_x + \underbrace{\begin{bmatrix} 0 & 0 & K_0 \\ 0 & 0 & 0 \\ 1/\rho_0 & 0 & 0 \end{bmatrix}}_{B} \begin{bmatrix} p \\ u \\ v \end{bmatrix}_y = 0$$

$$\begin{bmatrix} p \\ u \\ v \\ w \end{bmatrix}_t + \underbrace{\begin{bmatrix} 0 & K_0 & 0 & 0 \\ 1/\rho_0 & 0 & 0 & 0 \\ 0 & 0 & 0 & 0 \\ 0 & 0 & 0 & 0 \end{bmatrix}}_{A} \begin{bmatrix} p \\ u \\ v \\ w \end{bmatrix}_x + \underbrace{\begin{bmatrix} 0 & 0 & K_0 & 0 \\ 0 & 0 & 0 & 0 \\ 1/\rho_0 & 0 & 0 & 0 \\ 0 & 0 & 0 & 0 \end{bmatrix}}_{B} \begin{bmatrix} p \\ u \\ v \\ w \end{bmatrix}_y + \underbrace{\begin{bmatrix} 0 & 0 & 0 & K_0 \\ 0 & 0 & 0 & 0 \\ 0 & 0 & 0 & 0 \\ 1/\rho_0 & 0 & 0 & 0 \end{bmatrix}}_{C} \begin{bmatrix} p \\ u \\ v \\ w \end{bmatrix}_z = 0$$

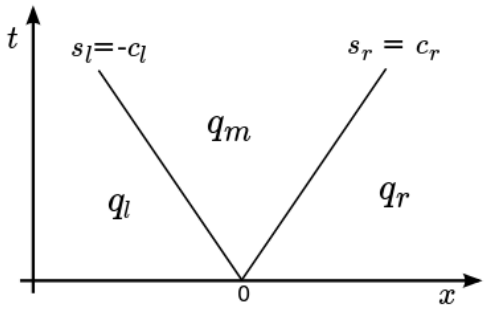

Figure 8.1: Structure of the solution to the Riemann problem in the $x - t$ plane.

where the velocity in x, y, z is u, v, w and the matrices A, B and C have those forms depending on the dimensionality.

8.1.2 Riemann problem with an interface

In one dimension we need to solve $q_t + Aq_x = 0$ with

$$q = \begin{bmatrix} p \\ u \end{bmatrix} \qquad A = \begin{bmatrix} 0 & K_0 \\ 1/\rho_0 & 0 \end{bmatrix}, \qquad q(x,0) = \begin{cases} q_l & \text{if } x \le 0, \\ q_r & \text{if } x > 0. \end{cases}$$

This is the Riemann problem to the one-dimensional acoustic equations, which we introduced in Section 7.1.1. Its solution can be obtained by transforming the system into two uncoupled advection equations, see [155]. When transformed back to the original coordinates the solution will have the structure shown in Figure 8.1: two propagating acoustic waves (one to the left and one to the right) with speeds c_l and c_l, the two initial conditions q_l and q_r in the far field and one more extra state in between the waves, q_m. If we can find c_l, c_r and q_m, we have solved the problem.

We will show how to obtain the solution to this Riemann problem, for details on the methodology, see [155]. We will begin by obtaining the eigenvector and eigenvalues of A. These are given by,

$$\lambda_l = -c_0, \quad r_l = \begin{bmatrix} -Z_0 \\ 1 \end{bmatrix}, \qquad \lambda_r = c_0, \quad r_r = \begin{bmatrix} Z_0 \\ 1 \end{bmatrix},$$

where $c_0 = \sqrt{K_0/\rho_0}$ is the speed of sound and $Z_0 = \rho_0 c_0$ is the impedance of the medium. The speeds of the left and right going acoustic waves are given by the eigenvalues: $s_l = -c_0$, $s_r = c_0$. However, we would like to have different materials in the left and right side, which

means different density (ρ_l and ρ_r) and bulk modulus (K_l and K_l), therefore

$$s_l = -c_l \qquad s_r = c_r \qquad \text{with :} \quad c_m = \sqrt{\frac{K_m}{\rho_m}},$$

with $m = l, r$. Using the fact that $K_m = c_m^2 \rho_m$ and recalling the specific acoustic impedance is given by $Z_m = \rho_m c_m = K_m / \sqrt{K_m/\rho_m}$, we can write the matrix of column eigenvectors $R = [r_l, r_r]$ as,

$$R = \begin{bmatrix} -Z_l & Z_r \\ 1 & 1 \end{bmatrix},$$

Let $\delta Q = [\Delta_p, \Delta_u]^T$ be the jump of q across the discontinuity. In order to solve the Riemann problem, we need to expand the jump across the discontinuity Δq as a linear combination of the eigenvectors,

$$\alpha_l r_l + \alpha_r r_r = \Delta q, \qquad \Rightarrow \qquad R\alpha = \Delta q.$$

We will need to obtain the value of α, solving this equation yields

$$\alpha_l = \frac{-\Delta_p + \Delta_u Z_r}{Z_l + Z_r}, \qquad \alpha_r = \frac{\Delta_p + \Delta_u Z_l}{Z_l + Z_r}.$$

We already know the wave speeds c_l and c_r and the initial states q_l and q_l. We only need to know the middle state q_m, which will be given by

$$q_m = q_l + \alpha_l r_l = q_l - \alpha_r r_r.$$

This solves the Riemann problem.

8.1.3 Riemann problem in 2D

When solving a two-dimensional problem, like $q_t + Aq_x + Bq_y = 0$, we can use dimensional splitting or un-split methods [155]. In any of those cases, we will need to solve a Riemann solver in the normal direction. In the x direction, this will involve solving $q_t + Aq_x = 0$ and in the y direction it will solve $q_t + Bq_y = 0$. We will only solve it in the x direction since it is completely analogous to solve it for the y direction. The procedure to solve this problem will be the same than for the one-dimensional Riemann problem already explained, so we will present the solution very briefly. As we already showed before, q will be a vector $q = (p, u, v)^T$ with p the pressure and u, v the velocities in x and y. We will start with the

A matrix,

$$A = \begin{bmatrix} 0 & K_0 & 0 \\ 1/\rho_0 & 0 & 0 \\ 0 & 0 & 0 \end{bmatrix}, \qquad R_A = \begin{bmatrix} -Z_0 & 0 & Z_0 \\ 1 & 0 & 1 \\ 0 & 1 & 0 \end{bmatrix},$$

where $R_A = [r_l, r_0, r_r]$ is the matrix of column eigenvectors and $Z_0 = \rho_0 c_0$ and $c_0 = \sqrt{K_0/\rho_0}$. Solving the system $R_A \alpha = \delta q = [\Delta_p, \Delta_u, \Delta_v]^T$, we obtain

$$\alpha_L = \frac{-\Delta_p + Z_0 \Delta_u}{2Z_0}, \qquad \alpha_0 = \Delta_v, \qquad \alpha_R = \frac{\Delta_p + Z_0 \Delta_u}{2Z_0},$$

and the speed $s_l = -c_0$, $s_0 = 0$ and $s_r = c_0$ correspond to the eigenvalues of the matrix A. Note in this case we assumed the same material on both sides. Comparing to the results in the previous section, it is straightforward to extend it to the case of different materials across an interface at $x = 0$. With this information, we can reconstruct the solution to the Riemann problem as before. The construction of the solution for the matrix B in the y direction is analogous.

Clawpack [44] has all the framework required to solve hyperbolic equations by solving Riemann problems on each grid cell. The key ingredient we need to feed into Clawpack is the Riemann solver. In order to implement the solution into Clawpack, we need to rewrite it in its wave formulation, where we update the value at cell $Q^n_{i,j}$, with i, j the indexes in space and n in time following the methods in Sections 7.4 and 7.3. The simplest way to couple the two dimensions is dimensional splitting [155], which will first use Godunov method[1] when sweeping in the i direction (normal direction) of the computational domain, and repeat the same in the j direction (transverse direction). Also, note Godunov's method requires the output of two Riemann problems: the one in edge $i - 1/2$ and the one in $i + 1/2$. The output of the Riemann solver routine for Clawpack should be given by the waves speeds and wave fluctuations. The waves speeds we already know from the eigenvalues in the previous section. In order to calculate the waves fluctuations $A^{\pm}\Delta Q_{i-1/2,j}$ from the left edge, we first need the waves given by $W_i = \alpha_i r_i$ with $i = l, 0, r$ and r_i the corresponding eigenvectors calculated previously. Solving the Riemann problem in the right edge is completely analogous. The positive and negative wave fluctuations $A^{\pm}\Delta Q_{i-1/2,j}$ will be given in terms of the speeds(eigenvalues) and the waves, $A^{+}\Delta Q_{i-1/2,j} = s_r W_r$, $A^{-}\Delta Q_{i-1/2,j} = s_l W_l$. Note the wave W_0 doesn't really make any difference in the fluctuations since it has speed zero.

[1] We mean high-resolution implementations of Godunov method, as shown in Section 7.4.

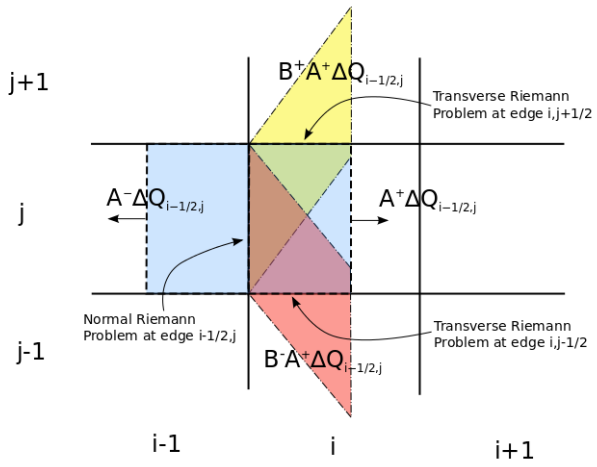

Figure 8.2: Structure of the transverse Riemann problem for computational grid cells. The left-going and right going fluctuations of the normal Riemann problem at the edge between grid cells $(i-1, j)$ and (i, j) is shown. The right-going fluctuation $A^+\Delta Q_{i-1/2,j}$ is decomposed into the up-going fluctuation $B^+A^+\Delta Q_{i-1/2,j}$ and the down-going fluctuation $B^-A^+\Delta Q_{i-1/2,j}$ by employing transverse Riemann solvers.

8.1.4 Transverse Riemann problem

In order to obtain second order accuracy using unsplit methods (not dimensional splitting) and improve stability in two-dimensional hyperbolic problems, the notion of a transverse Riemann solver was introduced in [154]. The transverse solver requires splitting the normal wave fluctuations $A^\pm\Delta Q_{i-1/2,j}$ at edge $i-1/2$ into transverse wave fluctuations $B^\pm A^+\Delta Q_{i-1/2,j}$ and $B^\pm A^-\Delta Q_{i-1/2,j}$; the former decomposition is shown in the following figure and explained in detail on [155].

We will only focus on $B^\pm A^+\Delta Q_{i-1/2,j}$, since the case for the left propagating wave is analogous. We begin by decomposing the normal wave fluctuation into a linear combination of transverse waves, which will follow the same equations and jacobian as before, so we obtain

$$A^+\Delta Q_{i-1/2,j} = R_y\beta = \beta_d r_d + \beta_m r_m + \beta_u r_u,$$

where the subindexes d, m and u denote down, middle and upper direction, and r_i are the corresponding column eigenvectors of B if sweeping in the x direction, or of A if sweeping on the y direction. In this case, we will only consider the case when sweeping in the x direction,

since the other is analogous, so the matrix of eigenvectors of B is $R_y = [r_d, r_m, r_u]$,

$$R_y = \begin{bmatrix} -Z_0 & 0 & Z_0 \\ 0 & 1 & 0 \\ 1 & 0 & 1 \end{bmatrix}.$$

We solve the system in the same way than the system for α. When we add the right input parameters for the eigenvectors, β is given by

$$\beta_d = \frac{-A_1^+ + z_0 A_3^+}{2Z_0}, \qquad \beta_m = A_2^+, \qquad \beta_u = \frac{A_1^+ + z_0 A_3^+}{2Z_0},$$

where the fluctuation vector $A^+\Delta Q_{i-1/2,j} = [A_1^+, A_2^+, A_3^+]$. The transverse wave speeds are given by the eigenvalues of R_y

$$s_d = -c_0 \quad s_m = 0 \quad s_u = c_0,$$

with $c_0 = \sqrt{K_0/\rho_0}$. The transverse waves are given by $W_i = \beta_i r_i$ with $i = d, m, u$, so the fluctuations that will be required to be fed into Clawpack are given by

$$B^+A^+\Delta Q_{i-1/2,j} = s_u W_u \qquad B^-A^+\Delta Q_{i-1/2,j} = s_d W_d.$$

Note once again the middle wave has speed zero, so it doesn't affect these fluctuations. This solution again assumed there was no interface. Instead of showing how this solution can be extended to the case with an interface, we will solve the most general version of the normal and transverse Riemann problem in the next section. This includes implementation of the solvers in a mapped grid and with an interface.

8.1.5 Riemann solvers across interface in a mapped grid

In order to solve the normal and transverse acoustics Riemann problems for general quadrilateral mapped grids, we will need to solve them in the normal and transverse direction to a grid cell. We can do this by the same process as before, but using a matrix that represents the problem in the normal or transverse direction. The Riemann problem in the normal direction of a grid edge is $q_t + A_n q_n = 0$, where q_n is the derivative in the normal to the edge direction, $A_n = n_x A + n_y B$, and $\hat{n} = (n_x, n_y)$ is the normal to the edge where the –normal or transverse– Riemann problem is being solved. The Jacobian matrix is

$$\mathbf{A_n} = \begin{bmatrix} 0 & n_x K_0 & n_y K_0 \\ n_x/\rho_0 & 0 & 0 \\ n_y/\rho_0 & 0 & 0 \end{bmatrix}.$$

Using different materials on the left and right side, the matrix of eigenvectors $R = [r_l, r_0, r_r]$ is now

$$R = \begin{bmatrix} -Z_l & 0 & Z_r \\ n_x & -n_y & n_x \\ n_y & n_x & n_y \end{bmatrix},$$

with $Z_i = \rho_i c_i$ and $c_i = \sqrt{K_i/\rho_i}$, where we now have two different values for the impedance, $i = l, r$, on the left and right side indicating different materials. The respective eigenvalues are again given by $s_l = -c_l$, $s_0 = 0$ and $s_r = c_r$.In order to solve the Riemann problem, we need to solve again $R\alpha = \delta q = [\Delta_p, \Delta_u, \Delta_v]^T$,

$$\alpha_l = \frac{-\Delta_p + Z_r(n_x\Delta_u + n_y\Delta_v)}{Z_l + Z_r} \qquad \alpha_0 = n_x\Delta_v - n_y\Delta_u \qquad \alpha_r = \frac{\Delta_p + Z_l(n_x\Delta_u + n_y\Delta_v)}{Z_l + Z_r}$$

In the Clawpack implementation, when employing the mapped grid, we need to scale the wave speeds s in the wave fluctuations by the factor $\gamma_x = dy_{phy}/dy_{com}$ if sweeping in the x direction, or $\gamma_y = dx_{phy}/dx_{com}$ if sweeping in the y direction. The quantity dx_{phy} denotes mesh grid spacing in x in the physical domain and dx_{com} in the computational one. The fluctuation for the normal solver in the mapped grid should then be

$$A^+\Delta Q^{map}_{i-1/2,j} = \gamma s_r \alpha_r r_r, \qquad A^-\Delta Q^{map}_{i-1/2,j} = \gamma s_l \alpha_l r_l,$$

where γ should be γ_x or γ_y depending on the sweeping direction. Analogously, the up-going and down-going eigenvectors for the transverse solver will be in principle the same, but with their corresponding normals $r_d = [Z_d, n_{dx}, n_{dy}]^T$, $r_u = [Z_d, n_{ux}, n_{uy}]^T$, and eigenvalues $s_u = c_u$ and $s_d = -c_d$. Solving the usual system results in,

$$\beta_d = \frac{-A_1^+ + Z_u(n_{mx}A_2^+ + n_{my}A_3^+)}{Z_u + Z_d}$$
$$\beta_u = \frac{A_1^+ + Z_d(n_{ux}A_2^+ + n_{uy}A_3^+)}{Z_u + Z_d},$$

where $A^+\Delta Q_{i-1/2,j} = [A_1^+, A_2^+, A_3^+]$, $\hat{n_d} = (n_{mx}, n_{my})$ is the normal to the lower edge of the middle cell and $\hat{n_u} = (n_{ux}, n_{uy})$ is the normal to lower edge of the upper cell. The fluctuations for the transverse solver in the mapped grid with an interface are then given by

$$B^+A^+\Delta Q^{map}_{i-1/2,j} = \gamma_u s_u \beta_u r_u$$
$$B^-A^+\Delta Q^{map}_{i-1/2,j} = -\gamma_m s_d \beta_d r_d,$$

where γ_u correspond to the scaling ratio of the bottom edge of the upper cell and γ_m to the scaling ratio of the bottom edge of the middle cell. The same process can be repeated for the left normal fluctuation $A^{-}\Delta Q_{i-1/2,j}$. Note the direction of the normal solver is the direction in which we are sweeping, which could be x or y direction of our computational domain.

8.2 One-dimensional Euler equations with interfaces

We use the nonlinear compressible Euler equations for compressible inviscid flow, which allow accurate modeling of shock wave formation and propagation. These equations model the conservation of mass, momentum, and energy and provide a direct connection to temperature, which may be important for some biomedical experiments, as shown in Section 10. In this type of experiment, we are not concerned with large-scale movement of the fluid, so viscosity does not play an important role; therefore, employing the inviscid equations is appropriate. In order to model different materials, we use different parameters in the equations of state (EOS) for each material, so we can model the different materials with the same equations. The one-dimensional Euler equations are

$$\begin{bmatrix} \rho \\ \rho u \\ E \end{bmatrix}_t + \begin{bmatrix} \rho u \\ \rho u^2 + p \\ u(E+p) \end{bmatrix}_x = 0, \tag{8.1}$$

where ρ is density, u velocity, E the internal energy and p the pressure and the subcripts x, t denote partial derivatives with respect x and t.

8.2.1 The Tammann equation of state (EOS)

The system of Eqs. 8.1 is closed with the addition of an EOS. It is usually given as a relation between pressure, density and specific internal energy, i.e. $p = p(\rho, e)$. The most well known EOS is the one for an ideal gas $p = (\gamma - 1)\rho e$, where γ is the ratio of heat capacities. While this EOS is very good for describing the behavior of most gases, it is not appropriate for modeling nearly incompressible materials like water or elastic solids.

Several alternatives exist; in this work, we will use the stiffened gas EOS, also known as the Tammann EOS. This equation of state is very useful to model a wide range of fluids even in the presence of strong shock waves [74]. The Tammann EOS is given by

$$p = (\gamma - 1)\rho e - \gamma p_\infty, \tag{8.2}$$

where γ and p_∞ can be determined experimentally for different materials. The internal energy e is related to the total energy E by $E = \rho e + \frac{1}{2}\rho u \cdot u$. The Tammann EOS and the ideal gas EOS are the same except for the extra term $-\gamma p_\infty$, where $\gamma,\ p_\infty > 0$. For fluids

with $p_\infty \gg p_{atm}$ (atmospheric pressure), the relative change in density, when changing the pressure, is very small. Consequently, the Tammann EOS is a good approximation for nearly incompressible fluids and can also be used to model acoustic waves in some elastic solids, like plastic. For sufficiently weak shocks the Tammann EOS can be further simplified to the Tait EOS, see [74], but for greater generality we use the Tammann EOS. Table 9.1 shows the Tammann EOS parameters for the materials used in the simulations presented in later chapters.

8.2.2 The Riemann problem for Euler equations

The Euler equations are a nonlinear hyperbolic system of conservation laws, so they can be efficiently solved with high-resolution shock-capturing finite volume methods (FVM). This is done by using the wave propagation algorithms described in [155] and implemented in Clawpack [44]. In order to be able to solve the equations numerically, we need to provide the Riemann solver, see Section 7.1.1. The Riemann problem for Euler equations can be stated as

$$\begin{aligned} & q + f(q)_x = 0, \qquad q(x,0) = \begin{cases} q_l & \text{if } x < 0 \\ q_r & \text{if } x > 0, \end{cases} \\ \text{with} \quad & q = [\rho, \rho u, E]^T \qquad f(q) = [\rho u, \rho u^2 + p, u(E+p)]^T, \end{aligned} \tag{8.3}$$

where the state vector q corresponds to the density, momentum and total energy. In general the EOS relates the pressure p to the density and internal energy, $p(\rho, e)$, where the internal energy can be obtained from $E = \rho e + \frac{1}{2}\rho u \cdot u$. An example of an EOS was given in section 8.2.1. The Euler equations in this work are solved by implementing a hybrid Riemann HLLC-exact type approximate solver for one-dimensional Euler equations with interfaces. This solver couples an HLLC approximate Riemann solver to an exact Riemann solver for the Tammann EOS and an Eulerian-Lagrangian description coupling at the interface. As the interfaces are represented by contact discontinuities, the HLLC solver is ideal to deal accurately with interface problems. Furthermore, the exact solver will serve as a reference solution to verify the numerical method.

From the well-known solution to the Euler equations for an ideal EOS [155, 248], we expect our solution will consist of two acoustic waves, the 1-wave and 3-wave (rarefactions or shocks), and a contact discontinuity, the 2-wave between them. The n-wave refers to the wave corresponding to the n-characteristic field (see [155]). This will separate our system in four states, q_l, q_{*l}, q_{*r}, q_r. The left state q_l will be connected to the state q_{*l} by a 1-wave, a shock wave or a rarefaction. The state q_{*l} and q_{*r} will be connected by a 2-wave, the contact discontinuity with equal pressure p_* and velocity u_* but different density on both sides. The states q_{*r} and q_r are connected by a 3-wave, which is a shock wave or a rarefaction.

The method can be extended to two dimensions by using dimensional splitting or trans-

verse solvers. The geometrical source terms can be resolved using a splitting method, see Section 7.6 or [155, 156]. In the next paragraphs, we show the modified HLLC Riemann solver and the exact Riemann solver for the Tammann EOS with discontinuous parameters.

8.2.3 A modified HLLC solver

The HLLC (Harten-Lax-van Leer-Contact) solver is an approximate Riemann solver for Eq. 8.3. This solver was derived in detail in Section 7.5.2. In this section, we will give an overview of the HLLC solver and provide a modified version that works better with interfaces between compressible and almost incompressible materials. The main idea of the HLLC solver is, given the left and right going wave speeds s_l and s_r by some algorithm or approximation, assume a wave configuration of three waves separating four constant states. The Riemann solution to the one-dimensional Euler equations consists of three waves, two acoustic waves with a contact discontinuity in between. The approximate solution for this method will be of the form

$$\tilde{q}(x,t) = \begin{cases} q_l & \text{if } \frac{x}{t} \leq s_l \\ q_{*l} & \text{if } s_l \leq \frac{x}{t} \leq s_*, \\ q_{*r} & \text{if } s_* \leq \frac{x}{t} \leq s_r, \\ q_r & \text{if } \frac{x}{t} \geq s_r, \end{cases}$$

where s_* is the approximate wave speed of the contact discontinuity. Assuming we can obtain s_l and s_r, we only need to find q_{*l}, q_{*r} and s_* to solve the problem. These quantities can be obtained by integrating over a box in the x,t plane using the Rankine-Hugoniot conditions and assuming constant pressure and normal velocity across the contact discontinuity, see [248]. The desired states and contact discontinuity speed are given by

$$q_{*k} = \frac{s_k q_k - f_k + p_* D}{s_l - s_*}, \quad \text{with:} \quad D = [0, 1, s_*],$$
$$s_* = \frac{p_r - p_l + \rho_l u_l (s_l - u_l) - \rho_r u_r (s_r - u_r)}{\rho_l (s_l - u_l) - \rho_r (s_r - u_r)},$$

where ρ_k, u_k with $k = l, r$ are the left or right density and speed in the Euler equations [248].

In order to calculate the wave speeds s_l and s_r, we will need to calculate the sound speed. This is where we require the EOS. A simple estimate is the one given by Davis [248] as

$$s_l = \min\{u_l - c_l, u_r - c_r\} \quad s_r = \max\{u_l + c_l, u_r + c_r\},$$

where u_k is the normal velocity and c_k is the sound speed on each side, $k = l, r$. Note that the easiest way to calculate the speed of sound is using the EOS $p = p(\rho, e)$. It is usually

given in the form,

$$c = \sqrt{\left.\frac{\partial p(\rho, e)}{\partial \rho}\right|_s} = \sqrt{\frac{\partial p(\rho, e)}{\partial \rho} + \frac{p(\rho, e)}{\rho^2}\frac{\partial p(\rho, e)}{\partial e}}, \tag{8.4}$$

where s is the entropy, and the first derivative is taken along the isentropic curve. As pointed out in Section 7.5.2, a possible improvement is to employ Roe averages in wave speed estimates $s_l = \min\{u_l - c_l, \tilde{u} - \tilde{c}\} \quad s_r = \max\{\tilde{u} + \tilde{c}, u_r + c_r\}$ where $\tilde{u}$ and $\tilde{c}$ are the Roe averages of the normal velocity and speed of sound respectively.

The HLLC solver just discussed works well for the one-dimensional Euler equations with an ideal gas EOS. However, we want to implement the HLLC solver with the Tammann EOS across an air-water or air-plastic interface. The difference between the parameters for different materials in the Tammann EOS are of several orders of magnitude as shown in Table 9.1. This generates instabilities in the HLLC solver, more so in the multi-dimensional setting. The instability is generated because we model the interfaces as being fixed in space; however, there is always a displacement of the contact discontinuity, i.e. the interface, even when the material is almost incompressible. The displacement is very small indeed, but it is big enough to render our numerical method unusable. In order to solve this issue, we model each material in Eulerian coordinates using the usual HLLC solver; if any of the cells is next to the interface, we modify our original HLLC or exact solver to work in Lagrangian coordinates, where the interface is actually fixed with respect to the reference frame. This is done by displacing the frame of reference by s_*,

$$\tilde{s_l} = s_l - s_* \quad \tilde{s_*} = 0 \quad \tilde{s_r} = s_r - s_* \tag{8.5}$$

For instance, assume we are running a one-dimensional simulation of the Euler equations, with a fixed interface modeled by a jump in the parameters of the EOS. The interface is aligned to the edge between cells i and $i+1$, the transformed Riemann solver will be as shown in Figure 8.3. This will ensure the contact discontinuity velocity is zero and consequently, the interface is modeled as fixed. The wave contributions will be the correct ones since we are just modifying the wave velocity and not the solution q's. There is, of course, an error made at the interface when coupling the two descriptions; however, as the displacements of the interface are very small due to very low compressibility, this error is small, and it doesn't cause instabilities as before.

In order to provide better accuracy along the interface, we will also implement an exact Riemann solver for the Tammann EOS. The HLLC solver will be used to model each of the materials in Eulerian coordinates, and the exact solver will be used to solve the Riemann problems at the interface. The transformation to Lagrangian coordinates for the exact solver is equivalent to the one in Eq. 8.5.

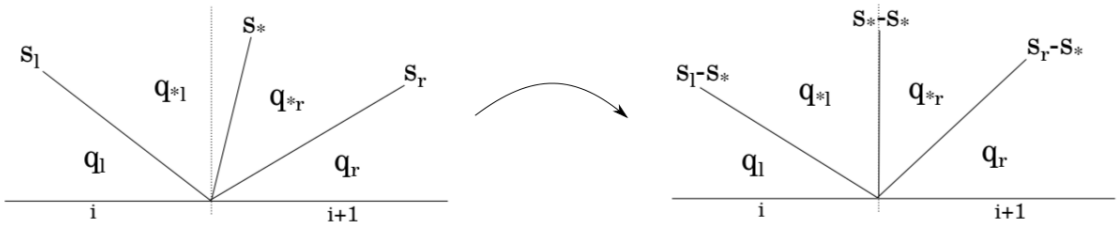

Figure 8.3: Transformation for the HLLC Riemann solver between grid cells i and $i+1$ from Eulerian coordinates to Lagrangian coordinates. The transformation can be employed for other Riemann solvers too.

8.2.4 Exact Riemann solver with Tammann EOS

The Riemann problem (Eq. 8.3) sometimes can also be solved exactly; the form of the solution will depend on the equations and the EOS being used. An exact solver for the Euler equations coupled with the Tammann EOS for constant parameters was given by Ivings & Toro [126]. In the next paragraphs, we obtain the exact Riemann solver for the Euler equations coupled with the Tammann EOS with different constant parameters on the left and right states. This can be extended numerically to general varying parameters, by averaging them on each cell and using this Riemann solver to provide the solution. The solver is based on the one provided in [126]; however, it extends it to include a jump in the Tammann EOS parameters between the left and right state.

We consider the one-dimensional Riemann problem for the Euler equations with the Tammann EOS. We want to solve the one-dimensional Euler equations,

$$\begin{bmatrix} \rho \\ \rho u \\ E \end{bmatrix}_t + \begin{bmatrix} \rho u \\ \rho u^2 + p \\ u(E+p) \end{bmatrix}_x = 0, \tag{8.6}$$

where ρ is density, u velocity, E the internal energy and p the pressure and the subcripts x, t denote partial derivatives with respect x and t. The Tammann EOS is given by $p = \rho e(\gamma_k - 1) - \gamma_k p_{\infty k}$ where e the specific internal energy and $k = l, r$ determines which coefficients to use for the EOS. The initial conditions are given by the left and right constant states $q_l = [\rho_l, \rho_l u_l, E_l]$ and $q_r = [\rho_r, \rho_r u_r, E_r]$. Note that the state of the system can also be written in terms of the primitive variables $[\rho, u, p]$ by using the equation of state.

As we mentioned before, the solution of the Euler equations will consist of the 1-wave and 3-wave (rarefactions or shocks), and a contact discontinuity, the 2-wave between them. The system will have four different solution states, q_l, q_{*l}, q_{*r}, q_r separated by the three waves. In order to figure out if the 1-wave and 3-wave are rarefactions or shocks, we will need to create

a function of the middle state pressure p_* that ensures the velocity u_* across the contact discontinuity is consistent. As we know the velocity on the left state u_l should be connected by a rarefaction or shock to u_*, we can calculate $u_* = u_l + [u]_1$ with $[u]_1$the jump of the velocity across the 1-wave. In a similar manner, we also know the 3-wave should be a shock or rarefaction, so we can calculate $u_* = u_r - [u]_3$; therefore, we define

$$\begin{aligned} \phi_l(p_*) = u_* = u_l - \mathcal{F}_l(p_*), \\ \phi_r(p_*) = u_* = u_r + \mathcal{F}_r(p_*). \end{aligned} \tag{8.7}$$

where $\mathcal{F}_{l,r}(p_*) = -[u]_{1,3}$ will change form depending if it's a shock or a rarefaction (signs were chosen for notation consistency). As we expect these two equations yield the same contact discontinuity velocity u_*, then

$$\Phi(p_*) = \phi_r(p_*) - \phi_l(p_*) = 0. \tag{8.8}$$

This nonlinear equation for p_* will yield the pressure p_* that provides consistency between the type of waves (rarefactions or shocks), their speeds and the contact discontinuity velocity u_*. As we mentioned before, the shape of $\phi_k(p_*)$ will depend on whether the states are connected by a shock wave or rarefaction. Once the p_* has been found, the contact discontinuity velocity can be found from Eq. 8.7. The only remaining quantity to calculate from the primitive variables is the density. Furthermore, we also need the speeds of the 1-wave and 3-wave. Once we write the explicit equations for our system, it will be clear how to obtain these quantities.

Before writing the equations explicitly, we should first note that having a rarefaction or shock in the 1-wave and 3-wave will depend on the pressure p_*. How can we know which one, can be answered by physical intuition. If the pressure is higher on the side toward which the wave is propagating, it will yield a rarefaction. If the pressure is lower, it will be a shock. This intuition is formalized as the entropy condition [155]. In the Euler equations, this yields four possible cases for the value $\Phi(p_*)$ of Eq. 8.8, just as in the solution using the ideal gas EOS [126, 155]:

- 1-rarefaction, 3-rarefaction: $p_* < p_l$ and $p_* < p_r$
  $\Phi(p_*) = \phi_r^R(p_*) - \phi_l^R(p_*)$,

- 1-shock, 3-rarefaction $p_l \leq p_* \leq p_r$
  $\Phi(p_*) = \phi_r^R(p_*) - \phi_l^S(p_*)$,

- 1-rarefaction, 3-shock $p_r \leq p_* \leq p_l$
  $\Phi(p_*) = \phi_r^S(p_*) - \phi_l^R(p_*)$,

- 1-shock, 3-shock: $p_* > p_l$ and $p_* > p_r$
  $\Phi(p_*) = \phi_r^S(p_*) - \phi_l^S(p_*)$,

where the index S, R indicates if the ϕ was obtained by using the Rankine-Hugoniot equations to connect states by shocks or the Riemann invariants to connect them by rarefactions respectively.

In the next paragraphs, we derive the functions ϕ_k^μ for all the four cases with $k = l, r$ and $\mu = R, S$. We show how to obtain the density and the missing wave speeds. In order to do so, we employ the Rankine-Hugoniot equations and the Riemann invariants. We will denote the speed of the 1-wave, s_l, the 2-wave, s_*, and the 3-wave s_r.

Rankine-Hugoniot conditions for shock waves

As we know the 1-wave and the 3-wave could each be a shock. In that case, the velocity of the wave, i.e. the shock, will be given by the Rankine-Hugoniot conditions. We will generalize this method for the 1-wave velocity s_l and the 3-wave velocity s_r, by employing s_k, with $k = l, r$.

The Rankine-Hugoniot conditions are in general given by $s_k\,(q_k - q_{*k}) = f(q_k) - f(q_{*k})$, where q is the vector state variable, $f(q)$ the vector state flux and s_k the shock velocity. For the Euler equations this can be easily rewritten as [126],

$$\rho_k \omega_k = \rho_{*k} \omega_*, \tag{8.9}$$

$$\rho_k \omega_k^2 + p_k = \rho_{*k} \omega_*^2 + p_{*k}, \tag{8.10}$$

$$\frac{1}{2}\omega_k^2 + h_k = \frac{1}{2}\omega_*^2 + h_{*k}, \tag{8.11}$$

where $k = l, r$, $\omega_k = u_k - s_k$, $\omega_* = u_* - s_k$ and the specific enthalpy is given by $h = e + (p + p_\infty)/\rho$ with e the specific internal energy that relates to the internal energy of our original variables by $E = \rho e + \rho u^2/2$. We will use these relations to find the $\phi_K^S(p_*)$ of Eq. 8.8 and the wave speeds s_k.

Finding $\phi_l^S(p_*)$ and $\phi_r^S(p_*)$ and s_l and s_r: We can start by defining the mass fluxes $\mathcal{Q}_k$ for $k = l, r$ as

$$\mathcal{Q}_l = \rho_l \omega_l = \rho_{*l} \omega_* \tag{8.12}$$

$$\mathcal{Q}_r = -\rho_r \omega_r = -\rho_{*r} \omega_*. \tag{8.13}$$

As $\omega_k = u_k - s_k$, from these two equations we can obtain the wave speeds in terms of Q_l and $\mathcal{Q}_r$,

$$s_l = u_l - \frac{\mathcal{Q}_l}{\rho_l}, \quad s_r = u_r + \frac{\mathcal{Q}_r}{\rho_r}. \tag{8.14}$$

We still need to find $\mathcal{Q}_l$ and $\mathcal{Q}_r$, so we substitute Eq. 8.12 and Eq. 8.13 into Eq. 8.10 to immediately obtain

$$\mathcal{Q}_l = \frac{\tilde{p}_{*l} - \tilde{p}_l}{\omega_l - \omega_*} = \frac{p_* - p_l}{u_l - u_*} \tag{8.15}$$

$$\mathcal{Q}_r = -\frac{\tilde{p}_{*r} - \tilde{p}_r}{\omega_r - \omega_*} = -\frac{p_* - p_r}{u_r - u_*}, \tag{8.16}$$

where $\tilde{p}_\kappa = p_\kappa + p_{\infty\kappa}$ is defined to simplify future notation with $\kappa = l, *l, *r$ and r. Note that $\tilde{p}_{*l} \neq \tilde{p}_{*r}$ and that $\tilde{p}_{*k} - \tilde{p}_k = p_* - p_k$ since $p_* = p_{*l} = p_{*r}$ and $p_{\infty k} = p_{\infty *k}$ $(k = l, r)$. Solving for u_* we obtain the equations,

$$\begin{aligned} u_* &= u_l - \frac{\tilde{p}_{*l} - \tilde{p}_l}{\mathcal{Q}_l} = \phi_l^S(p_*) \\ u_* &= u_r + \frac{\tilde{p}_{*r} - \tilde{p}_r}{\mathcal{Q}_r} = \phi_r^S(p_*) \end{aligned} \tag{8.17}$$

Comparing to Eqs. 8.7, we notice $\mathcal{F}_k(p_*) = \frac{p_* - p_k}{\mathcal{Q}_k}$. We also notice we have almost obtained the ϕ functions we are looking for, though we still need to find $\mathcal{Q}_l$ and $\mathcal{Q}_r$ in terms of known variables.

Finding $\mathcal{Q}_l$ and $\mathcal{Q}_r$: From Eq. 8.12 and Eq. 8.15, we know that

$$\frac{\tilde{p}_{*l} - \tilde{p}_l}{\omega_l - \omega_*} = \rho_l \omega_l.$$

Solving for ω_*, substituting the solution into Eq. 8.12 and substituting the w_l for $\mathcal{Q}_l/\rho_l$, we obtain a new equation that we can solve for $\mathcal{Q}_l$ that yields,

$$\mathcal{Q}_k = \sqrt{\rho_k \rho_{*k} \frac{\tilde{p}_{*k} - \tilde{p}_k}{\rho_{*k} - \rho_k}}. \tag{8.18}$$

with $k = l, r$, since we repeated the same process for $\mathcal{Q}_r$ and obtained exactly the same equation. However, we still don't know ρ_{*k}, for this we will need our third Rankine-Hugoniot condition (Eq. 8.11).

Finding ρ_{*l} and ρ_{*r}: From Eq. 8.11, we can obtain

$$\begin{aligned} h_{*k} - h_k &= \frac{1}{2}\left(w_k^2 - w_*^2\right) \\ &= \frac{1}{2}\left(\pm\frac{\mathcal{Q}_k^2}{\rho_k^2} \mp \frac{\mathcal{Q}_k^2}{\rho_{*k}^2}\right) \\ &= \frac{1}{2}\left(\frac{1}{\rho_k} + \frac{1}{\rho_{*k}}\right)(\tilde{p}_{*k} - \tilde{p}_k), \end{aligned} \tag{8.19}$$

where the sign above is used for $k = l$ and the one below for $k = r$, and we used Eq. 8.12 and Eq. 8.13 for the second line and Eq. 8.18 for the third line. We can now substitute the specific enthalpy $h = \gamma\tilde{p}/(\rho(\gamma - 1))$ in Eq. 8.19 to obtain,

$$\frac{\gamma_{*k}}{\gamma_{*k} - 1}\frac{\tilde{p}_{*k}}{\rho_{*k}} - \frac{\gamma_k}{\gamma_k - 1}\frac{\tilde{p}_k}{\rho_k} = \frac{1}{2}\left(\frac{1}{\rho_k} + \frac{1}{\rho_{*k}}\right)(\tilde{p}_{*k} - \tilde{p}_k).$$

As the interface is the contact discontinuity, the jump in the parameters is only across the contact discontinuity, so $\gamma_{*k} = \gamma_k$. Now we can solve for the unknown density,

$$\rho_{*k} = \rho_k \left(\frac{\frac{\tilde{p_*}}{\tilde{p_k}} + \frac{\gamma_k - 1}{\gamma_k + 1}}{\frac{\tilde{p_*}}{\tilde{p_k}}\frac{\gamma_k - 1}{\gamma_k + 1} + 1}\right). \tag{8.20}$$

Replacing this result into Eq. 8.18, we obtain $\mathcal{Q}_k$ in terms of p_* and known variables,

$$\mathcal{Q}_k = \sqrt{\rho_k \frac{\tilde{p}_{*k} + \tilde{p}_k\frac{\gamma_k - 1}{\gamma_k + 1}}{\frac{2}{\gamma_k + 1}}}. \tag{8.21}$$

With Eq. 8.17 and Eq. 8.21, we can calculate the $\phi_{l,r}^S$ nonlinear functions of p_* in terms of known variables. The functions $\phi_{l,r}^S$ allow us to construct Eq. 8.8 and solve it using a Newton method or other root finder in order to obtain the value of p_*. The Eqs. 8.17 will then yield the contact discontinuity speed $s_* = u_*$ in terms of p_*. Further on, we can calculate $\mathcal{Q}_l$ and $\mathcal{Q}_r$ from Eq. 8.21, and we can substitute in Eq. 8.14 to obtain the corresponding wave speeds. However, this will only solve the 4th case of Eq. 8.8, 1-shock and 3-shock solution. If any of our waves happens to be a rarefaction, we will also need to calculate the $\phi_{l,r}^R$ functions. This will be obtained using the Riemann invariants.

Riemann invariants for rarefaction waves

Riemann invariants are variables that remain constant through simple waves such as rarefactions. The Riemann invariants across the 2-wave are the pressure p_* and the normal velocity

u_*. The Riemann invariants for the 1-wave and 3-wave are the entropy and the quantities,

$$u_l + \frac{2c_l}{\gamma_l - 1} = u_* + \frac{2c_{*l}}{\gamma_l - 1}, \tag{8.22}$$

$$u_r - \frac{2c_r}{\gamma_r - 1} = u_* - \frac{2c_{*r}}{\gamma_r - 1}, \tag{8.23}$$

correspondingly. The speed of sound c_K is obtained by applying Eq. 8.4 to the Tammann EOS,

$$c_k = \sqrt{\gamma_k \frac{p_k + p_{\infty k}}{\rho_k}}. \tag{8.24}$$

As the entropy is invariant, we can use the Tammann EOS isentropic relation to obtain the density in the middle states,

$$\rho_{*k} = \rho_k \left(\frac{\tilde{p}_{*k}}{\tilde{p}_k} \right)^{1/\gamma}. \tag{8.25}$$

Solving Eq. 8.22 and Eq. 8.23 for u_* and using Eq. 8.24 and Eq. 8.25, we immediately obtain

$$u_* = u_l + \frac{2c_l}{\gamma_l - 1} \left[1 - \left(\frac{\tilde{p}_{*l}}{\tilde{p}_l} \right)^{\frac{\gamma_l - 1}{2\gamma_l}} \right] = \phi_l^R(p_*),$$

$$u_* = u_r - \frac{2c_r}{\gamma_r - 1} \left[1 - \left(\frac{\tilde{p}_{*r}}{\tilde{p}_r} \right)^{\frac{\gamma_r - 1}{2\gamma_r}} \right] = \phi_r^R(p_*).$$

As $\tilde{p}_\kappa = p_\kappa + p_{\infty\kappa}$, when we compare to Eqs. 8.7 we obtain the $\phi_{l,r}^R$ functions. The rarefaction head velocities will be given by $u_l - c_l$ and $u_r + c_r$; the tail velocities will be $u_* - c_{*l}$ and $u_* + c_{*r}$. For numerical purposes, a simple approximate velocity is provided for s_l and s_r as the average between the head and tail velocity.

In order to compute the complete structure of the rarefaction wave [126, 155], we can use the Riemann invariants from Eq. 8.22 and Eq. 8.23, along with Eq. 8.24 and the isentropic relation from Eq. 8.25. The solution for the 1-rarefaction wave along the rays $x/t = \xi =$

$u_{rar1} - c_{rar1}$ is then

$$u_{rar1}(\xi) = \frac{u_l(\gamma_l - 1) + 2(\xi + c_l)}{\gamma_l + 1},$$
$$\rho_{rar1} = \rho_l \left[\frac{u_{rar1}(\xi) - \xi}{c_l}\right]^{\frac{2}{\gamma_l - 1}},$$
$$p_{rar1} = \tilde{p}_l \left[\frac{u_{rar1}(\xi) - \xi}{c_l}\right]^{\frac{2\gamma_l}{\gamma_l - 1}} - p_{\infty l},$$

and for a 3-rarefaction wave along the rays $x/t = \xi = u_{rar3} + c_{rar3}$ is,

$$u_{rar3}(\xi) = \frac{u_r(\gamma_r - 1) + 2(\xi - c_r)}{\gamma_r + 1},$$
$$\rho_{rar3} = \rho_r \left[\frac{u_{rar3}(\xi) - \xi}{c_r}\right]^{\frac{2}{\gamma_r - 1}},$$
$$p_{rar3} = \tilde{p}_r \left[\frac{u_{rar3}(\xi) - \xi}{c_r}\right]^{\frac{2\gamma_r}{\gamma_r - 1}} - p_{\infty r}.$$

Now that we know the functions $\phi_{l,r}^{s,r}$ for the rarefactions, we can construct the function $\Phi(p_*)$ function from Eq. 8.8 for any of the 4 possible scenarios. The value of p_* will be found by numerically finding the roots of $\Phi(p_*) = 0$. Note which case to employ to calculate $\Phi(p_*)$ might change in each iteration of the root finder. Once p_* is found, u_*, ρ_{*l}, ρ_{*r}, s_l and s_r can be found using the relations we just derived depending if it's a shock or a rarefaction. As we know the three wave speeds s_l, s_* and s_r and the primitive variables $[\rho, u, p]$ on all the 4 states for all the possible cases, we have the solved the Riemann problem.

8.2.5 Implementation into Clawpack

These methods are implemented into the Clawpack 5.2.2 software [44]. This software employs Godunov's method [95] with high order corrections and limiters to better handle discontinuities[155]. In order to implement these methods into Clawpack, we need to write Godunov's method in the wave propagation form. Consider a state vector $q(x,t)$, a one dimensional conservation law is given by $q_t + f(q)_x = 0$. We partition the space in cells with index i and consider the cell average at time t to be $Q_i^n = \int_{x_{i-1/2}}^{x_{i+1/2}} q(x, t_n)dx$. Then the Godunov method is given by,

$$Q_i^{n+1} = Q_i^n - \frac{\Delta t}{\Delta x}(\underbrace{\mathcal{A}^- \Delta Q_{i+1/2}}_{\text{LeftEdge}} + \underbrace{\mathcal{A}^+ \Delta Q_{i-1/2}}_{\text{RightEdge}}) - \underbrace{\frac{\Delta t}{\Delta x}\left(\tilde{F}_{i+1/2} - \tilde{F}_{i-1/2}\right)}_{\text{HighResolution}}, \tag{8.26}$$

with,

$$\tilde{F}_{i\pm1/2} = \frac{1}{2}\sum_{p=1}^{m} |s^p_{i\pm1/2}| \left(1 - \frac{\Delta t}{\Delta x}|s^p_{i\pm1/2}|\right) \underbrace{\widetilde{\mathcal{W}}^p_{i\pm1/2}}_{\text{Limiter}}, \tag{8.27}$$

where $\mathcal{A}^-\Delta Q_{i\pm1/2} = \sum_{p=1}^{m}(s^p_{i\pm1/2})^-\mathcal{W}^p_{i\pm1/2}$ and $\mathcal{A}^+\Delta Q_{i\pm1/2} = \sum_{p=1}^{m}(s^p_{i\pm1/2})^+\mathcal{W}^p_{i\pm1/2}$ are the left and right going fluctuations of the edge of cell $i \pm 1/2$ respectively, with $(s^p_{i\pm1/2})^\pm$ indicating only those values of $s^p_{i\pm1/2}$ with sign $\pm$, m is the number of waves, $s^p_i \mp 1/2$ is the velocity of the p characteristic of the Riemann problem at edge $i \mp 1/2$, the wave $\mathcal{W}^p_{i\mp1/2}$ corresponds to the jump across that characteristic and $\widetilde{\mathcal{W}}^p_{i\pm1/2}$ is the limited version of the wave, see [155] for more details.

The numerical solution requires solving a Riemann problem on each cell edge of our partition in order to obtain the fluctuations. The Riemann solutions presented previously have provided the characteristic velocities s^p, and we can calculate the waves $\mathcal{W}^p$ by calculating the jump of q across the p characteristic. This information is calculated for each cell edge and fed into Clawpack, where the method from Eq. 8.26 is implemented. Chapter 9 contains one-dimensional implementations of these methods. In the next Sections, we will study two-dimensional implementations.

8.3 2D Axisymmetric Euler equations with interfaces

The three dimensional Euler Equations with cylindrical symmetry can be solved as two dimensional axisymmetric Euler Equations with additional source terms, see Figure 8.4. Solving this model is more simple and cost effective than solving the full three-dimensional equations. The axisymmetric model can be tackled by solving the two-dimensional Euler equations, and then incorporating operator splitting for the source term. The two-dimensional axisymmetric Euler equations (in cylindrical coordinates r,θ,z) take the form

$$\frac{\partial}{\partial t}\begin{bmatrix}\rho\\ \rho u_r\\ \rho u_z\\ E\end{bmatrix} + \frac{\partial}{\partial r}\begin{bmatrix}\rho u_r\\ \rho u_r^2 + p\\ \rho u_r u_z\\ u_r(E+p)\end{bmatrix} + \frac{\partial}{\partial z}\begin{bmatrix}\rho u_z\\ \rho u_r u_z\\ \rho u_z^2 + p\\ u_z(E+p)\end{bmatrix} = \begin{bmatrix}-(\rho u_r)/r\\ -(\rho u_r^2)/r\\ -(\rho u_r u_z)/r\\ -u_r(E+p)/r\end{bmatrix}, \tag{8.28}$$

where ρ is the density; u_r and u_z denote the velocities in the radial and axial direction, r and z respectively; E is the total energy and p is the pressure. We emphasize again that these equations have the exact same form as the two-dimensional Euler equations with the addition of geometrical source terms (the right hand side).

The conservation law for $q(x, y, t)$ takes the form $q_t + f(q)_x + g(q)_y = \psi(q, x, y, t)$. In two dimensions, the numerical cell average is calculated as $Q^n_{i,j} = \frac{1}{\Delta y \Delta x}\int_{C_{i,j}} q(x, y, t_n)dx\,dy$,

where $C_{i,j}$ is the cell $[x_{i-1/2}, x_{i+1/2}] \times [y_{j-1/2}, y_{j+1/2}]$. The source terms can be solved using a fractional-step method [155] by alternating between $q_t + f(q)_x + g(q)_y = 0$ and $q_t = \psi(q, x, y, t)$. The latter is an ordinary differential equation, which has an exact solution in the case of Eqs. 8.28, as shown in Section 10.4 and [55]. More complex source terms might require implementing another time stepping method like Runge-Kutta or TR-BDF2. In a similar manner, the simplest approach to solve the two dimensional system $q_t + f(q)_x + g(q)_y = 0$ is dimensional splitting. This is done again with a fractional-step method to split the two dimensional problem up into a sequence of one-dimensional problems alternating between solving $q_t + f(q)_x = 0$ and $q_t + g(q)_y = 0$. For more details and different splitting algorithms see [155].

Although dimensional splitting is simple to implement, we can obtain second-order accuracy and less numerical smearing simultaneously by using transverse propagation algorithms from [154]. This will require splitting the normal wave fluctuations $\mathcal{A}^{\pm}\Delta Q_{i\pm1/2,j}$ at edge $i \pm 1/2$ into transverse wave fluctuations $\mathcal{B}^{\pm}\mathcal{A}^{+}\Delta Q_{i\pm1/2,j}$ and $\mathcal{B}^{\pm}\mathcal{A}^{-}\Delta Q_{i\pm1/2,j}$. If the normal direction is x, then the normal fluctuations are calculated with the flux $f(q)$ and the transverse ones with the flux $g(q)$. Our specific model will require a very special kind of transverse solvers, which have been implemented in Section 10.4 and [55]; a generalized version of these solvers will be explored in detail later in this work.

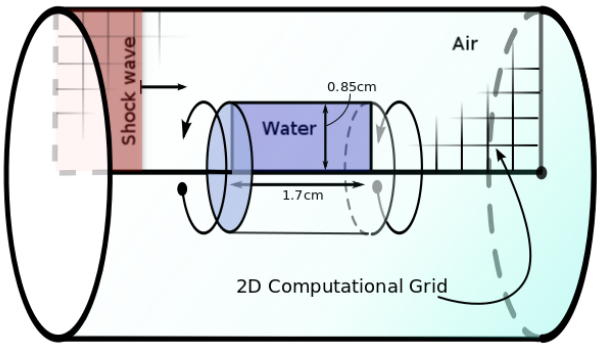

Figure 8.4: The axisymmetric model is obtained by revolving the 2D computational grid. The inner square corresponds to the air-water interface. The inside part is filled with water and the outside part is filled with air. All the outer boundaries are modeled with non-reflecting boundary conditions. The interface location was chosen following the source of this figure [55].

The two-dimensional axisymmetric model of Eq. 8.28 employing a Tammann equation of state with interfaces and transverse solvers were implemented in a traumatic brain injury application in Chapter 10 and [55]. This work showed how the geometry of the interface can be very relevant and even produce cavitation effects. The set up in Chapter 10 is essentially

the one shown in Figure 8.4. A cylindrical plastic container filled with water is placed inside a shock tube. The cylindrical outer boundary corresponds to a cylindrical cross section of the shock tube. The results shown in Section 9.2 and in [52] show the plastic interface can be neglected in the two-dimensional model. In Chapter 11, we will give a detailed exposition of the numerical methods for two-dimensional Euler equations in more general cases.

8.4 2D Elasticity equations with interfaces

In this section, we will give a brief introduction to the elasticity equations, and we will derive the normal Riemann solver for the two-dimensional equations with an interface. The normal solver is framed in a general way, so it can be implemented with a mapped grid. We will show how to recover the solver for a simple Cartesian grid, and we will also derive the transverse solver.

8.4.1 Elasticity equations

We present a brief intuitive derivation of the elasticity equation starting from the second law. Newton's second law the conservation of momentum for a solid of mass m is given by

$$\frac{dp}{dt} = F,$$

where $p = mu$ is the momentum, u the velocity and F the force. We will combine this with Hooke's law for a spring, which states that the force exerted by the spring is proportional to the distance it has been displaced from its equilibrium position, i.e. $F = -kx$, so we obtain

$$m\frac{d^2x}{dt^2} = -kx,$$

where x is the displacement from the spring's resting state. This is the well known harmonic oscillator and the simplest equation of elasticity. Now we will consider a three dimensional elastic media with constant density $\rho = m/V$, and velocity $\bar{u} = (u, v, w)$. In this case, Newton's law can be written

$$\rho\frac{d\bar{u}}{dt} = \frac{F}{V},$$

where d/dt will now correspond to the material derivative. The force felt by the elastic media can be rewritten in terms of the pressure as: $\frac{F}{V} = -\nabla p$; however, the pressure is a scalar, so it can only model forces that act in the same direction than the deformation, so we need a more general concept than pressure to model elastic media. This is given by the stress

tensor (same units as pressure: force per area),

$$\bar{\bar{\sigma}} = \begin{pmatrix} \sigma_{11} & \sigma_{12} & \sigma_{13} \\ \sigma_{21} & \sigma_{22} & \sigma_{23} \\ \sigma_{31} & \sigma_{32} & \sigma_{33} \end{pmatrix}, \qquad \frac{F}{V} = \nabla \cdot \bar{\bar{\sigma}}.$$

If $\sigma_{ij} = -p\delta_{ij}$, we obtain $\nabla \cdot \bar{\bar{\sigma}} = \nabla p$ as expected. Combining these two equation, we can actually write the elasticity equations as

$$\rho \frac{d\bar{u}}{dt} = \nabla \cdot \bar{\bar{\sigma}}.$$

For small displacements $\bar{u} \ll u$, the material derivative can be approximated by the partial derivative yielding the linear elasticity equations,

$$\rho \frac{\partial \bar{u}}{\partial t} = \nabla \cdot \bar{\bar{\sigma}}.$$

We have three equations and 12 unknown, so we still need some more equations. First of all, in most physical applications, the conservation of angular momentum imples the symmetry of the stress tensor, i.e. $\sigma_{ij} = \sigma_{ji}$, which eliminates three variables. The other six equations can be deduce from a generalized version of Hooke's law, the constitutive equation. It must also be linear in order to obtain linear equations. This relation relates the stresses to the strains (deformations) as the Hooke's law relates the forces to the elongation/compression of the spring, see [155] for an intuituve deduction of the following linear constitutive equation.

$$\begin{bmatrix} \sigma_{11} \\ \sigma_{22} \\ \sigma_{33} \\ \sigma_{12} \\ \sigma_{23} \\ \sigma_{13} \end{bmatrix} = \begin{bmatrix} \lambda+2\mu & \lambda & \lambda & 0 & 0 & 0 \\ \lambda & \lambda+2\mu & \lambda & 0 & 0 & 0 \\ \lambda & \lambda & \lambda+2\mu & 0 & 0 & 0 \\ 0 & 0 & 0 & 2\mu & 0 & 0 \\ 0 & 0 & 0 & 0 & 2\mu & 0 \\ 0 & 0 & 0 & 0 & 0 & 2\mu \end{bmatrix} \begin{bmatrix} \epsilon_{11} \\ \epsilon_{22} \\ \epsilon_{33} \\ \epsilon_{12} \\ \epsilon_{23} \\ \epsilon_{13} \end{bmatrix},$$

where the strain tensor is expressed in term of the displacement vector $\delta(x, y, z, t)$ as $\bar{\bar{\epsilon}} = \frac{1}{2}\left[\nabla\bar{\delta} + \left(\nabla\bar{\delta}\right)^T\right]$ and λ and μ are the Lamé parameters (analogous to the x and k in Hooke's law respectively). Differentiating by t this stress-strain relation we obtain the other six

equations to complete the system,

$$\begin{bmatrix} \sigma_{11} \\ \sigma_{22} \\ \sigma_{33} \\ \sigma_{12} \\ \sigma_{23} \\ \sigma_{13} \end{bmatrix}_t = \begin{bmatrix} \lambda+2\mu & \lambda & \lambda & 0 & 0 & 0 \\ \lambda & \lambda+2\mu & \lambda & 0 & 0 & 0 \\ \lambda & \lambda & \lambda+2\mu & 0 & 0 & 0 \\ 0 & 0 & 0 & 2\mu & 0 & 0 \\ 0 & 0 & 0 & 0 & 2\mu & 0 \\ 0 & 0 & 0 & 0 & 0 & 2\mu \end{bmatrix} \begin{bmatrix} u_x \\ v_y \\ w_z \\ (u_y+v_x)/2 \\ (v_z+w_y)/2 \\ (u_z+w_x)/2 \end{bmatrix}.$$

We can rewrite the nine equations in the form

$$\bar{q}_t + A\bar{q}_x + B\bar{q}_x + C\bar{q}_z = 0,$$

with

$$\bar{q} = \begin{bmatrix} \sigma_{11} \\ \sigma_{22} \\ \sigma_{33} \\ \sigma_{12} \\ \sigma_{23} \\ \sigma_{13} \\ u \\ v \\ w \end{bmatrix} \qquad A = \begin{bmatrix} 0 & 0 & 0 & 0 & 0 & 0 & -(\lambda+2\mu) & 0 & 0 \\ 0 & 0 & 0 & 0 & 0 & 0 & -\lambda & 0 & 0 \\ 0 & 0 & 0 & 0 & 0 & 0 & -\lambda & 0 & 0 \\ 0 & 0 & 0 & 0 & 0 & 0 & 0 & -\mu & 0 \\ 0 & 0 & 0 & 0 & 0 & 0 & 0 & 0 & 0 \\ 0 & 0 & 0 & 0 & 0 & 0 & 0 & 0 & -\mu \\ -1/\rho & 0 & 0 & 0 & 0 & 0 & 0 & 0 & 0 \\ 0 & 0 & 0 & -1/\rho & 0 & 0 & 0 & 0 & 0 \\ 0 & 0 & 0 & 0 & 0 & -1/\rho & 0 & 0 & 0 \end{bmatrix}$$

$$B = \begin{bmatrix} 0 & 0 & 0 & 0 & 0 & 0 & 0 & -\lambda & 0 \\ 0 & 0 & 0 & 0 & 0 & 0 & 0 & -(\lambda+2\mu) & 0 \\ 0 & 0 & 0 & 0 & 0 & 0 & 0 & -\lambda & 0 \\ 0 & 0 & 0 & 0 & 0 & 0 & -\mu & 0 & 0 \\ 0 & 0 & 0 & 0 & 0 & 0 & 0 & 0 & -\mu \\ 0 & 0 & 0 & 0 & 0 & 0 & 0 & 0 & 0 \\ 0 & 0 & 0 & -1/\rho & 0 & 0 & 0 & 0 & 0 \\ 0 & -1/\rho & 0 & 0 & 0 & 0 & 0 & 0 & 0 \\ 0 & 0 & 0 & 0 & -1/\rho & 0 & 0 & 0 & 0 \end{bmatrix}$$

$$C = \begin{bmatrix} 0 & 0 & 0 & 0 & 0 & 0 & 0 & 0 & -\lambda \\ 0 & 0 & 0 & 0 & 0 & 0 & 0 & 0 & -\lambda \\ 0 & 0 & 0 & 0 & 0 & 0 & 0 & 0 & -(\lambda+2\mu) \\ 0 & 0 & 0 & 0 & 0 & 0 & 0 & 0 & 0 \\ 0 & 0 & 0 & 0 & 0 & 0 & 0 & -\mu & 0 \\ 0 & 0 & 0 & 0 & 0 & 0 & -\mu & 0 & 0 \\ 0 & 0 & 0 & 0 & 0 & -1/\rho & 0 & 0 & 0 \\ 0 & 0 & 0 & 0 & -1/\rho & 0 & 0 & 0 & 0 \\ 0 & 0 & -1/\rho & 0 & 0 & 0 & 0 & 0 & 0 \end{bmatrix}$$

The three dimensional elasticity equations written in this form are ideal to solve the Riemann problem and implement numerically.

8.4.2 Riemann problem across interface in a mapped grid

The equations obtained in the previous section are easily simplified to its two dimensional version. The stress tensor will only have 3 entries: σ_{11}, σ_{22} and σ_{12}, and the velocity will have two: u and v. The normal Riemann problem will solve $\bar{q}_t + A\bar{q}_x = 0$ when sweeping in the x direction and $\bar{q}_t + B\bar{q}_y = 0$ when sweeping in the y direction. We can generalize this for a general quadrilateral mapped grid. The Riemann problem in the normal direction of a grid edge is $\bar{q}_t + A_n\bar{q}_n = 0$, where $\bar{q}_n$ is the derivative in the normal to the edge direction, $A_n = n_x A + n_y B$, and $\hat{n} = (n_x, n_y)$ is the normal to the edge where the Riemann problem is being solved. The Jacobian matrix is,

$$A_n = -\begin{bmatrix} 0 & 0 & 0 & n_x(\lambda+2\mu) & n_y\lambda \\ 0 & 0 & 0 & n_x\lambda & n_y(\lambda+2\mu) \\ 0 & 0 & 0 & n_y\mu & n_x\mu \\ n_x/\rho & 0 & n_y/\rho & 0 & 0 \\ 0 & n_y/\rho & n_x/\rho & 0 & 0 \end{bmatrix}.$$

Using $\hat{n} = (1,0)$ or $\hat{n} = (0,1)$, we recover A and B respectively. In order to solve the Riemann problem, we need the eigenvalues and eigenvectors of this matrix. We can obtain them symbolically with any of the standard packages.

The matrix of the five eigenvectors $R = [\bar{r_1}, \bar{r_2}, \bar{r_3}, \bar{r_4}, \bar{r_5}]$ is given by

$$R = \begin{bmatrix} \lambda_l + 2\mu_l n_x^2 & \lambda_r + 2\mu_r n_x^2 & -2\mu_l n_x n_y & -2\mu_r n_x n_y & n_y^2 \\ \lambda_l + 2\mu_l n_y^2 & \lambda_r + 2\mu_r n_y^2 & 2\mu_l n_x n_y & 2\mu_r n_x n_y & n_x^2 \\ 2\mu_l n_x n_y & 2\mu_r n_x n_y & \mu_l[n_x^2 - n_y^2] & \mu_r[n_x^2 - n_y^2] & -n_x n_y \\ n_x c_{pl} & -n_x c_{pr} & -n_y c_{sl} & n_y c_{sr} & 0 \\ n_y c_{pl} & -n_y c_{pr} & n_x c_{sl} & -n_x c_{sr} & 0 \end{bmatrix},$$

where each column correspond to the eigenvectors whose corresponding eigenvalues are

$$s_1 = -c_{pl}, \quad s_2 = c_{pr}, \quad s_3 = -c_{sl}, \quad s_4 = c_{sr}, \quad s_5 = 0,$$

with

$$c_p = \sqrt{\frac{\lambda + 2\mu}{\rho}}, \qquad c_s = \sqrt{\frac{\mu}{\rho}},$$

are the corresponding wave speeds. The first two eigenvalues (s_1, s_2) correspond to two pressure wave (P-waves) with the usual sound speed as eigenvalue. The next two eigenvalues (s_3, s_4) correspond to two shear waves (S-waves) with the shear speed as eigenvalues. Note the wave with eigenvalue zero doesn't cause any propagation, and it will not be relevant in solving the Riemann problem. The eigenvalues and eigenvectors can also be seen in [155].

In the matrix of eigenvectors, R, we took the liberty of using different Lamé parameters and density for the eigenvectors of waves propagating to the left than those propagating to the right. Note that changing these parameters automatically changes the wave speeds on each side of the Riemann problem discontinuity. In other words, the subindex for left (and right), l (and r), was added to the parameters of the eigenvector with negative (and positive) eigenvalue respectively. This denotes different values of the parameters on the left and right side of the discontinuity where the waves will be propagating. As the parameters λ, μ and ρ_0 are different across the discontinuity of the Riemann problem; we could interpret this as an interface between two materials. This will also allow the Riemann solver to solve variable coefficients problems for inhomogeneous materials as well.

In order to solve this linear Riemann problem, we need to obtain $\bar{\alpha}$ from the following equation

$$R\bar{\alpha} = \Delta\bar{q},$$

where $\delta\bar{Q} = [\Delta\sigma_{11}; \Delta\sigma_{22}; \Delta\sigma_{12}; \Delta u; \Delta v]$ is the jump of $\bar{q}$ across the discontinuity. We could invert R numerically to obtain $\bar{\alpha}$. In the case of linear elasticity equation, it can be done

analytically, and it yields

$$\alpha_1 = \frac{c_{pr}\left[\Delta\sigma_{11}n_x^2 + \Delta\sigma_{22}n_y^2 + 2n_xn_y\Delta\sigma_{12}\right] + (\lambda_r + 2\mu_r)(n_x\Delta u + n_y\Delta v)]}{\Delta_P},$$
$$\alpha_2 = \frac{c_{pl}\left[\Delta\sigma_{11}n_x^2 + \Delta\sigma_{22}n_y^2 + 2n_xn_y\Delta\sigma_{12}\right] - (\lambda_l + 2\mu_l)(n_x\Delta u + n_y\Delta v)}{\Delta_P},$$
$$\alpha_3 = \frac{c_{sr}\left[\Delta\sigma_{12}(n_x^2 - n_y^2) + n_xn_y(\Delta\sigma_{22} - \Delta\sigma_{11})\right] + \mu_r(n_x\Delta v - n_y\Delta u))}{\Delta_S},$$
$$\alpha_4 = \frac{c_{sl}\left[\Delta\sigma_{12}(n_x^2 - n_y^2) + n_xn_y(\Delta\sigma_{22} - \Delta\sigma_{11})\right] - \mu_l(n_x\Delta v - n_y\Delta u))}{\Delta_S},$$

with

$$\Delta_P = c_{pr}(\lambda_l + 2\mu_l) + c_{pl}(\lambda_r + 2\mu_r),$$
$$\Delta_S = \mu_l c_{sr} + \mu_r c_{sl}.$$

and corresponding speeds (eigenvalues):

$$s_1 = -c_{pl}, \quad s_2 = c_{pr}, \quad s_3 = -c_{sl}, \quad s_4 = c_{sr}, \quad s_5 = 0.$$

Note α_5 is not required, since its corresponding zero eigenvalue doesn't allow wave propagation. This information is enough to calculate the solution, since the vector $\bar{\alpha}_i$ represents the jump across the wave i that moves along the eigenvector $\bar{r}_i$ with speed s_i. Note when $\hat{n} = (1, 0)$ or $\hat{n} = (0, 1)$, we recover the normal Riemann solver for 2D Elasticity in a Cartesian grid.

Clawpack implementation

We solved the Riemann problem for a mapped grid, so we want it to solve a more complicated system than just a Riemann problem. Clawpack [44] has all the framework required to solve hyperbolic equations by solving Riemann problems on each grid cell. If we can provide the Riemann solver to Clawpack, it can do all the hard work for us. In order to implement the solution into Clawpack, we need to rewrite it in its wave formulation, where we update the value at cell $\bar{Q}^n_{i,j}$, with i, j the indexes in space and n in time following the two-dimensional extension of Eq. 7.8,

$$\bar{Q}^{n+1}_{i,j} = \bar{Q}^n_{i,j} - \frac{\Delta t}{\Delta x}\left[\mathcal{A}^+\Delta Q_{i-1/2,j} + \mathcal{A}^-\Delta Q_{i+1/2,j}\right] + \text{High order corrections \& limiters},$$

when sweeping in the i direction of the computational domain. Note this should be equivalent to sweeping in the normal direction of the physical domain when using a mapped grid, that's why it's important solve the Riemann problem normal to the edge between the grid cells. The same process is analogous in the j direction. Also note this equation requires output of two Riemann problems, the ones corresponding to edge $i-1/2$ and edge $i+1/2$. The output of the Riemann solver routine for Clawpack should be given by the waves speed and wave fluctuations. The wave speed we already know from the eigenvalues in the previous section. In order to calculate the wave fluctuations $\mathcal{A}^{\pm}\Delta Q_{i-1/2,j}$ from the left edge, we first need the waves given by

$$\mathcal{W}_i = \alpha_i \bar{r}_i$$

with $i = 1, 2, 3, 4$ and $\bar{r}_i$ the corresponding eigenvectors calculated previously. Solving the Riemann problem in the right edge is completely analogous. The positive and negative wave fluctuations $\mathcal{A}^{\pm}\Delta Q_{i-1/2,j}$ will be given in terms of the speeds(eigenvalues) and the waves,

$$\begin{aligned}\mathcal{A}^{+}\Delta Q_{i-1/2,j} &= s_2\mathcal{W}_2 + s_4\mathcal{W}_4\\ \mathcal{A}^{-}\Delta Q_{i-1/2,j} &= s_1\mathcal{W}_1 + s_3\mathcal{W}_3,\end{aligned}$$

When employing the mapped grid is important to remember to scale the wave speeds s in the wave fluctuations by the factor $\gamma_x = dy_{phy}/dy_{com}$ if sweeping in the x direction or $\gamma_y = dx_{phy}/dx_{com}$ when sweeping in the y direction, where dx_{phy} denotes mesh grid spacing in the physical domain and dx_{com} in the computational one. The fluctuation in the mapped grid should then be,

$$\begin{aligned}\mathcal{A}^{+}\Delta Q^{map}_{i-1/2,j} &= \gamma c_{pr}\mathcal{W}_2 + \gamma c_{sr}\mathcal{W}_4\\ \mathcal{A}^{-}\Delta Q^{map}_{i-1/2,j} &= -\gamma c_{pl}\mathcal{W}_1 - \gamma c_{sl}\mathcal{W}_3.\end{aligned}$$

We solved the Riemann problem for a mapped grid, so we want it to solve a more complicated system than just a Riemann problem. Clawpack has all the framework required to solve hyperbolic equations by solving Riemann problems on each grid cell. If we can provide the Riemann solver to Clawpack, it can do all the hard work for us. In order to implement the solution into Clawpack, we need to rewrite it in its wave formulation, where we update the value at cell $\bar{Q}^n_{i,j}$, with i, j the indexes in space and n in time following,

$$\bar{Q}^{n+1}_{i,j} = \bar{Q}^n_{i,j} - \frac{\Delta t}{\Delta x}\left[\mathcal{A}^{+}\Delta Q_{i-1/2,j} + \mathcal{A}^{-}\Delta Q_{i+1/2,j}\right] + \text{High order corrections \& limiters},$$

when sweeping in the i direction of the computational domain. Note this should be equivalent to sweeping in the normal direction of the physical domain when using a mapped grid, that's why it is important solve the Riemann problem normal to the edge between the grid cells.

The same process is analogous in the j direction. Also note this equation requires output of two Riemann problems: the one on edge $i-1/2$ and the one on $i+1/2$. The output of the Riemann solver routine for Clawpack should be given by the waves speed and wave fluctuations. The wave speed we already know from the eigenvalues in the previous section. In order to calculate the wave fluctuations $\mathcal{A}^{\pm}\Delta Q_{i-1/2,j}$ from the left edge, we first need the waves given by

$$\mathcal{W}_i = \alpha_i \bar{r_i}$$

with $i = 1, 2, 3, 4$ and $\bar{r_i}$ the corresponding eigenvectors calculated previously. Solving the Riemann problem in the right edge is completely analogous. The positive and negative wave fluctuations $\mathcal{A}^{\pm}\Delta Q_{i-1/2,j}$ will be given in terms of the speeds(eigenvalues) and the waves,

$$\mathcal{A}^{+}\Delta Q_{i-1/2,j} = s_2\mathcal{W}_2 + s_4\mathcal{W}_4$$
$$\mathcal{A}^{-}\Delta Q_{i-1/2,j} = s_1\mathcal{W}_1 + s_3\mathcal{W}_3,$$

When employing the mapped grid is important to remember to scale the wave speeds s in the wave fluctuations by the factor $\gamma_x = dy_{phy}/dy_{com}$ if sweeping in the x direction or $\gamma_y = dx_{phy}/dx_{com}$ when sweeping in the y direction, where dx_{phy} denotes mesh grid spacing in the physical domain and dx_{com} in the computational one. The fluctuation in the mapped grid should then be,

$$\mathcal{A}^{+}\Delta Q^{map}_{i-1/2,j} = \gamma c_{pr}\mathcal{W}_2 + \gamma c_{sr}\mathcal{W}_4$$
$$\mathcal{A}^{-}\Delta Q^{map}_{i-1/2,j} = -\gamma c_{pl}\mathcal{W}_1 - \gamma c_{sl}\mathcal{W}_3.$$

8.4.3 Transverse Riemann problem across interface in a mapped grid

The concept of transverse Riemann solver was introduced in Section 8.1.4. The transverse solver for elasticity equations will require splitting the normal wave fluctuations $\mathcal{A}^{\pm}\Delta Q_{i-1/2,j}$ at edge $i-1/2$ into transverse wave fluctuations $\mathcal{B}^{\pm}\mathcal{A}^{+}\Delta Q_{i-1/2,j}$ and $\mathcal{B}^{\pm}\mathcal{A}^{-}\Delta Q_{i-1/2,j}$; the former decomposition is shown in Figure 11.4 and explained in detail on [155]. In this section, we will focus on how to implement the transverse in a mapped grid.

We will only focus on $\mathcal{B}^{\pm}\mathcal{A}^{+}\Delta Q_{i-1/2,j}$, since the other case is analogous. We begin by decomposing the normal wave fluctuations into a linear combination of transverse waves, which will follow the same equations and Jacobian as before, so we obtain

$$\mathcal{A}^{+}\Delta Q_{i-1/2,j} = R\bar{\beta} = \beta_1\bar{r_1} + \beta_2\bar{r_2} + \beta_3\bar{r_3} + \beta_4\bar{r_4}.$$

In the context of mapped grids, note the eigenvectors $\bar{r_i}$ depend on the normal $\hat{n}$=(n_x, n_y), so if the left edge normal was used for the normal Riemann solver, we need to use the bottom

edge normal to calculate $\bar{r}_i$. This normal might also be different for the up-going and down-going fluctuation. If we are on a Cartesian grid, both up-going and down-going normal will be equal and if $\hat{n}$=$(1,0)$ was used for the normal solver, the transverse solver will use the bottom normal $\hat{n} = (0,1)$ or viceversa.

The eigenvectors will also depend on the parameters of each cell, and now we have three cells involved: the bottom one (down), the middle one, and the upper one. We will denote the wave speeds and parameters with the subindexes d, m and u to denote bottom, middle and upper respectively.

We solve the system in a very similar manner to the system for $\bar{\alpha}$. When we add the right input parameters for the eigenvectors, we obtain $\bar{\beta}$ is given by,

$$\begin{aligned}
\beta_1 &= \frac{c_{pm}\left[\mathcal{A}_1^+ n_{xm}^2 + \mathcal{A}_2^+ n_{ym}^2 + 2n_{xm}n_{ym}\mathcal{A}_3^+\right] + (\lambda_m + 2\mu_m)(n_{xm}\mathcal{A}_4^+ + n_{ym}\mathcal{A}_5^+)]}{\Delta_P^-}, \\
\beta_2 &= \frac{c_{pm}\left[\mathcal{A}_1^+ n_{xu}^2 + \mathcal{A}_2^+ n_{yu}^2 + 2n_{xu}n_{yu}\mathcal{A}_3^+\right] - (\lambda_m + 2\mu_m)(n_{xu}\mathcal{A}_4^+ + n_{yu}\mathcal{A}_5^+)}{\Delta_P^+}, \\
\beta_3 &= \frac{c_{sm}\left[\mathcal{A}_3^+(n_{xd}^2 - n_{yd}^2) + n_{xd}n_{yd}(\mathcal{A}_2^+ - \mathcal{A}_1^+)\right] + \mu_m(n_{xd}\mathcal{A}_5^+ - n_{yd}\mathcal{A}_4^+))}{\Delta_S^-}, \\
\beta_4 &= \frac{c_{sm}\left[\mathcal{A}_3^+(n_{xu}^2 - n_{yu}^2) + n_{xu}n_{yu}(\mathcal{A}_2^+ - \mathcal{A}_1^+)\right] - \mu_m(n_{xu}\mathcal{A}_5^+ - n_{yu}\mathcal{A}_4^+))}{\Delta_S^+},
\end{aligned}$$

with

$$\begin{aligned}
\Delta_P^- &= c_{pm}(\lambda_d + 2\mu_d) + c_{pd}(\lambda_m + 2\mu_m), \\
\Delta_P^+ &= c_{pu}(\lambda_m + 2\mu_m) + c_{pm}(\lambda_u + 2\mu_u), \\
\Delta_S^- &= \mu_d c_{sm} + \mu_m c_{sd}, \\
\Delta_S^+ &= \mu_m c_{su} + \mu_u c_{sm},
\end{aligned}$$

where $\mathcal{A}^+\Delta Q_{i-1/2,j} = [\mathcal{A}_1^+, \mathcal{A}_2^+, \mathcal{A}_3^+, \mathcal{A}_4^+, \mathcal{A}_5^+]$, (n_{xm}, n_{ym}) correspond to the bottom normal of the middle cell, (n_{xu}, n_{yu}) correspond to the bottom normal of the upper cell and the speeds were calculated with the same formulas as before with the λ, μ and ρ parameters that correspond to each cell.

The speeds (eigenvalues) are the same as before, but in the corresponding cell,

$$s_1^T = -c_{pd}, \quad s_2^T = c_{pu}, \quad s_3^T = -c_{sd}, \quad s_4^T = c_{su}, \quad s_5^T = 0.$$

The transverse waves are given by $W_i^T = \beta_i \bar{r}_i$, so the fluctuations are given by,

$$\mathcal{B}^+\mathcal{A}^+\Delta Q_{i-1/2,j} = s_2^T W_2^T + s_4^T W_4^T$$
$$\mathcal{B}^-\mathcal{A}^+\Delta Q_{i-1/2,j} = s_1^T W_1^T + s_3^T W_3^T,$$

Once again, when employing the mapped grid is important to remember to scale the wave speeds s in the wave fluctuations by the factor γ

$$\mathcal{B}^+\mathcal{A}^+\Delta Q^{map}_{i-1/2,j} = \gamma_u c_{pu} W_2^T + \gamma_u c_{su} W_4^T$$
$$\mathcal{B}^-\mathcal{A}^+\Delta Q^{map}_{i-1/2,j} = -\gamma_m c_{pd} W_1^T - \gamma_m c_{sd} W_3^T,$$

where γ_u correspond to the scaling ratio of the bottom edge of the upper cell and γ_m to the scaling ratio of the bottom edge of the middle cell. The same process can be repeated for the left normal fluctuation $\mathcal{A}^-\Delta Q_{i-1/2,j}$. An alternative approach to implement mapped grids is to use a one-dimensional Riemann solver by rotating the velocities before and after using the Riemann solver. This alternative approach will be more convenient to implement the Euler equations in a mapped grid, as done in Section 11.1.1.

Chapter 9

ONE-DIMENSIONAL SHOCK WAVES IN AIR-PLASTIC-WATER INTERFACES

In the work presented in Chapter 10, we make a computational model of a shock tube experiment for a biomedical application in traumatic brain injury. In this chapter, we will make a one-dimensional model of that experimental setup, which basically consists of a shock traveling through an air-plastic-water interface. We implement this using Euler equations for compressible inviscid flow, which allow accurate modeling of shock wave formation and propagation. These equations model the conservation of mass, momentum, and energy and provide a direct connection to temperature, which may be important for some biomedical experiments. In this type of experiment, we are not concerned with large-scale movement of the fluid, so viscosity does not play an important role; therefore, employing the inviscid equations is appropriate. In order to model different materials, we use the Tammann equation of state (EOS) that allows us to model compressible gas along with almost incompressible fluids or elastic solids by using different parameters in the EOS. This model has shown that if the plastic interface is very thin, it can be neglected. This result will be very helpful to model more complicated setups in higher dimensions, like in Chapters 10 and 11. The work presented in this chapter is based on our publication [52].

9.1 One-dimensional air-plastic-water interface model

In experimental setups inside shock tubes, it is common to find biological samples are placed inside plastic containers filled with aqueous solution. This requires modeling the shock wave interaction with the air-plastic-water interface. Before studying the full computational experiment, the first step is to start with a one-dimensional model that can implement these interfaces and study how relevant the thin plastic interface of the container is. We can begin with the one-dimensional Euler equations [155]

$$\frac{\partial}{\partial t}\begin{bmatrix} \rho \\ \rho u \\ E \end{bmatrix} + \frac{\partial}{\partial x}\begin{bmatrix} \rho u \\ \rho u^2 + p \\ u(E+p) \end{bmatrix} = 0, \tag{9.1}$$

where ρ is the density, u denote the velocities in the x (shock tube axis) direction, p is the pressure and E the total energy. This system has four variable, so we will need one more equation, the equation of state. This will also allow us to model the interface.

9.1.1 Tammann equations of state

In order to close the system of Eqs. 9.1, we will use again the Tammann EOS instroduced in Section 8.2.1, given by

$$p = (\gamma - 1)\rho e - \gamma p_\infty, \tag{9.2}$$

where γ and p_∞ can be determined experimentally for different materials. The different values of the parameters allow us to model different interfaces. The internal energy e is related to the total energy E by $E = \rho e + \frac{1}{2}\rho u \cdot u$. Table 9.1 shows the Tammann EOS parameters for the materials used in the Euler equations simulations presented here.

Material	γ	$p_\infty(GPa)$
Air (Ideal gas EOS)	1.4	0.0
Plastic (polystyrene)	1.1	4.79
Water	7.15	0.3

Table 9.1: Parameters for the Tammann EOS to model the different materials. Note the p_∞ values for plastic and water are in GPa and are several orders of magnitude above the atmospheric pressure. The parameters for air and water were taken from [74]. As polystyrene is a solid, γ was chosen to be close to 1, and p_∞ was adjusted to yield the right speed of sound in polystyrene [167].

9.2 Computational experiments

In this section, we simulate the one-dimensional Euler equations (Eqs. 10.1) with the numerical methods from Chapter 8. We explore the question of whether a thin plastic interface separating gas and liquid in a shock tube experiment can be ignored in computational experiments, specifically whether the magnitude of the shock wave transmitted from the gas to the liquid is insensitive to the intervening layer of plastic. In the laboratory experiments that motivated this work, which will be studied in next chapter, the walls of the plastic transwell container are thin relative to the dimensions of the interior, and the computations presented in [55] were simplified by omitting the plastic layer entirely. Here we justify that approximation by considering a simple one-dimensional model of a shock wave passing through layers of air-plastic-water. This will provide insight on the behavior of the shock wave; it will show what parameters are the most relevant, and it will show that it is not necessary to include the thin plastic interface in the computational model. We will begin with a one-dimensional air-plastic-water interface using Euler equations, and then we compare these results to the simpler one-dimensional air-water interface, omitting the plastic layer. We will further verify

our results with an analytic calculation for a thin interface in linear acoustics. A preliminary version of this study can also be found in the conference proceedings [52].

9.2.1 Air-plastic-water interface

We begin by studying an air-plastic-water interface with Euler equations (Eqs. 9.1) in one dimension. The first step is to input the right initial conditions into our simulation. The actual form of the initial shock wave traveling through the shock tube was obtained experimentally; the amplitude can be varied in the shock tube and in our computational simulations. The sensor outputs pressure amplitude as a function of time. Assuming an average speed of sound in air, it can be converted to a function of distance as shown in Figure 9.1. The shape can be broadly approximated by an idealized shock wave (dashed line in Figure 9.1). This approximated shape of the shock wave is introduced as the initial condition in the simulation, where a scaling factor is used to scale the amplitude; however, this is not a trivial procedure since we must input the density, momentum, and energy, and we only have the pressure. Using the isentropic EOS, the ideal gas EOS and the expression for the speed of sound, an educated guess for the initial condition in terms of the pressure is given far away from the transwell. This initial condition is then modified until we obtain the desired amplitude and shape of the shock wave front. The resulting shape of the shock wave before hitting the interface can be seen in Figure 9.2(a), where the scaling factor, in this case, was chosen arbitrarily. The pressure is measured in KPa with an ambient base pressure of 1ATM = 101.325KPa. The same procedure was used for the two-dimensional simulations.

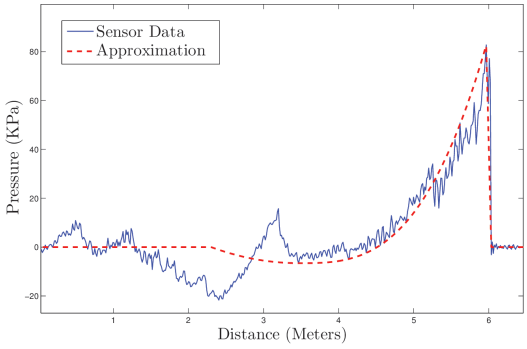

Figure 9.1: The shock wave form obtained from a sensor inside a shock tube is shown as the solid thin line. The coarse approximation to be used as an initial condition in our simulation is shown with a dashed line. An average speed of sound of $c = 344\ m/s$ is assumed. This figure was obtained from [55].

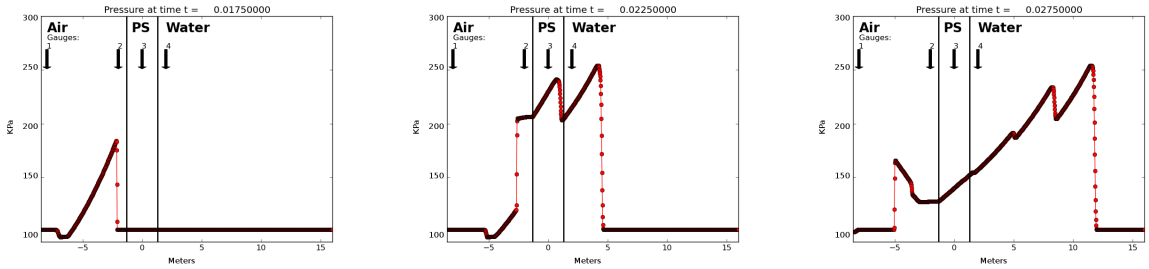

(a) (b) (c)

Figure 9.2: Shock wave crossing the air-plastic-water interface at different times. The arrows indicate the position of the 4 gauges that measure the pressure as a function of time. The gauges are numbered from left to right, and the plastic interface width for this case is 2.6m

The one-dimensional equations with the pair of interfaces are solved using the methods mentioned in Chapter 8. The different materials are modeled using different parameters for the Tammann EOS, see Section 8.2.1. The choice of parameters is shown in Table 9.1.

The solution of the shock wave crossing the interfaces between air, plastic, and water at different times is shown in Figure 9.2. It can be observed that every time the shock wave hits an interface, part of the wave is reflected and part of it is transmitted. This effect can occur multiple times depending on how the interfaces are set up. We can also observe that the amplitude of the shock wave increases as it passes from air to plastic and decreases when passing from plastic to water. This effect is due to the continuity of pressure and the change in compressibility. In order to keep the pressure at the interface continuous, the transmitted wave amplitude has to be the same as the sum of the incident wave and the reflected wave. When the compressibility is very high in the adjacent material, the interface will behave similarly to a solid wall. In this case, since the reflected wave will have an amplitude almost equal to the incident wave, the transmitted wave could have an amplitude almost twice as big as that of the incident wave. This explains why the pressure jump can increase or decrease when crossing an interface. Even for the one-dimensional case, we observe complex behavior due to interaction at the interface. These numerical simulations provide accurate insight in situations where simple intuition might be insufficient.

In Figure 9.1, we show from experimental data the initial shock wave profile in the air before hitting any interface; however, we are interested in the shape and amplitude of the shock wave in the water. In order to do so, we first need to know how important the plastic interface is in our model. Computationally, the plastic interface is hard to model because the width of the plastic is very small (mm) in comparison to the characteristic length of the experiment (length of the transwell [55]). The following experiment explores how the width

of the plastic interface affects the shock wave profile. Additionally, we show an accurate model can be obtained even when completely ignoring the plastic interface.

The maximum amplitude of the pressure profile was measured at gauges $2, 3$ and 4 of Figure 9.2 for different widths of the plastic interface. The plastic is always assumed to be centered at $x = 0$. The results are presented in Table 9.2. In Figure 10.7, the full pressure profiles as a function of time are shown at the three gauges for three of the plastic widths shown in Table 9.2.

Width (m)	Initial(KPa)	Gauge 2 (KPa)	Gauge 3 (KPa)	Gauge 4 (KPa)
2.6	184.06	247.76	305.88	258.24
1.4	184.06	207.53	298.19	259.71
0.6	184.06	187.72	283.72	274.90
0.2	184.06	183.31	282.34	280.18
0.1	184.06	183.31	284.29	283.55
0.0	184.06	184.40	-	284.26

Table 9.2: The maximum amplitude measured at three pressure gauges for different widths of the plastic interface. The initial shock wave is the same for all cases, and the gauge plots are placed before, inside and after the plastic interface as shown in Figure 9.2. The last row corresponds to the air-water interface.

The results in Table 9.2 and Figure 10.7 show the maximum amplitude at gauge 2 is reduced as the plastic width is decreased. Not surprisingly, this is a consequence of having less interference with the reflected shock wave, since the gauge is farther away from the interface as the plastic width is reduced. This effect is clearly shown in Figures 10.7a, 10.7d, 10.7g. The maximum amplitude at gauge 3 is somewhat diminished at first; however, it seems to be reaching a plateau around 280.0KPa. The behavior at gauge 3 is not trivial; the shock wave bounces back and forth several times, interfering with itself constantly. In Figures 10.7b, 10.7e, 10.7h, we can see the interference becomes so fast that the pressure profile in the plastic seems to converge to a shock wave shape as the plastic width is reduced. At gauge 4, we can observe the interference between the set of transmitted shock waves generated by the back and forth reflections within the plastic interface. As the plastic width is reduced, the time elapsed between the transmitted shock waves is reduced and the interference increased. Nonetheless, when the plastic width is very small, the interference becomes so fast that the pressure profile seems to converge again to a shock wave shape, as shown in Figures 10.7c, 10.7f, 10.7i. Furthermore, note the difference in the shock wave shape in Figures 10.7h, 10.7i is almost unnoticeable. It almost seems like the shock wave is only crossing one interface instead of two. This motivates the next experiment.

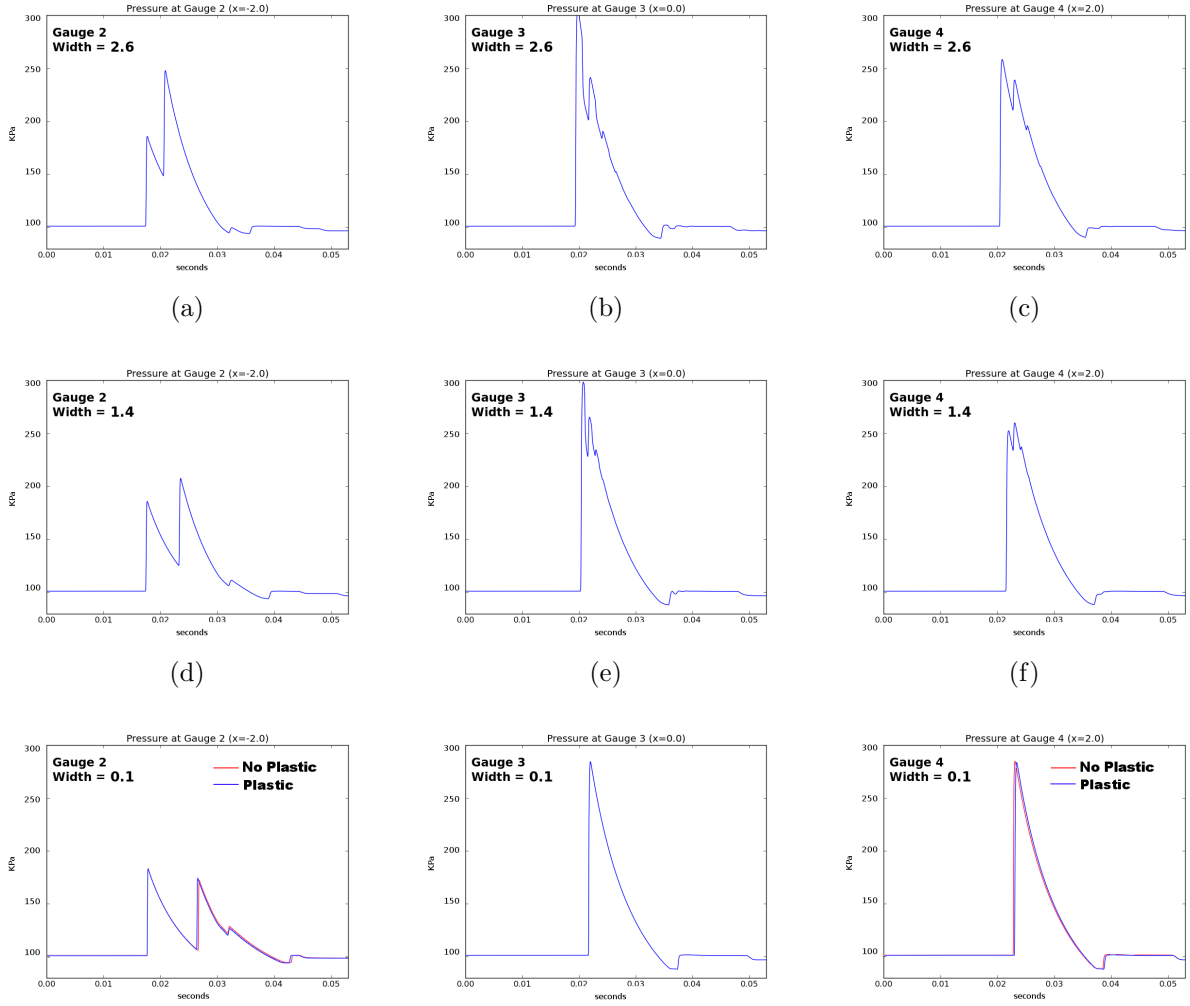

Figure 9.3: Pressure (KPa) gauge plots as a function of time (seconds). Each row of figures shows the three gauge plots for three different widths (2.6m, 1.4m and 0.1m) of the plastic interface, as shown in Table 9.2. The plots (g) and (i) for gauge 2 and 4 also show the pressure gauge plots when there is no plastic interface at all; the difference is almost unnoticeable. Also, note the red line in Figure 9.3(g) is completely overlapped by the blue line before the reflected shock appears; this is because the solutions between thin plastic and no plastic are exactly the same before interacting with the interface.

9.2.2 Air-water interface

In reality, the plastic is so thin that is really unnoticeable on larger scales. Furthermore, as the plastic is almost an incompressible medium, one should expect it would transfer the shock wave infinitely fast without energy loss. Therefore, instead of the triple material interface, now consider only an air-water interface. The result of this simulation is shown in Figure 9.4. The gauge plots for gauge 2 and 4 are shown in Figures 10.7g and 10.7i, along with the thin plastic results. The maximum amplitude in each of these gauges is presented in the last row of Table 9.2.

Comparing the air-water interface results against the ones for the smallest plastic width in the air-plastic-water interface case, we can observe the percentage error in the maximum pressure amplitude of gauge 4 is of 0.38%. This is also obvious from the thin plastic and no plastic comparison in Figures (10.7g, 10.7i). This result allowed us to simplify higher dimensional air-plastic-water interface problem to a simpler air-water interface in the work [55]. Nonetheless, the presence of the plastic is still modeled, since we force our interfaces to be fixed in space, just as a plastic container would force water to remain inside the container.

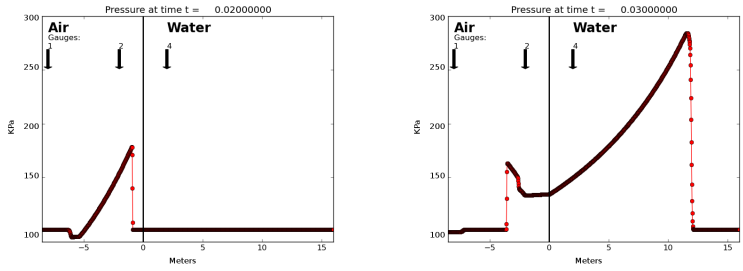

(a) (b)

Figure 9.4: Shock wave before and after crossing the air-water interface. The arrows indicate the position of the gauges that measure the pressure as a function of time. The gauges are the same as in Figure 9.2. Gauge 3 was removed since there is no plastic layer in this case.

Using computational experiments, we showed that there is not a significant difference in the transmitted shock wave between the air-plastic-water and the air-water interface. Therefore, thin plastic interfaces can be neglected in future computations. We also observed an amplification and elongation of the shock wave when crossing the interface. This effect is due to the different sound speed and compressibility of the materials. The amplitude of the initial pressure wave in the air increased by 54% when measured in the water. Since the shock intensity is much higher in water, where the endothelial cells sample is, the amplification effect is highly relevant to study injury mechanisms. Finally, the amplification effect also occurs when passing from air to plastic or any solid material, like bone. This means that

a pressure shock wave perceived as weak outside in air might be much more intense when traveling through the skull and the brain. Future work will involve an extension to three dimensions and implementation of two-phase models like those of Pelanti & Saurel [190, 222].

9.3 Air-plastic-water interface for linear acoustics

In order to further justify dropping the plastic layer, we consider the same situation of a thin intermediate layer for the case of linear acoustics. In this case, we can compute the exact solution of the transmitted pressure through the air-plastic-water interface as a function of the acoustic impedance of each material and the plastic width. This can be derived from the fact that an acoustic wave with incident pressure jump p_0 on the left of an interface between medium A (left) and B(right) produces a reflected and a transmitted wave with pressure jumps given by

$$p_T = p_0 \frac{2Z_B}{Z_A + Z_B} \qquad p_R = p_0 \frac{Z_B - Z_A}{Z_A + Z_B},$$

where Z_k denotes the acoustic impedance of medium k. These relations can be easily derived from linear acoustics [155]. Now consider a one-dimensional air-plastic-water interface. With this setup, there will be an infinite number of reflections in the plastic layer. The N^{th} wave contribution to the transmitted wave in water is given by

$$p_T^N = \frac{2Z_w}{Z_w + Z_p} \left(\frac{Z_a - Z_p}{Z_a + Z_p} \right)^{N-1} \left(\frac{Z_w - Z_p}{Z_w + Z_p} \right)^{N-1} \frac{2Z_p}{Z_p + Z_a} p_0,$$

where Z_a, Z_p, and Z_w are the air, plastic and water impedances. Each transmitted wave increases the pressure behind the initially transmitted wave slightly and the asymptotic final amplitude of the transmitted wave is given by the sum of all these contributions,

$$p_T^{total} = \sum_{N=1}^{\infty} p_T^N =$$
$$\frac{4Z_w Z_p p_0}{(Z_w + Z_p)(Z_p + z_a)} \sum_{N=0}^{\infty} \left(\frac{(Z_a - Z_p)(Z_w - Z_p)}{(Z_a + Z_p)(Z_w + Z_p)} \right)^N.$$

Summing this geometric series yields

$$p_T^{total} = p_0 \frac{2Z_w}{Z_w + Z_a}.$$

When the plastic layer is very thin, this asymptotic value is quickly reached, and we note that it is exactly the same as if the plastic interface didn't exist. The transmission coefficient

is the one computed directly from air into water. Note we assumed the pressure profile on the left was a constant p_0. However, this can be more complicated. It can have a decaying tail, in which case there will be interference from the tail in the reflected and transmitted waves. Nonetheless, assuming the plastic width is w_0, the time elapsed between two transmitted waves in the water interface is given by $\tau = 2w_0/c_p$, where c_p is the speed of sound in plastic. Therefore, as $w_0 \to 0$, the elapsed time $\tau \to 0$. As a consequence, the interference from the tail will also disappear and the plastic interface can be neglected without losing accuracy.

This calculation is an analytic result that shows that if the plastic interface is very thin in comparison to the experiment's characteristic length scales, the plastic interface can be neglected without losing much accuracy.

Chapter 10

APPLICATIONS TO BLAST-INDUCED BLOOD-BRAIN BARRIER (BBB) DISRUPTION

In this chapter, we apply the methods developed in the previous chapters to an application in Traumatic brain injury (TBI). In the TBI and medical community, there is growing concern that blast-exposed individuals are at risk of developing neurological disorders later in life. Therefore, it is important to understand the dynamic properties of blast forces on brain cells, including the endothelial cells that maintain the blood-brain barrier (BBB). The BBB regulates the passage of nutrients into the brain and protects it from toxins in the blood. In order to better understand the effect of shock waves on the BBB, we collaborated with an experimental group to develop a computational model of an *in vitro* experiment in which BBB endothelial cells are grown in transwell vessels and exposed to shocks inside a shock tube.

Extending the one-dimensional model presented in Chapter 9, we use two-dimensional axisymmetric Euler equations with a Tammann equation of state to model the experimental setup and the transwell materials. We also use the high-resolution shock-capturing finite volume methods based on Riemann solvers from Chapters 7 and 8 and the Clawpack software to solve these equations in a mixed Eulerian/Lagrangian frame. Our results indicate that the geometry of the transwell plays a significant role in the observed pressure time series in these experiments. We also found that pressures can fall below vapor pressure due to the interaction of reflecting and diffracting shock waves, suggesting that cavitation bubbles could be a damage mechanism. Computations that include a simulated hydrophone inserted in the transwell suggest that the instrument itself could significantly alter blast wave properties.

The reason we can use two-dimensional axisymmetric equations instead of the full three-dimensional ones is because experiments performed in a shock tube often exhibit cylindrical symmetry along the axis that goes through the center of the shock tube. This simplifies the three-dimensional equations into the two-dimensional axisymmetric Euler equations, which in cylindrical coordinates (r,θ,z) take the form

$$\frac{\partial}{\partial t}\begin{bmatrix}\rho\\ \rho u_r\\ \rho u_z\\ E\end{bmatrix}+\frac{\partial}{\partial r}\begin{bmatrix}\rho u_r\\ \rho u_r^2+p\\ \rho u_r u_z\\ u_r(E+p)\end{bmatrix}+\frac{\partial}{\partial z}\begin{bmatrix}\rho u_z\\ \rho u_r u_z\\ \rho u_z^2+p\\ u_z(E+p)\end{bmatrix}=\begin{bmatrix}-(\rho u_r)/r\\ -(\rho u_r^2)/r\\ -(\rho u_r u_z)/r\\ -u_r(E+p)/r\end{bmatrix}, \qquad (10.1)$$

where ρ is the density; u_r and u_z denote the velocities in the radial and axial direction, r and

z respectively; E is the total energy and p is the pressure. These equations have the same form as the two-dimensional Euler equations with the addition of geometrical source terms (the right hand side). A general discussion on the implementation of these into the numerical solution is given in Chapter 8. In Section 10.4.3, we show the numerical implementation of the source terms for the axisymmetric Euler equations.

It should be noted that the work from this chapter is part of the journal publication [55]. We will begin with an introduction to traumatic brain injury, the experimental setup used by our collaborators and an overview of the model.

10.1 Introduction: traumatic brain injury (TBI)

Traumatic brain injury (TBI) is the leading cause of death and disability for people under the age of 45 years [272]. Non-penetrating impacts to the head are also associated with increased risk of developing neurologic diseases that include Alzheimer's disease, Parkinson's disease, and amyotrophic lateral sclerosis [85, 196, 31, 149]. In addition, repetitive mild traumatic brain injury (mTBI) has been implicated in chronic traumatic encephalopathy [174, 72, 173, 37]. There is also growing evidence that repetitive low intensity non-impact blast wave exposure leads to mTBI, which similar to impact TBI, can initiate slow-developing and potentially permanent brain disturbances [172, 39, 40, 169, 178, 38, 263, 121, 97].

The current and long-term health consequences of TBI and mTBI are of great concern, particularly among military service members and Veterans, as well as civilian noncombatants [5]. Among US and coalition nations' military service members deployed to Iraq and Afghanistan, it is estimated that approximately 15% to 23% have mTBI [269, 115, 27, 242]. The majority of these mTBIs are blast-related [27, 187, 193, 168, 65], thus motivating the shock tube experiments described here.

Several sophisticated computational efforts (often employing commercial finite element software) have been made in modeling TBI. The majority of these efforts are aimed at modeling the effects of a blast in an idealized human, mouse or rat head [217, 10, 238, 239, 139, 276, 241, 259, 228, 232], sometimes including head-neck interactions [139, 114, 176]. Much of this past work has been recently reviewed in [103].

However, the mechanisms connecting blast wave exposure to mTBI are still not well understood. Clinical diagnostic neuroimaging approaches such as computerized tomography and magnetic resonance imaging (MRI) fail to detect mild injuries. This suggests that the injury mechanisms might occur at very small length scales, even at the scale of a single cell. Several hypothesis have been proposed: the disruption of BBB integrity [226, 122, 191]; cerebral vasospasm mechanotransduced by the blast wave [6]; impairment of axonal functionality [163, 164]; shock wave excitation of phonons that decay into lower frequency oscillations [143] and the formation of cavitating bubbles [182, 176, 175, 202, 277, 189, 96], among others.

In this work, along with a group of experimentalists, we study blast-induced BBB using differentiated brain-derived microvessel endothelial cells, considered the biologically most relevant *in vitro* approach for investigating BBB function [122, 123] (see Section B for further discussion). Understanding such experiments is important since they isolate one possible cause of TBI — results show that blast functionally disturbs the BBB endothelial cell tight junction protein expression patterns. However, it is still extremely difficult to obtain accurate experimental measurements of the mechanical stresses exerted at the endothelial cells' location due to blast exposure, which could help relate specific damage mechanisms with experimental outcomes. In order to provide accurate quantitative data on the strength of the shock wave at this location, we developed a computational model which focuses on this particular experimental paradigm.

The primary goal of this work is to computationally model the pressures to which BBB endothelial cells grown in a fluid-filled chamber placed in a shock tube are actually subjected. The results obtained illustrate the fact that the geometry of the chamber plays a large role in this, and suggest the possibility of cavitation occurring in this experimental system. More generally they can aid in interpreting and understanding the experimental results. We also show that the introduction of a hydrophone into the experiment, as might be done in an attempt to measure the pressures experimentally, could itself change the outcome of the experiment and the likelihood of cavitation occurring.

In an *in vivo* setting, the complexity of skull/bone anatomy, as well as the diffuse anatomy of the microvessel web in the brain, makes computational efforts to model BBB dysfunction extremely challenging. In contrast to this, the simple axisymmetric geometry of the *in vitro* system facilitates an accurate numerical investigation. As explained further below in detail, this requires novel numerical algorithms to solve compressible Euler equations coupled with a Tammann equation of state (EOS) across interfaces with large jumps in the material parameters at the interface between air and liquid. Numerical and exact methods for Euler equations with a Tammann EOS have been studied and developed previously, e.g. [126, 43, 220, 221, 229] among others; however, to the best of our knowledge, the numerical algorithms developed for this work are the only ones specifically developed to model an experimental setup with fixed sharp interfaces with a big jump in the parameters. We present some description of the methods and a verification study. These methods are studied in more detail in [52, 53] and could be adapted to study related experiments.

10.1.1 The effects of blast exposure on BBB cells

One of the early manifestations of central nervous system (CNS) injury following TBI is BBB disruption [87, 245, 218]. The BBB is responsible for maintaining and regulating separation between the CNS and the circulating peripheral blood supply [19, 279]. In the brain, many cell types work together to regulate the BBB. However, the most important functional components of the BBB are the endothelial cells themselves, which comprise the

microvessels that supply the brain. Brain endothelial cells establish specialized connections called tight junctions with other adjoining endothelial cells at points of cell-to-cell contact. This gives rise to an extremely low-permeability cellular barrier that separates the luminal (blood supply) side of the BBB from the abluminal (CNS) side of the BBB. Significantly, there is evidence that BBB disruption may play an important role in the delayed neurologic disorders associated with mTBI [226].

Recent studies have demonstrated that even mild blast exposures are capable of disrupting the BBB [1, 274, 159, 211]. In spite of this important progress, much work remains in order to understand the mechanisms by which mild blast exposure compromises BBB integrity. One approach to address this issue is to study tight junctions using more simplified *in vitro models* of the BBB [20, 21, 179]. In this experiment, mouse brain-derived endothelial cells (MBECs) were isolated and grown on permeable nylon support membranes, and then incubated in standard cylindrical transwell tissue culture chambers, as illustrated in Figure 10.1(a). Under these conditions, MBECs form an endothelial cell monolayer with mature tight junctions that functionally mimic the BBB [19, 279]. The cylindrical transwell chamber was then completely filled with tissue culture media, sealed against leaks, placed inside a shock tube, and exposed to the blast, as shown in Figure 10.1(b). Blast exposure has been shown to impair tight junction integrity under *in vitro* conditions, as well [122].

Compared to *in vivo* conditions, in which the BBB is comprised of a highly elaborate matrix of microvessels in the brain, this *in vitro* BBB system offers a much simpler geometry, with a planar MBEC monolayer positioned uniformly within a defined cylindrical containment vessel (e.g. tissue culture chamber).

Although far removed from an actual brain, this *in vitro* approach provides the functional and anatomical precision required to correlate computed shock wave dynamics at a specific BBB that has a defined orientation with respect to propagating shock waves. Such combined anatomical and temporal precision is not possible under *in vivo* experimental conditions. In addition, more complex computational models of the brain cannot directly assess actual BBB biological function.

Importantly, the model presents new computational opportunities to better estimate the biomechanical forces associated with blast overpressure exposure and thereby derive more refined assessments of how forces elicited by blast exposure affect BBB integrity under conditions that are biologically and independently quantifiable.

After exposure to the shock wave illustrated in Figure 10.1(b), tests were performed to measure the integrity of the BBB. The results in Figure 10.2A demonstrate that increasing blast intensity produced a highly statistically significant decrease in trans-endothelial electrical resistance (TEER) 24 hours post exposure ($p \leq 0.00001$). In addition, there was a statistically significant negative correlation between peak blast intensities (range: 0 – 13.9 psi) and TEER(Pearson $r = -.603$, $p < 0.00001$).

In a separate group of MBEC monolayers, the experimentalists we worked with also mea-

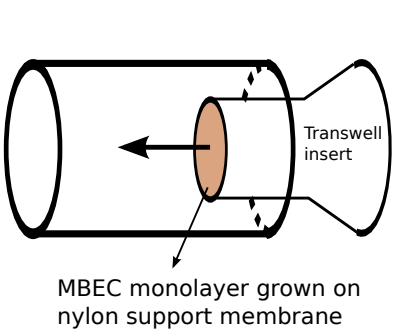

(a) Transwell

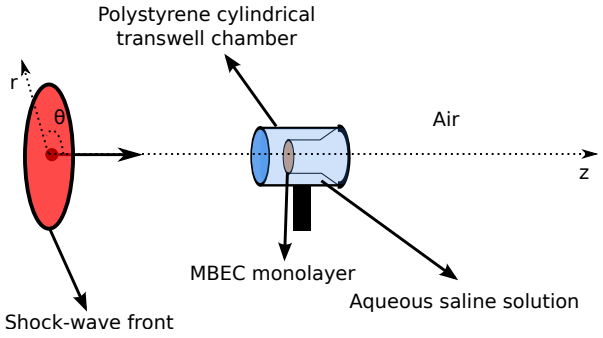

(b) Experimental setup

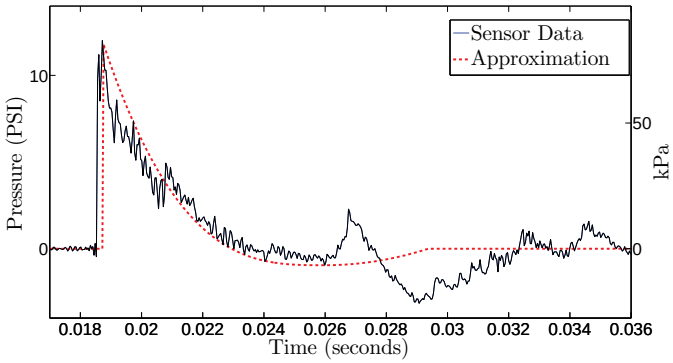

(c) Shock wave profile

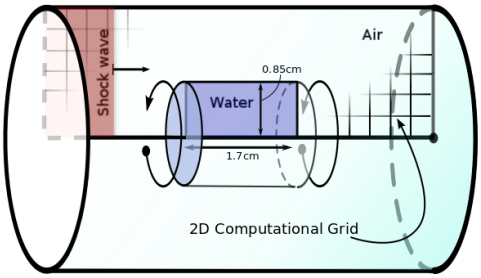

(d) 2D axisymmetric model

Figure 10.1: (a) Polystyrene transwell chamber illustration. The transwell insert with the MBEC monolayers placed into the chamber filled with an aqueous solution. (b) Cartoon of experimental system, showing the orientation of the transwell in the shock tube. The shock wave travels from the left through the air hitting the polystyrene transwell wall first, then the aqueous saline solution, and finally the endothelial cells sample. (c) The shock wave front profile obtained from a sensor before hitting the transwell as a function of time is shown as the solid line. The approximation to be used as an initial condition in the simulations herein is shown with a dashed line. (d) The 3D axisymmetric shock tube model is obtained by revolving the 2D computational grid. The inside of the inner square corresponds to the cylindrical transwell filled with aqueous saline solution, modeled here as water. The rest of the computational domain is a cylindrical cross section of the shock tube filled with air.

sured blast-induced leakage of [^{14}C]-labeled sucrose from the luminal transwell compartment (i.e., peripheral circulating blood supply) into the abluminal transwell compartment (i.e., CNS side). In keeping with the TEER measurements, Figure 10.2B shows that increasing

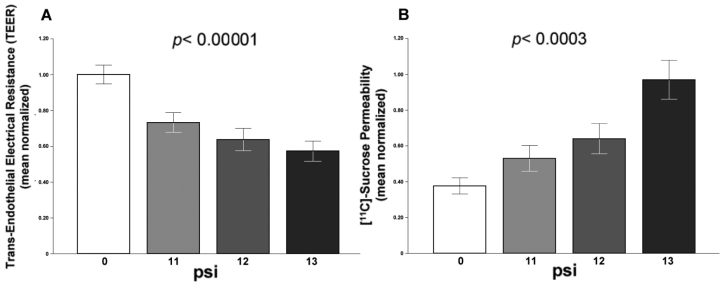

Figure 10.2: (A) Trans-endothelial electrical resistance (TEER) was significantly decreased in a blast dose dependent fashion ($p \leq 0.00001$). Histogram denotes mean normalized TEER at 24 hours after a sham exposure (0 psi) (n=26) or a single mild blast exposure with a peak amplitude of 11.0-11.9 psi (11), 12.0-12.9 psi (12), or 13.0-13.9 psi (13) (n = 15, 12, and 9, respectively). (B) MBEC monolayer permeability to radioactively labeled [^{14}C]-sucrose was significantly increased in a blast dose dependent way ($p \leq 0.0003$) with the same blast exposure regimen as in panel A (blast intensity: 0, 11.0-11.9, 12.0-12.9, and 13.0-13.9 psi; n = 7, 4, 3, and 4, respectively). Error bars indicate standard error of the mean (SEM).

blast intensity increased MBEC monolayer permeability to [^{11}C]-sucrose ($p \leq 0.0003$). Consistent with this they found a statistically significant correlation between overall peak blast intensities (range: 0–13.9 psi) and [^{14}C]-sucrose permeability (Pearson $r = .695$, $p < 0.001$).

10.1.2 The computational model

The previous experimental results along with others presented in Section B confirm that blast waves produce quantifiable and functional damage to BBB tissue. However, the physical and/or biochemical mechanisms through which blast damages brain tissue is not yet known. In order to gain insight on what some of these mechanisms might be, we have developed a computational model based on the BBB experiment —shown in Figure 10.1(b) and described in the previous section— that reproduces the dynamics and forces within the transwell chamber. The data computed with our model would be extremely difficult to obtain empirically, and moreover the introduction of a measuring device would affect the outcome of the experiment, as will be explored in detail in Section 10.2.

The computational model for this particular experiment consists of a rectangular grid modeling the cylindrical axisymmetric cross-section of the shock tube. A rectangular subsection of this grid models the polystyrene cylindrical transwell, filled with saline solution (modeled as water), which is surrounded by air. The setup is shown in Figure 10.1(b).

Some of the main issues that have been addressed with the computational model presented in the next sections are:

- determine the shock wave interaction with an air-polystyrene-water interface, as in the experiment from Figure 10.1(b), to verify that the polystyrene layer can be omitted in the computation;
- explore the three-dimensional edge effects of the cylindrical transwell;
- determine whether cavitation may be possible;
- explore how much the insertion of a hydrophone might modify measurements.

A necessary first step towards understanding the mechanical response of BBB cells under shock loading is to determine the forces acting on the cells in the laboratory experiments. The shock strength increases as the shock passes from air into the fluid-filled transwell, but the small diameter of the transwell results in waves also propagating in from the sides. When the shock wave hits the distal end of the transwell a reflected rarefaction wave is generated that interacts with the waves from the sides and multiple wave reflections lead to a complex signal.

Moreover, the strong rarefaction waves propagating in the transwell could result in fluid pressure values that are below the vapor pressure, in which case cavitation bubbles may form. As cavitation bubbles collapse they can focus considerable kinetic energy that is capable of disrupting or destroying cellular membranes [183, 42, 273, 30, 96]. Nonetheless, cavitation is a very complicated process that not only depends on the pressure but also on the amount of dissolved gas and other properties of the fluid or tissue. Moreover, cavitation thresholds in the brain are variable and still largely unknown [251, 170, 250, 171]. In this work, we are only concerned with the possibility of cavitation in the saline solution in the transwell, which was not de-gassed in the experiment reported here.

The computational results obtained herein — although they provide limited answers — support the possibility of collapsing cavitation bubbles as one possible damage mechanism within the experimental arrangement. Note the algorithms and software developed are more widely applicable and could be adapted to study related experiments. For instance, cavitation could perhaps be directly modeled by extending these methods using a six-equation two-phase numerical model instead of Euler equations [190, 221].

In the next section, we will show the results provided by the computational model. In Section 10.3, we give details of its numerical implementation, followed by further discussion in Section 10.5.

10.2 Two-dimensional axisymmetric simulation

We will present the results of the computational version of the experiment shown in Figure 10.1(b). The setup consists of the polystyrene transwell filled with saline solution, modeled

as water, without the endothelial cells, since these are too thin to be included in the model. Nonetheless, we can still measure the pressure intensity as a function of time at the point where the cells are located.

In the work [52] that was presented in the previous chapter, we implemented a one-dimensional version of the experimental system in Figure 10.1(b) by zooming in on the left face of the transwell chamber. The one-dimensional model consists of only two interfaces: air, polystyrene and water. Since the polystyrene walls of the transwell are very thin relative to the characteristic length of the experiment, we study the effect of decreasing the thickness of the polystyrene layer on the transmitted shock wave. We showed in the previous chapter that when the polystyrene interface is thin enough in comparison to the transwell length, the results are effectively the same as without it. This result allows us to set up our two-dimensional axisymmetric model with only one fixed interface between air and saline solution and completely neglect the effect of the polystyrene walls. The results and methods from this section are explained in more detail elsewhere [52].

In the next Sections, we will explore the full axisymmetric two-dimensional model that will allow us to study the edge effects and possible cavitation. Finally, we repeat this experiment with the addition of an hydrophone-shaped inclusion in order to determine how the inclusion of such a pressure-measuring device might affect the experiment.

10.2.1 Results, cavitation and edge effects

Neglecting the thin plastic interface, we constructed the two-dimensional axisymmetric computational model. The implementation was done using the methods of Chapter 8 to solve the two-dimensional axisymmetric Euler equations (Eqs. 10.1) coupled with the Tammann equation of state (EOS) (Eq. 10.2) to model the different materials. The three-dimensional solution is recovered from revolving the solution on the two-dimensional grid as shown in Figure 10.1(d), so the model is effectively three-dimensional. The geometry of the air and water interfaces is also shown. The air and water parameters for the Tammann EOS are the ones given in Table 10.1. Furthermore, to provide an accurate model, we need to model length scales according to the experiment. The cylindrical transwell filled with water (saline solution) is 1.7 cm long with a radius of 0.85cm; it can be modeled as a two-dimensional rectangle before being revolved. The shock wave is modeled by feeding the profile shown in Figure 10.1(c) to the left boundary of the computational domain. However, on the time and length scales of the simulation, we only observe the shock wave and an essentially constant pressure behind the shock, since the rarefaction wave that reduces the pressure behind the shock wave decays over roughly 3 msec while the computation is run for only 134 μs.

The results from the simulation are shown for different times in Figure 10.3 as contour and pseudo-color plots of the pressure in the two-dimensional cross section. The corresponding one-dimensional pressure profiles along the axis of rotation are shown in the lower figure of each frame. Several relevant effects can be observed. The amplitude of the pressure is

increased as expected from the previous one-dimensional calculations [52]. Also, we can see that the geometry affects the pressure profile as well as the ongoing reflections inside the cylindrical transwell. Of particular interest is the fourth time frame of Figure 10.3, where the reflected wave has a pressure below water vapor pressure at room temperature. Since the water at room temperature can become gas when the pressure is below the vapor pressure, cavitation is possible. It is known that cavitating bubbles can be responsible for cell detachment and cell membrane poration [183, 42] and could be a possible mechanism of injury to the endothelial cells of the BBB.

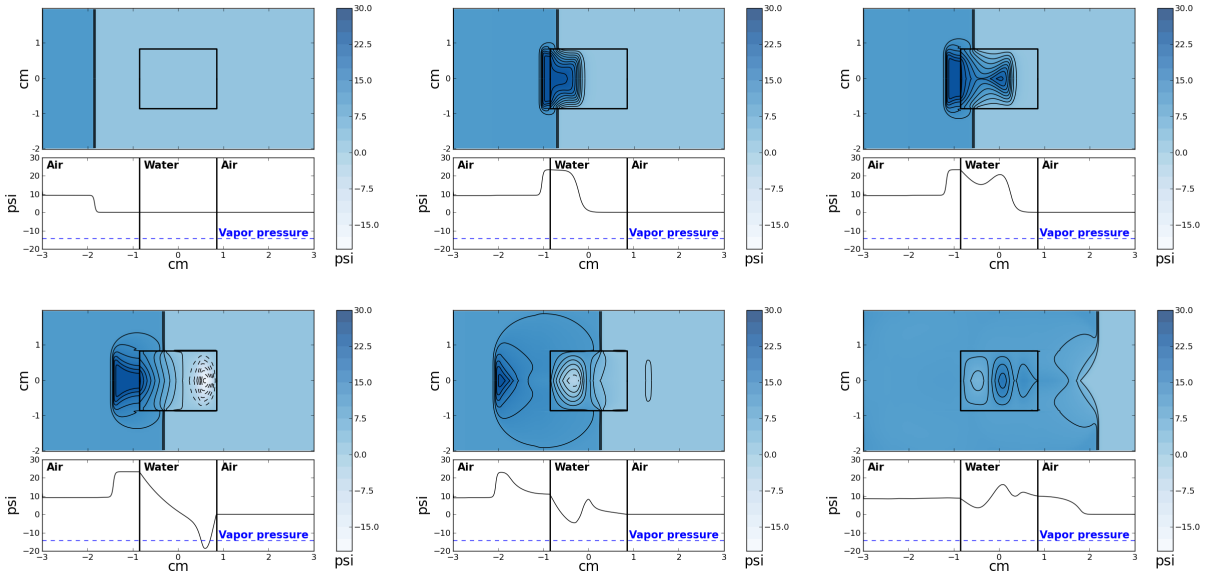

Figure 10.3: Axisymmetric simulation output at six different times points $t = 30$, 60, 63.2, 69.6, 84.8 and 134.4 μs. Two-dimensional pressure contour plots of a planar cross section of the cylinder are shown, along with pressure trace along the axis. Water vapor pressure is also shown indicating where cavitation might be possible. Distance is displayed in centimeters and pressure in psi, where atmospheric pressure corresponds to 0 psi.

To further understand these effects, we can observe Figure 10.5 where the axisymmetric model is compared to the one-dimensional one. The geometrical edge effects are clearly seen in the second frame, where the pressure profile exhibits a decay in the amplitude after the shock wave has crossed the interface. This is due to the presence of the cylindrical transwell walls parallel to the axis of rotation. As noted elsewhere [52], pressure values below atmospheric pressures do not appear in the one-dimensional case, illustrating that low pressure values that might produce cavitation are a direct consequence of the geometrical edge effects.

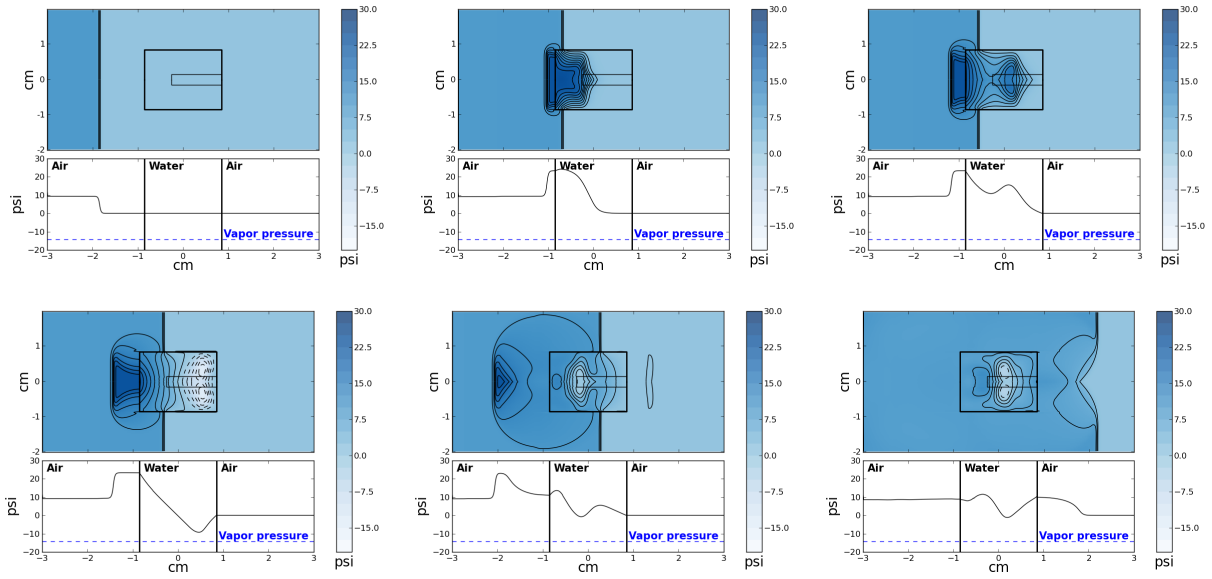

Figure 10.4: Same as Figure 10.3 but with an hydrophone inserted. Note that in Frame 4 the pressure does not go below the vapor pressure in this case.

As we mentioned before, we are employing a two-dimensional axisymmetric computational model, which effectively models three-dimensional shock wave propagation. In Figure 10.6, we show a three-dimensional visualization of the solution by revolving the solution of frames 1,3 and 6 of Figure 10.3. The figure shows three-dimensional pressure contours, and it is included to emphasize the fact that we are modeling propagation of waves in three dimensions.

10.2.2 Effects of introducing a hydrophone

One might like to experimentally measure the pressure at the location of the endothelial cells in the transwell in order to determine the force applied to the membrane and the possibility of cavitation. The experimentalists we worked with attempted to introduce a customized version of the Y-104 hydrophone (Sonic Concepts, Bothell WA) in some of the laboratory experiments, but they were unable to gather sufficiently high quality low-frequency data to compare with our numerical results. They did not pursue these experiments because we realized that the introduction of this device could directly affect the signal being measured, reducing the value of such data. A significant advantage of the computational model is that we can measure the pressure at computational gauge locations without interfering with the wave propagation.

We can use the computational model to gain insight on how much the introduction of an

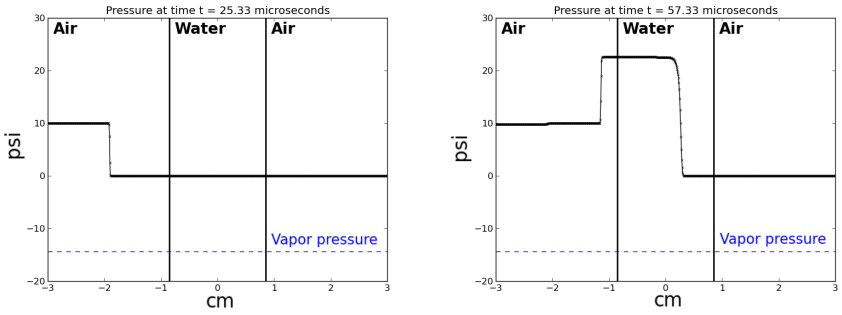

(a)

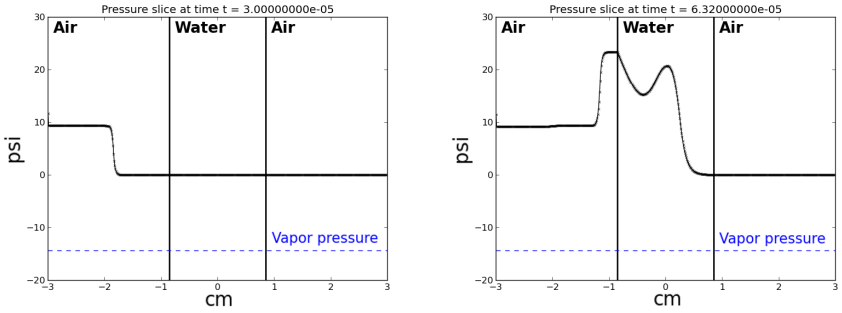

(b)

Figure 10.5: (a) Pressure shown at two time frames from a one-dimensional simulation. Left: The initial shock approaching the interface. Right: The reflected and transmitted shocks. (b) Pressure along the axis at the same two times, from the two-dimensional axisymmetric simulation. The edge effects in the pressure profile are evident in the second time frame.

hydrophone would change the experimental results. To this end, we include an axisymmetric computational hydrophone down the center of the transwell in the following simulations, with a diameter of 2.85mm to match the Y-104 model. The main effect that concerns us when incorporating the hydrophone in the simulation is the reflection of acoustic waves back into the liquid. The hydrophone is not uniquely composed of a single material and it is designed to have a net impedance of the same order of magnitude as water ($\sim 1.5 \times 10^6 Pa \cdot s/m$). Furthermore, solids usually have impedances higher than water, so we can simply model the hydrophone as a general elastic solid with such properties. For this work, we model it as made of polystyrene with the parameters from Table 10.1 and a resulting impedance of ($\sim 2.4 \times 10^6 Pa \cdot s/m$). Modifying the impedance of the hydrophone material in the simulations through nine values within the same order of magnitude ($2 \times 10^6 Pa \cdot s/m$ to $7 \times 10^6 Pa \cdot s/m$) did not change any of the qualitative results presented here.

The computational results with the hydrophone are shown in Figure 10.4. We note

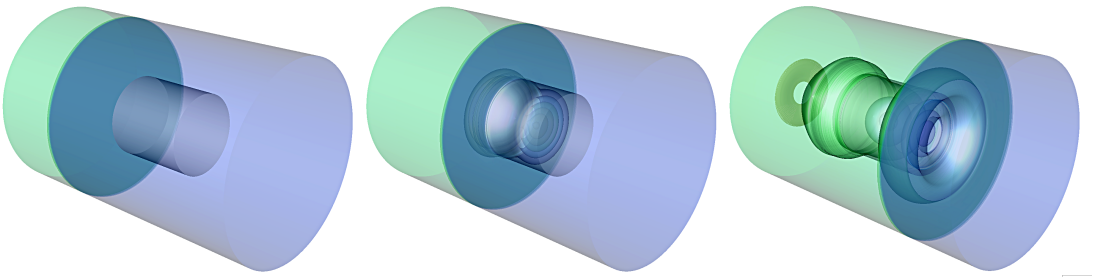

Figure 10.6: Three-dimensional visualization by revolving the solution of frames 1, 3 and 6 of the two-dimensional axisymmetric results from Figure 10.3. The cylindrical transwell can be well appreciated on the first frame. The visualization shows the pressure contours, darker contours correspond to higher pressure. Its purpose is to emphasize that the two-dimensional axisymmetric model is effectively modeling three-dimensional wave propagation.

there is a significant difference between the results obtained in comparison to those without the hydrophone from Figure 10.3. These data indicate that, in principle, hydrophone and intracranial pressure sensors placed in a small enclosed volume can alter shock wave propagation in functionally significant ways. This has implications also for rodent experiments, as we see that an intracranial pressure sensor placed within a volume comparable to that of a rodent skull can significantly alter shock wave dynamics, sufficient to change conditions that may favor cavitation.

In order to better quantify the difference between the experiment with and without the hydrophone, we placed three gauges at key points in both systems. In Figure 10.7, we can observe the comparison between the pressure profile as a function of time in the three chosen points. We can see the pressure only falls below vapor pressure in Gauge 2 and Gauge 3 when the hydrophone is not present. We can conclude that the inclusion of an hydrophone in the experimental system eliminated the possibility of observing cavitation. More importantly, measuring the pressure profile with a hydrophone in an experimental system like this one, affects the observed pressure profile, which supports the use of a computational model for quantifiable insight and answers to some experimental issues.

10.3 The mathematical model

In this section, we give an outline of the numerical implementation, summarizing the general methods used in Clawpack as well as the original approaches and implementations that were designed uniquely for this work.

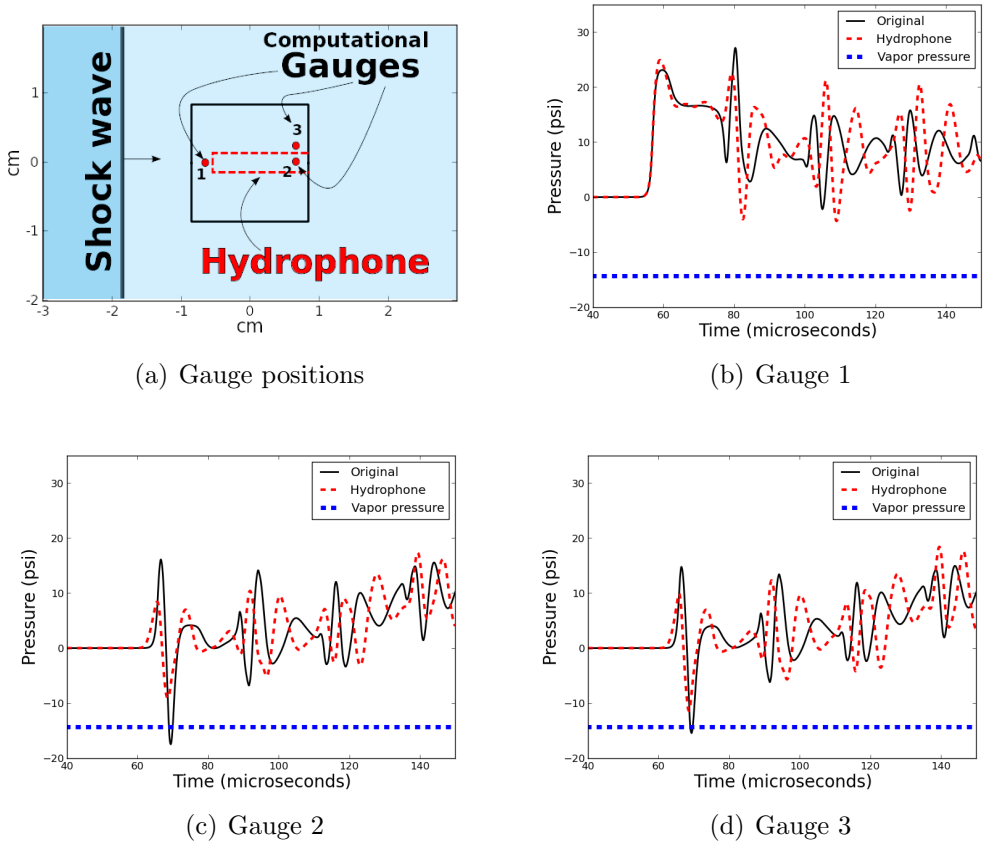

(a) Gauge positions

(b) Gauge 1

(c) Gauge 2

(d) Gauge 3

Figure 10.7: Comparison of the pressure at computational gauges when a hydrophone is introduced with the pressure in the absence of a hydrophone. The location of three gauges is shown on the first frame. The pressure profiles (psi) as a function of time (μs) are shown for the three gauges. The output of the original simulation without the hydrophone is plotted with a solid line; the output of the simulation with the hydrophone is plotted on a dashed line and the vapor pressure is plotted with a thick dashed line. Note that the pressure falls below vapor pressure in the original simulation at Gauge 2 and Gauge 3 but not when the hydrophone is introduced. Also note that in the presence of the hydrophone, Gauge 2 becomes irrelevant.

10.3.1 The Euler equations

We use the inviscid Euler equations for compressible flow, with different parameters in the equations of state (EOS) for each material. The axisymmetric Euler equations in cylindrical coordinates (r,θ,z) take the form of Eqs. 10.1. These equations have the same form as the two-dimensional Euler equations with the addition of geometrical source terms (right hand

side). These source terms are further discussed in Section 10.4.3.

For the computational model, we must handle wave propagation in liquid and elastic solids as well as in the air. To handle this range of materials we use the stiffened gas equation of state (SGEOS), also known as the Tammann EOS, which was introduced in Section 8.2.1. This equation of state is very useful to model a wide range of fluids even in the presence of strong shock waves and was successfully used in [74, 76] to model shock wave propagation in tissue and bone. The Tammann EOS is given by

$$p = (\gamma - 1)\rho e - \gamma p_\infty, \tag{10.2}$$

where γ and p_∞ can be determined experimentally for different materials and conditions. The choice of parameters for some materials is shown in Table 10.1. It is worth mentioning again that for sufficiently weak shocks the Tammann EOS can be further simplified to the Tait EOS, which neglects the energy coupling. In [74] this was shown to be adequate for modeling shocks in fluids and solids in the context of shock wave therapy. In this work, we will employ the Tammann EOS since it provides a more comprehensive approach and conserves the energy coupling that could be useful to relate to thermodynamic quantities.

Material	γ	$p_\infty(GPa)$
Air (Ideal gas EOS)	1.4	0.0
Polystyrene	1.1	4.79
Water	7.15	0.3

Table 10.1: Parameters for the Tammann EOS to model the different materials. The parameters for air and water were taken from [74]. Since the polystyrene is a solid, γ was chosen very close to 1, and p_∞ was adjusted to yield the right speed of sound in polystyrene. The saline solution in the transwell should have parameters very close to water.

10.4 Numerical methods

The Euler equations (Eqs. 10.1) are a hyperbolic system of conservation laws, so they can be solved employing finite volume methods (FVM). This is done by using the wave propagation algorithms described in detail elsewhere [155, 154] and implemented in Clawpack [44]. The fundamental problem that needs to be solved at each cell interface of our computation is the well known Riemann problem. A general one-dimensional Riemann problem for a system of conservation laws was already introduced in Section 7.1.1 and in particular for Euler equations in Section 8.2.2.

When employing finite volume methods, we need to introduce the concept of cell average: $Q_i^n = \frac{1}{\Delta x}\int_{x_{i-1/2}}^{x_{i+1/2}} q(x, t_n)dx$, where i is the cell number and n the time step index. At the edge

between two cells, the Riemann problem initial condition would be determined by $q_\ell = Q^n_{i-1}$ and $q_r = Q^n_i$. After solving the Riemann problems at every cell edge, we can average the respective contributions to obtain the new cells average after a time Δt. The reader is referred elsewhere [154, 155] for a detailed exposition of the algorithms.

The equations of motion are solved by implementing a hybrid Riemann HLLC-exact Riemann solver for the Euler equations with interfaces. This Riemann solver is based on the solvers from Sections 8.2.3 and 8.2.4. It couples a Eulerian HLLC (Harten-Lax-van Leer-Contact) approximate Riemann solver, see [249, 248] to a Lagrangian exact Riemann solver for the Euler equations with a Tammann EOS [1]. As the interfaces are represented by contact discontinuities, the HLLC solver is ideal to deal accurately with interface problems. The method can be extended to two and three dimensions, retaining second order accuracy, by implementing transverse solvers with an unsplit method [154]. We designed the transverse Riemann solvers as approximate solvers based on linear acoustics and adapted them to deal with interfaces. The source terms for the axisymmetric case are resolved using an operator splitting [155, 156]. A detailed description of the hybrid HLLC-exact normal Riemann solver for the Euler equations with the Tammann EOS with discontinuous parameters is presented in [52], in the context of one-dimensional problems. The extension of this solver to a Riemann solver normal to a cell interface in two space dimensions is straightforward and will not be discussed here. For the unsplit wave propagation algorithms implemented in Clawpack, this must be augmented with a transverse Riemann solver, as described in the Section 10.4.2. The source terms that arise from axisymmetry are handled via a fractional step approach described in Section 10.4.3.

10.4.1 Verification

In this section, we will verify that the finite volume methods coupled with the hybrid Riemann HLLC-exact Riemann solver for the Euler equations with a Tammann EOS give the correct solution for a simple model problem. As the studies in Section 10.2 are concerned with the dynamics of a shock wave traveling in an air-water-air system with two interfaces, we use this example as the test case. The exact analytic solutions of Riemann problems for Euler equations are only available in one dimension, so we restrict our verification to a one-dimensional test. This analysis will test the accuracy of the approximate hybrid Riemann solver, the key ingredient of our numerical method, also in the two-dimensional extension of the algorithm.

The test problem is illustrated in the x–t plane diagram on the left of Figure 10.8. We will use a one-dimensional version of our algorithms, where we have an incoming shock of the same shape and intensity than the one used for Figure 10.3. We divide the domain into three materials: air-water-air, as in the original problem. At the time the shock hits the air-water

[1] A Lagrangian version of the HLLC solver can be also used

interface at point A, we can view the problem as a Riemann problem and compare it to the exact solution. Furthermore, after the transmitted shock travels to the second interface, we have a second Riemann problem and can repeat the same procedure at the water-air interface at point B and also compare the transmitted and reflected waves to the exact solution at that point. However, it should be noted that in the numerical algorithm the incoming shock is not perfectly sharp, so we cannot expect a perfect match between our numerical solution and the exact solution.

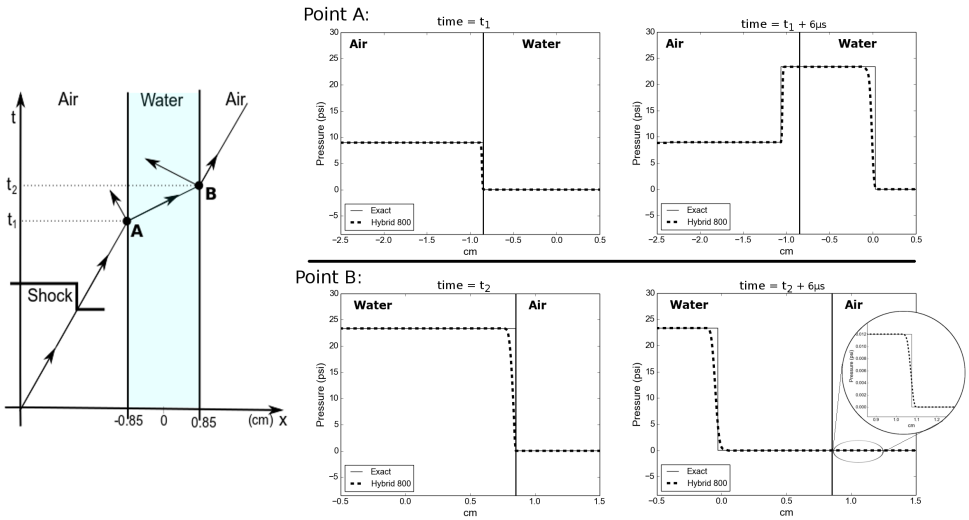

Figure 10.8: Verification study of the numerical methods. On the left, we show the x–t plane of an incoming shock that hits the air-water interface at point A. The transmitted shock then hits the water-air interface at point B. For both points, we show the solution when the shock hits the interface and another one $6\mu s$ later. The exact solution can be constructed as described in the text and is compared with the numerical solution computed using the hybrid HLLC-exact solver with 800 grid points. The air and water materials were modeled using the parameters from Table 10.1.

At point A in Figure 10.8, we provide two plots: one just before the shock hits the air-water interface at t_1 where we can frame the problem as a Riemann problem, and the second one $6\mu s$ later. Both plots show two curves, one using the exact Riemann solver for the Euler equations with the Tammann EOS, with a jump in the parameters [53, 126], and the other one is the numerical solution using the hybrid HLLC-exact solver for the Riemann problems that arise at each cell interface every time step.

The same procedure is repeated in point B of Figure 10.8. The first plot shows the transmitted shock from the exact Riemann solution at point A, just before hitting the water-air interface at time t_2, and the second one $6\mu s$ later. Notice in this last plot that there

appears to be no transmitted wave. However, the zoomed-in bubble shows that there is a very weak transmitted shock at this interface of magnitude roughly 0.013 psi. Due to the much lower density of air relative to water, this interface acts nearly like a free boundary and the reflected wave is a rarefaction wave, which is difficult to appreciate from the figure since the difference between the rarefaction head and tail speeds is very small. At both points in Figure 10.8, we can see a very good agreement between our numerical solution and the exact solution. Furthermore, in Figure 10.9, we provide a convergence test. We chose to show it using the second plot at point B of Figure 10.8 since it gathers information of transmitted and reflected waves from both interfaces. Figure 10.9 shows that the solution converges as we refine the resolution of our numerical solution.

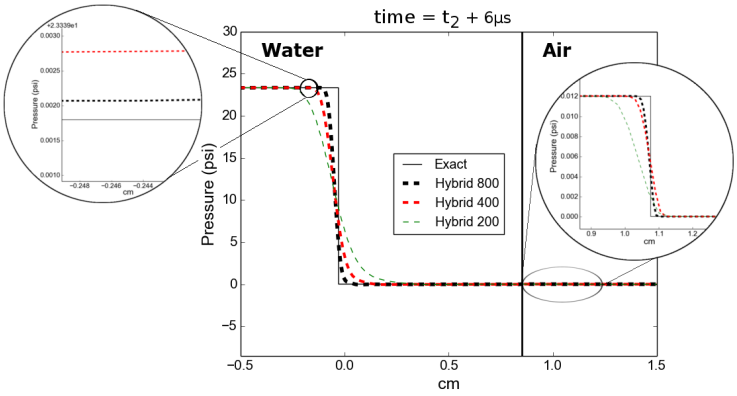

Figure 10.9: The last plot in Figure 10.8 is recomputed with three different numerical resolutions to show convergence. The numerical solutions are computed using the hybrid HLLC-exact solver with 200, 400 and 800 grid points. Two zoomed in regions in key areas are shown.

10.4.2 Transverse Riemann solvers

We introduced the concept of transverse Riemann solver in Section 8.1.4. This solver takes the results of a Riemann solution in the direction normal to a cell interface and splits it into components moving in the transverse direction that contribute to updating the solution in the adjacent rows of grid cells. Other alternatives also exist for solving multi-dimensional conservation laws that attempt to use more fully multi-dimensional Riemann solutions, for example in work of Roe [216] and Fey [82, 83]. Of particular relevance to the approximate Riemann solver approach used here is the work of Balsara [17, 18], who defines two-dimensional HLLC Riemann solvers that accept four input states that come together at an edge and outputs the multi-dimensionally upwinded fluxes in both directions. A comparison between these two approaches could be of relevance in future studies.

For the present problem with sharp interfaces between very different materials, instabilities were seen to easily arise, particularly at the corners of the rectangular region representing the transwell. A special transverse solver was developed that we now describe, based on the solver for acoustics in a heterogeneous media that is described in Section 21.5 of [155]. Note that for two-dimensional problems on rectangular grids, the cell average is calculated as $Q^n_{i,j} = \frac{1}{\Delta y \Delta x} \int_{C_{i,j}} q(x, y, t_n) dx\, dy$, where $C_{i,j}$ is the cell $[x_{i-1/2}, x_{i+1/2}] \times [y_{j-1/2}, y_{j+1/2}]$.

We recall the basic idea of a transverse solver in Figure 11.4. For a constant coefficient linear hyperbolic system of equations $q_t + Aq_x + Bq_y = 0$, the jump in normal flux between adjacent cells, $A\Delta Q_{i-1/2} = A(Q_{i,j} - Q_{i-1,j})$, is split via the normal Riemann solver into "fluctuations" $A^-\Delta Q_{i-1/2}$ and $A^+\Delta Q_{i-1/2}$ that correspond to the net contribution of all left-going or right-going waves to the cell averages on either side. Here $A^\pm = R\Lambda^\pm R^{-1}$ where $A = R\Lambda R^{-1}$ is the eigen-decomposition of A and $\Lambda^\pm$ are the diagonal matrices in which either the negative or positive eigenvalues have been set to zero. Each fluctuation, e.g. $A^+\Delta Q_{i-1/2}$, is then further split into down-going and up-going components $B^-A^+\Delta Q_{i-1/2}$ and $B^+A^+\Delta Q_{i-1/2}$, based on the matrices B^+ and B^-.

In the case of variable coefficients or nonlinear problems, the general notation $\mathcal{B}^-\mathcal{A}^+\Delta Q_{i-1/2}$ and $\mathcal{B}^+\mathcal{A}^+\Delta Q_{i-1/2}$ is used for these two vectors. For variable coefficient acoustics, as described in [155], the up-going fluctuation from the transverse splitting is based on eigenvectors of B_{ij} and $B_{i,j+1}$, while the down-going fluctuation is based on eigenvectors of B_{ij} and $B_{i,j-1}$. For a nonlinear problem $q_t + f(q)_x + g(q)_y = 0$, the eigen-decomposition of some averaged Jacobian $g'(q)$ is generally used for the transverse Riemann solver.

The present problem involves both nonlinearity and varying material properties. Since we are modeling the almost incompressible liquid in a Lagrangian frame of reference [52], the transverse Riemann problem will mostly be concerned with the two acoustic waves. In order to derive the approximate transverse solver, we will rely on linearized acoustic equations around ρ_0, u_0 [155] in terms of the density and momentum,

$$\begin{bmatrix} \rho \\ \rho u \end{bmatrix}_t + \underbrace{\begin{bmatrix} 0 & 1 \\ c^2 & 0 \end{bmatrix}}_{\tilde{B}(Q)} \begin{bmatrix} \rho \\ \rho u \end{bmatrix}_y = 0, \tag{10.3}$$

where we use y as the space variable to emphasize this is solved in the transverse direction, c is the sound speed and $\tilde{B}(Q)$ can be understood as a lower dimensional approximation of the transverse Jacobian $g'(Q_0)$ for the Euler equations. Note we assumed $u_0 = 0$, which is equivalent to assume we are in a Lagrangian frame of reference. The eigenvectors of the Jacobian of the system are given by $[1, \pm c]$ and the eigenvalues by $\pm c$; however, when solving the transverse Riemann problem, we might have different materials and sound speeds in the cell above or below. Instead of evaluating the whole Jacobian in one state, as in a Roe linear solver [215], we will evaluate the eigenvectors according to their location. These will be given

by $v_u = [1, c_u]$ for the upward acoustic wave and $v_d = [1, -c_d]$ for the downward acoustic wave with eigenvalues c_u and $-c_d$. Here u and d refer to cells $(i, j+1)$ and (i, j) when computing $\mathcal{B}^+\mathcal{A}^+\Delta Q_{i-1/2,j}$ and to cells (i, j) and $(i, j-1)$ when computing $\mathcal{B}^-\mathcal{A}^+\Delta Q_{i-1/2,j}$. The matrix of eigenvectors R and its inverse are given by,

$$R = \begin{bmatrix} 1 & 1 \\ c_u & -c_d \end{bmatrix}, \quad R^{-1} = \frac{1}{c_u + c_d} \begin{bmatrix} c_d & 1 \\ c_u & -1 \end{bmatrix}.$$

The up-going and down-going fluctuations for $\mathcal{A}^+\Delta Q_{i-1/2,j}$ are obtained by expanding the fluctuation in terms of these two eigenvectors or waves, $\mathcal{A}^+\Delta Q_{i-1/2,j} = \alpha_u v_u + \alpha_d v_d$, so we need to solve $R\alpha = \mathcal{A}^+\Delta Q_{i-1/2,j}$, Note that the required fluctuation $\mathcal{A}^+\Delta Q_{i-1/2,j}$ for the Euler equations is a 4 dimensional vector with fluctuations in density, normal momentum, transverse momentum and internal energy. As we are only interested in the acoustic waves, we will assume the fluctuations in normal momentum and energy are negligible, so we define the acoustic part of the fluctuation as the first and third entry of the 4 dimensional vector, i.e. $\mathcal{A}^+_{ac}\Delta Q_{i-1/2,j} = [\mathcal{A}^+_{\Delta Q1}, \mathcal{A}^+_{\Delta Q3}]$. Solving the system for the vector $\alpha = R^{-1}\mathcal{A}^+_{ac}\Delta Q_{i-1/2,j}$, we obtain

$$\alpha_u = \frac{1}{c_u + c_d}\left(c_d\mathcal{A}^+_{\Delta Q1} + \mathcal{A}^+_{\Delta Q3}\right),$$
$$\alpha_d = \frac{1}{c_u + c_d}\left(c_u\mathcal{A}^+_{\Delta Q1} - \mathcal{A}^+_{\Delta Q3}\right).$$

The up-going and down-going acoustic fluctuations are given by the velocity times the waves,

$$\mathcal{B}^+_{ac}\mathcal{A}^+\Delta Q_{i-1/2,j} = c_u\alpha_u v_u,$$
$$\mathcal{B}^-_{ac}\mathcal{A}^+\Delta Q_{i-1/2,j} = -c_d\alpha_d v_d.$$

We require to solve two of these transverse solvers for the Euler equations as shown in the grid in Figure 11.4. We will only consider the up-going fluctuation of the transverse solver at $(i, j+1/2)$ and the down-going fluctuaction of the solver at $i, j-1/2$. This yields the full fluctuations as

$$\mathcal{B}^+\mathcal{A}^+\Delta Q_{i-1/2,j} = \frac{c_3\left(c_2\mathcal{A}^+_{\Delta Q1} + \mathcal{A}^+_{\Delta Q3}\right)}{c_3 + c_2}\begin{bmatrix} 1 \\ 0 \\ c_3 \\ 0 \end{bmatrix},$$

$$\mathcal{B}^-\mathcal{A}^+\Delta Q_{i-1/2,j} = \frac{-c_1\left(c_2\mathcal{A}^+_{\Delta Q1} - \mathcal{A}^+_{\Delta Q3}\right)}{c_1 + c_2}\begin{bmatrix} 1 \\ 0 \\ -c_1 \\ 0 \end{bmatrix},$$

where c_1, c_2 and c_3 are the speeds of sound in cells $(i, j-1)$, (i, j) and $(i, j+1)$ respectively and the non-acoustic fluctuations were neglected. The sound speeds are calculated with the pressure, density and the parameters of the Tammann EOS in the respective cell with $c = \sqrt{\gamma \frac{p+p_\infty}{\rho}}$. Note this process is repeated in exactly the same manner for the left going fluctuation $\mathcal{A}^- \Delta Q_{i-1/2,j}$ of the normal Riemann problem.

10.4.3 Geometrical source terms

In order to solve for the source terms of Eqs. 10.1, we need to apply a splitting method, see [155]. In the first half time step, we solve the homogeneous version of Eqs. 10.1 over the whole grid, and in the second step we solve the system of ODEs obtained by ignoring the flux terms,

$$\frac{d}{dt}\begin{bmatrix} \rho \\ \rho u_r \\ \rho u_z \\ E \end{bmatrix} = \begin{bmatrix} -(\rho u_r)/r \\ -(\rho u_r^2)/r \\ -(\rho u_r u_z)/r \\ -u_r(E+p)/r \end{bmatrix}. \tag{10.4}$$

This equation can be solved with any explicit time integrator method like forward Euler and Runge-Kutta methods or an implicit solver, such as TR-BDF2. However, this particular system can be solved exactly. Consider the first equation of Eqs. 10.4 and multiply it by u_r, then

$$\begin{aligned} u_r \frac{d\rho}{dt} &= \frac{\rho u_r^2}{r}, \\ \Rightarrow \frac{d\rho u_r}{dt} - \frac{du_r}{dt}\rho &= -(\rho u_r^2)/r, \end{aligned}$$

where we used the product rule. Now substituting the second equation of Eqs. 10.4 into this result, we obtain $\frac{du_r}{dt} = 0$, so u_r is constant. The same procedure can be applied to obtain that u_z is also constant.

As the total energy is given by $E = \rho e + \frac{1}{2}\rho(u_r^2 + u_z^2)$, where the Tammann EOS (Eq. 10.2) allows the substitution $\rho e = (p + \gamma p_\infty)/(\gamma - 1)$. As u_r and u_z are constant, we can differentiate the energy, $E_t = (\rho e)_t = \frac{1}{\gamma - 1} p_t$. These results in conjunction with the fourth equation of Eqs. 10.4, yield $p_t = -(u_r/r)[\gamma(p + p_\infty) + \frac{1}{2}(\gamma - 1)\rho(u_r^2 + u_z^2)]$. We now have a full system of equations in the primitive variables:

$$\begin{aligned} &\frac{d\rho}{dt} = -(u_r/r)\rho, \quad \frac{du_r}{dt} = 0, \quad \frac{du_z}{dt} = 0, \\ &\frac{dp}{dt} = -(u_r/r)\left(\gamma(p + p_\infty) + \frac{1}{2}(\gamma - 1)\rho(u_r^2 + u_z^2)\right). \end{aligned}$$

The first three equations can easily be solved, and the fourth equation can also be solved with the solution of the first one and an integrating factor. Using the fact that the initial conditions for the computation are the variables at time t^n, and we want the solution at time $t^{n+1} = t^n + \Delta t$, we obtain

$$\begin{aligned}
\rho^{n+1} &= \exp\left(-\frac{\Delta t u_r^n}{r}\right)\rho^n, \qquad u_r^{n+1} = u_r^n, \qquad u_z^{n+1} = u_z^n, \\
p^{n+1} &= \exp\left(-\frac{\Delta t \gamma u_r^n}{r}\right)p^n - p_\infty\left(1 - \exp\left(-\frac{\Delta t \gamma u_r^n}{r}\right)\right) \\
&\quad - \frac{\rho^n}{2}\left((u_r^n)^2 + (u_z^n)^2\right)\left[\exp\left(-\frac{\Delta t u_r^n}{r}\right) - \exp\left(-\frac{\Delta t \gamma u_r^n}{r}\right)\right], \\
E^{n+1} &= \frac{p^{n+1} + \gamma p_\infty}{\gamma - 1} + \frac{1}{2}\rho^{n+1}\left((u_r^n)^2 + (u_z^n)^2\right).
\end{aligned} \tag{10.5}$$

The parameters γ and p_∞ are given by the Tammann EOS in Eq. 10.2. The equations we just obtained allow us to calculate one-time step of Eqs. 10.1 in our splitting method. Note these source terms are never singular in the computation; when using finite volume methods, the quantities are evaluated at cell centers, so $r > 0$.

10.5 Discussion and future directions

A computational model was designed to better understand the physical forces developed by blast-induced shock waves that can damage brain endothelial cells in an *in vitro* model of the BBB. The numerical modeling of the experiment employs finite volume methods and requires coupling a highly compressible material (air) with a nearly incompressible liquid contained in a fixed region in space. The coupling is accomplished by employing a Tammann EOS and designing both normal and transverse Riemann solvers that can couple these two materials — one in a Eulerian frame of reference and the other in a Lagrangian frame of reference. Results show the shock wave pressure amplitude and velocity increase when crossing from air to the water (saline solution). This is in agreement with the one-dimensional simulations described by us previously [52], as well as other works mentioned in a recent review [103]. One aspect of the potential relevance of this effect lies in the underestimation of the pressure intensities experienced by the cells when one considers only the amplitude and kinetic properties of a standard open field blast overpressure.

Comparison of the computational results here to the one-dimensional tests performed in [52] show that the transwell geometry is very relevant. The edge effects from the cylinder, combined with the rarefaction wave arising when the shock reflects off the distal end of the transwell, can generate low enough pressure to potentially produce cavitation, which could be a cause of cell damage [183]. The simulation with a hydrophone in place does not show

low enough pressure values to produce cavitating bubbles. These results indicate that the computational model could be useful to experimentalists in analyzing how the introduction of a measuring device affects the outcome of the experiment and the likelihood of cavitation being a BBB tissue damage mechanism.

Although based on an idealized model, our computational approach allows us to measure the pressure profile at any point and at the exact location of the biological sample without interfering with the actual experimental setup. This task would be extremely difficult to obtain empirically. The high-resolution signal obtained by our computational method allows us to apply it to identify regions with low enough pressure to potentially produce cavitation. Furthermore, our results allow us to suggest cavitation as a damage mechanism that might explain the experimental results, for instance, the mislocalization of the tight junction proteins, ZO1, and claudin-5, that functionally disturb the BBB. This kind of study can clarify the qualitative behavior of the system and, where it is impossible for experimentalists. It can also suggest possible connections between damage mechanisms and anatomical, functional, morphological, and molecular specificity, obtained from the experimental results.

The computational model developed in this work was designed for a specific application; however, the methods developed can be adapted and applied to other experiments with similar simplified geometry. These methods can also be extended to other geometries and the Clawpack software (with adaptive mesh refinement) can be applied in situations where a logically rectangular grid can be mapped to a quadrilateral two-dimensional grid. This can include situations in which the interface is circular or of other smooth shape lacking corners using the sort of mappings proposed in [34], which have been used for elastic and poroelastic wave propagation problems in the work of Lemoine [150, 151]. Extension of the methods proposed in this work to such cases is currently under way and will be reported elsewhere [53]. This extension is clinically relevant; it allows detailed studies of the pressure signal obtained by shock waves interacting directly with the skull in conditions that might not be feasible experimentally, emphasizing the importance of having a computational model available.

The computational simulations were evaluated up through the first 200 microseconds. As seen in Figure 10.1(c), this corresponds to a very short time period behind the shock, before the bulk of the trailing rarefaction wave has passed the transwell. Planned future work includes the refinement of our numerical method to carry out the simulation to longer times. This can be of relevance given the negative pressure values and oscillations that arise on millisecond time scales, as well as the secondary reflection-induced shock, see Figure 10.1(c). These features, along with the internal reflections might also cause or even increase cavitation effects.

Some other possible future research directions include extension of the computational methods to arbitrary interface geometry and to two-phase models that can simulate cavitation. In addition, the *in vitro* system coupled with the computational model can be used

for future clinically relevant studies. The ability to determine pressure traces at the precise location of the planar endothelial cell monolayer could be used as an input into a mechanical model of membrane dynamics during blast wave propagation. This would permit new and highly refined estimates of the physical forces that brain endothelial cells may be exposed to, such as high frequency BBB oscillations that may disrupt cellular functions even without gross brain displacements.

An important novel aspect of this approach is that these estimates can be correlated to specific quantifiable measurements of cellular damage, dysfunction of the BBB as a system of interacting cells, and even aberrant subcellular protein trafficking where it is possible to investigate the mechanisms by which blast alters how critical BBB proteins, such as claudin-5 (Section B, Figure 5.2) are misdirected inside cells away from tight junctions.

The simulation code developed in this work is available at [54], along with the raw data and SPSS statistical analysis discussed below in Section B.4. The simulation code relies on Clawpack [44] and the results presented here were obtained with Version 5.2.2.

Chapter 11

HIGH-RESOLUTION SHOCK-CAPTURING INTERFACE METHODS EXTENSIONS

In the previous chapter, the collaboration to study traumatic brain injury (TBI) with the experimental group at the Seattle Veterans Administration (VA) Hospital brought to our attention the need for very specific numerical methods [55]. Many experiments performed by the TBI community, as well as in other biomedical disciplines, employ a shock-tube, where they introduce samples to be studied after being exposed to a shock wave. These samples can vary from transwells filled with aqueous solution and cell culture to live mice [45, 55, 96, 97, 103, 121, 122, 218]. Within the shock-tube, the shock wave travels through highly compressible gas before hitting the sample, typically a nearly incompressible material with a fixed location in space. The physical effects of the shock wave hitting the sample are not usually evident from experimental data nor easy to obtain through experimental techniques.

The methods developed in this chapter were motivated by this application. However, they are extended to more general cases, so they can be useful in other contexts as well. In order to successfully model the shock wave/sample interaction, we develop numerical methods that can couple the shock wave dynamics of compressible gas with almost incompressible materials, like plastic, water or even bone and brain. Some of these methods have already been discussed in Chapter 10 and in [55]. In this Chapter, we will give a detailed explanation of the numerical methods and their implementation; extend them to more complicated interface geometries, enhance their stability in highly refined grids, improve their resolution and efficiency using adaptive mesh refinement (AMR) [29], and further study their convergence. Although our simulations can only model idealized scenarios, they can help provide detailed insight into the behavior of the shock wave interaction with interfaces. For instance, in the previous two chapters and in [52, 55], we obtain the dynamics of a shock wave impacting an interface that models a specific TBI experiment. It also strongly suggested cavitation as a possible damage mechanism, an issue that has been a subject of extensive study among the TBI community [55, 96, 160, 175, 176, 182, 189, 202, 277].

Although there is an extensive body of work on computational fluid dynamics with interfaces that is relevant and might be applicable to this type of problems, such as [43, 75, 103, 161, 190, 221, 222, 252, 260] among others, the novel methods presented here are tailored to specifically, model a set of experiments performed with a shock tube.

The methods presented here are based on finite volume methods for hyperbolic problems

in their wave propagation form shown in Section 7.3 and in [155]. The methods were implemented into Clawpack 5.2.2 [44]. The key ingredient in these methods is the Riemann solver, which must be specifically designed to deal with highly nonlinear waves interacting with interfaces between materials having very different properties. The basic Riemann solvers were already explored in Section 8.2 and 8.3. In this Chapter, we will provide an extension of these methods to deal with interfaces in mapped grids and with AMR, as well as convergence studies to verify the method. The work presented in this chapter is based on the journal publication [53].

The numerical methods and implementation details are explained in this paper; the code is available on GitHub with a BSD license [51].

11.1 Two dimensional axisymmetric Euler equations with AMR

The three dimensional Euler equations with cylindrical symmetry can be solved as two dimensional axisymmetric Euler Equations with additional source terms, see Eqs. 10.1 and Figure 8.4. The conservation law for $q(x, y, t)$ takes the form $q_t + f(q)_x + g(q)_y = \psi(q, x, y, t)$, so the methodology to solve this equation is the one presented in Section 8.3.

The two-dimensional axisymmetric model of Eqs. 10.1 employing a Tammann equation of state with interfaces and transverse solvers were implemented in a traumatic brain injury application in [55]. This work showed how the geometry of the interface can be very relevant and even produce cavitation effects. The set up in [55] and in this work is essentially the one shown in Figure 8.4. A cylindrical plastic container filled with water is placed inside a shock tube. The cylindrical outer boundary corresponds to a cylindrical cross section of the shock tube. The results shown in Chapter 9 and in [52] show the plastic interface can be neglected in the two-dimensional model.

In this section, the model implemented in [55] is extended to work with AMR capabilities in Clawpack [44, 29]. The AMR implementation requires interpolating the value from coarser grid cells into the finer ones. However, when this interpolation is done across the interface, it will cause instabilities due to the big jump in the EOS parameters across the interface. In order to address this issue, we had to make sure that when a refinement patch intersects the interface, the interpolation for the finest grids is performed only using grid cells corresponding to the same material. For instance, if we need to refine a water grid cell, which is adjacent to the air interface, we will only use the values of adjacent cells corresponding to other water grid cells to obtain the interpolated values in the refined cells. It should be noted that the interface is always aligned to the cell edges, so there are no grid cells that contain two materials. This is also true for the mapped grid case studied below. Figure 11.1 shows the pressure contours for six different time points for a shock wave traveling in air and hitting a water interface fixed in space, as illustrated in Figure 8.4. The grid is plotted on top showing AMR in action with 4 levels of refinement. The first, second and third coarser grid

levels are shown explicitly. The level four refinement is plotted as patches that indicate the highest refinement. Additionally, the code allows us to add gauges to observe the pressure as a function of time at any given point.

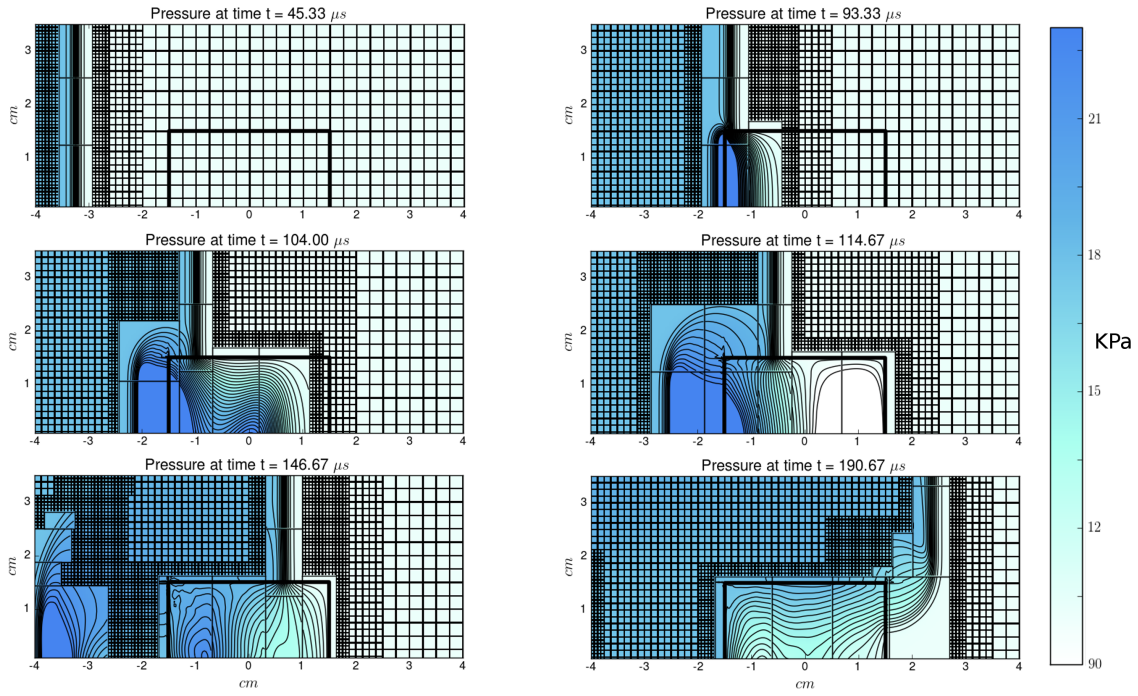

Figure 11.1: Axisymmetric simulation pressure contour plots at six different times points $t = 45.33, 93.33, 104, 114.67, 146.67$ and $190.67\ \mu s$, using four levels of AMR. The parameters employed to model water and air for the Tammann EOS are the ones in Table 9.1. The pressure amplitude is given along the color bar in KPa. The interface separating air and water is marked as a thick black line, and considering the axis of symmetry is the x axis, it models a cylindrical water interface immersed in air. The shock wave travels from the left to right. The first, second and third AMR grid refinement levels are plotted explicitly while the fourth level just shows the refinement patches for clarity. The pressure contours are only shown in the highest refinement level.

In addition to the implementation of these methods in [52, 55], we now show an extension of the algorithms for a mapped grid with adaptive mesh refinement (AMR).

11.1.1 Two-dimensional axisymmetric model in a mapped grid

These algorithms can also be used on a mapped grid where the quadrilateral grid cells are not necessarily rectangular. We will first consider how to implement the normal Riemann solver

in the mapped grid. This will require a mapping from a Cartesian grid to a quadrilateral grid, which will tell us the normal at each cell edge where we are solving the Riemann solver as well as the scaling of the edges and the scaling of the areas of the cells. The mapped normal Riemann solver can be done using the same solver as in the Cartesian case by following these steps:

- Define a mapping;
- Use the normal at each mapped cell edge to rotate the velocities from the computational domain into normal and transverse components in the physical domain;
- Solve the Riemann problem as usual with the rotated velocities and calculate the waves;
- Rotate the waves back into the computational domain;
- Use the cell edge and area scaling to modify the algorithm in Eq. 8.26, see [155].

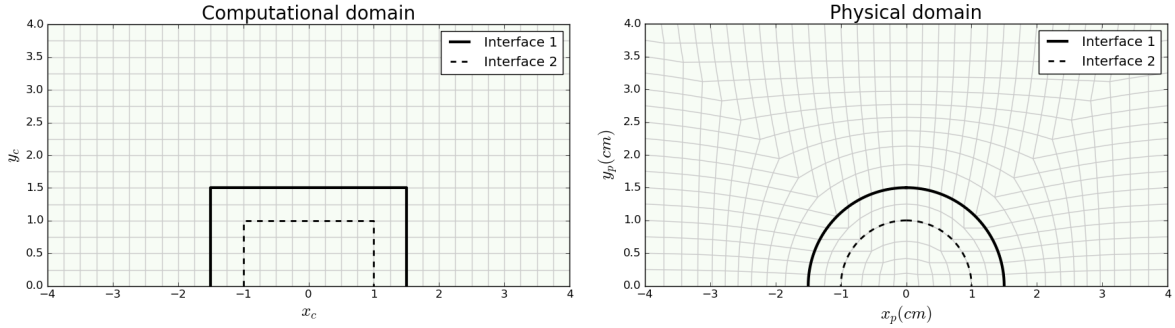

Figure 11.2: Computational and physical mapped grid of a circular shell inclusion based on the mapping in [34]. The mapping provides two possible circular interfaces, so considering the model is axisymmetric along the x axis, it can be used to model a spherical interface or a spherical thick shell interface. The locations of two possible interfaces are shown as thick continuous and dashed lines in both domains.

The mapping of Figure 11.2 is based on the mappings of [34]. Consider a computational point (x_c, y_c) on a rectangular grid such that $x_c > 0$ and $|y_c| < x_c \equiv d$. The vertical line segment from $(d, -d)$ to (d, d) will be mapped to a circular arc with radius $R(d)$ that intersect the identity diagonals at $(D(d), -D(d))$ and $(D(d), D(d))$. The center of such a circular arc is then given by $(x_0, y_0) = (D(d) - \sqrt{R(d)^2 - D(d)^2}, 0)$, and the point in the computational

grid is mapped to the physical grid point (x_p, y_p) by

$$y_p = y_c D(d)/d,$$
$$x_p = x_0 + \sqrt{R(d)^2 - y_p^2}.$$

In the mapping of Figure 11.2 we have indicated two interfaces: the inner one at radius r_i (1cm) and the outer one at radius r_o (1.5cm) from the origin. The size of the square domain in the computational grid where the mapping is applied is given by a third parameter r_m (4cm), with $r_m > r_o > r_i$. The square domain is centered at the origin and the length of each side is $2r_m$. In order to determine the mapping, we need to choose $R(d)$ and $D(d)$ in the three regions defined by the two interfaces. One option that works well, as shown in Figure 11.2, is given by

$$D(d) = \begin{cases} r_m \frac{d}{\sqrt{2}} \\ r_m \frac{d}{\sqrt{2}} \\ \frac{r_o}{\sqrt{2}} + \frac{\left(d - \frac{r_o}{r_m}\right)\left(r_m - \frac{r_o}{\sqrt{2}}\right)}{1 - \frac{r_o}{r_m}} \end{cases}, \quad R(d) = \begin{cases} r_i & d \le \frac{r_i}{r_m} \\ d r_m & \frac{r_i}{r_m} < d \le \frac{r_o}{r_m} \\ r_m \left[\frac{1 - \frac{r_o}{r_m}}{1-d}\right]^{\left(\frac{r_m}{r_o} + \frac{1}{2}\right)} & d > \frac{r_o}{r_m} \end{cases}.$$

Note this is only for the eastern sector of the computational grid, where $x_c > 0$ and $|y_c| < x_c$; the other sections are analogous [34].

Some of the quadrilateral cells in the physical domain are nearly triangular, with two adjacent edges nearly colinear. In spite of this, the wave-propagation algorithm with transverse solvers described below works quite robustly in general as discussed further in [34]. However, when there is also a large jump in material parameters at the interface and the grids are adaptively refined there can be some stability issues as discussed further below.

Once the mapping is defined, we proceed by rotating the normal and transverse momentum components q^2 and q^3 of the Euler equations in the computational grid by using the normal at the current edge of the mapped grid, $\hat{n} = (n_x, n_y)$,

$$\begin{bmatrix} q^2_{ph} \\ q^3_{ph} \end{bmatrix} = \begin{bmatrix} n_x & n_y \\ -n_y & n_x \end{bmatrix} \begin{bmatrix} q^2 \\ q^3 \end{bmatrix},$$

where q^2_{ph} and q^3_{ph} now point in the normal and transverse direction in the physical domain (mapped grid). Using these quantities, we solve the normal Riemann solver as usual to obtain the speeds and waves s^p_{ph} and $\mathcal{W}^p_{ph}$, and we rotate the waves back to the computational domain,

$$\begin{bmatrix} \mathcal{W}^2 \\ \mathcal{W}^3 \end{bmatrix} = \begin{bmatrix} n_x & -n_y \\ n_y & n_x \end{bmatrix} \begin{bmatrix} \mathcal{W}^2_{ph} \\ \mathcal{W}^3_{ph} \end{bmatrix}.$$

Finally, we scale the speeds s^p_{ph} by the edge scaling to obtain s^p and employ the capacity function (cell area scaling) into a modified version of the algorithm in Eq. 8.26 found on [155].

The transverse solvers will also be applied on the mapped grid, but this requires more careful consideration because of our treatment of interfaces with huge jumps in the Tammann EOS parameters. This will be explained in detail in the next subsection. In this work, we implemented the 2D axisymmetric model into the mapped grid of Figure 11.2. Although the mapping is two-dimensional and shows half circular inclusions interfaces, the axisymmetry along the x axis convert these interfaces into spherical shells. This mapped grid was selected because it could be used to model a skull in computational TBI experiments. Note the mapping allows an inner interface that could even be used to model the thickness of a skull. The code is set up so arbitrary mappings with other interface geometries can be implemented.

In Figure 11.3, we show a sample simulation of the pressure contours for the mapped grid at six different points in time. It only employs one interface along the outer circular inclusion shown in the grid of Figure 11.2. Once again the outer part of the circular inclusion is modeled as air and the inner material as water using the same set of parameters as Figure 11.1. This figure also shows AMR in action with 4 levels of refinement, and it is also possible to add gauges to observe the pressure as a function of time at any given point in the grid. AMR does not need many additional considerations in terms of the mapped grid since it works on the computational domain, which is still Cartesian. However, it is worth mentioning that the region around the interface is refined to the highest level from the beginning of the simulation. This is to avoid instabilities caused by employing AMR along an interface with huge jumps in the parameters while using a mapped grid with almost triangular grid cells (see Figure 11.2). If any of the conditions is relaxed, i.e. we use a smaller jump in the parameters or use a less severe mapped grid as in Figure 11.1, this initial refinement along the interface is no longer required to avoid instabilities.

11.1.2 Transverse Riemann solvers in a mapped grid

A transverse solver for a Cartesian grid was implemented in [55]. In this section, we show the extension of this transverse Riemann solver for a mapped grid. This solver takes the results of a normal Riemann solver and splits it into components moving in the transverse direction. As mentioned in [55], a special transverse solver needs to be developed due to instabilities at the interface. This is based on the solver for acoustics in a heterogeneous media that is described in Section 21.5 of [155].

We recall the basic idea of a transverse solver for a constant coefficient linear hyperbolic system of equations $q_t + Aq_x + Bq_y = 0$, the jump in normal flux between adjacent cells, $\mathcal{A}\Delta Q_{i-1/2} = \mathcal{A}(Q_{i,j} - Q_{i-1,j})$, is split via the normal Riemann solver into left-going and right-going "fluctuations" $\mathcal{A}^-\Delta Q_{i-1/2}$ and $\mathcal{A}^+\Delta Q_{i-1/2}$. Each fluctuation $\mathcal{A}^+\Delta Q_{i-1/2}$, is then further split into down-going and up-going components $\mathcal{B}^-\mathcal{A}^+\Delta Q_{i-1/2}$ and $\mathcal{B}^+\mathcal{A}^+\Delta Q_{i-1/2}$,

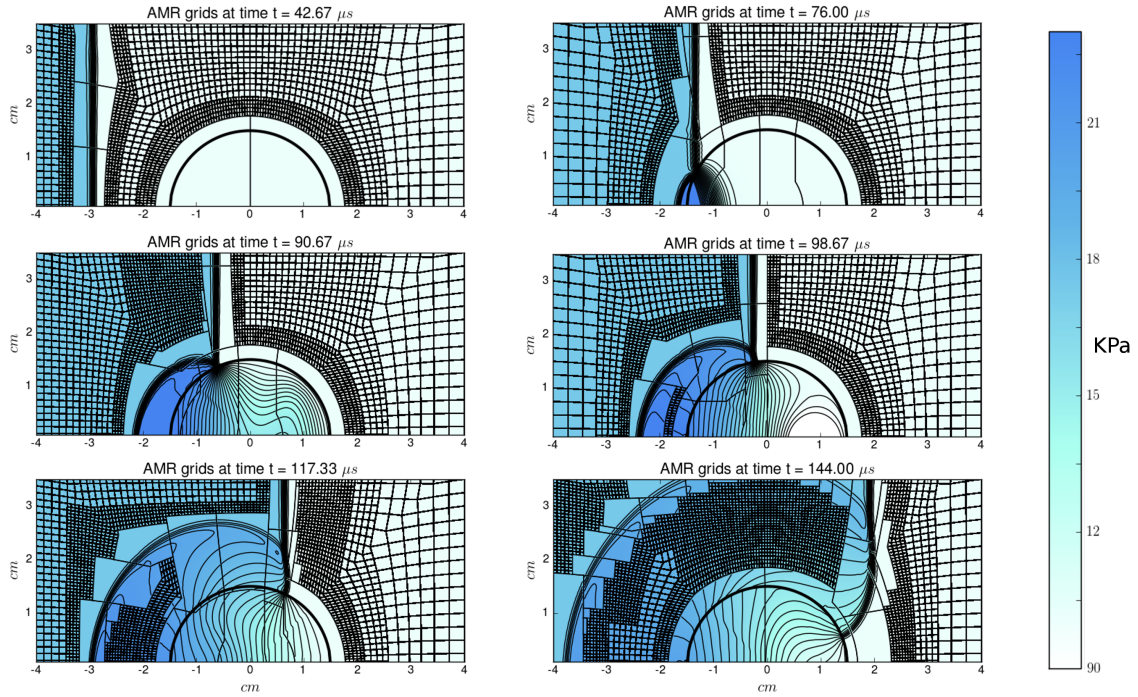

Figure 11.3: Pressure contour plots of axisymmetric simulation on a mapped grid with a circular inclusion at six different times points $t = 42.67$, 76, 90.67, 98.67, 117.33 and 144 μs, using four levels of AMR. The plot is analogous to that of Figure 11.1; however, in this figure the interface separating air and water is circular, which models a spherical water interface. Also note, the region around the interface is refined from the beginning to avoid instabilities when using AMR around corners in the mapped grid.

based on the matrices B^+ and B^-.

In the case of variable coefficients or nonlinear problems, the general notation $\mathcal{B}^-\mathcal{A}^+\Delta Q_{i-1/2}$ and $\mathcal{B}^+\mathcal{A}^+\Delta Q_{i-1/2}$ is used for these two vectors. For variable coefficient acoustics, as described in [155], the up-going fluctuation from the transverse splitting is based on eigenvectors of B_{ij} and $B_{i,j+1}$, while the down-going fluctuation is based on eigenvectors of B_{ij} and $B_{i,j-1}$.

At the interface with an almost incompressible liquid, it is difficult to figure out an accurate and stable implementation of the transverse Riemann problem. This is because Euler equations, with a big jump in the parameters at the interface, are extremely sensitive to instabilities. Our first approach was to expand the normal wave as a function of linearized eigenvectors corresponding to the transverse grid cells [155] of the Euler equations. However, this approach resulted in instabilities at the interface. In order to work around this issue, we will follow the same approach as [55] and derive an approximate transverse Riemann solver based on acoustic equations, which capture the acoustic waves while avoiding instabilities.

In this interface, we will mostly be concerned with the two acoustic waves. In order to derive it, let $\hat{n} = (n_x, n_y)$ be the transverse unitary normal vector and linearize the acoustic equations around ρ_0, u_0 and v_0, with u_0 and v_0 the velocity in the x and y direction respectively [155]. In terms of the density and momentum,

$$\begin{bmatrix} \rho \\ \rho u \\ \rho v \end{bmatrix}_t + \underbrace{\begin{bmatrix} 0 & n_x & n_y \\ n_x c^2 & 0 & 0 \\ n_y c^2 & 0 & 0 \end{bmatrix}}_{\tilde{B}(Q)} \begin{bmatrix} \rho \\ \rho u \\ \rho v \end{bmatrix}_{\hat{n}} = 0, \tag{11.1}$$

where the derivative is taken in the normal direction $\hat{n}$, c is the sound speed and $\tilde{B}(Q)$ can be understood as a lower dimensional approximation of the transverse Jacobian $g'(Q_0)$ for the Euler equations. Note we assumed $u_0 = 0$, which is equivalent to move into a Lagrangian frame of reference.

As we might have different materials and sound speeds in the cell above or below, we calculate the eigenvectors and evaluate them according to their location. The matrix of eigenvectors is

$$R = \begin{bmatrix} 1 & 1 & 0 \\ n_x c_U & -n_x c_D & -n_y \\ n_y c_U & -n_y c_D & n_x \end{bmatrix},$$

where the sound speeds c_U and $-c_D$ are the eigenvalues corresponding to the first two column eigenvectors, v_u and v_d. The eigenvalue for the third one v_0 is 0. The subindex u and d refer to cells $(i, j+1)$ and (i, j) when computing $\mathcal{B}^+\mathcal{A}^+\Delta Q_{i-1/2,j}$ and to cells (i, j) and $(i, j-1)$ when computing $\mathcal{B}^-\mathcal{A}^+\Delta Q_{i-1/2,j}$.

The up-going and down-going fluctuations for $\mathcal{A}^+\Delta Q_{i-1/2,j}$ are obtained by expanding the fluctuation in terms of these eigenvectors or waves, $\mathcal{A}^+\Delta Q_{i-1/2,j} = \alpha_U v_U + \alpha_D v_D + \alpha_0 v_0$, so we need to solve $R\alpha = \mathcal{A}^+\Delta Q_{i-1/2,j}$, which yields

$$\begin{aligned} \alpha_U &= \frac{1}{c_U + c_D}\left(c_D \mathcal{A}_1^+ + n_x \mathcal{A}_2^+ + n_y \mathcal{A}_3^+\right), \\ \alpha_D &= \frac{1}{c_U + c_D}\left(c_U \mathcal{A}_1^+ - n_x \mathcal{A}_2^+ - n_y \mathcal{A}_3^+\right), \end{aligned}$$

and α_0 is not relevant since it corresponds to the zero eigenvalue. Note that the required fluctuation $\mathcal{A}^+\Delta Q_{i-1/2,j}$ for the Euler equations is a four-dimensional vector with fluctuations in density, normal momentum, transverse momentum, and energy. As we are only interested

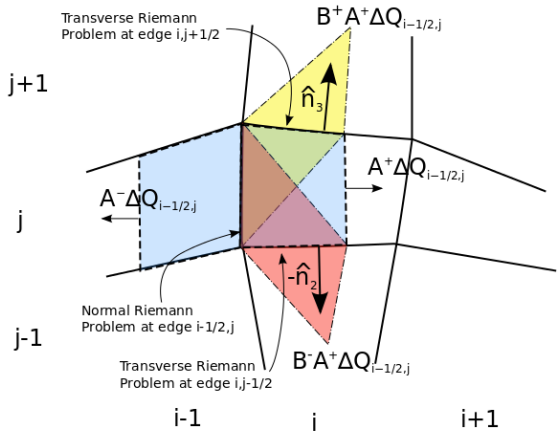

Figure 11.4: Transverse solvers diagram in physical grid cells after applying the mapping. The left-going and right going fluctuations of the normal Riemann problem at the edge between grid cells $(i-1,j)$ and (i,j) is shown. The right-going fluctuation $\mathcal{A}^+\Delta Q_{i-1/2,j}$ is decomposed into the up-going fluctuation $\mathcal{B}^+\mathcal{A}^+\Delta Q_{i-1/2,j}$ and the down-going fluctuation $\mathcal{B}^-\mathcal{A}^+\Delta Q_{i-1/2,j}$ by employing transverse Riemann solvers in the computational grid. This is an extension of the transverse solvers implemented in [55] into mapped grids.

in the acoustic waves, we will assume the fluctuations in energy are negligible, so we define the acoustic part of the fluctuation as the first second and third entry of the 4 dimensional vector, i.e. $\mathcal{A}^+_{ac}\Delta Q_{i-1/2,j} = [\mathcal{A}^+_1, \mathcal{A}^+_2, \mathcal{A}^+_3]$.

The up-going and down-going acoustic fluctuations are given by the velocity times the waves,

$$\mathcal{B}^+_{ac}\mathcal{A}^+\Delta Q_{i-1/2,j} = c_U \alpha_U v_U,$$
$$\mathcal{B}^-_{ac}\mathcal{A}^+\Delta Q_{i-1/2,j} = -c_D \alpha_D v_D.$$

We will need to solve two of these transverse solvers for the Euler equations as shown in the grid in Figure 11.4. We will only consider the up-going fluctuation of the transverse solver at $(i, j+1/2)$ and the down-going fluctuation of the solver at $i, j-1/2$. This yields the full

fluctuations as

$$\mathcal{B}^{+}\mathcal{A}^{+}\Delta Q_{i-1/2,j} = \frac{c_3\left(c_2\mathcal{A}_1^{+} + n_{3x}\mathcal{A}_2^{+} + n_{3y}\mathcal{A}_3^{+}\right)}{c_3 + c_2}\begin{bmatrix} 1 \\ n_{3x}c_3 \\ n_{3y}c_3 \\ 0 \end{bmatrix},$$

$$\mathcal{B}^{-}\mathcal{A}^{+}\Delta Q_{i-1/2,j} = \frac{-c_1\left(c_2\mathcal{A}_1^{+} - n_{2x}\mathcal{A}_2^{+} - n_{2y}\mathcal{A}_3^{+}\right)}{c_1 + c_2}\begin{bmatrix} 1 \\ -n_{2x}c_1 \\ -n_{2y}c_1 \\ 0 \end{bmatrix},$$

where c_1, c_2 and c_3 are the speeds of sound in cells $(i, j-1)$, (i, j) and $(i, j+1)$ respectively, the normals $\hat{n}_3$ and $\hat{n}_2$ are the normals to the upper edge and the lower edge, as shown in Figure 11.4, and the non-acoustic fluctuations were neglected. The sound speeds are calculated with the pressure, density and the parameters of the Tammann EOS in the respective cell with $c = \sqrt{\gamma\frac{p+p_\infty}{\rho}}$. This is repeated analogously for the left going fluctuation $\mathcal{A}^{-}\Delta Q_{i-1/2,j}$ of the normal Riemann problem. These transverse Riemann solvers were also implemented in the simulations shown in Figure 11.3.

11.2 Transmission-based limiters

When the mesh is refined heavily by AMR, high-frequency unphysical oscillations appear in the water. Their wavelength scales with the mesh resolution, and they are hard to observe in the coarser grids due to numerical diffusion. These oscillations originate in the corner of the interface and they do not dissipate. This is caused by small errors produced by the Riemann solvers at the interface; these errors propagate in the normal and transverse direction. In the corner grid cell, these errors occur once when sweeping the solver on the grid horizontally and once again when sweeping vertically, producing oscillations. A sample of this phenomena can be observed in Figure 11.5, where we show the convergence study for a pressure gauge at (-1cm,0) and a schlieren plot of the pressure that shows the oscillations being produced at the corner of the interface. The convergence will be further studied in Section 11.4.

This issue can be improved by adjusting how the waves at the interface are limited. The limited waves from Eq. 8.27 are given by

$$\widetilde{\mathcal{W}}^{p}_{i\pm1/2} = \phi(\theta)^{p}_{i\pm1/2}\mathcal{W}^{p}_{i\pm1/2},$$

where $\phi(\theta)$ is the flux-limiter function [155] and θ is a measurement of the smoothness of the function. There are several ways to choose the θ parameter to limit the waves coming out of the edges at $i - 1/2$. For a linear problem with two waves, where the 1-waves propagate to the left and the 2-waves to the right (like acoustics), we can measure the smoothness θ

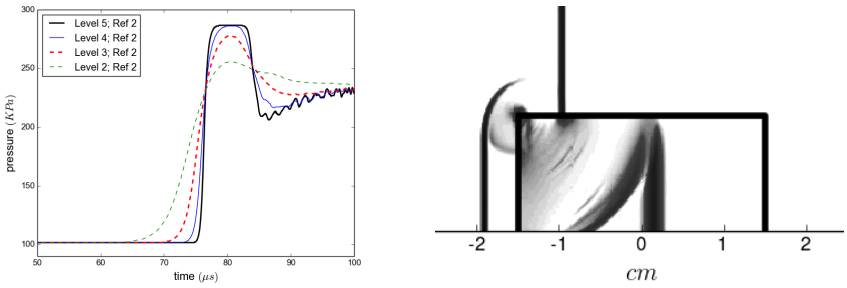

Figure 11.5: In the first plot, we show a convergence study at a gauge at (-1cm,0). The curves shown are for four different AMR levels of refinement up to level 5, where each level doubles the resolution of the previous one. Oscillations are clearly seen in level 5 refinement. The second plot shows a schlieren plot for the pressure where one can appreciate the oscillations produced at the corner of the interface.

by comparing the magnitude of adjacent waves. The corresponding θ parameters can be obtained as $\theta^1_{i-1/2} = \|\mathcal{W}^1_{i+1/2}\|/\|\mathcal{W}^1_{i-1/2}\|$ and $\theta^2_{i-1/2} = \|\mathcal{W}^2_{i-3/2}\|/\|\mathcal{W}^2_{i-1/2}\|$, see [155]. In the case of nonlinear equations, the approach is similar; however, the eigenvectors of adjacent waves are no longer co-linear in phase space across adjacent cells, so we need to do a projection into the corresponding eigenvectors. For the nonlinear case, the θ parameter is given by $\theta^1_{i-1/2} = (\mathcal{W}^1_{i+1/2} \cdot \mathcal{W}^1_{i-1/2})/(\mathcal{W}^1_{i-1/2} \cdot \mathcal{W}^1_{i-1/2})$ and $\theta^2_{i-1/2} = (\mathcal{W}^2_{i-3/2} \cdot \mathcal{W}^2_{i-1/2})/(\mathcal{W}^2_{i-1/2} \cdot \mathcal{W}^2_{i-1/2})$, see [155]. The diagrams in Figure 11.6 give some visual intuition into which waves we are comparing. This is the standard implementation in Clawpack [44].

In the case where there is a big jump in the parameters across an interface, the eigenvectors of a wave on different sides of the interface are significantly different. In this case, it is more appropriate to separate one of the adjacent waves into its transmitted and reflected component, as if it actually had crossed the interface, and use the transmitted wave to limit the other adjacent wave. For instance assume the interface is at the edge $i-1/2$ shown in Figure 11.6, the original limiter compares the projection of $W^1_{i+1/2}$ (into the corresponding eigenvector at $i-1$) with $W^1_{i-1/2}$ to limit $W^1_{i-1/2}$. However, if the interface has a big jump in the parameters, it is better to separate $W^1_{i+1/2}$ into its reflected and transmitted components and compare the transmitted component of the wave $T^1_{i-1/2}$ with $W^1_{i-1/2}$ to limit $W^1_{i-1/2}$. These type of limiters are called transmission based limiters, originally developed in [86] for acoustics equations in heteregeneous media. In this case, the θ parameters are given by

$$\theta^1_{i-1/2} = \frac{\|\mathcal{T}^1_{i-1/2}\|}{\|\mathcal{W}^1_{i-1/2}\|} \quad \theta^2_{i-1/2} = \frac{\|\mathcal{T}^2_{i-1/2}\|}{\|\mathcal{W}^2_{i-1/2}\|}, \tag{11.2}$$

where the transmitted waves $\mathcal{T}^{(1,2)}_{i-1/2}$ are as shown in Figure 11.6 correspondingly. This requires

calculating the transmitted waves, which might follow different procedures depending on the equations we are using.

In this section, we extend the methods in [86] for acoustic equations to limit the acoustic waves in Euler equations. In order to do so, lets recall that we can rewrite the one-dimensional acoustic equations in terms of the density and the momentum [55, 155],

$$\begin{bmatrix} \rho \\ \rho u \end{bmatrix}_t + \begin{bmatrix} 0 & 1 \\ c^2 & 0 \end{bmatrix} \begin{bmatrix} \rho \\ \rho u \end{bmatrix}_x = 0, \tag{11.3}$$

where c is the sound speed, the eigenvalues of the system at a cell interface are the left and right sound speeds, $\lambda_{1,2} = -c_{i-1}, c_i$, and the corresponding eigenvectors $r^1_{i-1} = [1, -c_{i-1}]$ and $r^2_i = [1, c_i]$. As we assume different materials accross the interface $c_{i-1} \neq c_i$. Following the first diagram of Figure 11.6 and Eqs. 11.2, in order to calculate $\theta^1_{i-1/2}$, we need to know $\mathcal{T}^1_{i-1/2}$, which is the transmitted wave from wave $\mathcal{W}^1_{i+1/2}$ coming from cell i to cell $i-1$. In order to do so, we first write the wave $\mathcal{W}^1_{i+1/2}$ in terms of the corresponding eigenvector $\mathcal{W}^1_{i+1/2} = \alpha^1_{i+1/2} r^1_i$, which we already know from solving the Riemann problem, see [155]. Then we decompose it into the eigenvectors of the corresponding two cells to obtain the transmitted and reflected contributions,

$$\alpha^1_{i+1/2} \begin{bmatrix} 1 \\ -c_i \end{bmatrix} = \beta^1_{i+1/2} \begin{bmatrix} 1 \\ -c_{i-1} \end{bmatrix} + \beta^2_{i+1/2} \begin{bmatrix} 1 \\ c_i \end{bmatrix}.$$

This yields two equations with two unknowns, so we can solve for the $\beta^1_{i+1/2}$,

$$\beta^1_{i+1/2} = \alpha^1_{i+1/2} \frac{2c_i}{c_{i-1} + c_i}.$$

This quantity multiplied by the eigenvector r^1_{i-1} corresponds to the transmitted wave. With this information, and using that $\mathcal{W}^1_{i-1/2} = \alpha^1_{i-1/2} r^1_{i-1}$, we can now calculate the θ parameter,

$$\theta^1_{i-1/2} = \frac{\|\mathcal{T}^1_{i-1/2}\|}{\|\mathcal{W}^1_{i-1/2}\|} = \frac{\alpha^1_{i+1/2}}{\alpha^1_{i-1/2}} \left(\frac{2c_i}{c_{i-1} + c_i} \right),$$
$$\theta^2_{i-1/2} = \frac{\|\mathcal{T}^2_{i-1/2}\|}{\|\mathcal{W}^2_{i-1/2}\|} = \frac{\alpha^2_{i-3/2}}{\alpha^2_{i-1/2}} \left(\frac{2c_{i-1}}{c_i + c_{i-1}} \right),$$

where $\theta^2_{i-1/2}$ is calculated in the same manner by following the second diagram from Figure 11.6. The sound speeds can be obtained from the Tammann EOS by using Eq. 8.4 and Eq. 8.24. Also note the limiters work on the waves in the computational domain, so it is not necessary to do any additional adjustments when using a mapped grid.

These limiters greatly improve the observed oscillations as shown in the first plot of Figure

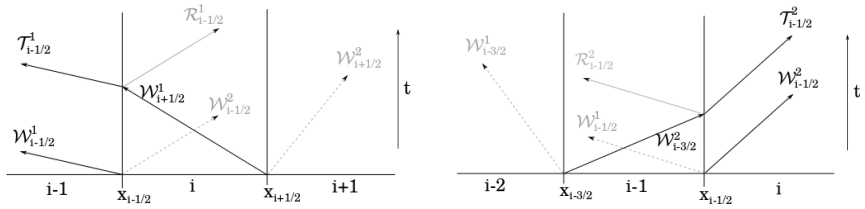

Figure 11.6: Two diagrams are shown to illustrate the waves being compared in the different kind of limiters at the edge $i-1/2$, between grid cells $i-1$ and i. The first diagram shows the waves that are involved in determining $\theta^1_{i-1/2}$ for the limiting behavior of $\mathcal{W}^1_{i-1/2}$. The second one shows the waves involved in determining $\theta^2_{i-1/2}$ for the limiting behavior of $\mathcal{W}^2_{i-1/2}$. The notation is $\mathcal{T}$ for transmitted waves and $\mathcal{R}$ for reflected ones.

11.7 where the level 5 refinement no longer shows significant oscillations. Note these limiters are approximate since we are using the acoustic equations rewritten in terms of density and momentum to limit the Euler equations, and they don't fully suppress the oscillations in higher refinement levels as we will see in the next Section.

11.3 Convergence and modified minmod limiter

A verification study for the one-dimensional case was performed in a previous work [55]. In that work, we verified that the finite volume methods coupled with the hybrid Riemann HLLC-exact Riemann solver for the Euler equations with a Tammann EOS converge to the correct solution for a simple model problem. However, the exact analytic solutions of Riemann problems for Euler equations are only available in one dimension, so we restricted our verification to a one-dimensional test. Nonetheless, as the Riemann problem is still the key ingredient of higher-dimensional numerical methods, the analysis from [55] is still relevant for the two-dimensional extension of the algorithm.

In addition to the verification study presented in [55], in this work we will provide a convergence test for the two-dimensional axisymmetric model. As there are no exact solutions for the two-dimensional equations, the convergence test only shows the numerical algorithm converges to a solution as the mesh is refined. The convergence tests were performed using several gauges for the Cartesian grid simulations of Figure 11.1. In the first plot in Figure 11.7, we show the convergence test for the gauge at (-1cm,0). Note the appearance of high-frequency oscillations in the most refined level (level 6) even after applying the transmission-based limiters. The plot at the bottom-left of Figure 11.7 shows these oscillations for the finest grid in a schlieren pressure plot. The origin of this oscillations is the same as before.

These oscillations can be suppressed by adding some numerical viscosity to the water material. This is not entirely unphysical since the water is a viscous media. In order to

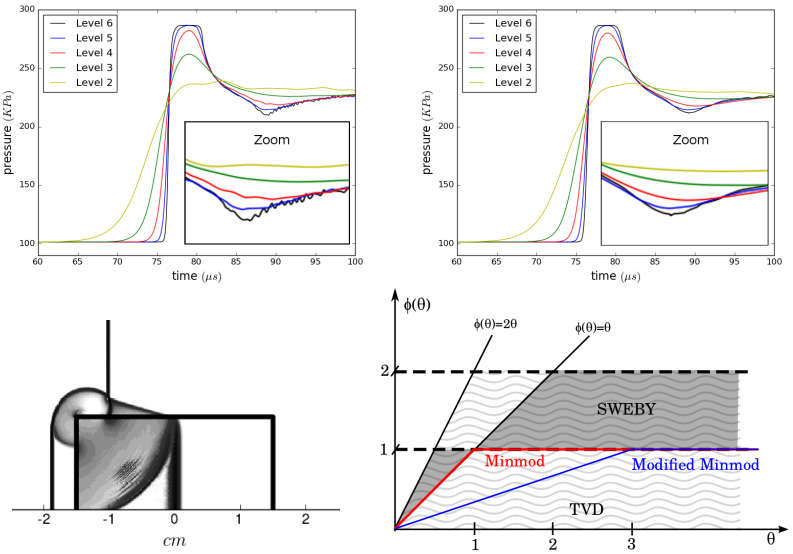

Figure 11.7: The first two plots show the convergence tests at a gauge in (-1cm,0) for the two dimensional axisymmetric model with AMR on a Cartesian grid. The curves are shown for different levels of refinement allowed in AMR, where each level doubles the resolution of the previous one. In the first plot one can appreciate numerical high frequency oscillations in the finer grids; however, this are almost fully supressed in the second figure by using a more diffusive limiter, the modified minmod limiter. The third plot shows a schlieren plot of the pressure with level 6 refinement when using the original minmod limiter. It shows high-frequency oscillations propagating from the corner that do not dissipate. The fourth plot shows the TVD region (wavy lines) and the Sweby region (shaded) [155] as well as the corresponding minmod and modified minmod limiter.

do so, we implement a new limiter for the water grid cells, which we refer to as modified minmod. The original minmod limiter uses the flux-limiter function $\phi(\theta) = \text{minmod}(1, \theta)$ [155]. The minmod limiter is the most dissipative second-order total variation diminishing (TVD) limiter. This is shown in the flux-limiter function plot at the bottom-right of Figure 11.7. The region covered in wavy lines is the region where the limiter can be TVD, and the shaded region shows the Sweby region where limiter can be second-order accurate; the corresponding flux-limiter function for the minmod limiter is shown too. In order to add more numerical viscosity, we use a modified minmod limiter $\phi(\theta) = \text{minmod}(1, \theta/3)$. Although we lose second order accuracy for the Euler Equations, this limiter still provides physical solutions due to water viscosity. The scaling factor within the flux-limiter function (1/3) was chosen to be as close to 1 as possible to keep as much overlap with the Sweby region as possible while also supressing the oscillations; this parameter can be easily adjusted in the

code, which is available in [51]. The resulting convergence study after applying the modified minmod limiter can be appreciated in the second plot of Figure 11.7, where we can observe the oscillations were suppressed and that our method converges. Analogous results were obtained for the other gauges.

11.4 Discussion of methods

We developed a two-dimensional axisymmetric shock-capturing high-resolution numerical model to study shock wave dynamics when crossing a fixed interface between a compressible fluid (air) and an almost incompressible material (water). These methods have been designed to complement TBI and other biomedical experiments performed in a shock tube. The common setup in these experiments consists of a shock wave traveling through air and impacting a plastic container. The container is usually very thin, and it is often filled with an aqueous solution where the biological sample is placed. In our computational simulations, the container is modeled as an interface fixed in space. The aim of these methods and simulations is to provide experimentalists measurements of relevant variables inside the container, like pressure, that would otherwise be very difficult to obtain experimentally. This can help us understand better the on-going physical dynamics that experimental samples in specifc experiments undergo and explain possible damage mechanisms. It should be noted the methods developed here can be extended to other scenarios.

We first provided the one-dimensional methods employed in detail and their implementation into Clawpack [44]. In Chapter 9, we showed that there is not a significant difference between the transmitted shock wave when removing the thin plastic interface separating air and water. Furthermore, we observed an amplification and elongation of the shock wave. This effect is accounted for by the different material compressibility. The amplitude of the initial pressure wave in the air increased in 54% when measured in the water. This amplification effect was highly relevant in the injury mechanisms studied in Chapter 10, and it generally occurs when passing from air to water or a solid material.

The methods were extended to two dimensions and implemented on a mapped grid, which allows more complicated interface geometries as long as the mapping is provided. We provided as a proof of concept a circular inclusion mapping, which maps the rectangular interface into a circular one. In the axisymmetric case, this mapping models a spherical interface. In addition, the algorithms were adapted to work with AMR to increase resolution and efficiency of the code. Additional mathematical work has to be performed to improve the accuracy and stability of the numerical method. Transverse Riemann solvers for the mapped grid were developed to improve the accuracy. Transmission-based limiters and the minmod modified limiter were implemented at the interface and in the water to suppress numerical oscillations at heavily refined AMR patches. A more primitive version of these methods was already employed in a specific mild TBI applicationin the previous chapter,

and we expect they can be extended and used in new applications. The three-dimensional model with a spherical shell inclusion could be specifically useful in TBI applications to model an idealized skull of a mouse inside the shock tube or a human head exposed to a shock, a problem of much interest to the TBI community as shown by some previous studies [10, 114, 139, 176, 217, 228, 232, 238, 239, 241, 259, 276] among others. The code where all these methods are implemented is available with a BSD license [51].

Chapter 12

SUMMARY AND FUTURE WORK

12.1 Summary

The introduction chapter of this thesis showed the relevance of conservative dynamics in two areas within applied mathematics: stochastic processes and numerical methods for hyperbolic conservation laws. Although the dynamics of these two problems are quite different, both require enforcing conservation to obtain accurate models and stable numerical algorithms. In the case of stochastic processes, the conservation of probability has to be enforced, with special care at reaction boundaries and at boundaries in contact with material/chemical potential baths. In the case of numerical methods for hyperbolic problems, the conservation of specific physical quantities, like mass, momentum, and/or energy has to be enforced in each grid cell, with specific emphasis on interfaces between compressible and almost incompressible media. Chapter 1 also provided a basic introduction to the two main parts of this thesis related to these two areas.

The first part of this thesis is related to the area of stochastic processes. In specific, it dealt with stochastic biochemical reaction-diffusion systems. Chapters 2 and 3 gave an overview of some of the most relevant theory and results in spatially homogeneous biochemical reaction systems and in biochemical reaction-diffusion systems, respectively. These chapters provided the theory and tools that are currently being used to model, understand and simulate biochemical processes at cellular and sub-cellular scales.

Chapter 4 is based on our journal publication [56]. In this chapter, we presented theoretical and numerical kinetic Monte Carlo studies of the robustness of FCS theory in the non-linear limit of bimolecular reactions with a small number of molecules. FCS is a well-established and widely used experimental method to determine chemical rate constants, diffusion coefficients and other properties of stochastic reaction-diffusion systems. The experimental method is particularly attractive since it allows minimal invasive studies of live biological specimens with high spatial and temporal resolution. The theoretical framework for interpreting experimental data was developed in 1970s based on a linear kinetic theory, which is expected to be accurate if the stochastic fluctuations are in the linear regime. We found, however, that current FCS theory can produce significant errors at mesoscopic scales, which is highly relevant in experimental studies of cellular and sub-cellular processes.

Chapter 5 is attributed to the journal publication [57]. This chapter dealt with some essential issues with diffusion-influenced reaction theory. Most of the current algorithms to simulate biochemical reaction-diffusion systems use some formulation of diffusion-influenced

reaction theory as its fundamental building block. Although it has been studied extensively, diffusion-influenced reactions for reversible bimolecular reactions are not easy to fully understand from a stochastic perspective. In this chapter, this deficiency was addressed by developing a discrete time and state stochastic process based on over-damped Langevin dynamics for bimolecular diffusion-controlled reversible reactions. The model yields the probability distribution dynamics and simple Markovian algorithms to compute particle-based simulations, ensuring consistency between the two as well as conservation of probability. In the continuous limit, it recovers the original diffusion-influenced model. It also unifies previous particle-based approaches with the analytic theory for reversible diffusion-controlled reactions. These results allowed us to fully understand reversible diffusion-influenced reactions as stochastic processes.

Chapter 6 is currently a work in progress being prepared for publication [58]. This chapter uses the discrete model from Chapter 5 to introduce probabilistic interpretations of Smoluchowski's original concentration-based diffusion-influenced reaction model within the context of non-equilibrium thermodynamics. Most cell-scale biological systems are open reaction-diffusion systems at mesoscopic scales, so they can only be truly understood in the light of non-equilibrium statistical mechanics. This work shows that Smoluchowski's diffusion-influenced reaction theory is nothing more than a mean-field approximation of a non-equilibrium statistical mechanical system in a canonical or a grand-canonical ensemble (depending on the boundary condition), which is fully defined as a stochastic process. Additionally, this chapter suggests a new model based on coupled-diffusion that allows a much more robust and general framework to deal with diffusion-influenced reactions, and more generally, with reaction-diffusion processes.

The second part of this thesis is related to numerical methods for hyperbolic problems, in particular high resolution shock-capturing methods for interface problems. Chapter 7 provided an overview of high resolution shock-capturing finite volume methods for hyperbolic conservation laws. Chapter 8 showed how to apply these methods to deal with interfaces in acoustic equations, Euler equations and elasticity equations. It also provided detailed implementations on mapped grids and higher-dimensional problems. It should be noted some of the results in this chapter are from original publications, but they fitted better in this introductory chapter. These two chapters provided the theoretical and computational framework to develop and implement numerical methods for interface problems in the applications studied in Chapters 9, 10 and 11.

Chapter 9 is a part of the published conference proceedings [52]. The study in this chapter was motivated by experimental studies in traumatic brain injury (TBI) to further develop the TBI application from Chapter 10. It was done with our collaborators at the Seattle Veterans Administration (VA) Hospital, who have been doing experiments to understand how blast waves can produce mild TBI (mTBI). In this chapter, we described how recent research has demonstrated that low-intensity non-impact blast wave exposure frequently

leads to mTBI. We also emphasized that the mechanisms connecting the blast waves and the mTBI remain unclear. In the core of this chapter, we developed conservative finite volume methods for interface-shock wave interaction to simulate the TBI experiments performed by our collaborators. This helped us gain insight that was hard to obtain by experimental means. We showed the implementation of a one-dimensional model of their experimental setup using Euler equations for compressible fluids, which are coupled with a Tammann equation of state (EOS) to model compressible gas along with almost incompressible fluids or elastic solids. A hybrid HLLC-exact Eulerian-Lagrangian Riemann solver for Tammann EOS with a jump in the parameters was developed to numerically solve these equations. The model showed that if the plastic interface is very thin, it can be neglected. This result is fundamental to explore further the TBI application in Chapter 10.

Chapter 10 was based on the journal publication [55]. It is the core of the collaboration with the experimental group at the Seattle VA Hospital, who study the underlying biological mechanisms behind blast-induced mild traumatic brain injury (mTBI). One of the main proposed hypotheses is the blood-brain barrier (BBB) disruption. The BBB is a highly selective permeability barrier formed around brain blood vessels that prevents passage of toxins from the blood into the brain. Using the results from Chapter 9, we developed a computational model of an in-vitro experiment of blast-induced BBB disruption performed by the experimentalists at the VA Hospital. We modeled the propagation of shock waves through interfaces between air plastic and water using the Euler equations with a Tammann EOS. The equations were solved numerically using high-resolution shock-capturing methods and novel Riemann solvers to accurately model the shock-interface interaction. The three-dimensional results indicate pressures can fall below the vapor pressure due to the interaction of reflecting and diffracting shock waves, suggesting that cavitation bubble collapse could be a possible BBB damage mechanism.

The work from Chapter 11 has been submitted to a journal for publication [53]. The work in this chapter mainly extended the numerical methods developed in Chapters 9 and 10 to more general cases and usability. We showed how to extend the methods to be able to employ mapped grids and adaptive mesh refinement (AMR), which required modifying the numerical methods along the interface. We showed these modifications involved the development of new Riemann solvers, limiters and interpolation algorithms for AMR. The main objective of the work presented in this chapter is to provide a detailed account of a generalized and more applicable version of the numerical algorithms as well as free software with a BSD license, see the repository at github.com/maojrs/Interface_Euler_AMR. The code from Chapter 10 is also accessible at github.com/maojrs/BBB_experiment. In this way, the research community can reproduce and use the methods and software developed here in their own research.

12.2 Future directions

A future project related to the first part of this thesis is on bistable stochastic reaction-diffusion systems in non-equilibrium steady state. Bistability is an intrinsic phenomenon found in many biological systems. The switching between metastable equilibria can be highly unpredictable, so it is important to develop comprehensive mathematical models of bistable chemical reactions. Furthermore, biological systems are in general open systems whose steady state is a not in equilibrium. For instance, the work [258] uses the Schlögl model to study the differences between deterministic and stochastic models applied to bistability through a thermodynamic perspective. However, these studies have not taken spatial inhomogeneity into account, which is essential in realistic biological models. In order to assess the relevance of spatial diffusion in bistable processes, I plan to use the theoretical framework we have been developing to extend these ideas to spatially inhomogeneous biochemical systems.

Another possible future project concerns the second part of this thesis. The numerical algorithms presented in Chapters 9 and 10, and further extended in Chapter 11, could be used to model the propagation of shock waves from air to a spherical thick interface. This interface could be an idealized model of a skull of a human or a mouse to study the physical effects of mild shocks in TBI. Furthermore, we can try to model the brain and bone as elastic solids by coupling Euler equations with the elasticity equations. This will allow a more accurate method that models the shear stresses experienced by the skull and brain. Unlike many software packages and algorithms developed to study TBI, the algorithms are available in full detail in [52, 53, 55], and the software is available for free with a BSD licensed, so they can be used by the research community.

Although the two main parts of this thesis have clearly followed different research tracks, they have a point of convergence in my future research in stochastic reaction-diffusion theory and numerical methods applied to cellular dynamics. A relevant example where this convergence can be appreciated is given by the probabilistic dynamics of chemical kinetics at cellular and sub-cellular scale. These dynamics can be described using several approaches: the chemical master equation (CME) for spatially homogeneous systems, the reaction-diffusion master equation (RDME) for coarse-grained spatially non-homogeneous systems and coupled Fokker-Planck equations with reaction boundaries or Markovian-switching for spatially non-homogeneous systems. In Chapter 2, we showed the CME (and the RDME equivalently) can be approximated by its continuous counterpart, the Fokker-Planck equation, where the "spatial diffusion" variable becomes the state space. More generally, any of these approaches involves solving high-dimensional coupled Fokker-Planck equations or their analog discrete versions. As we showed in the introduction, the Fokker-Planck equations can be written in conservation form; taking into account they are parabolic, we could devise numerical methods that are inspired by the high-resolution shock-capturing methods for hyperbolic conservation laws. It is also possible to begin directly from the discrete CME or RDME an apply the same flux-differencing numerical methodology to enforce probability conservation.

However, we already mentioned the CME, the RDME and the Fokker-Planck equations can be very high-dimensional even for relatively simple systems. This issue renders traditional computational simulations prohibitively expensive. In order to obtain the most relevant information on the probabilistic dynamics of these systems, we require applying a coarse-graining approach. This will likely require a combination of conservative numerical methods implemented within the theoretical framework of non-equilibrium statistical mechanics and reduction of order to obtain thermodynamically relevant information of the system and be able to apply the results to relevant problems.

Appendix A

A SURVEY ON STOCHASTIC DIFFERENTIAL EQUATIONS

In this section, we will show some analytic solutions of simple stochastic differential equations (SDEs) related to this thesis. These can be found in many textbooks and notes on the subject, like [73, 88, 184, 140, 225, 240] and others. However, we compile some basic solutions as a reference to the reader that is not familiarized with SDEs. We also briefly discuss the issue between the Ito and Stratonovich approach, so the reader can be familiarized with the concepts of integrals of Brownian motion.

The most basic SDE is a Wiener process with drift,

$$dX_t = \mu dt + \sigma dW_t.$$

As μ and σ are constant, we can directly integrate this equation to yield

$$X_t = X_0 + \mu t + \sigma W_t.$$

This shows how to calculate the random variable X_t in terms of a Gaussian random variable W_t with mean zero and variance equal to t. In computational terms, we can easily sample W_t and input its value into the recipe given by the solution to the SDE to obtain a sampled value of the random variable X_t. In many applications, the numerical implementations of SDEs solutions is fundamental. For these endeavors the reader is referred to the excellent review article [111].

As shown in some of the following examples, in order to solve an SDE, we want to express the random variable we are looking for in terms of functions or integrals of a Gaussian random variable with mean zero and variance t, i.e. in terms of a W_t (a Wiener process). We will show some examples below.

A.1 Geometric Brownian motion

We will begin with a very simple example of geometric Brownian motion. Consider the SDE

$$dX_t = X_t dW_t.$$

An equivalent ODE would be given by using a smooth variable dw instead of dW_t, so

$$\frac{dX}{dw} = X \qquad \Rightarrow \qquad \int \frac{dX}{X} = w \qquad \Rightarrow \qquad \ln(X) = w + c_0 \qquad \Rightarrow \qquad X = X_0 e^w.$$

We will use this as inspiration to solve the SDE. Analogously to the ODE case, we can focus on $\ln(X_t)$, which we will refer to as $f(X_t) = \ln(X_t)$. If we can obtain this quantity, we can solve the SDE by taking the exponential on both sides of the equation. In order to obtain $f(X_t)$, or more precisely $df(X_t) = f(X_t + dX_t) - f(X_t)$, we can directly apply Ito's lemma from Eq. 3.2 to $f(X_t)$. However, this step can be done more intuitively by simply doing a Taylor expansion up to second order and then substituting dW_t^2 for dt.

$$\begin{aligned} df(X_t) = d\ln(X_t) = d\ln(X_t) &= \frac{\partial}{\partial x}[\ln(X_t)]dX_t + \frac{\partial}{\partial x^2}[\ln(X_t)]\frac{dX_t^2}{2} \\ &= \frac{\partial}{\partial x}[\ln(X_t)]X_t dW_t + \frac{\partial}{\partial x^2}[\ln(X_t)]\frac{X_t^2 dt}{2} \\ &= dW_t - \frac{dt}{2} \end{aligned}$$

Note that the first line is basically a Taylor expansion. Also see the second order term becomes relevant because $dW_t^2 \sim dt$, which is the essence of Ito's lemma. Doing this Taylor expansion in this way is equivalent to directly applying Ito's lemma. Integrating, we obtain

$$\begin{aligned} f(X_t) = \ln(X_t) &= W_t - \frac{t}{2} + c_0 \\ \Rightarrow \qquad X_t &= X_0 e^{W_t - t/2}. \end{aligned} \tag{A.1}$$

If the solution was the same than in the ODE case, $X_t = X_0 e^{W_t}$, Ito's lemma from Eq. 3.2 applied to $X_t = f(W_t) = X_0 e^{W_t}$ would yield

$$\begin{aligned} d(X_0 e^{W_t}) &= \frac{\partial X_0 e^{W_t}}{\partial w} + \frac{\partial X_0 e^{W_t}}{\partial w^2} dW_t^2 \\ &= X_0 e^{W_t} dW_t + X_0 \frac{e^{W_t}}{2} dt \end{aligned}$$

as $X_t = X_0 e^{W_t}$, then we obtain

$$dX_t = X_t dW_t + \frac{X_t}{2} dt.$$

Note this is not the SDE, we wanted to solve. It has an extra drift term; therefore, the correct solution is $X_t = X_0 e^{W_t - t/2}$. This last result is actually helpful to convert from the Ito interpretation into the Stranonovich one, see below or [88, 225, 254] for details on this

issue.

A.1.1 The Black-Scholes model

The Black-Scholes model is used in mathematical finance to estimate the price of options over time in the market. We will mostly be concerned in the solution to the Black-Sholes equation for educational purposes in the context of SDEs.

The Black-Scholes model can be written as an SDE,

$$dX_t = \mu X_t dt + \sigma X_t dW_t, \qquad X(0) = X_0, \tag{A.2}$$

which is a general geometric Brownian motion. In order to solve this SDE, we can apply the same procedure as before. Consider $f(X_t) = \ln(X_t)$ and do a Taylor expansion (or directly apply Ito's lemma from Eq. 3.2 to yield

$$\begin{aligned} df(X_t) = d\ln(X_t) &= \frac{1}{X_t}\overbrace{X_t(\mu dt + \sigma dW_t)}^{dX_t} - \frac{1}{X_t^2}\overbrace{\frac{X_t^2(\mu dt + \sigma dW_t)^2}{2}}^{dX_t^2} \\ &= \mu dt + \sigma dW_t - \left(\frac{\mu^2 dt^2}{2} + \mu dt dW_t + \frac{\sigma^2 dW_t^2}{2}\right). \end{aligned}$$

We only care about the first order terms, though notice again dW_t^2 goes like dt, so the term with dW_t^2 should be considered as first order, therefore

$$d\ln(X_t) = \mu dt + \sigma dW_t - \frac{\sigma^2 dt}{2}.$$

Integrating and taking the exponential, we obtain the solution as

$$X_t = X_0 \exp\left[\sigma W_t + t\left(m - \frac{\sigma}{2}\right)\right]. \tag{A.3}$$

Note that taking the natural logarithm of Eq. A.1 and Eq. A.3, we see that the $\ln(X_t)$ follows a Brownian motion, or more specifically a Wiener process with drift. This is the definition of geometric Brownian motion, a continuous time stochastic process in which the logarithm of the random variable is a Wiener process.

A.1.2 An alternate method

A somewhat more general and alternate approach to solve the geometric Brownian motion from Eq. A.2 is to assume a solution of the form $X_t = f(t, y)$, where $y = W_t$. Ito's lemma

from Eq. 3.2, yields

$$df = \left(\frac{\partial f}{\partial t} + \frac{1}{2} \frac{\partial^2 f}{\partial y^2} \right) dt + \frac{\partial f}{\partial y} dW_t.$$

Note we are assuming the function $f(t, y)$ is smooth, so there is no problem in taking derivatives in any of the two variables, even if one of them will be substituted by a random variable. As $df = dX_t$, we can equate this equation term by term with Eq. A.2. This yields two identities that need to be fulfilled

$$\begin{aligned} \frac{\partial f}{\partial t} + \frac{1}{2} \frac{\partial^2 f}{\partial x^2} &= \mu X_t = \mu f, \\ \frac{\partial f}{\partial y} &= \sigma X_t = \sigma f. \end{aligned}$$

Integration of the second identity immediately yields

$$f(t, y) = \alpha(t) e^{\sigma y}, \tag{A.4}$$

where $\alpha(t)$ plays the role of a constant. We now substitute this result into the first identity to obtain an equation for $\alpha(t)$

$$\alpha'(t) = \alpha(t) \left(\mu - \frac{\sigma^2}{2} \right).$$

The solution of this ODE is simply

$$\alpha(t) = \alpha_0 e^{\mu - \frac{\sigma^2}{2} t}.$$

Remembering that the variable y points to W_t, we can substitute $\alpha(t)$ into Eq. A.4 and write the final solution as

$$f(t, W_t) = X_0 \exp \left[\sigma W_t + t \left(\mu - \frac{\sigma^2}{2} \right) \right].$$

A.2 The Ornstein–Uhlenbeck process

The Ornstein–Uhlenbeck process is a modification of a Wiener process where the Brownian particle tends to move towards a central location with a greater attraction when the particle is farther away from the given central location. It is in essence a Wiener process with a drift

that depends linearly on the random variable, $a + bX_t$, so

$$dX_t = (a + bX_t)dt + \sigma dW_t,$$

with a, b and σ constants. It is more intuitive to write it in the form

$$dX_t = \theta(\mu_0 - X_t)dt + \sigma dW_t, \tag{A.5}$$

where $a = \theta\mu_0$ and $b = -\theta$. We will first assume $\sigma = 0$, so we have the ODE,

$$\frac{dX_t}{dt} = \theta(\mu_0 - X_t).$$

The solution of this ODE is straightforward and yields,

$$X_t = \mu_0 - (\mu_0 - X_0)e^{-\theta t}.$$

We can immediately see that as $t \to \infty$, $X_t \to \mu$. There is this attraction towards the central location μ_0 and θ measures how strong is the attraction. The idea behind the Ornstein–Uhlenbeck process is to add noise to this process.

In order to solve the Ornstein–Uhlenbeck process from Eq. A.5, we begin with an ansatz of a function we could apply Ito's lemma, which is inspired in the solution of the ODE version, $f(X_t) = X_t e^{\theta t}$. Applying Ito's lemma from Eq. 3.2, we obtain

$$\begin{aligned} df = d(X_t e^{\theta t}) &= X_t \theta e^{\theta t} dt + e^{\theta t} dX_t \\ &= X_t \theta e^{\theta t} dt + e^{\theta t}(\theta(\mu_0 - X_t)dt + \sigma dW_t) \\ &= e^{\theta t}\theta\mu_0 dt + e^{\theta t}\sigma dW_t. \end{aligned}$$

Integrating, we obtain the solution in terms of an Ito integral,

$$\begin{aligned} X_t e^{\theta t} &= X_0 + e^{\theta t}\mu_0 + \int_0^t e^{\theta s}\sigma dW_s, \\ \Rightarrow \qquad X_t &= X_0 e^{-\theta t} + \mu_0 + e^{-\theta t}\int_0^t e^{\theta s}\sigma dW_s \\ \Rightarrow \qquad X_t &= \mu_0 + e^{-\theta t}\left(X_0 + \int_0^t e^{\theta s}\sigma dW_s\right). \end{aligned} \tag{A.6}$$

The Ito integral in this case has no analytic form, but it ca easily be approximated numerically, see [111, 140].

A.3 The Langevin equation

The equations we previously solved might not have been directly related to the work in this thesis. However, the Langevin equation is very relevant in the context of this thesis, and in order to solve it, we require some of the methods we just presented. The Langevin equation is an SDE that describes the movement of a Brownian particle, where each of the collisions with other particles is modeled through a noise term in the velocity. This means that the collisions are modeled by uncorrelated jumps in the velocity with mean zero and variance t, i.e. a white noise term [254]. The Langevin SDE can be stated following Newton's second law of the conservation of momentum

$$\begin{aligned} dX_t &= V_t dt \\ m dV_t &= -\eta V_t dt - \frac{\partial U(x)}{\partial x} dt + \xi(t) dt, \end{aligned}$$

where X_t and V_t are the position and velocity of the Brownian particle. The second equation is Newton's second law, η is a damping coefficient, $U(x)$ is the potential function for a force field and $\xi(t)dt = \sqrt{2k_B T} dW_t$. The quantities k_B and T correspond to the Boltzmann constant and the temperature of the surrounding medium.

The first equation is actually a simple ODE, so we can integrate it

$$X_t = X_0 + \int_0^t V_s ds. \tag{A.7}$$

The second equation is nothing more than an Ornstein–Uhlenbeck process, so the solution is simply given by Eq. A.6,

$$V_t = -\frac{1}{\eta}\frac{\partial U}{\partial x} t + e^{-\eta t/m} \left(V_0 + \frac{1}{m} \int_0^t e^{\eta s/m} \xi(s) ds \right)$$

where the relation to the parameters from Eq. A.6 is given by $\theta = \eta/m$ and $\mu_0 = -\partial_x U(x)/\eta$. Substituting this result into Eq. A.7 yields our solution

$$X_t = X_0 + \frac{1}{\eta}\frac{\partial U}{\partial x} t + \int_0^t \left[e^{-\eta s/m} \left(V_0 + \frac{1}{m} \int_0^s e^{\eta \tau/m} \xi(\tau) d\tau \right) \right] ds.$$

The inner integral is of course an Ito integral since $\xi(t)dt = \sqrt{2k_B T} dW_t$.

A.4 Stratonovich vs Ito's approach

The Stratonovich and Ito's approaches are two different ways to define integrals of Brownian motion and both are relevant in different applications. In this section, we will try to develop

some intuition of what it means to integrate with respect to Brownian motion and on the main differences between the Stratonovich and Ito's approach. In many physical scenarios, Stratonovich's approach seems somewhat more relevant since it does not assume fractal Brownian motion. However, Ito's approach is extremely relevant for many other applications, and it is key in rigorous mathematical derivations.

In both cases, the integral is defined in terms of the trajectory of a particle following Brownian dynamics. In essence, Stratonovich's approach assumes that the Brownian dynamics arise from Newtonian collisions between the particle and the particles of the medium, so it always has two times sufficiently close that a particle only moved on a straight line, known as mean free path. In the case of Ito's approach, the Brownian paths are fractal, so it doesn't matter how small of a time interval you choose; the path will never be a straight line; it will always look like a ragged nowhere differentiable curve. It is, in some sense, a mathematical idealization of the trajectory of a physical Brownian particle.

In order to be more precise on the different ways to define integrals of Brownian motion, we will consider the following SDE

$$dy(t) = \mu(t)dt + \sigma(t)dW(t).$$

Note we changed slightly the notation than the one used in previous examples, where the time dependence of the random variable is now denoted explicitly. This will make some of the next calculations a little more clear. Direct integration up to time $t = T$ yields

$$y(t) = y(0) + \int_0^T \mu(t)dt + \int_0^T \sigma(t)dW(t).$$

The first integral on the right hand side is a simple Riemann integral, so it can be defined simply by discretizing the time interval $[0, T]$ in $N - 1$ intervals of size δt

$$\lim_{\delta t \to 0} \sum_{j=0}^{N-1} \mu^*(t_j)(t_{j+1} - t_j).$$

where $t_j = j\delta t$, $N\delta t = T$ and $\mu^*(t^j)$ is any reasonable approximation to the value of $\mu(t)$ in that interval. Two possibilities are simply using the left value $\mu^*(t^j) = \mu((t_j)$ or the trapezoidal rule $\mu^*(t^j) = (\mu(t_j) + \mu(t_{j+1}))/2$. Regardless, which approximation we use, in the limit $\delta t \to 0$, we will recover the same value for the integral. The second integral will be a bit more complicated than that; it is an integral of Brownian motion that we have to carefully define. This new integral can be geometrically understood in a similar way to the Riemann integral. The Riemann integral $\int_0^T \mu(t)dt$ is the area under the curve of $\mu(t)$ in the $t, \mu(t)$ plane. The integral of a Brownian motion, like $\int_0^T \sigma(t)dW(t)$, can be better understood if we first think of the $t, W(t)$ plane, where we can see the Brownian trajectory

as a function of time, like shown in Figure A.1. Then, we draw a third axis $\sigma(t)$, and we draw the corresponding values on top. However, this can be tricky since $W(t)$ is a Brownian

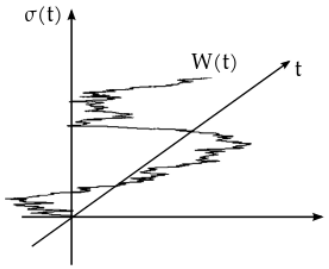

Figure A.1: This figure shows the trajectory of a Brownian particle $W(t)$ as a function of time t; we also draw a third axis $\sigma(t)$ as a function only of t. In general, this can be function of t, $W(t)$ or anything else.

trajectory. Following an analogous approach to how Riemann sums are defined, we can try to define it as the limit of a discrete sum by dividing the integration interval into intervals of length δt, then

$$\int_0^T \sigma(t)dW(t) \approx \sum_{j=0}^{N-1} \sigma^*(t_j)(W(t_{j+1}) - W(t_j)),$$

where $W(t_j)$ is a Wiener process, i.e. a random variable with mean zero, normally distributed independent increments, see Section 3.1.1. This definition is in some sense an extension to a RiemannStieltjes integral using a measure of unbounded variation, like a Wiener process $W(t)$. For a given time discretization, this will yield an approximation to the Brownian trajectory by a discrete set of points connected through straight lines, as shown by the thick black lines on the two top images of Figure A.2 for three and six time points discretizations respectively. We can now calculate the values of $\sigma(t)$ for the corresponding trajectory. In the case of Figure A.2, we uses the left point approximation for a given time interval, so $\sigma^*(t_j) = \sigma(t_j)$. The shaded rectangles show an approximation of the are under the curve in the $t, W_t, \sigma(t)$ coordinates. However, this area is not the geometrical interpretation of the integral of a Brownian motion. We need to project these shaded rectangles into the $W(t), \sigma(t)$ plane, as shown in the bottom two images of Figure A.2. As we take the limit $\delta t \to 0$, we will obtain more and more time points in the time interval. The integral of a Brownian motion is the area given by the sum of all these rectangles in the $W(t), \sigma(t)$ plane

as $\delta t \to 0$.

However, this definition is not unique as with the Riemann integral. Different choices of $\sigma^*(t_j)$ will yield different limiting results. For instance, two possible choices are given by the left point and the trapezoidal rule,

1. $\sigma^*(t_j) = \sigma(t_j)$,

2. $\sigma^*(t_j) = \dfrac{\sigma(t_j) + \sigma(t_{j+1})}{2}$.

In the case of Riemann integrals, any given choice yields the same limit. However, in the case of integrals of Brownian motion, different choices of $\sigma^*(t_j)$ will yield different limits as $\delta t \to 0$. Furthermore, we should also consider the case where $\sigma(t)$ depends on the random variable itself, i.e. $\sigma(t, y(t))$, so the two possibilities become

1. $\sigma^*(t_j, y(t_j)) = \sigma(t_j, y(t_j))$,

2. $\sigma^*(t_j, y(t_j)) = \dfrac{\sigma(t_j, y(t_j)) + \sigma(t_{j+1}, y(t_{j+1}))}{2}$.

The first choice will yield the Ito integral and the second will yield the Stratonovich integral. Note for the second case, instead of choosing $\sigma^*(t_j, y(t_j)$, we could have chosen $\sigma(t_j^*, y(t_j^*))$ or $\sigma^*(t_j^*, y^*(t_j)$, where

$$t_j^* = \frac{t_j + t_{j+1}}{2}. \qquad y^*(t_j) = \frac{y(t_j) + y(t_{j+1})}{2}.$$

Any of these two last cases will yield the Stratonovich integral as a limiting result, as stated in [225]. A very common exercise to notice the different limiting behaviors is solving the integral $\int W(t)dW(t)$ by calculating its limiting behavior. We can calculate this integral using the Ito approach, where $\sigma^*(t_j) = W(t_j)$

$$\begin{aligned}
\int_0^T W(t)dW(t) &\approx \sum_{j=0}^{N-1} W(t_j)(W(t_{j+1}) - W(t_j)) \\
&= \frac{1}{2}\sum_{j=0}^{N-1} W(t_{j+1})^2 - W(t_j)^2 - (W(t_{j+1}) - W(t_j))^2 \\
&= \frac{1}{2}\left(W(T)^2 - W(0)^2\right) - \frac{1}{2}\underbrace{\sum_{j=0}^{N-1}(W(t_{j+1}) - W(t_j))^2}_{T}
\end{aligned}$$

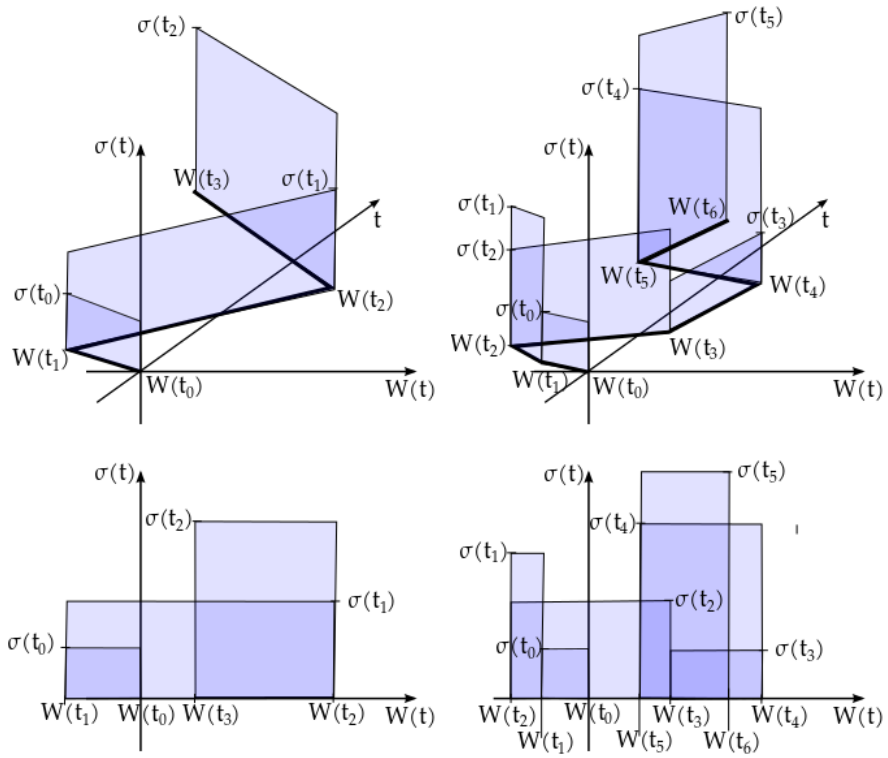

Figure A.2: Top two figures: the thick path shows a discrete approximation of the Brownian path showin in Figure A.1, and the areas under the curve $\sigma(t)$ along the Brownian trajectory $W(t)$ are approximated by the sum of the area in the shaded areas. The first one only divides the interval in three time points t_1, t_2 and t_3; the second one uses six time points in the same interval. As $\delta t \to 0$, the number of time points in the interval grows to infinity as well. The bottom two figures show a projection of the top two figures into the plane $W(t), \sigma(t)$. The sum of all the areas of the different shaded rectangles yield an approximation to the integral of a Brownian motion. The integral is recovered as $\delta t \to 0$. Note this is done for only one possible Brownian path; the integral of a Brownian motion is a random variable that represents the integrals of all the possible Brownian paths. Also note this figures use Ito's approach since $\sigma^*(t_j) = \sigma(t_j)$.

By definition $W(0) = 0$, we can also recognize the second term with the sum as the quadratic variation we calculated in Section 3.1.2. As we take the limit $\delta \to 0$, we know from the result from Eq. 3.1 that it simply converges to its mean T. Therefore, the Ito integral yields

$$\int_0^T W(t)dW(t) = \frac{1}{2}(W(T)^2 - T).$$

The Stratonovich approach will yield a different result, we write the same expression but now we use $\sigma^*(t_j) = (W(t_j) + W(t_{j+1})/2$, so

$$\begin{aligned}\int_0^T W(t)dW(t) &\approx \sum_{j=0}^{N-1} \frac{W(t_j) + W(t_{j+1})}{2}(W(t_{j+1}) - W(t_j)) \\ &= \frac{1}{2}\sum_{j=0}^{N-1} W(t_{j+1})^2 - W(t_j)^2 \\ &= \frac{1}{2}\left(W(T)^2 - W(0)^2\right).\end{aligned}$$

Once again $W(0) = 0$, so the Stratonovich integral simply yields

$$\int_0^T W(t)dW(t) = \frac{1}{2}W(T)^2.$$

Therefore the different approaches yield different results

- Ito integral $\to \int_0^t W(s)dW(s) = \frac{1}{2}(W(t)^2 - t)$,
- Stratonovich integral $\to \int_0^t W(s)dW(s) = \frac{1}{2}W(t)^2$,

This is done in even more detail and rigor in many of the usual references [88, 111, 140, 225]. However, it is harder to find how to interpret these differences in a way that the reader gains some intuition. In the next paragraphs, I will show how can we intuitively interpret these two approaches and when are they relevant.

Stratonovich's integral seem to follow what we expect from ordinary calculus; however, Ito's integral has an extra term. This term actually comes from the fact that the quadratic variation is not zero. The fact that the quadratic variation is not zero comes from the fractal nature of Brownian paths, which makes Brownian motion nowhere differentiable. This means that, even though Brownian paths are continuous, knowing the value at some point in time doesn't allow us to know/predict the value at some other near point in time, not even if it is infinitesimally close. Basically, Taylor expansions are nowhere valid. The

fact that we cannot really "know" the future from our current state speaks of some inner unpredictability. This is accurately captured by Ito's approach because it uses the left sided approximation $\sigma^*(t_j) = \sigma(t_j)$, so it does not assume any knowledge of the future from a given point in time. However, Stratonovich's approach uses the midpoint approximation $\sigma^*(t_j) = (\sigma(t_j) + \sigma(t_{j+1}))/2$, so it assumes some knowledge of the future at t_{j+1}. This approach immediately kills this unpredictability, so Stratonovich approach does not really represent integration with respect to fractal and nowhere differentiable Brownian motion. It is, in some sense, a more physical approach since the Brownian dynamics can be understood as a consequence of Newtonian collisions between the particle and the particles of the medium, so there are always two sufficiently close times such that the particle only moved on a straight line.

A more precise account of the previous logic is given by [254]. In Ito's approach, i.e., in a fully fractal Brownian motion, we have that

$$\mathbb{E}[W(t)W(s)] = \delta(t-s), \tag{A.8}$$

which basically means the autocorrelation function of $W(t)$ is proportional to a delta. This is another way to phrase the fractal nature, the non-zero quadratic variation or the unpredictability we mentioned before. If the correlation is zero, except when $t = s$, it means that what we know at the current time does not really tell us anything about future times. However, in many applications, this is not true, and this fact is reflected in the autocorrelation function of the noise term. Instead of a simple delta, we can have a small sharp peak as an autocorrelation function; we can say the sharp peak has a width/duration of $\tau_c > 0$. The Stratonovich approach is recovered as $\tau_c \to 0$. This means that if in our application of interest the autocorrelation function is not a delta, then Stratonovich approach is the correct approach to use. Ito's approach cannot even be formulated if we do not assume $\tau_c = 0$ since we need non-zero quadratic variation, so Eq. A.8 has to be assumed true from the beginning.

The question remains when to use which approach? We already have a hint of the answer in terms of the autocorrelation function. In order to provide a full answer, we have to distinguish between two types of noise in a system.

- *External noise:* This type of noise is usually produced by an external random force, like in the case of a Brownian particle in Physics. When this type of noise is removed, the deterministic equation should still make sense. In these cases, the noise will only be approximately white, i.e. its autocorrelation function will be a small sharp peak, but not quite a delta. In these cases, Stratonovich approach is suitable for the reasons established earlier.

- *Internal noise:* The systems itself consists of discrete elements with some kind of inherent stochasticity, which cannot be removed, like in chemical kinetics or population

dynamics. The deterministic approach to these problems is merely an approximation to the stochastic dynamics. However, these applications are usually more accurately described in terms of jump processes and Master equations. Nonetheless, they can be approximated by diffusion processes, in which case Ito's approach would be more appropriate.

It should also be noted that for mathematical endeavors, Ito's approach provides a more sound and robust framework to develop mathematical theory that can be as relevant for mathematical applications. Also one can easily convert the results from one description into the other by adding a term into the drift part of the stochastic differential equation. Consider the following SDE under Ito's convention

$$dX_t = \mu(X_t, t)dt + \sigma(X_t, t)dW_t.$$

When integrating this equation, it will get the extra term characteristic of Ito's integral. Therefore, we can write an equivalent SDE following Stratonovich's approach where the extra term is absorbed into the drift of the SDE,

$$dX_t = \left(\mu(X_t, t) - \frac{1}{2}\sigma(X_t, t)\frac{\partial}{\partial x}\sigma(X_t, t)\right) + \sigma(X_t, t)dW_t.$$

These two SDEs are equivalent as long as the first one is integrated using Ito's approach and the second one using Stratonovich's approach. Similarly, the Stratonovich SDE

$$dX_t = \mu_s(X_t, t)dt + \sigma_s(X_t, t)dW_t,$$

can be rewritten as an Ito SDE,

$$dX_t = \left(\mu_s(X_t, t) + \frac{1}{2}\sigma_s(X_t, t)\frac{\partial}{\partial x}\sigma_s(X_t, t)\right)dt + \sigma_s(X_t, t)dW_t.$$

These equivalence relations are straightforward to derive by using the definition of Ito/Stratonovich integral along with Ito's lemma, see [88] for details.

Appendix B

IN-VITRO BBB EXPERIMENT RESULTS AND METHODOLOGY

In this appendix, we provide details related to the methodology of the experimental component behind the work described in Chapter 10. This work was mostly done by our collaborators [55].

Using well-established methods [20, 21, 179] mouse brain-derived endothelial cells (MBECs), purified from wild-type C57BL6 mice, were grown on permeable nylon support membranes in standard transwell chambers (see Figure 10.1(a)) and formed endothelial cell monolayer tight junctions that functionally mimic the BBB, which is responsible for maintaining and regulating separation between the central nervous system (CNS) and the circulating peripheral blood supply [19, 279]. The transwell chambers were filled completely with an aqueous solution (serum-free DMEM/F12 medium containing bFGF (1 ng/ml) and hydrocortisone (500 nM)). For blast exposure, the transwells were secured in the shock tube with the bottom of the transwell facing the oncoming shock wave (see Figure 1.2). For all experiments, BBB cells were exposed to a single mild blast of indicated intensity (psi).

In addition to the experiment presented in Section 10.1.1, we performed another experiment to investigate the effects of the shock tube blast exposure on tight junction morphology. Singly blasted (13-13.9 psi) or sham-treated monolayers were immunostained with antibodies recognizing the tight junction-associated scaffolding protein, ZO-1 [243] 24 hours after treatment and then imaged using laser confocal microscopy. ZO-1 expression in sham-treated MBEC monolayers appeared morphologically normal with ZO-1 immunostaining tightly restricted to the interposing plasma membrane domains at points of cell-to-cell contact (Figure B.1A). In marked contrast to this, blast exposure induced ragged, hypertrophic appearing tight junctions (Figure B.1B). In addition, ZO-1 expression appeared mislocalized in association with peri- abluminal and/or peri-luminal plasma membranes domains. This expression pattern is also consistent with diffuse intracellular cytoplasmic ZO-1 mislocalization.

The confocal images in Figure B.1A and Figure B.1B are maximum-field projections comprised of 27 merged images collected at 0.2μm step intervals in the z-axis orthogonal to the plane of the MBEC monolayer, thereby representing a total depth of 5.4μm that encompassed the full cross-sectional width of the MBEC monolayers. Figure B.1C and Figure B.1D depict three-dimensional serial reconstructions of images in the upper panels projected at oblique angles. For ease of reference, the arrowheads denote the same cell-to-cell contact points in panels A, C and B, D (sham and blast-exposed, respectively). From

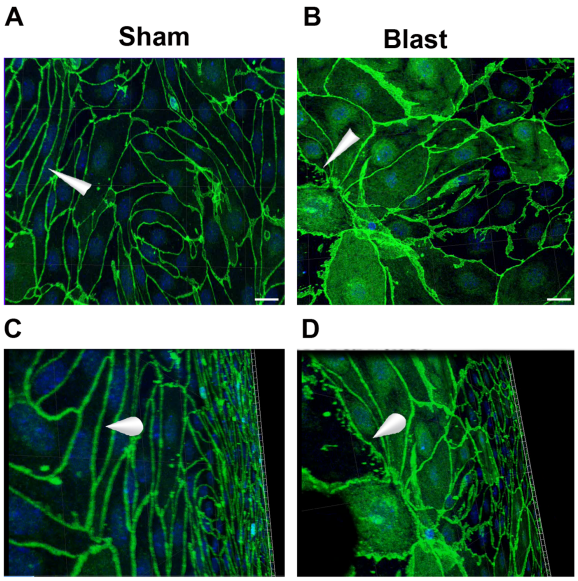

Figure B.1: (A) Laser confocal microscopy reveals normal ZO-1 expression patterns expressed specifically at uniform, well-defined tight junctions along cell-to-cell interfaces within the plane of the brain-derived microvessel endothelial cell monolayer. (B) In contrast to the sham condition, ZO-1 expression in blast-exposed endothelial cells is highly dystrophic with widespread mislocalization in cellular domains remote from tight junctions. Panels A and B show a merged, serial reconstruction comprised of 27 images acquired at 0.2μm intervals along the z-axis orthogonal to the plane parallel with the MBEC cell monolayer. (C and D) Lower panels show oblique x-y-z plane views of the panels above (A,B), thereby permitting an improved assessment of blast-induced tight junction dysmorphology compared to normal sham tight junctions. Nuclei are stained blue with Dapi. Arrowheads denote the same cell-to-cell contact domains in the corresponding sham (A, C) and blast (B, D) images. Scale bars = 20μm.

these oblique angles the degree of blast-induced tight junction dysmorphology and ZO-1 mislocalization are more easily appreciated (Also, see supplementary videos).

Claudin-5 is a tight junction-specific membrane bound protein [128] that is a critical regulator of BBB permeability [181]. Figure B.2 shows that a single mild blast exposure also markedly disrupted claudin-5 expression. As with Z0-1, claudin-5 immunostaining revealed aberrant, hypertrophic appearing tight junctions in the blast-exposed monolayers. In addition, the asymmetric peri-nuclear claudin-5 immunostaining clearly demonstrates that blast exposure caused it to become aberrantly retained within the cells, thus raising the possibility that normal polarized subcellular trafficking of claudin-5 into and/or away from tight junction domains may be disrupted in the blast-exposed MBECs.

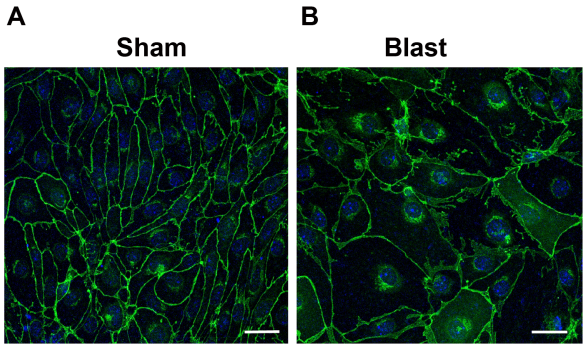

Figure B.2: (A) Laser confocal microscopy reveals normal claudin-5 expression at tight junctions localized along cell-to-cell contacts of the MBEC monolayer. (B) In contrast to the sham controls, claudin-5 expression in blast-exposed endothelial cells is dysmorphic, indicative of aberrant tight junction structure. In addition, claudin-5 is broadly mislocalized and accumulates in asymmetric peri-nuclear intracellular compartments, strongly suggesting that blast exposure induces aberrant subcellular trafficking of claudin-5. Nuclei are stained blue with Dapi. Scale bars = 25μm.

These data suggest that blast exposure causes mislocalization of the tight junction proteins, ZO1 and claudin-5, away from tight junctions. Previous work using the continuous cell line, bEnd.3 showed that blast causes a loss of ZO1 and claudin-5 [122, 123]. This difference could be because bEnd.3 cells are less differentiated than brain-derived microvessel endothelial cells, and which form barriers with lower TEER values than primary brain endothelial cultures used in this report [60]. Nonetheless, our findings in BMECs and in vitro blast studies using bEnd.3 cells [122, 123], collectively demonstrate that blast exposure disturbs expression of proteins critical for maintaining BBB integrity.

Mechanistically, protein mislocalization suggests a dynamic alteration in the cellular process of adjusting to injury, whereas overall tight junction protein loss may suggest co-attending endothelial cell death or impaired protein production or increased tight junction proteolysis. Increasingly, tight junction protein mislocalization is viewed as an underlying pathology in diseases with BBB disruption and is the pattern, for example, in inflammatory conditions [61, 12].

B.1 Culture of primary brain microvascular endothelial cells

Brain microvascular endothelial cells (BMECs) were isolated from 6-8 week old CD-1 mice based on established standard with some modifications procedures [45, 127]. All procedures involving animal subjects were carried out following protocols approved by the Veterans Affairs Puget Sound Health Care System Institution Animal Use and Care Committee

(IACUC). Briefly, meninges were removed from freshly dissected brain cortices, and then the brain was minced. The minced brain matter was ground using a Dounce homogenizer in Dulbecco's Modified Eagle's Medium/Nutrient Mixture F-12 Ham (DMEM/F12; Sigma-Aldrich) supplemented with gentamicin ($50\mu g/ml$; Sigma-Aldrich). 30% Dextran (v/v; from Leuconostoc spp., MW 70,000 Da; Sigma-Aldrich) was added to the homogenate 1:1 and supplemented with 10% bovine serum albumin (BSA, Sigma-Aldrich) to achieve a final concentration of 0.1%. The mixture was centrifuged at 3000 g for 25 min at 4°C. The pellet obtained after the centrifugation was re-suspended in DMEM/F12, filtered through a $70\mu m$ nylon mesh, and centrifuged again at 1000 g for 10 min at room temperature (RT). The resulting pellet was digested at 37°C for 30 min with DMEM/F12 containing collagenase (0.2 U/ml), dispase (1.6 U/ml; collagenase/dispase, Roche Life Sciences) and DNase I ($10\mu g/ml$; Sigma-Aldrich). The digested vessel suspension was filtered through a $21\mu m$ nylon mesh. The filtrate was washed several times with DMEM/F12, and the resulting capillary suspension was seeded on dishes coated with collagen type IV (0.1 mg/ml; Sigma-Aldrich) and fibronectin (0.1 mg/ml; Sigma-Aldrich). BMECs were cultured in BMEC medium, consisting of DMEM/F12 supplemented with 20% plasma-derived fetal bovine serum (Animal Technologies), 1% GlutaMAX (Life Technologies), basic fibroblast growth factor (bFGF, 1 ng/ml; Roche Life Sciences), heparin ($100\mu g/ml$), insulin ($5\mu g/ml$), transferrin ($5\mu g/ml$), selenium (5 ng/ml) (Insulin-transferrin-selenium medium supplement; Life Technologies), and gentamicin ($50\mu g/ml$; Sigma-Aldrich. Puromycin (4 μg/ml; Sigma-Aldrich) was added to BMEC medium for the first 48 hours after plating to remove pericytes and increase endothelial cell purity [192]. Cultures were maintained at 37°C in a humidified atmosphere of 5% CO_2 / 95% air. The medium was changed 24 hours after plating to remove non-adherent cells, red blood cells, and debris. At 48 hours after plating, the medium was changed again with new medium containing all the components listed above, except puromycin. The purified primary BMECs were used to construct in-vitro models when 80% confluent (typically the 5th day after isolation).

B.2 Construction of the in-vitro blood-brain barrier model

Monolayers of brain microvascular endothelial cells were used for all experiments. Endothelial cells were briefly treated with 0.25% Trypsin-EDTA (Sigma-Aldrich) and seeded on the inside of a fibronectin-collagen type IV (0.1 mg/ml, each) coated polyester membrane ($0.33cm^2, 0.4\mu m$ pore size) of a transwell-clear insert (Corning, Tewksbury MA) at a density of 4×104 cells per well. The medium used to plate the cells each of the transwells fitted to a 24-well plate contained all the components of BMEC medium, listed above, with the addition of hydrocortisone ($500nM$; Sigma-Aldrich). The medium in the luminal chamber was changed 24 hours after seeding. BMEC monolayers were cultured for 3 days before use in blast experiments. Transendothelial electrical resistance (TEER, in $\Omega \times cm^2$) was measured

using an ohmmeter equipped with an STX-2 electrode (World Precision Instruments; Sarasota, FL). The TEER of cell-free transwell-clear inserts was subtracted from obtained values. TEER was measured immediately prior to blast exposure and 24 hours post-exposure.

B.3 Exposure of BMEC to Blast

Transwells were placed into the blasting apparatus, consisting of a modified 24-well plate configuration containing only 4 wells of the 24-well plates with a rubber gasket fitted to the modified plate. The medium was discarded from the luminal side of the transwell inserts and the inserts were placed in the middle two chambers of the blasting apparatus. The wells were filled completely with serum-free DMEM/F12 medium containing bFGF (1 ng/ml) and hydrocortisone (500 nM). A rubber gasket was placed between the filled wells and the lid of the apparatus to completely seal the chambers without air bubbles. The treatment apparatus (a single row of 4 transwell chambers with the two chambers in the middle containing the membrane inserts with BMECs) was then taped firmly to a rigid steel frame with 1/4 inch wire mesh, mounted in the blast tube, and exposed to a single mild blast (range: 11.0 to 13.9 peak psi). Non-blasted sham controls were prepared and processed as above but were not exposed to a blast. Following treatment (blast or sham), the medium was aspirated from the chambers. The inserts were placed in a 24-well plate with fresh serum-free medium and returned to 37°C in a humidified atmosphere of 5% CO_2/95% air.

B.4 Transendothelial permeability

Permeability to [14C]-sucrose was measured 24 hours after exposure to blast. Transwell inserts were first washed with physiological buffer containing 1% bovine serum albumin ($141mM$ NaCl, $4.0mM$ KCl, $2.8mM$ $CaCl_2$, $1.0mM$ $MgSO_4$, $1.0mM$ NaH_2PO_4, $10mM$ HEPES, $10mM$ D-glucose and 1% BSA, pH 7.4). The inserts were placed in a new 24-well plate containing $600\mu l$ physiological buffer with 1% BSA in the abluminal chamber. To initiate permeability experiments, [14C]-sucrose ($150,000cpm/well$) in physiological buffer with 1% BSA was added to the luminal chamber and $500\mu l$ samples were collected from the abluminal chamber at 10, 20, 30, and 45 min. When samples were removed from the abluminal chamber, an equal volume of fresh 1% BSA/physiological buffer was immediately added to the abluminal chamber to replace the sample volume. Liquid scintillation fluid was added to each sample and the radioactivity was measured using a liquid scintillation counter. The permeability coefficient and clearance of [^{14}C]-sucrose was calculated according to previously published methods [49]. Clearance was expressed as microliters of radioactive tracer diffusing from the luminal to the abluminal chamber, and it was calculated using the initial amount of radioactivity in the loading chamber and the measured amount of radioactivity in the collected samples. Clearance (μL) = [C]C $\times$ VC / [C]L, where [C]L was the initial amount of radioactivity per microliter of the solution loaded into the insert (in

$cpm/\mu L$), [C]C was the radioactivity per microliter in the collected sample (in $cpm/\mu l$), and VC is the volume of collecting chamber (in μl). The clearance volume increased linearly with time. The volume cleared was plotted versus time, and the slope was estimated by linear regression analysis. The slope of clearance curves for the BMEC monolayer plus transwell membrane was denoted by PS_{app}, where PS is the permeability $\times$ surface area product (in μL/min). The slope of the clearance curve with a transwell membrane without BMECs was denoted by $PS_{membrane}$. The real PS value for the BMEC monolayer (PS_e) was calculated from $1/PS_{app} = 1/PS_{membrane} + 1/PS_e$. The PS_e values were divided by the surface area of the transwell inserts to generate the endothelial permeability coefficient (P_e, in $\mu l/(\text{min/cm}^2)$). Statistical analysis of TEER and sucrose permeability data was carried out using standard one-way analysis of variance (ANOVA) and were performed using SPSS software (IBM, Armonk NY). p values for correlations between blast intensity and TEER or sucrose permeability denote two-tailed statistical significance outcomes of a Pearson correlation.

B.5 Confocal Microscopy

BMECs were washed in PBS and fixed with 4% paraformaldehyde for 10 minutes at 4C. Cells were permeabilized with 0.1% TRITON-X100 for 10 min at RT and blocked with 5% BSA for 30 min at RT. They were then incubated for 1 hour at RT with primary antibody, ZO-1 (AbCam, Cambridge, UK) or claudin-5 (AbCam, Cambridge, UK), followed by incubation with Alexa Fluor 488 conjugated secondary antibody (Life Technologies, Carlsbad, CA). The monolayer-net was then mounted on slides using Prolong Gold anti-fade with DAPI (Life Technologies, Grand Isle, NY) to stain cell nuclei. The monolayers were imaged using a TCS SP5 confocal microscope (Leica, Buffalo Grove, IL) with a 20×0.7 numerical aperture objective. Only representative monolayer fields of cellular interfaces expressing claudin-5 and ZO-1 were imaged from 6 blast-exposed and 6-sham endothelial cultures. The monolayer-nets were imaged using a $0.2\mu m$ z-plane step size for 27 slices representing a total depth of $5.4\mu m$. Primary antibodies for claudin-5 and ZO-1 were purchased from Zymed (San Francisco, CA). Serial three-dimensional reconstructions of confocal images were carried out using Imaris software (Bitplane, South Windsor, CT). Figures were prepared using Photoshop and Imaris software using only linear brightness and contrast adjustments that were applied identically among control and blast-exposed specimens for each figure all image acquisition parameters were held constant in acquiring data for both identical control and blast-exposed specimens for each experiment.

BIBLIOGRAPHY

[1] P. Abdul-Muneer, H. Schuetz, F. Wang, M. Skotak, J. Jones, S. Gorantla, M. C. Zimmerman, N. Chandra, and J. Haorah, *Induction of oxidative and nitrosative damage leads to cerebrovascular inflammation in an animal model of mild traumatic brain injury induced by primary blast*, Free Radical Biology and Medicine, 60 (2013), pp. 282–291.

[2] R. Abgrall and S. Karni, *Computations of compressible multifluids*, Journal of Computational Physics, 169 (2001), pp. 594–623.

[3] N. Agmon, *Diffusion with back reaction*, The Journal of Chemical Physics, 81 (1984), pp. 2811–2817.

[4] N. Agmon and A. Szabo, *Theory of reversible diffusion-influenced reactions*, The Journal of Chemical Physics, 92 (1990), pp. 5270–5284.

[5] D. Al-Anbaki, F. Meyer, A. Edan, and H. Lippert, *The spectrum of war-like injuries in children and teenagers during a post-war wave of violence in Iraq*, Zentralblatt fur Chirurgie, 133 (2008), pp. 306–309.

[6] P. W. Alford, B. E. Dabiri, J. A. Goss, M. A. Hemphill, M. D. Brigham, and K. K. Parker, *Blast-induced phenotypic switching in cerebral vasospasm*, Proceedings of the National Academy of Sciences, 108 (2011), pp. 12705–12710.

[7] D. F. Anderson, *Incorporating postleap checks in tau-leaping*, The Journal of Chemical Physics, 128 (2008), p. 054103.

[8] D. F. Anderson and T. G. Kurtz, *Continuous time markov chain models for chemical reaction networks*, in Design and Analysis of Biomolecular Circuits, Springer, 2011, pp. 3–42.

[9] ——, *Stochastic analysis of biochemical systems*, vol. 1, Springer, 2015.

[10] J. D. Anderson, *Modern compressible flow: with historical perspective*, vol. 12, McGraw-Hill New York, 1990.

[11] P. W. Anderson et al., *More is different*, Science, 177 (1972), pp. 393–396.

[12] I. E. András, H. Pu, M. A. Deli, A. Nath, B. Hennig, and M. Toborek, *Hiv-1 tat protein alters tight junction protein expression and distribution in cultured brain endothelial cells*, Journal of Neuroscience Research, 74 (2003), pp. 255–265.

[13] S. S. Andrews and D. Bray, *Stochastic simulation of chemical reactions with spatial resolution and single molecule detail*, Physical Biology, 1 (2004), p. 137.

[14] P. Ao, C. Kwon, and H. Qian, *On the existence of potential landscape in the evolution of complex systems*, Complexity, 12 (2007), pp. 19–27.

[15] L. Arnold, *On the consistency of the mathematical models of chemical reactions*, in Dynamics of Synergetic Systems, Springer, 1980, pp. 107–118.

[16] M. Baer and J. Nunziato, *A two-phase mixture theory for the deflagration-to-detonation transition (ddt) in reactive granular materials*, International Journal of Multiphase Flow, 12 (1986), pp. 861–889.

[17] D. S. Balsara, *A two-dimensional HLLC riemann solver for conservation laws: Application to Euler and magnetohydrodynamic flows*, Journal of Computational Physics, 231 (2012), pp. 7476–7503.

[18] D. S. Balsara, M. Dumbser, and R. Abgrall, *Multidimensional HLLC riemann solver for unstructured meshes–with application to Euler and MHD flows*, Journal of Computational Physics, 261 (2014), pp. 172–208.

[19] W. Banks, *Blood-brain barrier as a regulatory interface.*, in Forum of Nutrition, vol. 63, 2010, p. 102.

[20] W. A. Banks, A. B. Coon, S. M. Robinson, A. Moinuddin, J. M. Shultz, R. Nakaoke, and J. E. Morley, *Triglycerides induce leptin resistance at the blood-brain barrier*, Diabetes, 53 (2004), pp. 1253–1260.

[21] W. A. Banks, P. Pagliari, R. Nakaoke, and J. E. Morley, *Effects of a behaviorally active antibody on the brain uptake and clearance of amyloid beta proteins*, Peptides, 26 (2005), pp. 287–294.

[22] T. M. Bartol Jr, B. Land, E. E. Salpeter, and M. M. Salpeter, *Monte carlo simulation of miniature endplate current generation in the vertebrate neuromuscular junction.*, Biophysical Journal, 59 (1991), p. 1290.

[23] A. Batakis and V. H. Nguyen, *On the exit distribution of partially reflected Brownian motion in planar domains*, Potential Analysis, 38 (2013), pp. 537–548.

[24] D. A. Beard and H. Qian, *Chemical Biophysics: Quantitative Analysis of Cellular Systems*, Cambridge University Press, 2008.

[25] D. Bedeaux and P. Mazur, *Brownian motion and fluctuating hydrodynamics*, Physica, 76 (1974), pp. 247–258.

[26] D. Bedeaux, I. Pagonabarraga, J. O. De Zárate, J. Sengers, and S. Kjelstrup, *Mesoscopic non-equilibrium thermodynamics of non-isothermal reaction-diffusion*, Physical Chemistry Chemical Physics, 12 (2010), pp. 12780–12793.

[27] R. S. Bell, A. H. Vo, C. J. Neal, J. Tigno, R. Roberts, C. Mossop, J. R. Dunne, and R. A. Armonda, *Military traumatic brain and spinal column injury: a 5-year study of the impact blast and other military grade weaponry on the central nervous system*, Journal of Trauma and Acute Care Surgery, 66 (2009), pp. S104–S111.

[28] O. G. Berg, *On diffusion-controlled dissociation*, Chemical Physics, 31 (1978), pp. 47–57.

[29] M. J. Berger and R. J. LeVeque, *Adaptive mesh refinement using wave-propagation algorithms for hyperbolic systems*, SIAM Journal on Numerical Analysis, 35 (1998), pp. 2298–2316.

[30] T. A. Bigelow, T. Northagen, T. M. Hill, and F. C. Sailer, *The destruction of escherichia coli biofilms using high-intensity focused ultrasound*, Ultrasound in Medicine & Biology, 35 (2009), pp. 1026–1031.

[31] J. Bower, D. Maraganore, B. Peterson, S. McDonnell, J. Ahlskog, and W. Rocca, *Head trauma preceding PD a case-control study*, Neurology, 60 (2003), pp. 1610–1615.

[32] K. Burdzy, Z.-Q. Chen, et al., *Discrete approximations to reflected Brownian motion*, Annals of Probability, 36 (2008), pp. 698–727.

[33] C. Bustamante, *In singulo biochemistry: When less is more*, Annual Review of Biochemistry, 77 (2008), pp. 45–50.

[34] D. A. Calhoun, C. Helzel, and R. J. LeVeque, *Logically rectangular grids and finite volume methods for PDEs in circular and spherical domains*, SIAM Review, (2008), pp. 723–752.

[35] Y. Cao, D. T. Gillespie, and L. R. Petzold, *Avoiding negative populations in explicit poisson tau-leaping*, The Journal of Chemical Physics, 123 (2005), p. 054104.

[36] ——, *Efficient step size selection for the tau-leaping simulation method*, The Journal of Chemical Physics, 124 (2006), p. 044109.

[37] I. Cernak, *Chronic traumatic encephalopathy in a national football league player*, Neurosurgery, 57 (2005), pp. 128–134.

[38] I. Cernak and L. J. Noble-Haeusslein, *Traumatic brain injury: an overview of pathobiology with emphasis on military populations*, Journal of Cerebral Blood Flow & Metabolism, 30 (2009), pp. 255–266.

[39] I. Cernak, J. Savic, Z. Malicevic, G. Zunic, P. Radosevic, I. Ivanovic, and L. Davidovic, *Involvement of the central nervous system in the general response to pulmonary blast injury*, Journal of Trauma-Injury, Infection, and Critical Care, 40 (1996), pp. 100S–104S.

[40] I. Cernak, Z. Wang, J. Jiang, X. Bian, and J. Savic, *Ultrastructural and functional characteristics of blast injury-induced neurotrauma*, Journal of Trauma-Injury, Infection, and Critical Care, 50 (2001), pp. 695–706.

[41] A. Chatterjee and D. G. Vlachos, *An overview of spatial microscopic and accelerated kinetic Monte Carlo methods*, Journal of Computer-Aided Materials Design, 14 (2007), pp. 253–308.

[42] H. Chen, A. A. Brayman, W. Kreider, M. R. Bailey, and T. J. Matula, *Observations of translation and jetting of ultrasound-activated microbubbles in mesenteric microvessels*, Ultrasound in Medicine & Biology, 37 (2011), pp. 2139–2148.

[43] A. Chertock, S. Karni, and A. Kurganov, *Interface tracking method for compressible multifluids*, ESAIM: Mathematical Modelling and Numerical Analysis, 42 (2008), pp. 991–1019.

[44] Clawpack Development Team, *Clawpack software*, 2014. Version 5.2.2, http://www.clawpack.org.

[45] C. Coisne, L. Dehouck, C. Faveeuw, Y. Delplace, F. Miller, C. Landry, C. Morissette, L. Fenart, R. Cecchelli, P. Tremblay, et al., *Mouse syngenic in vitro blood–brain barrier model: a new tool to examine inflammatory events in cerebral endothelium*, Laboratory Investigation, 85 (2005), pp. 734–746.

[46] F. C. Collins and G. E. Kimball, *Diffusion-controlled reaction rates*, Journal of Colloidal Science, 4 (1949), pp. 425–437.

[47] ——, *Diffusion-controlled reactions in liquid solutions*, Industrial and Engineering Chemistry, 41 (1949), pp. 2551–2553.

[48] R. Courant, K. Friedrichs, and H. Lewy, *On the partial difference equations of mathematical physics*, IBM Journal, 11 (1967), pp. 215–234.

[49] M.-P. Dehouck, P. Jolliet-Riant, F. Brée, J.-C. Fruchart, R. Cecchelli, and J.-P. Tillement, *Drug transfer across the blood-brain barrier: Correlation between in vitro and in vivo models*, Journal of Neurochemistry, 58 (1992), pp. 1790–1797.

[50] S. DeKosky, *Traumatic brain injuryfootball, warfare, and long-term effects*, New England journal of ..., (2010), pp. 1293–1296.

[51] M. J. Del Razo and R. J. LeVeque, *Code and data to accompany [53].* Github `https://github.com/maojrs/Interface_Euler_AMR/`, 2015.

[52] M. J. Del Razo and R. J. LeVeque, *Computational study of shock waves propagating through air-plastic-water interfaces*, Bulletin of the Brazilian Mathematical Society, New Series 47(2), 1-16, HYP2014 conference proceedings. (2015).

[53] ——, *Numerical methods for interface coupling of compressible and almost incompressible fluids*, (submitted to SIAM Journal on Scientific Computing), (2015).

[54] M. J. Del Razo, Y. Morofuji, J. S. Meabon, B. R. Huber, E. R. Peskind, W. A. Banks, P. D. Mourad, R. J. LeVeque, and D. G. Cook, *Code and data to accompany [55].* Github `https://github.com/maojrs/BBB_experiment/`, 2015.

[55] M. J. Del Razo, Y. Morofuji, J. S. Meabon, B. R. Huber, E. R. Peskind, W. A. Banks, P. D. Mourad, R. J. LeVeque, and D. G. Cook, *Computational and in vitro studies of blast-induced blood-brain barrier disruption*, SIAM Journal on Scientific Computing, 38 (2016), pp. B347–B374.

[56] M. J. Del Razo, W. Pan, H. Qian, and G. Lin, *Fluorescence correlation spectroscopy and nonlinear stochastic reaction–diffusion*, The Journal of Physical Chemistry B, 118 (2014), pp. 7037–7046.

[57] M. J. Del Razo and H. Qian, *A discrete stochastic formulation for reversible bimolecular reactions via diffusion encounter*, Communications in Mathematical Sciences, 14 (2016), pp. 1741–1772.

[58] ——, *On coupled diffusion processes and mesoscopic transition theory under a chemical/material bath*, ((in preparation)).

[59] M. Delbrück, *Statistical fluctuations in autocatalytic reactions*, Journal of Chemical Physics, 8 (1940), pp. 120–124.

[60] M. A. Deli, C. S. Ábrahám, Y. Kataoka, and M. Niwa, *Permeability studies on in vitro blood–brain barrier models: physiology, pathology, and pharmacology*, Cellular and Molecular Neurobiology, 25 (2005), pp. 59–127.

[61] O. B. Dimitrijevic, S. M. Stamatovic, R. F. Keep, and A. V. Andjelkovic, *Effects of the chemokine ccl2 on blood–brain barrier permeability during ischemia–reperfusion injury*, Journal of Cerebral Blood Flow & Metabolism, 26 (2006), pp. 797–810.

[62] M. Doi, *Stochastic theory of diffusion-controlled reaction*, Journal of Physics A: Mathematical and General, 9 (1976), p. 1479.

[63] A. Donev, V. V. Bulatov, T. Oppelstrup, G. H. Gilmer, B. Sadigh, and M. H. Kalos, *A first-passage kinetic monte carlo algorithm for complex diffusion–reaction systems*, Journal of Computational Physics, 229 (2010), pp. 3214–3236.

[64] B. Drawert, S. Engblom, and A. Hellander, *URDME: a modular framework for stochastic simulation of reaction-transport processes in complex geometries*, BMC Systems Biology, 6 (2012), p. 76.

[65] J. P. Dreier, *Neuroimaging, behavioral, and psychological sequelae of repetitive combined blast/impact mild traumatic brain injury in Iraq and afghanistan war veterans*, in Journal of Neurotrauma, vol. 31, 2014, pp. A2–A2.

[66] M. Ehrenberg and R. Rigler, *Rotational brownian motion and fluorescence intensify fluctuations*, Chemical Physics, 4 (1974), pp. 390–401.

[67] B. Einfeldt, *On godunov-type methods for gas dynamics*, SIAM Journal on Numerical Analysis, 25 (1988), pp. 294–318.

[68] A. Einstein, *Investigations on the Theory of the Brownian Movement*, Courier Dover Publications, 1956.

[69] E. L. Elson and D. Magde, *Fluorescence correlation spectroscopy. i. conceptual basis and theory*, Biopolymers, 13 (1974), pp. 1–27.

[70] E. L. Elson and W. W. Webb, *Concentration correlation spectroscopy: a new biophysical probe based on occupation number fluctuations*, Annual Review of Biophysics, 4 (1975), pp. 311–334.

[71] R. Erban and S. J. Chapman, *Stochastic modelling of reaction–diffusion processes: algorithms for bimolecular reactions*, Physical Biology, 6 (2009), p. 046001.

[72] D. M. Erlanger, K. C. Kutner, J. T. Barth, and R. Barnes, *Forum neuropsychology of sports-related head injury: Dementia pugilistica to post concussion syndrome*, The Clinical Neuropsychologist, 13 (1999), pp. 193–209.

[73] L. C. Evans, *An Introduction to Stochastic Differential Equations*, vol. 82, American Mathematical Society, 2012.

[74] K. Fagnan, R. LeVeque, and T. Matula, *Computational models of material interfaces for the study of extracorporeal shock wave therapy*, Communications in Applied Mathematics and Computational Science, 8 (2014), pp. 159–194.

[75] K. Fagnan, R. J. LeVeque, T. J. Matula, and B. MacConaghy, *High-resolution finite volume methods for extracorporeal shock wave therapy*, in Hyperbolic Problems: Theory, Numerics, Applications, Springer, 2008, pp. 503–510.

[76] K. M. Fagnan, *High-resolution Finite Volume Methods for Extracorporeal Shock Wave Therapy*, PhD thesis, University of Washington, 2010.

[77] D. Fange, O. G. Berg, P. Sjöberg, and J. Elf, *Stochastic reaction-diffusion kinetics in the microscopic limit*, Proceedings of the National Academy of Sciences, 107 (2010), pp. 19820–19825.

[78] R. P. Fedkiw, T. Aslam, B. Merriman, and S. Osher, *A non-oscillatory Eulerian approach to interfaces in multimaterial flows (the ghost fluid method)*, Journal of Computational Physics, 152 (1999), pp. 457–492.

[79] G. Feher and M. Weissman, *Fluctuation spectroscopy: Determination of chemical reaction kinetics from the frequency spectrum of fluctuations*, Proceedings of the National Academy of Sciences, 70 (1973), pp. 870–875.

[80] J. Feng, *The hydrodynamic limit for the reaction diffusion equation- an approach in terms of the GPV method*, Journal of Theoretical Probability, 9 (1996), pp. 285–299.

[81] K. W. Ferrara, M. A. Borden, and H. Zhang, *Lipid-shelled vehicles: engineering for ultrasound molecular imaging and drug delivery.*, Accounts of Chemical Research, 42 (2009), pp. 881–892.

[82] M. Fey, *Multidimensional upwinding I. The method of transport for solving the Euler equations*, Journal of Computational Physics, 143 (1998), pp. 159–180.

[83] ——, *Multidimensional upwinding II. decomposition of the Euler equations into advection equations*, Journal of Computational Physics, 143 (1998), pp. 181–199.

[84] R. P. Feynman, R. B. Leighton, and M. Sands, *The Feynman Lectures on Physics, Desktop Edition*, vol. 1, Basic books, 2013.

[85] S. Fleminger, D. Oliver, S. Lovestone, S. Rabe-Hesketh, and A. Giora, *Head injury as a risk factor for alzheimers disease: the evidence 10 years on; a partial replication*, Journal of Neurology, Neurosurgery & Psychiatry, 74 (2003), pp. 857–862.

[86] T. R. Fogarty and R. J. LeVeque, *High-resolution finite-volume methods for acoustic waves in periodic and random media*, The Journal of the Acoustical Society of America, 106 (1999), pp. 17–28.

[87] M. Fujita, E. P. Wei, and J. T. Povlishock, *Intensity-and interval-specific repetitive traumatic brain injury can evoke both axonal and microvascular damage*, Journal of Neurotrauma, 29 (2012), pp. 2172–2180.

[88] C. W. Gardiner, *Handbook of Stochastic Methods*, vol. 3, Springer Berlin, 1985.

[89] B. Geers, I. Lentacker, N. N. Sanders, J. Demeester, S. Meairs, and S. C. De Smedt, *Self-assembled liposome-loaded microbubbles: The missing link for safe and efficient ultrasound triggered drug-delivery.*, Journal of the Controlled Release Society, 152 (2011), pp. 249–56.

[90] M. A. Gibson and J. Bruck, *Efficient exact stochastic simulation of chemical systems with many species and many channels*, The Journal of Physical Chemistry A, 104 (2000), pp. 1876–1889.

[91] D. T. Gillespie, *Approximate accelerated stochastic simulation of chemically reacting systems*, The Journal of Chemical Physics, 115 (2001), pp. 1716–1733.

[92] ——, *Stochastic chemical kinetics*, in Handbook of Materials Modeling, Springer, 2005, pp. 1735–1752.

[93] ——, *Stochastic simulation of chemical kinetics*, Annual Review of Physical Chemistry., 58 (2007), pp. 35–55.

[94] D. T. Gillesple, *Exact stochastic simulation of coupled chemical reactions*, The Journal of Physical Chemistry, 81 (1977), pp. 2340–2361.

[95] S. K. Godunov, *A difference method for numerical calculation of discontinuous solutions of the equations of hydrodynamics*, Matematicheskii Sbornik, 89 (1959), pp. 271–306.

[96] J. Goeller, A. Wardlaw, D. Treichler, J. O'Bruba, and G. Weiss, *Investigation of cavitation as a possible damage mechanism in blast-induced traumatic brain injury*, Journal of Neurotrauma, 29 (2012), pp. 1970–1981.

[97] L. E. Goldstein, A. M. Fisher, C. A. Tagge, X.-L. Zhang, L. Velisek, J. A. Sullivan, C. Upreti, J. M. Kracht, M. Ericsson, M. W. Wojnarowicz, et al., *Chronic traumatic encephalopathy in blast-exposed military veterans and a blast neurotrauma mouse model*, Science Translational Medicine, 4 (2012), pp. 134ra60–134ra60.

[98] I. V. Gopich, K. M. Solntsev, and N. Agmon, *Excited-state reversible geminate reaction. i. two different lifetimes*, Journal of Chemical Physics, 110 (1999), pp. 2164–2174.

[99] I. V. Gopich and A. Szabo, *Kinetics of reversible diffusion influenced reactions: the self-consistent relaxation time approximation*, The Journal of Chemical Physics, 117 (2002), pp. 507–517.

[100] A. Gräslund, R. Rigler, and J. Widengren, *Single Molecule Spectroscopy in Chemistry, Physics and Biology*, Springer, 2010.

[101] D. S. Grebenkov, *Partially reflected brownian motion: a stochastic approach to transport phenomena*, Focus on Probabability Theory, (2006), pp. 135–169.

[102] D. Groot and P. Mazur, *Non-equilibrium Thermodynamics*, Dover, 1984.

[103] R. K. Gupta and A. Przekwas, *Mathematical models of blast-induced TBI: current status, challenges, and prospects*, Frontiers in Neurology, 4 (2013).

[104] M. Hairer, *A theory of regularity structures*, Inventiones mathematicae, 198 (2014), pp. 269–504.

[105] P. Hänggi, P. Talkner, and M. Borkovec, *Reaction-rate theory: Fifty years after Kramers*, Reviews of Modern Physics, 62 (1990), p. 251.

[106] J. Hattne, D. Fange, and J. Elf, *Stochastic reaction-diffusion simulation with mesoRD*, Bioinformatics, 21 (2005), pp. 2923–2924.

[107] A. Hellander, S. Hellander, and L. Per, *Coupled mesoscopic and microscopic simulation of stochastic reaction diffusion processes in mixed dimensions*, Technology, pp. 1–28.

[108] S. Hellander, A. Hellander, and L. Petzold, *Reaction rates for mesoscopic reaction-diffusion kinetics*, Physical Review E, 91 (2015), p. 023312.

[109] M. a. Hemphill, B. E. Dabiri, S. Gabriele, L. Kerscher, C. Franck, J. a. Goss, P. W. Alford, and K. K. Parker, *A possible role for integrin signaling in diffuse axonal injury.*, PlOS One, 6 (2011), p. e22899.

[110] W. J. Heuett and H. Qian, *Grand canonical markov model: a stochastic theory for open nonequilibrium biochemical networks*, The Journal of Chemical Physics, 124 (2006), p. 044110.

[111] D. J. Higham, *An algorithmic introduction to numerical simulation of stochastic differential equations*, SIAM review, 43 (2001), pp. 525–546.

[112] T. L. Hill, *Approach of certain systems, including membranes, to steady state*, Journal of Chemical Physics, 54 (1971), pp. 34–35.

[113] T. L. Hill and I. W. Plesner, *Studies in irreversible thermodynamics. ii. a simple class of lattice models for open systems*, Journal of Chemical Physics, 43 (1965), pp. 267–285.

[114] J. Ho and S. Kleiven, *Dynamic response of the brain with vasculature: a three-dimensional computational study*, Journal of Biomechanics, 40 (2007), pp. 3006–3012.

[115] C. W. Hoge, D. McGurk, J. L. Thomas, A. L. Cox, C. C. Engel, and C. A. Castro, *Mild traumatic brain injury in us soldiers returning from Iraq*, New England Journal of Medicine, 358 (2008), pp. 453–463.

[116] J. Hopfield, *Physics, computation, and why biology looks so different*, Journal of Theoretical Biology, 171 (1994), pp. 53–60.

[117] F. C. Hoppensteadt and C. Peskin, *Mathematics in medicine and the life sciences*, vol. 10, Springer Science & Business Media, 2013.

[118] X. Hu, N. Adams, and G. Iaccarino, *On the HLLC Riemann solver for interface interaction in compressible multi-fluid flow*, Journal of Computational Physics, 228 (2009), pp. 6572–6589.

[119] X. Hu, B. Khoo, N. Adams, and F. Huang, *A conservative interface method for compressible flows*, Journal of Computational Physics, 219 (2006), pp. 553–578.

[120] K. Huang, H. Wu, H. Yu, and D. Yan, *Cures for numerical shock instability in HLLC solver*, International Journal for Numerical Methods in Fluids, 65 (2011), pp. 1026–1038.

[121] B. R. Huber, J. S. Meabon, T. J. Martin, P. D. Mourad, R. Bennett, B. C. Kraemer, I. Cernak, E. C. Petrie, M. J. Emery, E. R. Swenson, et al., *Blast exposure causes early and persistent aberrant phospho-and cleaved-tau expression in a murine model of mild blast-induced traumatic brain injury*, Journal of Alzheimer's disease, 37 (2013), pp. 309–323.

[122] C. D. Hue, S. Cao, S. F. Haider, K. V. Vo, G. B. Effgen, E. Vogel III, M. B. Panzer, C. R. Bass, D. F. Meaney, and B. Morrison III, *Blood-brain barrier dysfunction after primary blast injury in vitro*, Journal of Neurotrauma, 30 (2013), pp. 1652–1663.

[123] C. D. Hue, S. Cao, C. R. Dale Bass, D. F. Meaney, and B. Morrison III, *Repeated primary blast injury causes delayed recovery, but not additive disruption, in an in vitro blood–brain barrier model*, Journal of Neurotrauma, 31 (2014), pp. 951–960.

[124] S. A. Isaacson, *Relationship between the reaction–diffusion master equation and particle tracking models*, Journal of Physics A: Mathematical and Theoretical, 41 (2008), p. 065003.

[125] ——, *A convergent reaction-diffusion master equation*, The Journal of Chemical Physics, 139 (2013), p. 054101.

[126] M. Ivings, D. Causon, and E. Toro, *On Riemann solvers for compressible liquids*, International Journal for Numerical Methods in Fluids, 28 (1998), pp. 395–418.

[127] A. Jacob, B. Hack, E. Chiang, J. G. Garcia, R. J. Quigg, and J. J. Alexander, *C5a alters blood-brain barrier integrity in experimental lupus*, The FASEB Journal, 24 (2010), pp. 1682–1688.

[128] R. Jan, P. Jonas, K. Christian, P. Anna, G. Dorothee, K. Gerd, P. Joerg, et al., *Molecular and structural transmembrane determinants critical for embedding*

claudin-5 into tight junctions reveal distinct four helix bundle arrangement, Biochemical Journal, (2014).

[129] A. K. Kapila, R. Menikoff, J. B. Bdzil, S. F. Son, and D. S. Stewart, *Two-phase modeling of deflagration-to-detonation transition in granular materials: Reduced equations*, Physics of Fluids, 13 (2001), p. 3002.

[130] M. Karplus and J. A. McCammon, *Molecular dynamics simulations of biomolecules.*, Nature structural biology, 9 (2002), pp. 646–52.

[131] J. Keener and J. Sneyd, *Mathematical Physiology*, Springer, 1998.

[132] J. Keizer, *Theory of rapid bimolecular reactions in solution and membranes*, Accounts of Chemical Research, 18 (1985), pp. 235–241.

[133] ——, *Diffusion effects on rapid bimolecular chemical reactions*, Chemical Reviews, 87 (1987), pp. 167–180.

[134] ——, *Statistical Thermodynamics of Nonequilibrium Processes*, Springer, 1987.

[135] S. S. Khokhlova and N. Agmon, *Comparison of alternate approaches for reversible geminate recombination*, Bulletin of the Korean Chemical Society, 33 (2012), p. 1021.

[136] H. Kim and K. J. Shin, *Exact solution of the reversible diffusion-influenced reaction for an isolated pair in three dimensions*, Physical Review Letters, 82 (1999), pp. 1578–1581.

[137] H. Kim, K. J. Shin, and N. Agmon, *Excited-state reversible geminate recombination with quenching in one dimension*, Journal of Chemical Physics, 111 (1999), pp. 3791–3799.

[138] M. T. Klann, A. Lapin, and M. Reuss, *Stochastic simulation of signal transduction: impact of the cellular architecture on diffusion.*, Biophysical Journal, 96 (2009), pp. 5122–9.

[139] S. Kleiven, *Predictors for traumatic brain injuries evaluated through accident reconstructions*, tech. rep., SAE Technical Paper, 2007.

[140] P. E. Kloeden and E. Platen, *Numerical Solution of Stochastic Differential Equations*, Springer, Berlin, 1995.

[141] H. A. Kramers, *Brownian motion in a field of force and the diffusion model of chemical reactions*, Physica, 7 (1940), pp. 284–304.

[142] E. B. Krissinel' and N. Agmon, *Spherical symmetric diffusion problem*, Journal of Computational Chemistry, 17 (1996), pp. 1085–1098.

[143] Y. Kucherov, G. K. Hubler, and R. G. DePalma, *Blast induced mild traumatic brain injury/concussion: A physical analysis*, Journal of Applied Physics, 112 (2012), p. 104701.

[144] T. G. Kurtz, *The relationship between stochastic and deterministic models for chemical reactions*, The Journal of Chemical Physics, 57 (1972), pp. 2976–2978.

[145] P. Langevin, *Sur la théorie du mouvement brownien*, Comptes Rendus de l'Acadmie des Sciences Paris, 146 (1908).

[146] M. Lax, *Fluctuations from the nonequilibrium steady state*, Reviews of Modern Physics, 32 (1960), p. 25.

[147] P. Lax and B. Wendroff, *Systems of conservation laws*, Communications on Pure and Applied Mathematics, 13 (1960), pp. 217–237.

[148] L. Lee and R. J. LeVeque, *An immersed interface method for incompressible navierstokes equations* , Society, 25 (2003), pp. 832–856.

[149] E. J. Lehman, M. J. Hein, S. L. Baron, and C. M. Gersic, *Neurodegenerative causes of death among retired national football league players*, Neurology, 79 (2012), pp. 1970–1974.

[150] G. I. Lemoine, *Numerical modeling of poroelastic-fluid systems using high-resolution finite volume methods*, PhD thesis, University of Washington, 2013.

[151] G. I. Lemoine and M.-Y. Ou, *Finite volume modeling of poroelastic-fluid wave propagation with mapped grids*, SIAM Journal of Scientific Computing, 36 (2014). `http://arxiv.org/abs/1305.2952`.

[152] G. I. Lemoine, M. Y. Ou, and R. J. LeVeque, *High-resolution finite volume modeling of wave propagation in orthotropic poroelastic media*, SIAM Journal on Scientific Computing, 35 (2013), pp. B176–B206.

[153] R. J. LeVeque, *Numerical Methods for Conservation Laws*, vol. 132, Springer, 1992.

[154] ——, *Wave propagation algorithms for multidimensional hyperbolic systems*, Journal of Computational Physics, 131 (1997), pp. 327–353.

[155] R. J. LeVeque, *Finite Volume Methods for Hyperbolic Problems*, Cambridge, 2002.

[156] ——, *Finite Difference Methods for Ordinary and Partial Differential Equations: Steady State and Time Dependent Problems*, Cambridge University Press, 2007.

[157] M. Levitt, *The birth of computational structural biology.*, Nature structural biology, 8 (2001), pp. 392–3.

[158] G. N. Lewis, *A new principle of equilibrium*, Proceedings of the National Academy of Sciences, 11 (1925), p. 179.

[159] Y. Li, M. Chavko, J. L. Slack, B. Liu, R. M. McCarron, J. D. Ross, and J. J. Dalle Lucca, *Protective effects of decay-accelerating factor on blast-induced neurotrauma in rats*, Acta Neuropathologica Communications, 1 (2013), p. 52.

[160] T. Liu, B. Khoo, and W. Xie, *Isentropic one-fluid modelling of unsteady cavitating flow*, Journal of Computational Physics, 201 (2004), pp. 80–108.

[161] T. Liu, B. Khoo, and K. Yeo, *Ghost fluid method for strong shock impacting on material interface*, Journal of Computational Physics, 190 (2003), pp. 651–681.

[162] D. Magde, E. L. Elson, and W. W. Webb, *Thermodynamic fluctuations in a reacting system measurement by fluorescence correlation spectroscopy*, Physical Review Letters, 29 (1972), pp. 705–708.

[163] P. D. Maia and J. N. Kutz, *Compromised axonal functionality after neurodegeneration, concussion and/or traumatic brain injury*, Journal of Computational Neuroscience, 27 (2014), pp. 317–332.

[164] ——, *Identifying critical regions for spike propagation in axon segments*, Journal of Computational Neuroscience, 36 (2014), pp. 141–155.

[165] X. Mao and C. Yuan, *Stochastic differential equations with Markovian switching*, World Scientific, 2006.

[166] R. A. Marcus and N. Sutin, *Electron transfers in chemistry and biology*, BBA Bioenergetics, 811 (1985), pp. 265–322.

[167] H. F. Mark, *Encyclopedia of polymer science and technology, concise*, John Wiley & Sons, 2013.

[168] S. C. Matthews, I. A. Strigo, A. N. Simmons, R. M. O'Connell, L. E. Reinhardt, and S. A. Moseley, *A multimodal imaging study in us veterans of operations iraqi and enduring freedom with and without major depression after blast-related concussion*, Neuroimage, 54 (2011), pp. S69–S75.

[169] M. A. Mayorga, *The pathology of primary blast overpressure injury*, Toxicology, 121 (1997), pp. 17–28.

[170] N. McDannold, N. Vykhodtseva, and K. Hynynen, *Targeted disruption of the blood–brain barrier with focused ultrasound: association with cavitation activity*, Physics in Medicine and Biology, 51 (2006), p. 793.

[171] N. McDannold, N. Vykhodtseva, and K. Hynynen, *Blood-brain barrier disruption induced by focused ultrasound and circulating preformed microbubbles appears to be characterized by the mechanical index*, Ultrasound in Medicine & Biology, 34 (2008), pp. 834–840.

[172] A. C. McKee, R. C. Cantu, C. J. Nowinski, E. T. Hedley-Whyte, B. E. Gavett, A. E. Budson, V. E. Santini, H.-S. Lee, C. A. Kubilus, and R. A. Stern, *Blast injuries of the lung: development, prognosis and possible therapy*, Vojnosanit Pregl., 54 (1997), pp. 91–102.

[173] ——, *Chronic traumatic encephalopathy in athletes: progressive tauopathy following repetitive head injury*, Journal of Neuropathology and Experimental Neurology, 68 (2009), p. 709.

[174] A. C. McKee and M. E. Robinson, *Military-related traumatic brain injury and neurodegeneration*, Alzheimer's & Dementia, 10 (2014), pp. S242–S253.

[175] D. F. Moore, A. Jérusalem, M. Nyein, L. Noels, M. S. Jaffee, and R. A. Radovitzky, *Computational biologymodeling of primary blast effects on the central nervous system*, Neuroimage, 47 (2009), pp. T10–T20.

[176] W. C. Moss, M. J. King, and E. G. Blackman, *Skull flexure from blast waves: a mechanism for brain injury with implications for helmet design*, Physical Review Letters, 103 (2009), p. 108702.

[177] J. D. Murray, *Mathematical Biology I: An Introduction, vol. 17 of Interdisciplinary Applied Mathematics*, Springer, New York, NY, USA,, 2002.

[178] J. Murthy, J. Chopra, and D. Gulati, *Subdural hematoma in an adult following a blast injury: Case report*, Journal of Neurosurgery, 50 (1979), pp. 260–261.

[179] R. Nakaoke, J. S. Ryerse, M. Niwa, and W. A. Banks, *Human immunodeficiency virus type 1 transport across the in vitro mouse brain endothelial cell monolayer*, Experimental Neurology, 193 (2005), pp. 101–109.

[180] A. Neumaier, *Molecular modeling of proteins and mathematical prediction of protein structure*, SIAM Review, 39 (1997), pp. 407–460.

[181] T. Nitta, M. Hata, S. Gotoh, Y. Seo, H. Sasaki, N. Hashimoto, M. Furuse, and S. Tsukita, *Size-selective loosening of the blood-brain barrier in claudin-5–deficient mice*, The Journal of Cell Biology, 161 (2003), pp. 653–660.

[182] M. K. Nyein, A. M. Jason, L. Yu, C. M. Pita, J. D. Joannopoulos, D. F. Moore, and R. A. Radovitzky, *In silico investigation of intracranial blast mitigation with relevance to military traumatic brain injury*, Proceedings of the National Academy of Sciences, 107 (2010), pp. 20703–20708.

[183] C.-D. Ohl, M. Arora, R. Ikink, N. de Jong, M. Versluis, M. Delius, and D. Lohse, *Sonoporation from jetting cavitation bubbles*, Biophysical Journal, 91 (2006), pp. 4285–4295.

[184] B. Oksendal, *Stochastic Differential Equations: An Introduction with Applications*, Springer Science & Business Media, 2013.

[185] L. Onsager, *Reciprocal relations in irreversible processes. II.*, Physical Review, 38 (1931), p. 2265.

[186] L. Onsager and S. Machlup, *Fluctuations and irreversible processes*, Physical Review, 91 (1953), pp. 1505–1512.

[187] B. D. Owens, J. F. Kragh Jr, J. C. Wenke, J. Macaitis, C. E. Wade, and J. B. Holcomb, *Combat wounds in operation iraqi freedom and operation enduring freedom*, Journal of Trauma and Acute Care Surgery, 64 (2008), pp. 295–299.

[188] I. Pagonabarraga, A. Pérez-Madrid, and J. Rubi, *Fluctuating hydrodynamics approach to chemical reactions*, Physica A: Statistical Mechanics and its Applications, 237 (1997), pp. 205–219.

[189] M. B. Panzer, B. S. Myers, B. P. Capehart, and C. R. Bass, *Development of a finite element model for blast brain injury and the effects of csf cavitation*, Annals of Biomedical Engineering, 40 (2012), pp. 1530–1544.

[190] M. Pelanti and K.-M. Shyue, *A mixture-energy-consistent six-equation two-phase numerical model for fluids with interfaces, cavitation and evaporation waves*, Journal of Computational Physics, 259 (2014), pp. 331–357.

[191] J. R. Perez-Polo, H. C. Rea, K. M. Johnson, M. A. Parsley, G. C. Unabia, G. Xu, S. K. Infante, D. S. DeWitt, and C. E. Hulsebosch, *Inflammatory consequences in a rodent model of mild traumatic brain injury*, Journal of Neurotrauma, 30 (2013), pp. 727–740.

[192] N. Perriere, P. Demeuse, E. Garcia, A. Regina, M. Debray, J.-P. Andreux, P. Couvreur, J.-M. Scherrmann, J. Temsamani, P.-O. Couraud, et al., *Puromycin-based purification of rat brain capillary endothelial cell cultures. effect on the expression of blood–brain barrier-specific properties*, Journal of Neurochemistry, 93 (2005), pp. 279–289.

[193] E. R. Peskind, D. G. Cook, et al., *Cerebrocerebellar hypometabolism associated with repetitive blast exposure mild traumatic brain injury in 12 Iraq war veterans with persistent post-concussive symptoms*, Neuroimage, 54 (2011), pp. S76–S82.

[194] E. R. Peskind, E. C. Petrie, D. J. Cross, K. Pagulayan, K. McCraw, D. Hoff, K. Hart, C.-E. Yu, M. a. Raskind, D. G. Cook, and S. Minoshima, *Cerebrocerebellar hypometabolism associated with repetitive blast exposure mild traumatic brain injury in 12 Iraq war Veterans with persistent post-concussive symptoms.*, NeuroImage, 54 Suppl 1 (2011), pp. S76–82.

[195] E. Pines, D. Huppert, and N. Agmon, *Geminate recombination in excited-state proton-transfer reactions: numerical solution of the Debye–Smoluchowski equation with backreaction and comparison with experimental results*, The Journal of Chemical Physics, 88 (1988), pp. 5620–5630.

[196] B. L. Plassman, R. Havlik, D. Steffens, M. Helms, T. Newman, D. Drosdick, C. Phillips, B. Gau, K. Welsh-Bohmer, J. Burke, et al., *Documented head injury in early adulthood and risk of alzheimers disease and other dementias*, Neurology, 55 (2000), pp. 1158–1166.

[197] A. V. Popov and N. Agmon, *Three-dimensional simulation verifies theoretical asymptotics for reversible binding*, Chemical Physics Letters, 340 (2001), pp. 151–156.

[198] ——, *Three-dimensional simulations of reversible bimolecular reactions: the simple target problem*, The Journal of Chemical Physics, 115 (2001), pp. 8921–8932.

[199] T. Prüstel and M. Meier-Schellersheim, *Exact green's function of the reversible diffusion-influenced reaction for an isolated pair in two dimensions*, The Journal of Chemical Physics, 137 (2012), p. 054104.

[200] ——, *Theory of reversible diffusion-influenced reactions with non-markovian dissociation in two space dimensions*, The Journal of Chemical Physics, 138 (2013), p. 104112.

[201] ——, *Rate coefficients, binding probabilities, and related quantities for area reactivity models*, The Journal of Chemical Physics, 141 (2014), p. 194115.

[202] A. Przekwas, M. Somayaji, and Z. Chen, *A mathematical model coupling neuroexcitation, astrocyte swelling and perfusion in mild TBI*, in International State-of-the-Science Meeting on Non-Impact, Blast-Induced Mild Traumatic Brain Injury, VA Herndon, 2009.

[203] H. Qian, *An asymptotic comparative analysis of the thermodynamics of non-covalent association*, Journal of Mathematical Biology, 41 (2000), pp. 331–340.

[204] ——, *Phosphorylation energy hypothesis: open chemical systems and their biological functions*, Annual Review of Physical Chemistry., 58 (2007), pp. 113–142.

[205] ——, *Cellular biology in terms of stochastic nonlinear biochemical dynamics: emergent properties, isogenetic variations and chemical system inheritability*, Journal of Statistical Physics, 141 (2010), pp. 990–1013.

[206] ——, *Nonlinear stochastic dynamics of mesoscopic homogeneous biochemical reaction systems — An analytical theory*, Nonlinearity, 24 (2011), pp. R19–R49.

[207] H. Qian and L. M. Bishop, *The chemical master equation approach to nonequilibrium steady-state of open biochemical systems: linear single-molecule enzyme kinetics and nonlinear biochemical reaction networks*, International Journal of Molecular Sciences, 11 (2010), pp. 3472–3500.

[208] H. Qian and S. Kou, *Statistics and related topics in single-molecule biophysics*, Annual Review of Statistics and Its Application, 1 (2014), pp. 465–492.

[209] A. Raj and A. van Oudenaarden, *Nature, nurture or chance: Stochastic gene expression and its consequences*, Cell 135, (2008).

[210] J. Raynal, *Computing as a language of physics*, IAEA, Vienna, 281 (1972).

[211] R. D. Readnower, M. Chavko, S. Adeeb, M. D. Conroy, J. R. Pauly, R. M. McCarron, and P. G. Sullivan, *Increase in blood–brain barrier permeability, oxidative stress, and activated microglia in a rat model of blast-induced traumatic brain injury*, Journal of Neuroscience Research, 88 (2010), pp. 3530–3539.

[212] D. Reguera, J. Rubi, and J. Vilar, *The mesoscopic dynamics of thermodynamic systems*, The Journal of Physical Chemistry B, 109 (2005), pp. 21502–21515.

[213] D. V. Reneer, R. D. Hisel, J. M. Hoffman, R. J. Kryscio, B. T. Lusk, and J. W. Geddes, *A multi-mode shock tube for investigation of blast-induced traumatic brain injury.*, Journal of Neurotrauma, 28 (2011), pp. 95–104.

[214] R. Rigler and E. Elson, *Fluorescence Correlation Spectroscopy: Theory and Applications.*, Springer Series in Chemical Physics, vol. 65, 2001.

[215] P. L. Roe, *Approximate riemann solvers, parameter vectors, and difference schemes*, Journal of Computational Physics, 43 (1981), pp. 357–372.

[216] ——, *Discrete models for the numerical analysis of time-dependent multidimensional gas dynamics*, in Upwind and High-Resolution Schemes, Springer, 1986, pp. 451–469.

[217] J. S. Ruan, T. B. Khalil, and A. I. King, *Finite element modeling of direct head impact*, tech. rep., SAE Technical Paper, 1993.

[218] V. Rubovitch, M. Ten-Bosch, O. Zohar, C. R. Harrison, C. Tempel-Brami, E. Stein, B. J. Hoffer, C. D. Balaban, S. Schreiber, W.-T. Chiu, et al., *A mouse model of blast-induced mild traumatic brain injury*, Experimental Neurology, 232 (2011), pp. 280–289.

[219] P. G. Saffman and M. Delbrück, *Brownian motion in biological membranes*, Proceedings of the National Academy of Sciences, 72 (1975), pp. 3111–3113.

[220] R. Saurel and R. Abgrall, *A simple method for compressible multifluid flows*, SIAM Journal on Scientific Computing, 21 (1999), pp. 1115–1145.

[221] R. Saurel and O. Lemetayer, *A multiphase model for compressible flows with interfaces, shocks, detonation waves and cavitation*, Journal of Fluid Mechanics, 431 (2001), pp. 239–271.

[222] R. Saurel, F. Petitpas, and R. A. Berry, *Simple and efficient relaxation methods for interfaces separating compressible fluids, cavitating flows and shocks in multiphase mixtures*, Journal of Computational Physics, 228 (2009), pp. 1678–1712.

[223] J. Schöneberg and F. Noé, *ReaDDy-A software for particle-based reaction-diffusion dynamics in crowded cellular environments*, PlOS One, 8 (2013), p. e74261.

[224] J. M. Schurr, *The role of diffusion in bimolecular solution kinetics*, Biophysical Journal, 10 (1970), p. 700.

[225] Z. Schuss, *Theory and applications of stochastic processes: an analytical approach*, vol. 170, Springer Science & Business Media, 2009.

[226] A. K. Shetty, V. Mishra, M. Kodali, and B. Hattiangady, *Blood brain barrier dysfunction and delayed flogical deficits in mild traumatic brain injury induced by blast shock waves*, Frontiers in Cellular Neuroscience, 8 (2014).

[227] D. Shoup and A. Szabo, *Role of diffusion in ligand binding to macromolecules and cell-bound receptors*, Biophysical Journal, 40 (1982), pp. 33–39.

[228] D. I. Shreiber, A. C. Bain, and D. F. Meaney, *In vivo thresholds for mechanical injury to the blood-brain barrier*, tech. rep., SAE Technical Paper, 1997.

[229] K.-M. Shyue, *An efficient shock-capturing algorithm for compressible multicomponent problems*, Journal of Computational Physics, 142 (1998), pp. 208–242.

[230] M. v. Smoluchowski, *Versuch einer mathematischen theorie der koagulationskinetik kolloider lösungen*, Zeitschrift fuer Physikalische Chemie, 92 (1917), p. 9.

[231] T. Sokolowski, L. Bossen, T. Miedema, and N. Becker, *Greens function reaction dynamicsan exact and efficient way to simulate intracellular pattern formation*, in ICNAAM 2010: International Conference of Numerical Analysis and Applied Mathematics 2010, vol. 1281, AIP Publishing, 2010, pp. 1342–1345.

[232] A. Sundaramurthy, A. Alai, S. Ganpule, A. Holmberg, E. Plougonven, and N. Chandra, *Blast-induced biomechanical loading of the rat: an experimental and anatomically accurate computational blast injury model*, Journal of Neurotrauma, 29 (2012), pp. 2352–2364.

[233] K. R. Swanson, E. Alvord, and J. Murray, *Virtual brain tumours (gliomas) enhance the reality of medical imaging and highlight inadequacies of current therapy*, British Journal of Cancer, 86 (2002), pp. 14–18.

[234] P. K. Sweby, *High resolution schemes using flux limiters for hyperbolic conservation laws*, SIAM Journal on Numerical Analysis, 21 (1984), pp. 995–1011.

[235] A. Szabo, *Theory of diffusion-influenced fluorescence quenching*, The Journal of Physical Chemistry, 93 (1989), pp. 6929–6939.

[236] A. Szabo, K. Schulten, and Z. Schulten, *First passage time approach to diffusion controlled reactions*, The Journal of Chemical Physics, 72 (1980), pp. 4350–4357.

[237] K. Takahashi, S. Tănase-Nicola, and P. R. Ten Wolde, *Spatio-temporal correlations can drastically change the response of a mapk pathway*, Proceedings of the National Academy of Sciences, 107 (2010), pp. 2473–2478.

[238] E. G. Takhounts, R. H. Eppinger, J. Q. Campbell, R. E. Tannous, E. D. Power, and L. S. Shook, *On the development of the simon finite element head model*, tech. rep., SAE Technical Paper, 2003.

[239] E. G. Takhounts, S. A. Ridella, V. Hasija, R. E. Tannous, J. Q. Campbell, D. Malone, K. Danelson, J. Stitzel, S. Rowson, and S. Duma, *Investigation of traumatic brain injuries using the next generation of simulated injury monitor (simon) finite element head model*, Stapp Car Crash J, 52 (2008), pp. 1–31.

[240] H. M. Taylor and S. Karlin, *An Introduction to Stochastic Modeling*, Academic press, 2014.

[241] P. A. Taylor and C. C. Ford, *Simulation of blast-induced early-time intracranial wave physics leading to traumatic brain injury*, Journal of Biomechanical Engineering, 131 (2009), p. 061007.

[242] H. Terrio, L. A. Brenner, B. J. Ivins, J. M. Cho, K. Helmick, K. Schwab, K. Scally, R. Bretthauer, and D. Warden, *Traumatic brain injury screening: preliminary findings in a us army brigade combat team*, The Journal of Head Trauma Rehabilitation, 24 (2009), pp. 14–23.

[243] S. Tokuda, T. Higashi, and M. Furuse, *ZO-1 knockout by talen-mediated gene targeting in MDCK cells: Involvement of ZO-1 in the regulation of cytoskeleton and cell shape*, PlOS One, 9 (2014), p. e104994.

[244] M. Tomita, K. Hashimoto, K. Takahashi, T. S. Shimizu, Y. Matsuzaki, F. Miyoshi, K. Saito, S. Tanida, K. Yugi, J. C. Venter, et al., *E-cell: software environment for whole-cell simulation.*, Bioinformatics, 15 (1999), pp. 72–84.

[245] O. Tomkins, A. Feintuch, M. Benifla, A. Cohen, A. Friedman, and I. Shelef, *Blood-brain barrier breakdown following traumatic brain injury: a possible role in posttraumatic epilepsy*, Cardiovascular Psychiatry and Neurology, 2011 (2011).

[246] D. C. Torney and H. M. McConnell, *Diffusion-limited reaction rate theory for two-dimensional systems*, Proceedings of the Royal Society of London, Series A, 387 (1983), pp. 147–170.

[247] ——, *Diffusion-limited reactions in one dimension*, The Journal of Physical Chemistry, 87 (1983), pp. 1941–1951.

[248] E. F. Toro, *Riemann Solvers and Numerical Methods for Fluid Dynamics*, Springer, 2008.

[249] E. F. Toro, M. Spruce, and W. Speares, *Restoration of the contact surface in the HLL-Riemann solver*, Shock Waves, 4 (1994), pp. 25–34.

[250] Y.-S. Tung, J. J. Choi, B. Baseri, and E. E. Konofagou, *Identifying the inertial cavitation threshold and skull effects in a vessel phantom using focused ultrasound and microbubbles*, Ultrasound in Medicine & Biology, 36 (2010), pp. 840–852.

[251] Y.-S. Tung, F. Vlachos, J. J. Choi, T. Deffieux, K. Selert, and E. E. Konofagou, *In vivo transcranial cavitation threshold detection during ultrasound-induced blood–brain barrier opening in mice*, Physics in Medicine and Biology, 55 (2010), p. 6141.

[252] H. Udaykumar, R. Mittal, and P. Rampunggoon, *Interface tracking finite volume method for complex solid–fluid interactions on fixed meshes*, Communications in Numerical Methods in Engineering, 18 (2002), pp. 89–97.

[253] G. E. Uhlenbeck and L. S. Ornstein, *On the theory of the brownian motion*, Physical Review, 36 (1930), p. 823.

[254] N. G. Van Kampen, *Stochastic Processes in Physics and Chemistry*, vol. 1, Elsevier, 1992.

[255] B. Van Leer, *Towards the ultimate conservative difference scheme. v. a second-order sequel to godunov's method*, Journal of Computational Physics, 32 (1979), pp. 101–136.

[256] J. S. van Zon and P. R. Ten Wolde, *Green's-function reaction dynamics: A particle-based approach for simulating biochemical networks in time and space*, The Journal of Chemical Physics, 123 (2005), p. 4910.

[257] ——, *Simulating biochemical networks at the particle level and in time and space: Green's function reaction dynamics*, Physical Review Letters, 94 (2005), p. 128103.

[258] M. Vellela and H. Qian, *Stochastic dynamics and non-equilibrium thermodynamics of a bistable chemical system: the Schlögl model revisited*, Journal of The Royal Society Interface, 6 (2009), pp. 925–940.

[259] W. Wakeland and B. Goldstein, *A computer model of intracranial pressure dynamics during traumatic brain injury that explicitly models fluid flows and volumes*, in Intracranial Pressure and Brain Monitoring XII, Springer, 2005, pp. 321–326.

[260] C. Wang, H. Tang, and T. Liu, *An adaptive ghost fluid finite volume method for compressible gas–water simulations*, Journal of Computational Physics, 227 (2008), pp. 6385–6409.

[261] F.-S. Wang, C.-J. Wang, H.-J. Huang, H. Chung, R.-F. Chen, and K. D. Yang, *Physical shock wave mediates membrane hyperpolarization and ras activation for osteogenesis in human bone marrow stromal cells*, Biochemical and Biophysical Research Communications, 287 (2001), pp. 648–655.

[262] H. Wang, C. S. Peskin, and T. C. Elston, *A robust numerical algorithm for studying biomolecular transport processes*, Journal of Theoretical Biology, 221 (2003), pp. 491–511.

[263] D. L. Warden, L. M. French, L. Shupenko, J. Fargus, G. Riedy, M. E. Erickson, M. S. Jaffee, and D. F. Moore, *Case report of a soldier with primary blast brain injury*, Neuroimage, 47 (2009), pp. T152–T153.

[264] A. Weisberger, S. Friess, and E. Lewis, *Techniques of organic chemistry*, Vol. III, Part I, Interscience, New York, (1953).

[265] G. H. Weiss, *Overview of theoretical models for reaction rates*, Journal of Statistical Physics, 42 (1986), pp. 3–36.

[266] M. B. Weissman, *Fluctuation spectroscopy*, Annual Review of Physical Chemistry., 32 (1981), pp. 205–232.

[267] D. J. Wilkinson, *Stochastic Modelling for Systems Biology*, CRC press, 2011.

[268] S. Wils and E. De Schutter, *STEPS: Modeling and simulating complex reaction-diffusion systems with Python*, Frontiers in Neuroinformatics, 3 (2009), p. art. no. 15.

[269] B. E. Wojcik, C. R. Stein, K. Bagg, R. J. Humphrey, and J. Orosco, *Traumatic brain injury hospitalizations of us army soldiers deployed to afghanistan and Iraq*, American Journal of Preventive Medicine, 38 (2010), pp. S108–S116.

[270] X. S. Xie, P. J. Choi, G.-W. Li, N. K. Lee, and G. Lia, *Single-molecule approach to molecular biology in living bacterial cells*, Annual Review of Biophysics, 37 (2008), pp. 417–444.

[271] X. S. Xie and J. Trautman, *Single-molecule optical studies at room temperature*, Annual Review of Physical Chemistry, 49 (1998), pp. 441–480.

[272] Y. Xiong, A. Mahmood, and M. Chopp, *Animal models of traumatic brain injury*, Nature Reviews Neuroscience, 14 (2013), pp. 128–142.

[273] Z. Xu, J. B. Fowlkes, and C. A. Cain, *A new strategy to enhance cavitational tissue erosion using a high-intensity, initiating sequence*, Ultrasonics, Ferroelectrics and Frequency Control, IEEE Transactions on, 53 (2006), pp. 1412–1424.

[274] S. Yeoh, E. D. Bell, and K. L. Monson, *Distribution of blood–brain barrier disruption in primary blast injury*, Annals of Biomedical Engineering, 41 (2013), pp. 2206–2214.

[275] L. Zhilin and L. R. J, *The immersed interface method for elliptic equations with discontinuous coefficients and singular sources*, SIAM Journal on Numerical Analysis, 31 (2011), pp. 1019–1044.

[276] C. Zhou, T. Khalil, and A. I. King, *Viscoelastic response of the human brain to sagittal and lateral rotational acceleration by finite element analysis*, in Proceedings of the International Research Council on the Biomechanics of Injury conference, vol. 24, International Research Council on Biomechanics of Injury, 1997, pp. 35–48.

[277] M. Ziejewski, G. Karami, and A. Akhatov, *Selected biomechanical issues of brain injury caused by blasts*, Brain Injury, 4 (2007), pp. 10–15.

[278] R. M. Ziff, E. Gulari, and Y. Barshad, *Kinetic Phase Transitions in an Irreversible Surface-Reaction Model*, Physical Review Letters, (1986).

[279] B. V. Zlokovic, *Neurovascular pathways to neurodegeneration in alzheimer's disease and other disorders*, Nature Reviews Neuroscience, 12 (2011), pp. 723–738.